

UTILIZING FLUIDIC PLATFORMS FOR THE DEVELOPMENT OF *IN VITRO*
PHARMACOKINETIC/PHARMACODYNAMIC MODELS

By

Sarah Yvonne Lockwood

A DISSERTATION

Submitted to
Michigan State University
in partial fulfillment of the requirements
for the degree of

Chemistry – Doctor of Philosophy

2014

ABSTRACT

UTILIZING FLUIDIC PLATFORMS FOR THE DEVELOPMENT OF *IN VITRO* PHARMACOKINETIC/PHARMACODYNAMIC MODELS

By

Sarah Yvonne Lockwood

The pharmaceutical industry is constantly developing new therapies and treatments, while the cost of the drug discovery process currently is estimated at two billion dollars, spent over a 12-15 year period. Adding to the cost associated with bringing a drug to market is the high attrition rate, with only 1 in every 10,000 compounds being approved by the Food and Drug Administration. Interest in reassessing existing research procedures for improved efficiency has recently been garnering attention. Specifically, pharmacology studies, which utilize *in vivo* studies to obtain pharmacokinetic (PK) and pharmacodynamic (PD) information during the preclinical stage of the drug discovery process, have been a focal point. By complimenting the *in vivo* studies with *in vitro* models, an increase in efficiency is able to be realized by a reduction in consumed materials.

In this dissertation, a diffusion-based dynamic *in vitro* (DDIV) PK model, fabricated on a microfluidic polydimethyl siloxane (PDMS) platform, was used to characterize the loading and elimination of a PK profile. However, challenges traditionally associated with the microfluidic devices, such as the fragility of the membrane due to device flexibility, reusability, and lack of automation make long-term PK studies incredibly difficult to perform, as well as reproduce.

DDIV models fabricated on a rigid three-dimensional (3D) printed platform are rugged, reusable, and amenable to automation when integrated with a disposable cell culture insert. The 3D printed DDIV PK/PD device was characterized using fluorescein (332.31 g/mol) and validated using the antibiotic levofloxacin (361.37 g/mol). The loading profiles were achieved by flowing concentrated analyte through the device channels while adding buffer to the membrane insert to create a concentration gradient across the porous membrane, thereby allowing diffusion from the channel into the insert. Parameters related to the loading portion of a PK curve, such as loading time, flow rate, volume of the insert, and initial concentration in the channel were characterized. The profiles obtained during the characterization of the initial concentrations (7.5, 15, 30 μM) in the channel yielded a prediction model for both the concentration along the loading profile and the maximum concentration (C_{max}) at a given loading time.

Elimination of analyte from the membrane insert was proven to undergo first order rate kinetics. The elimination profile, and the resulting elimination rate constant are used to obtain the half-life. Ultimately, a prediction model for the half-life will be crucial to the characterization of the DDIV model, however preliminary gradient studies highlighted the importance of a correction factor pertaining to the amount of analyte absorbed by the device. Upon complete characterization, the reusable 3D printed DDIV PK/PD millifluidic device will allow researchers to mimic *in vivo* dosing regimens on an *in vitro* platform, resulting in a useful tool to be used in tandem with animal models.

By failing to prepare, you are preparing to fail.
-Benjamin Franklin

ACKNOWLEDGEMENTS

I would first like to thank the organizations, which funded my research, thereby making this dissertation possible. The College of Natural Science and the Graduate School helped fund travel to the many conferences I have attended throughout my four years. Merck was responsible for the majority of my research, particularly the transition to 3D printing. I would also like to thank the RTSF Mass Spectrometry Facility for all of their assistance running samples and fielding my many questions, especially Lijun Chen. A special thanks goes to Dr. Brian Wright of the Department of Electrical and Computer Engineering, for all of his help answering my enquiries pertaining to 3D printing and the associated Computer Aided Design Software.

I would also like to thank my guidance committee, Dr. Gary Blanchard, Dr. John McCracken, and Dr. Anne Dorrance. Their support throughout the years was both beneficial and much appreciated. Furthermore, I would like to thank Dr. Kathy Severin who was always willing to help train or offer advice. CEM185H with Kathy was by far my favorite teaching experience during my time in graduate school.

I have been fortunate with a wonderful research group (2010-2014) who have become like family. I would like to thank Dr. Kari Anderson, Dr. Suzanne Summers, and Dr. Steve Halpin for their guidance and patience during my first years in the group. Specifically, Steve for performing some of the

preliminary *in vitro* pharmacokinetic studies and Kari, who collaborated with me for some of the early 3D printing prototypes. I was a first year in the Spence group with Mrs. Jayda Erkal, Ms. Yueli Liu, and Ms. Bethany Gross. I am forever grateful for their support and tenacity through all of the ups and downs of graduate school. Furthermore, I would like to thank Jayda for teaching me what it really meant to study and for all of her work during our bacteria dosing collaboration.

I would also like to thank my advisor, i.e., mentor, Dr. Dana Spence for all of his encouragement over the last four years. Under his guidance I have grown, not only as a researcher but also as a person. I would like to thank Spence for bringing his strong family values into the research group and treating us like family. This mentality truly makes the Spence group a unique and exceptional place to do research.

Lastly, I would like to extend my gratitude toward my family for their constant encouragement, not only through graduate school but also throughout my life. I am blessed to have had supportive, caring parents. I would like to thank my dad for instilling a mentality for hard work and finishing the job that is started. I would like to thank my mom for inspiring my curiosity and love of science/learning from a young age. I would also like to thank my fiancé, Luke, for his patience throughout this process. I will be forever grateful for his selflessness, especially during my second year. His willingness to spend excessive time in the chemistry building just so we could spend time together when I was working long hours, made trying times enjoyable, fond memories. Thank you.

TABLE OF CONTENTS

LIST OF TABLES	xi
LIST OF FIGURES	xii
CHAPTER 1	1
INTRODUCTION.....	2
1.1 Pharmaceutical Industry Current State of Affairs.....	2
1.2 General Drug Development Process.....	5
1.2.1 Drug Prediscovery.....	5
1.2.2 Drug Discovery.....	6
1.2.3. Drug Development.....	6
1.2.3.1 Preclinical.....	6
1.2.3.2 Pharmacodynamics.....	7
1.2.3.3 Pharmacokinetics.....	9
<i>Absorption</i>	9
<i>Distribution</i>	11
<i>Metabolism</i>	14
<i>Excretion</i>	15
<i>Pharmacokinetic Parameters</i>	15
1.2.3.4 <i>In Vivo</i> Animal Pharmacokinetics.....	19
1.2.3.5 <i>In Vitro</i> Pharmacokinetics.....	21
<i>Static Models</i>	23
<i>Dilution Based Dynamic Models</i>	23
<i>Diffusion-Based Dynamic Models</i>	25
1.2.3.6 Clinical Trials.....	27
<i>Phase I</i>	27
<i>Phase II</i>	28
<i>Phase III</i>	28
1.3 Microfluidic Applications.....	28
1.3.1 Pharmacokinetic/Pharmacodynamic Microfluidic Platforms.....	30
REFERENCES	33
CHAPTER 2	47
UTILIZING POLYDIMETHYL-SILOXANE-BASED MICROFLUIDIC DEVICES FOR ANALYSIS OF ENDOTHELIUM-DERIVED NITRIC OXIDE PRODUCTION STIMULATED BY ADENOSINE TRIPHOSPHATE RELEASED FROM RED BLOOD CELLS INCUBATED WITH HYDROXYUREA.....	48

2.1 Red Blood Cells and the Vascular System.....	48
2.1.1 Red Blood Cell-Derived Adenosine Triphosphate.....	50
2.1.2 Mechanism of Nitric Oxide Stimulation.....	52
2.2 Sickle Cell Disease.....	53
2.2.1 Use of Hydroxyurea as a Sickle Cell Disease Treatment.....	54
2.3 Utilizing Microfluidics for Investigating <i>In Vitro</i> Cell to Cell Interactions.....	55
2.4 Adenosine Triphosphate Release in Hydroxyurea Incubated Human Red Blood Cells.....	56
2.5 Experimental.....	57
2.5.1 Materials and Methods.....	57
2.5.1.1 Fabrication of Master.....	57
2.5.1.2 Polydimethyl Siloxane (PDMS) Device Fabrication.....	60
2.5.1.3 Preparation of Regents.....	64
<i>Collection and Purification of Human Red Blood Cells.....</i>	64
<i>Immobilizing Endothelial Cells in Wells.....</i>	64
2.5.2 Fluorescence Determination of Nitric Oxide Released from Endothelial Cells.....	65
2.5.2.1 Macroscope Fluorescence Detection.....	65
2.5.4.2 Plate Reader Fluorescence Detection.....	69
2.6 Results and Discussion.....	71
2.6.1 Macroscope Fluorescence Detection of Endothelium Nitric Oxide Stimulated from Red Blood Cell-Derived Adenosine Triphosphate.....	71
2.6.2 Plate Reader Fluorescence Detection of Endothelium Nitric Oxide Stimulated from Red Blood Cell Derived Adenosine Triphosphate.....	74
REFERENCES.....	77
CHAPTER 3.....	85
POLYDIMETHYL SILOXANE BASED MICROFLUIDIC DEVICES FOR THE ANALYSIS OF DRUG DIFFUSION ACROSS A POROUS POLYCARBONATE MEMBRANE.....	86
3.1 <i>In Vitro</i> Pharmacokinetics.....	86
3.1.1 Hollow Fiber Chamber Reactor.....	88
3.2 Experimental.....	92
3.2.1 Preparation of Reagents.....	92
<i>Fluorescein Stock and Working Solutions.....</i>	92
<i>Levofloxacin, Linezolid, Raltegravir, Ciprofloxacin Stock and Working Solutions.....</i>	92
3.2.2 Preparation of Microfluidic Device.....	93
3.2.3 HUH-7 Cell Storage, Preparation, and Immobilization.....	93
<i>Thawing from Cryostorage.....</i>	95
<i>Cell Splitting and Maintenance</i>	95
<i>Immobilization of HUH-7 in PDMS Microfluidic Device.....</i>	97

3.2.4 Pumping and Gradient System.....	99
3.2.5 Multiple Reaction Monitoring Ultra Performance Liquid Chromatography Mass Spectrometry (MRM-LC/MS/MS) for Analysis of Drug Transport.....	99
3.3 Results and Discussion.....	101
3.3.1 Validate Drug Loading Profiles.....	102
3.3.2 Verification of Complete Mixing in Channel.....	105
3.3.3 Validation of Drug Elimination Profiles and Manipulation of Elimination Half-Lives.....	105
3.3.4 Physical Manipulation of Device Design to Decrease the Half Life.....	111
3.3.5 Effect of Culturing Cells in the Loading Well on Overall Drug Transport.....	113
3.3.5.1 Effect of adhered HUH-7 Cells on Drug Loading Profiles.....	113
3.3.5.2 Effect of Adhered HUH-7 Cells on Drug Elimination Profiles.....	116
REFERENCES	120
CHAPTER 4	123
A THREE DIMENSIONAL PRINTING PLATFORM FOR THE DEVELOPMENT AND CHARACTERIZATION OF A DIFFUSION-BASED DYNAMIC <i>IN VITRO</i> MILLIFLUIDIC PHARMACOKINETIC MODEL.....	124
4.1 Introduction.....	124
4.1.1 Three Dimensional Printing.....	124
4.1.2 History and Concepts.....	125
4.2 Experimental.....	127
4.2.1 Fabrication of 3D Printed Device.....	127
4.2.1.1 Initial Design.....	127
4.2.1.2 3D Printed Fabrication.....	132
4.2.2 Preparation of Reagents.....	132
4.2.2.1 Fluorescein Stock and Working Solutions.....	132
4.2.2.2 Levofloxacin Stock and Working Solutions.....	132
4.2.2.3 Ciprofloxacin Stock and Working Internal Standard Solutions.....	133
4.2.3. Pumping System.....	133
4.2.4 Plate Reader Analysis of Fluorescein.....	134
4.2.5 Mass Spectrometry Analysis of Levofloxacin.....	135
4.3 Results and Discussion.....	136
4.3.1 Characterization of the Loading Profile.....	136
4.3.1.1 Impact of Flow Rate.....	136
4.3.1.2 Impact on Loading Volume.....	138
4.3.1.3 Impact of Loading Time.....	140
4.3.1.4 Impact of Initial Concentration.....	142

4.3.1.5 Prediction Model of Loading Concentration.....	144
4.3.1.6 Proof of Concept for Loading Prediction Model.....	148
4.3.1.7 C _{max} Prediction Model.....	150
4.3.1.8 C _{max} Prediction Model Proof of Concept.....	150
4.3.2 Characterization of the Elimination Profile.....	154
4.3.2.1 First Order Rate Kinetic Studies.....	154
4.3.2.2 Manipulation of Half-Lives.....	161
4.3.2.3 Characterization of Analyte Absorption into 3D Printed Material.....	171
REFERENCES.....	181
CHAPTER 5.....	185
FUTURE DIRECTIONS.....	186
5.1 Applications for Diffusion Based Dynamic <i>In Vitro</i> Pharmacokinetic Model.....	186
5.2 Further Characterization.....	187
5.3 3D Cell Culture Incorporation in the 3D Printed <i>In Vivo</i> Device.....	188
5.3.1 Experimental Method.....	189
5.3.1.1 Preparations of Solutions.....	189
<i>Fluorescein Stock and Working Solution.....</i>	<i>189</i>
<i>Irinotecan Stock and Working Solutions.....</i>	<i>189</i>
<i>Camptothecin Stock and Working Internal Standard Solutions.....</i>	<i>189</i>
5.3.1.2 Analysis of Irinotecan using Multiple Reaction Monitoring Liquid Chromatography-Mass Spectrometry.....	190
5.3.2 Results and Discussion.....	192
5.3.2.1 Validating Existing Prediction Model.....	192
5.3.2.2 Elimination Profile.....	194
5.4 Multiple Day Dosing of Bacteria for Future Antibacterial Resistance Studies.....	197
5.4.1 Experimental Method.....	198
5.4.1.1 Preparation of Solutions.....	198
<i>Levofloxacin Stock and Working Solutions</i>	<i>198</i>
<i>Ciprofloxacin Stock and Working Internal Standard Solutions.....</i>	<i>199</i>
5.4.1.2 Bacteria Culture Growth, Purification, and Viability Assay.....	199
5.4.2 Results and Discussion.....	201
5.4.2.1 Multiple Day Dosing of <i>Escherichia coli</i> with Levofloxacin.....	201
5.4.2.2 Characterization of Multiple Dosing Before Steady State.....	203
5.5 3D Printed Custom Labware.....	206
REFERENCES.....	214

LIST OF TABLES

Table 3.1 LC/MS/MS Parameters for Levofloxacin, Linezolid, Raltegravir, and Clopidogrel. Table depicting LC/MS/MS parameters, e.g., molecular weight, parent ion, retention time, cone voltage, collisional energy and collisional gas.....96

Table 4.1 Numerical Representation of Parameters Associated with Figure 4.9; Prediction Model Validation. Table is color coded for equation for the concentration based prediction model. Based upon the loading time and a maximum desired concentration the concentration at a certain point can be determine within error. $n \geq 4$; error: standard deviation.....147

Table 4.2 Numerical Representation of Figure 4.17. The determination of the half-lives in Figure 4.17 is numerically represented. Information and values relating to the statistically similar half lives, the linear lines (r^2), and the slope of the linear lines used to calculate the half-lives can be found in the table. $n \geq 4$; $p > 0.05$; error: standard deviation.....160

Table 4.3 Absorbance of Fluorescein into the Channel Correction Factor Proof of Concept. Based on the correction factor correcting the concentration of fluorescein in the channel to account for absorption into the channel, derived in Figure 4.17, specific concentrations are flowed through the channel and sampled (5 μ L) in the open well. The original initial concentrations (2.5, 5.0, 7.5 μ M) fluorescein yielded concentrations under the well of 1.25 ± 0.22 , 2.24 ± 0.56 , and 3.35 ± 0.60 , respectively. The loss of concentration from the syringe to the well indicates that fluorescein is absorbing into the walls of the channel. From Figure 4.17, the initial concentrations were corrected (4.33, 8.66, 12.99 μ M) to result in theoretical concentrations under the well of 2.5, 5.0, 7.5 μ M, respectively. The resulting values were statistically the same as the theoretical values (2.97 ± 0.50 , 4.66 ± 0.45 , 7.98 ± 1.42). $n \geq 4$; $p > 0.05$; error: standard deviation.....178

LIST OF FIGURES

Figure 1.1 Drug discovery and Development Process. The drug discovery and development process is comprised of a series of stages, Development, Preclinical, Clinical, and Approval. The initial development stage involves the identification of approximately 10,000 target compounds. After optimization studies analyzing parameters such as solubility, efficacy, and toxicity the target compounds are narrowed to less than 250 lead target compounds which enter the Preclinical stage. In the Preclinical stage studies focused on the dosing, safety, toxicology and pharmacology take priority. Human *in vivo* studies are preformed in the Clinical stage, which is comprised of three phases. Upon completion of Phase III the researchers apply for a New Drug Application seeking FDA approval for the drug candidate. Utilizing *in vitro* PK/PD models in tandem with the *in vivo* animal models during the Preclinical stage, specifically the pharmacology portion would facilitate better decision making therefore eliminate a drug prior to reaching the costly clinical trials.....4

Figure 1.2 Pharmacodynamic Profile and Parameters. A PD profile is obtained by plotting the observed effect with respect concentration. Various parameters such as efficacy and potency are obtained from PD profiles.....8

Figure 1.3 Pharmacokinetic Profile and Parameters. A PK profile is obtained by taking the concentration in plasma verse time. Various parameters such area under the curve, absorbance rates, elimination rate constants, half-life, and maximum concentrations can be obtained with PK profiles.....10

Figure 1.4 Schematic of a One and Two Compartment Model. Top. One compartment model is the simplest model, where uniform, simultaneous absorbance is assumed. Sample is located in the central compartment in direct contact with the flow. Bottom. Two compartment model where drug is flowed through the central compartment and out to waste. Drug transports from the central reservoir to the peripheral compartment, which contains sample.....13

Figure 1.5 Multiple Day Dosing Steady State. Example of a three day dosing PK profiles assuming the dosing has achieved steady state.....18

Figure 1.6 Schematic of Parallel or Composite *In Vivo* Sampling. An example of a typical composite *in vivo* sampling. The drug is administered to all animal samples. At specific time points, one animal is sampled and the concentration of drug in the plasma determined, i.e., in the schematic, Animal 1 was sampled for time point 1, Animal 2 was sampled for time point 2, etc.....20

Figure 1.7 Various types of Pharmacokinetic and Pharmacodynamics *In Vitro* Models. *Top.* Static *in vitro* model where a sample is in a constant environment and dosed. Drug concentration is not able to be manipulated. *Middle.* The dilution based *in vitro* model introduces flow into the sample reservoir to manipulate concentration but sample is lost. *Bottom.* In a diffusion based *in vitro* model the sample is conserved by isolating from the flow. Analyte diffuses to the sample compartment from the central compartment while toxic metabolites, produced by the sample simultaneously diffuses into the flow where it goes to waste.22

Figure 2.1 Proposed Sources of Nitric Oxide in Resistance Vessels, as well as, Adenosine Triphosphate Elicited Nitric Oxide Production in Endothelial Cells. Cross section of a resistance vessel (Left), showing only endothelial cells, RBC, and smooth muscle cells. Zoomed in version (Top Right) shows potential sources of NO in the vascular system; NO produced from RBC or the subsequent RBC derived ATP stimulation of NO production in endothelial cells. The ATP elicited NO synthesis is further depicted on bottom left. ATP binds to the purinergic receptor, P_{2Y}, which allows an influx of calcium ion into the cell, thereby stimulating e-NOS to convert L-arginine to L-citrulline.....49

Figure 2.2 Proposed Signal Transduction Mechanism for Red Blood Cell Release of Adenosine Triphosphate in Response to Stimuli. GPCR activates the G protein in response to a conformation. The G protein subsequently triggers AC, which produces cAMP. PKA is activated by cAMP, which then phosphorylates the CFTR. ATP is then release but the remainder of the mechanism, whether the CFTR or another unidentified channel is responsible, is unknown.....51

Figure 2.3 Silicon Master and Polydimethyl Siloxane based device Fabrication. Silicon master fabrication (Top) involves spin coating SU-8 photoresist, applying a transparent mask with printed features and exposing a UV light source for an allotted amount of time. Upon removing the excess photoresist cured features are revealed. The completed master is then covered with degassed (Bottom) PDMS and baked to cure, before being peeled off the master.....59

Figure 2.4 Macroscopic Fluorescence Microfluidic Device Schematic, Cross Section and Actual Image. Schematic (Top) shows the layout for the PDMS based microfluidic device as well as a cross section of the device with RBCs flowing through the channel and endothelial cells culturing in the detection well. ATP, released from the RBCs, diffuses across the porous polycarbonate layer where it stimulates NO production from the endothelial cells. Subsequent

fluorescence detection was observed using a macroscope. An actual image of the PDMS based microfluidic device (Bottom, 4 inch diameter) utilized.....61

Figure 2.5 Plate Reader Fluorescence Microfluidic Device Schematic, Cross Section and Actual Image. Schematic (Top Right) shows the layout for the PDMS based microfluidic device. An actual image of the PDMS based microfluidic device (Bottom, 4 inch diameter) utilized. Cross section of the device (Bottom) showing RBCs flowing through the channel and endothelial cells culturing in the detection well. ATP, released from the RBCs, diffuses across the porous polycarbonate layer where NO production is stimulated from the endothelial cells. Subsequent fluorescence detection was observed using a plate reader and a modified 96 well plate.....63

Figure 2.6 Experimental Set Up for All Microfluidic Devices. RBC samples were delivered to the devices by syringe pumps (6 $\mu\text{L}/\text{min}$) and fused silica capillary tubing (50 μm i.d.). Oven was kept at 37 $^{\circ}\text{C}$ throughout the duration of the experiment.....66

Figure 2.7 Macroscope and Florescent Images of Confluent Cells and DAF-FM. Image of macroscope (Left) used for fluorescence detection. Confluent cells (Top Right) stained with Hoechst 33342 dye. Fluorescence of DAF-FM in same detection well, post RBC flow.....68

Figure 2.8 Progression of Layout for Integrating the PDMS Microfluidic Device with a High Throughput Plate Reader. Top Right: Glass Plate, notched at the top by the glass shop, filled bottom of plate reader 96 well plate holder. Top Left: Post flow, device is lined up on glass plate. Bottom Left: Modified 96 well plate is positioned above microfluidic device. The bottoms of wells in row 6 and 9 were removed to allow for fluorescence measurements. Bottom Right: Top view of the modified plate with microfluidic device positioned underneath.....70

Figure 2.9 Fluorescence Detection of HU Incubated RBC derived ATP Elicited NO Production in bPAECs (Macroscope). Here, bPAECs were cultured in the detection wells and DAF-FM probe was loaded into the wells prior to pumping. Fluorescence was detected using a fluorescence macroscope. NO release from bPAECs was observed after pumping 7% solutions of RBCs incubated with various conditions (HU, L-NAME, Ca^{2+} free buffer). The NO release from bPAECs increased significantly (*) when RBCs incubated with HU were flowed, confirming that HU can increase NO release from bPAECs. When NO release is inhibited in bPAECs using L-NAME, the difference in NO release between HU incubated and the control is statistically insignificant, suggesting only NOS produced from bPAECs is responsible for observed NO. Moreover, when RBC NOS was inhibited by L-NAME, the RBC sample incubated with HU has NO production statistically similar to basal levels. This suggests that RBC

derived NO can affect bPAEC NO production, potentially indirectly through the mechanism of HU induced RBC ATP release. Further confirming the role of RBC derived NO, when RBC samples are prepared in calcium free buffer any previously observed increases are negated. $n \geq 3$ devices and $p < 0.0001$. Error = S.E.M.....72

Figure 2.10 Fluorescence Detection of HU Incubated RBC derived ATP Elicited NO Production in bPAECs (Plate Reader). Although the experimental set up was identical to Figure 2.9, the detection platform for this experiment was measured using a commercial plate reader. As in Figure 4, when 7% RBCs are incubated with HU, a significant increase in NO is observed. Upon incubation of the bPAECs and RBCs with L-NAME the increases of NO production in the HU incubated samples were reduced to below basal levels. When bPAECs are incubated for 30 minutes with PPADS, a purinergic receptor antagonist, prior to flowing 7% RBCs no significant increase in NO release is observed, suggesting that RBC derived ATP is necessary to observe an increase in NO release from bPAECs. $n \geq 3$ devices and $p < 0.005$. Error = S.E.M.....75

Figure 3.1 Conventional Pharmacokinetic Profile and Corresponding Parameters. Schematic of a typical oral administered pharmacokinetic curve and the various parameters, e.g., absorbance rate, C_{max} , elimination rate constant, half-life, AUC, that can be obtained from the aforementioned curve...87

Figure 3.2 Hollow Fiber Chamber Reactor. HFRC set up with a zoomed in image of the closed cartridge containing porous capillaries and cells. Image reproduced with permission from Fiber Cell Systems89

Figure 3.3 Hollow Fiber Chamber Reactor Cross Section Schematic and Image. Schematic of HFRC cross section (Top) showing diffusion action of nutrients and drug from the capillaries to the extra capillary space, with the simultaneous removal of waste. An image of a open HFRC cartridge showing porous capillaries (Bottom). Image reproduced with permission from Fiber Cell Systems.....90

Figure 3.4 Schematic and Image of a Polydimethyl Siloxane Diffusion-based Dynamic In Vitro Microfluidic Pharmacokinetic Model. Schematic of the microfluidic PDMS device used for in vitro PK studies, which consists of two PDMS slabs separated by a porous polycarbonate membrane (Top). An image of an actual PDMS device (Bottom).....94

Figure 3.5 Graphical Representations of the Concentrations in the Channel during the Various Gradients. While flowing just buffer (Blue Line) there is no drug being flowed through the channel. However, during the 1 hour gradient, 75% of the concentrated drug added to the detection well is flowed for 1 hour before being reduced to 50% of the concentrated drug, which is flowed for the

subsequent hour. The concentration in the channel is further reduced to 25% drug, which is flowed for an hour before being flowing buffer the remainder of the time. A similar, stepwise reduction in concentration concept is followed for the 2 hour gradient, where 75% of the concentration in the detection well is flowed through the channel for 2 hours before switching to 50% drug. The concentration is further reduced every 2 hours before just buffer is flowing through the channel.....98

Figure 3.6 Schematic of a Cross Section at the Detection Well, Polycarbonate Membrane and Channel Interface. Loading, or absorbance, of drug is achieved by flowing concentrated drug through channel while adding buffer to the detection well. Drug diffuses from the channel to the membrane (Left). Clearance or elimination, of a drug is attained by reversing the concentration gradient. Buffer is flowed through the channel, thereby allowing the diffusion of drug from the well to the channel (Right).....100

Figure 3.7 Validation of the Loading of the Detection Well with Various Concentrations of Linezolid, Levofloxacin, and Raltegravir. Various concentrations (1, 2, 3, 4 μM) of linezolid, levofloxacin, and raltegravir were pumped through the channels with 12 μL of PSS lacking BSA. After 1 hour, 5 μL was sampled from the detection well, diluted with 200 μL buffer, before further dilution with the internal standard working solution. $n \geq 3$; error: standard deviation.....103

Figure 3.8 Validation of Mixing in Serpentine Channels by Fluorescence. A solution of 100 μM fluorescein was flowed through the bottom of the Y channel while water was flowed through the top of the Y channel. Using a macroscope, the mixing of the two solutions in the serpentine channels is monitored. At the completion of the serpentine the solutions are successfully and completely mixed.....104

Figure 3.9 Various Elimination Profiles for Linezolid. The solid black line with black circles represents the quickest elimination with buffer flowing through the channel and concentrated drug (2 μM) in the detection well. The gray dotted lines with white circles represents a manipulation of the concentration of drug in the channel to alter the half-life. The half-life is further increased when the gradient is increased to 2 hours increments. The general trend was apparent but lacked quantitation reproducibility therefore the curves shown are an example of an n of 1.....106

Figure 3.10 Various Elimination Profiles for Levofloxacin. The solid black line with black circles represents the quickest elimination with buffer flowing through the channel and concentrated drug (2 μM) in the detection well. The gray dotted lines with white circles represents a manipulation of the concentration

of drug in the channel to alter the half-life. The half-life is further increased when the gradient is increased to 2 hours increments. The general trend was apparent but lacked quantitation reproducibility therefore the curves shown are an example of an n of 1.....107

Figure 3.11 Various Elimination Profiles for Raltegravir. The solid black line with black circles represents the quickest elimination with buffer flowing through the channel and concentrated drug (2 μM) in the detection well. The gray dotted lines with white circles represents a manipulation of the concentration of drug in the channel to alter the half-life. The half-life is further increased when the gradient is increased to 2 hours increments. The general trend was apparent but lacked quantitation reproducibility therefore the curves shown are an example of an n of 1.....108

Figure 3.12 Manipulating the Physical Design of the Microfluidic Device to Influence Elimination. Initial designs of the microfluidic device had channel diameters of 200 μm . Upon increasing the channel diameter under the wells (see inset) the half life decreased to approximately 30 min. n = 1.....110

Figure 3.13 Various Alterations to the Physical Design of the Microfluidic Device to Influence Elimination. As seen in Figure 3.11, mask A is the full mask design with the increased surface area. Due to leaking, mask B was temporarily employed before it was also subject to membrane failure. Both masks C and D were also designs used that resulted in bulk fluid transport....112

Figure 3.14 Impact on Diffusion of Levofloxacin upon Adherence of HUH-7 cells in the Detection Well. HUH-7 cells were seeded in the detection well and various concentrations of drug (0, 1, 2, 3, 4, 5, 6, 7 μM). A significant impact on diffusion was not observed until the more concentrated samples (6 and 7 μM). n \geq 3; p < 0.005; Error: SEM.....114

Figure 3.15 Impact on Diffusion of Raltegravir upon Adherence of HUH-7 cells in the Detection Well. HUH-7 cells were seeded in the detection well and various concentrations of drug (0, 1, 2, 3, 4, 5, 6, 7 μM). A significant impact on diffusion was not observed until the more concentrated samples (6 and 7 μM). n \geq 3; p < 0.005; Error: SEM.....115

Figure 3.16 Impact on Elimination Diffusion of Linezolid upon Adherence of HUH-7 cells in the Detection Well. HUH-7 cells were seeded in the detection well and 2 μM of concentrated drug was added. Buffer alone was flowed through the channel for the fastest elimination (Black line/circles). Various gradients of drug concentrations were also flowed under the well (40 min: Black dashes/triangles; 1 hour: Gray dashed/white circles). The general trend was

apparent but lacked quantitation reproducibility therefore the curves shown are an example of an n of 1117

Figure 3.17 Impact on Elimination Diffusion of Levofloxacin upon Adherence of HUH-7 cells in the Detection Well. HUH-7 cells were seeded in the detection well and 2 μM of concentrated drug was added. Buffer alone was flowed through the channel for the fastest elimination (Black line/circles). Various gradients of drug concentrations were also flowed under the well (40 min: Black dashes/triangles; 1 hour: Gray dashed/white circles). The general trend was apparent but lacked quantitation reproducibility therefore the curves shown are an example of an n of 1118

Figure 3.18 Impact on Elimination Diffusion of Raltegravir upon Adherence of HUH-7 cells in the Detection Well. HUH-7 cells were seeded in the detection well and 2 μM of concentrated drug was added. Buffer alone was flowed through the channel for the fastest elimination (Black line/circles). Various gradients of drug concentrations were also flowed under the well (40 min: Black dashes/triangles; 1 hour: Gray dashed/white circles). The general trend was apparent but lacked quantitation reproducibility therefore the curves shown are an example of an n of 1119

Figure 4.1 Examples of a CAD File, Low Resolution .STL File and a High Resolution .STL File with a Zoomed in Cutout. CAD files (Top Left) are 3D models that are able to be saved as .STL files, thereby breaking the 3D images into a series of triangles. A low resolution .STL (Top Right) contains less triangles than a high resolution (Bottom Left) .STL file. In the high resolution cylinder showed, the triangles in such close proximity they are hard to individually depict, therefore a zoomed in cutout is shown on the bottom right, in which the triangles can be depicted.....126

Figure 4.2 Image of the Computer Aided Design File for the 3D Printed Base. CAD file of the 3D printed base with corresponding dimensions.....128

Figure 4.3 Schematic of a Cross Section of a 3D printed Device and Actual Images of Several Prototypes. A schematic depicting a cross section of the 3D printed device (Top) is shown with commercial fittings, syringe, and disposable membrane insert. An early prototype (A) has 8 channels and is fabricated in TangoWhite material. Also, female commercial fittings were affixed by epoxy to the device to allow for integration of the male commercial fittings. In the current prototype (B), threads could directly be printed into the device, thereby simplifying the setup. Current devices, modeled after 24 well plates, are fabricated with an optically clear, VeroClear material with O-rings simultaneously printed with the rubbery TangoBlack.....130

Figure 4.4 Characterization of the Flow Rate in the 3D Printed *In Vitro* PK device. While holding other parameters constant, i.e., insert volume (75 μL), initial concentration (15 μM), and loading time (1 hour), the flow rate was varied to see the impact on diffusion, specifically the C_{max} . The flow rates (2.5, 5.0, 7.5, 10.0, 15.0 $\mu\text{L}/\text{min}$) yielded PK profiles that were statistically the similar. $n \geq 4$; $p > 0.05$; error: standard deviation.....137

Figure 4.5 Characterization of the Loading Volume in the 3D Printed *In Vitro* PK device. As seen in Figure 4.4, to characterize the loading volume, parameters, such as, flow rate (10 $\mu\text{L}/\text{min}$), initial concentration (15 μM), and loading time (1 hour), were held constant while the loading volume was varied to see the impact on diffusion, specifically the C_{max} . The loading volumes, i.e., 50, 100, 150 μL , yielded PK profiles that indicated the lower the initial volume had a more concentrated C_{max} , while the larger volume was a more diluted sample. $n \geq 4$; $p < 0.01$; error: standard deviation.....139

Figure 4.6 Characterization of the Loading Volume in the 3D Printed *In Vitro* PK device. As seen in Figure 4.4, to characterize the loading volume, parameters, such as, flow rate (10 $\mu\text{L}/\text{min}$), initial concentration (15 μM), and loading time (1 hour), were held constant while the loading volume was varied to see the impact on diffusion, specifically the C_{max} . The loading volumes, i.e., 50, 100, 150 μL , yielded PK profiles that indicated the lower the initial volume had a more concentrated C_{max} , while the larger volume was a more diluted sample. $n \geq 4$; $p < 0.01$; error: standard deviation.....141

Figure 4.7 Characterization of the Initial Channel Concentration in the 3D Printed *In Vitro* PK Device. To characterize the initial concentration's effect on the C_{max} when various parameters, such as, flow rate (10 $\mu\text{L}/\text{min}$), loading volume (75 μL), and loading time (1 hour), were held constant, the initial volume was varied. The initial concentrations used were 7.5, 15, 30 μL , which resulted in the higher concentration yielding the highest C_{max} and vice versa. $n \geq 3$; $p < 0.01$; error: standard deviation.....143

Figure 4.8 Prediction Model for the Concentration along the Loading Portion of the PK Curve. A prediction model was obtained by taking the slope of the loading portion of Figure 4.7 and plotting it against the initial concentration flowed through the channel. The slope of the linear line can be used for a prediction model predicting concentrations at specific time points. $n \geq 3$; error: standard deviation.....145

Figure 4.9 Prediction Model for the Concentration along the Loading Portion of the PK Curve Validation. To validate the prediction model, a theoretical C_{max} was set to 6.5 μM and the loading time was varied (5, 10, 15, 20, 25 min) to obtain the initial concentration that will be flowed through the channel. At the specified loading time, the resulting C_{max} was statistically within the

theoretical C_{max} . Note, the prediction model was based off of a linear correlation but the curves have a quadratic relationship. $n \geq 4$; $p > 0.05$; error: standard deviation.....146

Figure 4.10 Proof of Concept for the Prediction Model for the Concentration along the Loading Portion of the PK Curve. The proof of concept of the prediction model is tested by choosing a drug, which has a molecular mass comparable to that of fluorescein, e.g., levofloxacin. The desired concentration was 25.6 μM with a loading time of 1 hr. The concentration in the syringes, derived from the prediction model for 1 hour of flow was 167.27 μM . The desired concentration was 25.6 μM with a loading time of 1 hr. Experimentally, the fluorescein and levofloxacin were statistically the same and at 1 hour the concentration was within error as the theoretical concentration. Importantly, the experimental C_{max} is $43.0 \pm 4.1 \mu\text{M}$; $n \geq 4$; $p > 0.05$; error: standard deviation.....149

Figure 4.11 Reworking Figure 4.9 to Explore a Quadratic Relationship. The concentrations in the insert, from Figure 4.9, were analyzed for a quadratic relationship by taking the square root of the concentration. The resulting linear lines were indicative of a quadratic relationship and a new prediction model based off this correlation. $n \geq 4$151

Figure 4.12 Prediction Model for the C_{max} after a Specific Loading Time. A prediction model was obtained by taking the slope of the linear lines, after taking the square root of the concentration in the insert, in Figure 4.9 and plotting it against the initial concentration flowed through the channel. The resulting slope of the linear line can be used for a prediction model predicting concentrations at specific time points. $n \geq 4$; error: standard deviation.....152

Figure 4.13 Proof of Concept of the Prediction Model for the C_{max} for Specific Loading Times. The proof of concept of the prediction model, similar to that seen in Figure 4.10, used levofloxacin an a comparable molecule to fluorescein. The desired C_{max} was 25.6 μM with a loading time of 1 hr. The concentration in the syringes, derived from the prediction model was 119.28 μM . Experimentally, the fluorescein ($21.21 \pm 7.37 \mu\text{M}$) and levofloxacin ($23.07 \pm 5.42 \mu\text{M}$) were statistically the same as the desired C_{max} . $n \geq 3$; $p > 0.05$. error: standard deviation.....153

Figure 4.14 Mimicking an IV Dosing PK Profile to Characterize the Elimination Parameters. Loading the insert with 4 μM of fluorescein while flowing DI water through the channel. Every 30 min 5 μL was sampled from the insert, diluted with 100 μL DI water, and analyzed with a plate reader after all samples were taken. $n = 4$; error: standard deviation.....155

Figure 4.15 Manipulating Figure 4.14 to show First Order Kinetics and Obtain Elimination Rate Constant and Half Life. The natural log was taken of the concentrations in the insert obtained in Figure 4.14 and plotted with respect to time. A linear line is indicative of first order rate kinetics. The slope of the linear line is equivalent to the elimination rate constant (K_{EL}). The half-life is obtained by: $0.693/K_{EL}$. $r^2 = 0.9548$156

Figure 4.16 Depletion Profiles when Manipulating the Concentration in the Membrane. Various concentrations (2.5, 5.0, 7.5, 10, 15 μM) were added to the membrane insert in the same quantity (75 μL). DI water is flowed at 10 $\mu\text{L}/\text{min}$ through the channel while 5 μL is sampled from the insert every 30 min over 6 hours. $n \geq 4$; error: standard deviation.....158

Figure 4.17 Determining the Half-Lives of the Elimination Profiles in Figure 4.16. The natural log is taken of the concentrations in the insert reported in Figure 4.16 and plotted against the time. The slopes of the resulting linear lines is equivalent the elimination rate constant (K_{EL}), from which, the half live can be determined. The half-lives are all statistically the same (numerical representation can be found in Table 4.2), despite having different initial concentrations, which is indicative of first order rate kinetics. $n \geq 4$; $p > 0.05$; error: standard deviation.....159

Figure 4.18 Images of Gradient Setup with T-junctions. Left. Image of experimental set up using T-junctions to merge concentrated fluorescein solutions with DI water. Right. Zoomed in image of complex setup of capillaries, T-junctions, and 3D printed device.....162

Figure 4.19 Manipulation of Half Life using Gradients Introduced through T-Junction. Using a concentrated fluorescein concentration of 5 μM and deionized water various gradients were achieved through the used of flow rates, e.g., 75%: fluorescein (0.6 $\mu\text{L}/\text{min}$), water (0.2 $\mu\text{L}/\text{min}$); 50%: fluorescein (7.5 $\mu\text{L}/\text{min}$), water (2.5 $\mu\text{L}/\text{min}$); 25%: fluorescein (5.0 $\mu\text{L}/\text{min}$), water (5.0 $\mu\text{L}/\text{min}$); 0%: fluorescein (0 $\mu\text{L}/\text{min}$), water (10 $\mu\text{L}/\text{min}$). The membrane insert contains 75 μL of 5 μM fluorescein. Only buffer is flowed under the membrane insert under the blank depletion. The gradient is changed every hour or every 2 hours in order to manipulate the concentration gradient experienced by the membrane insert. $n \geq 6$; error: standard deviation.....163

Figure 4.20 Manipulation of Half Life using Gradients Introduced through T-Junction. Using a concentrated fluorescein concentration of 5 μM and deionized water various gradients were achieved through the used of flow rates, e.g., 75%: fluorescein (0.6 $\mu\text{L}/\text{min}$), water (0.2 $\mu\text{L}/\text{min}$); 50%: fluorescein (7.5 $\mu\text{L}/\text{min}$), water (2.5 $\mu\text{L}/\text{min}$); 25%: fluorescein (5.0 $\mu\text{L}/\text{min}$), water (5.0 $\mu\text{L}/\text{min}$); 0%: fluorescein (0 $\mu\text{L}/\text{min}$), water (10 $\mu\text{L}/\text{min}$). The membrane insert contains 75 μL of 5 μM fluorescein. Only buffer is flowed under the membrane insert under the blank

depletion. The gradient is changed every hour or every 2 hours in order to manipulate the concentration gradient experienced by the membrane insert. $n \geq 6$; error: standard deviation.....165

Figure 4.21 Natural Log of Concentration in Insert verse Time Derived from 4.20. The natural log of the concentration in the insert obtained in Figure 4.20, with respect to time yields information such as elimination rate constant, half life, and kinetic order. The three gradients still were first order rate kinetics with linear relationships, i.e., $r^2 = 0.9707, 0.9176,$ and 0.9645 for blank, 1 hour and 2 hour gradients, respectively. A significant difference ($p < 0.001$) in half-life was observed between the blank (1.69 ± 0.45 hours) and the 1 (5.55 ± 1.99 hours) and 2 hour (6.11 ± 2.34 hours) gradients, however there was no statistical difference between the 1 and 2 hour gradients ($p > 0.05$). $n \geq 6$; error: standard deviation.....166

Figure 4.22 Images of 3D Printed T-Junction with Locking Mechanism in 3D Printed Device. Top. 3D printed T-junction and single fitting comprised of VeroClear. Bottom. Images of setup with locking mechanisms, resulting in an overall simplified setup.....168

Figure 4.23 Image of the Computer Aided Design File for the Base 3D Printed Device. Schematic of the CAD file for the 3D printed base, along with dimensions. The bottom image is a zoomed in portion of the inlet/outlets of the locking mechanism, with the corresponding dimensions.....169

Figure 4.24 Image of the Computer Aided Design File for the 3D Printed Y-Junction. Schematic of the CAD file for the 3D printed Y-junction, along with dimensions.....170

Figure 4.25 Manipulation of Half Life using Gradients Introduced through Locking Mechanism T-Junction (5 μM). Similar to the original set up, however, T-junctions were directly incorporated into the 3D printed devices using a locking mechanism. The same concentrated fluorescein (5 μM) was used in the membrane insert (75 μL), as well as in the syringes with deionized water to introduce various gradients achieved through the used of flow rates, e.g., 75%: fluorescein (0.6 $\mu\text{L}/\text{min}$), water (0.2 $\mu\text{L}/\text{min}$); 50%: fluorescein (7.5 $\mu\text{L}/\text{min}$), water (2.5 $\mu\text{L}/\text{min}$); 25%: fluorescein (5.0 $\mu\text{L}/\text{min}$), water (5.0 $\mu\text{L}/\text{min}$); 0%: fluorescein (0 $\mu\text{L}/\text{min}$), water (10 $\mu\text{L}/\text{min}$). Only buffer is flowed under the membrane insert under the blank depletion. The gradient is changed every hour or every 2 hours in order to manipulate the concentration gradient experienced by the membrane insert. $n \geq 6$; error: standard deviation.....172

Figure 4.26 Natural Log of Concentration in Insert verse Time Derived from 4.25 (5 μM). Similar to Figure 4.21, the natural log of the concentration in the insert obtained in Figure 4.25, with respect to time yields information such as

elimination rate constant, half life, and kinetic order. The three gradients still were first order rate kinetics with linear relationships, i.e., $r^2 = 0.9067$, 0.9406 , and 0.9877 for blank, 1 hour and 2 hour gradients, respectively. A significant difference ($p < 0.001$) in half-life was observed between the blank (1.78 ± 0.45 hours), 1 hour (3.42 ± 0.79 hours) and 2 hour (6.01 ± 1.44 hours) gradients. $n \geq 6$; error: standard deviation.....173

Figure 4.27 Manipulation of Half Life using Gradients Introduced through Locking Mechanism T-Junction (10 μM). Similar to the experimental set up with the T-junctions being directly incorporated into the 3D printed devices using a locking mechanism. An increased concentrated fluorescein (10 μM) was used in the membrane insert (75 μL), as well as in the syringes with deionized water to introduce various gradients achieved through the used of flow rates, e.g., 75%: fluorescein (0.6 $\mu\text{L}/\text{min}$), water (0.2 $\mu\text{L}/\text{min}$); 50%: fluorescein (7.5 $\mu\text{L}/\text{min}$), water (2.5 $\mu\text{L}/\text{min}$); 25%: fluorescein (5.0 $\mu\text{L}/\text{min}$), water (5.0 $\mu\text{L}/\text{min}$); 0%: fluorescein (0 $\mu\text{L}/\text{min}$), water (10 $\mu\text{L}/\text{min}$). Only buffer is flowed under the membrane insert under the blank depletion. The gradient is changed every hour or every 2 hours in order to manipulate the concentration gradient experienced by the membrane insert.....174

Figure 4.28 Natural Log of Concentration in Insert verse Time Derived from 4.27 (10 μM). Similar to Figure 4.21, the natural log of the concentration in the insert obtained in Figure 4.27, with respect to time yields information such as elimination rate constant, half-life, and kinetic order. The three gradients still were first order rate kinetics with linear relationships, i.e., $r^2 = 0.9108$, 0.9860 , and 0.9699 for blank, 1 hour and 2 hour gradients, respectively. No significant difference ($p > 0.05$) in half-life was observed between the blank (1.81 ± 0.25 hours), 1 hour (2.73 ± 0.90 hours) and 2 hour (3.30 ± 1.99 hours) gradients. $n \geq 6$; error: standard deviation.....175

Figure 4.29 Absorbance of Fluorescein into the Device Channels and Correction Factor for Expected Concentration. Various concentrations of fluorescein (2.5-100 μM) were flowed through the channels for an hour and sampled (5 μL). Samples were diluted with 100 μL of DI water analyzed in a plate reader. The resulting concentrations were plotted against the initial concentrations and a best fit linear line drawn through the lines ($r^2 = 0.9975$; slope = 0.5772). From the aforementioned line a concentration correction factor can be made from the resulting slope (Concentration in Well = Slope*Initial Concentration), therefore, if a concentration of 2.5 μM was desired in the well a concentration of 4.33 μM would need to the initial concentration. $n \geq 3$; error: standard deviation.....177

Figure 5.1 Validating Irinotecan Loading Profile with Prediction Model. Irinotecan (586.68 g/mol) is a larger molecule than fluorescein (332.31 g/mol), which was the molecule, originally used to formulate the prediction model. Both

analytes were flowed at initial concentrations 52.6 μM with irinotecan resulting in a C_{max} of $9.97 \pm 0.67 \mu\text{M}$, which is significantly less than fluorescein's C_{max} ($13.82 \pm 1.09 \mu\text{M}$; $p < 0.001$). Therefore irinotecan needs a specific prediction model characterized. $n \geq 4$, error = standard deviation.....193

Figure 5.2 Elimination Profile for Irinotecan. Irinotecan ($5.78 \mu\text{M}$) was added to the membrane insert ($75 \mu\text{L}$) while deionized water was flowed through the channel. Samples ($5 \mu\text{L}$) were taken every 30 minutes. $n \geq 4$, error = standard deviation.....195

Figure 5.3 Validating First Order Rate Elimination. The natural log of the concentration in the insert with respect to time derived from Figure 5.2 resulted in a linear relationship ($r^2 = 0.9742$). The linear relationship is indicative of first order rate kinetics. The half-life, obtained from the slope of the line was 1.96 hours.....196

Figure 5.4 Multiple Day Dosing of *Escherichia coli* with the Levofloxacin Antibiotic. Concentrated levofloxacin ($119.28 \mu\text{M}$) was flowed through the channels for 1 hour, with the desired C_{max} reaching $25.6 \mu\text{M}$, before being swapped for BSA free PSS buffer while *E. coli* was seeded in the cell culture inserts. The process was repeated over three days while the *E. coli* sample was monitored for cell death at the conclusion of each day. The resulting, significantly similar C_{max} , based on days were $18.66 \pm 6.48 \mu\text{M}$, $25.64 \pm 4.23 \mu\text{M}$, $20.01 \pm 5.27 \mu\text{M}$. $n \geq 4$202

Figure 5.5 Schematic of Multiple Dosing Prior to, and Reaching Steady State. A schematic of the concentration verse time graph representing multiple dosings before steady state in the therapeutic range is reached.....204

Figure 5.6 Preliminary Example of Multiple Dosing over 5.5 Hours on the 3D Printed *In Vitro* Device. Three sets of dosings of concentrated fluorescein ($120 \mu\text{M}$) were administered over 5.5 hours. The concentrated fluorescein was flowed through the channel for 30 minutes before being switched with deionized water for 1 hour and repeated a total of two more times. The red arrows indicate the beginning of flow for the concentrated fluorescein. $n \geq 4$, error = standard deviation.....205

Figure 5.7 Images of 3D Printed Custom Labware. A. Comparison of the commercially purchased T-junction fitting and the 3D printed T-junction fitting. B. 3D printed base to hold the 3D printed device while simultaneously collecting waste.....207

Figure 5.8 Computer Aided Design Images of 3D Printed Custom Labware. CAD file of the 3D printed base holder from various viewpoints, along with specific dimensions.....208

Figure 5.9 Images of the 3D Printed Peristaltic Pump Setup. Top. Images of 3D printed pump setup while tubing was incorporated with the 3D printed device containing endothelial cells and constantly perfusing media. In the image, the tube that traditionally holds media contains fluorescein for aesthetic purposes. Bottom. Zoomed in image of the 3D printed pump. Behind the pump is the 24V battery. The terminals are connected to a circuit board, i.e., on/off switch and speed control, contained below the pump and connected to the motor. The setup is isolated and can be contained in an incubator for at least 12 hour periods.....210

Figure 5.10 Computer Aided Design Model of the 3D Printed Peristaltic Pump Setup. CAD file of the 3D printed peristaltic pump with all of the 3D printed parts in place.....211

Figure 5.11 Computer Aided Design Model of the 3D Printed Peristaltic Pump Setup and Corresponding Dimensions. CAD file of the 3D printed peristaltic pump with all of the 3D printed parts in place from the top, side, and front views. Corresponding dimensions are noted from the various view points.....212

CHAPTER 1

INTRODUCTION

1.1 Pharmaceutical Industry Current State of Affairs

The ever incessant demand for new therapies and treatments drives the drug discovery and development process of the pharmaceutical industry. The cost associated with bringing a drug to market has breached a billion dollars, i.e., 1.24 billion in 2005,¹ and continues to rise due to low success rates coupled with a long, cumbersome drug development time frame (approximately 12.5 years).²⁻⁴ The drug development model currently employed by pharmaceutical companies involves supplementing ongoing research for new drugs by utilizing blockbuster patents held by the pharmaceutical companies. Before the patent expiration of the blockbuster drug that funds the current drug discovery and developmental research, the pharmaceutical company requires a hit on a new blockbuster drug, thereby sustaining the funding for further development of drug targets to continue the cycle of funding.^{2,5,6} This cycle is increasingly difficult to maintain due to such factors as risk evaluation, mitigation strategies, and post-market clinical studies. All of these are required by the Food and Drug Administration Amendment Acts⁷ passed in 2007, which lengthen clinical studies, increase overall costs, and are accompanied by a reduced number of drugs obtaining approval.^{6,8,9} To counteract the aforementioned challenges of developing a successful drug, pharmaceutical companies are complementing their own agenda by acquiring small companies that have developed blockbuster drugs of their own. Another, increasingly popular trend in 'Big Pharma' is to utilize contract research

organizations (for example, Eli Lilly outsourcing to Covance) for the majority of analysis, resulting in the pharmaceutical companies filling the role of management versus the traditional, all encompassing, drug development cycle of synthesis to sales.¹⁰ By outsourcing research assays to contract research organizations, pharmaceutical companies are better able to manage resources increase efficiency, and reducing overhead costs, while still retaining ownership of the target drugs, which the larger companies can then bring through the more costly clinical trials, marketing, and sales.

Existing research procedures are another area in which increased efficiency can be addressed and reassessed. Various research technologies, e.g., high throughput screening, proteomics, and metabolomics, have potential to reform for the development process by increasing efficiency¹¹ and introducing new target leads, but the projected gains have yet to make it to market. Between 1993-2003, funding by the National Institutes of Health and spending of pharmaceutical companies doubled without an increase quantity of drugs reaching approval.⁸ Therefore, a reappraisal of the drug development process may be required to increase the number of drugs reaching the market.

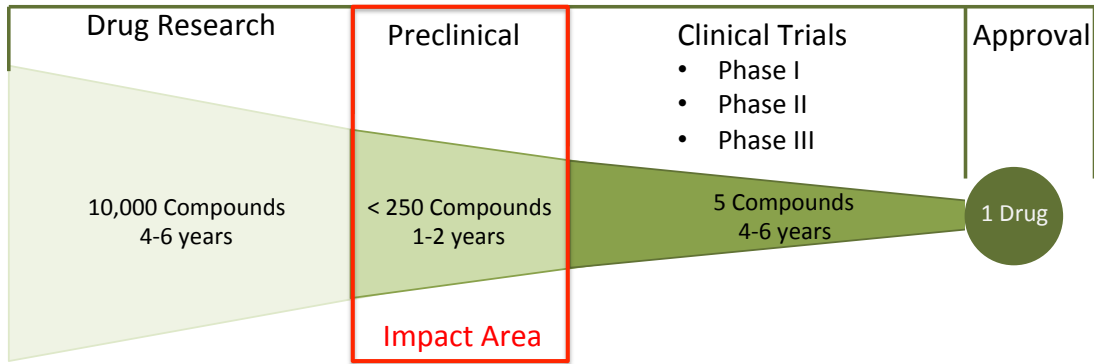


Figure 1.1 Drug discovery and Development Process. The drug discovery and development process is comprised of a series of stages, Development, Preclinical, Clinical, and Approval. The initial development stage involves the identification of approximately 10,000 target compounds. After optimization studies analyzing parameters such as solubility, efficacy, and toxicity the target compounds are narrowed to less than 250 lead target compounds which enter the Preclinical stage. In the Preclinical stage studies focused on the dosing, safety, toxicology and pharmacology take priority. Human *in vivo* studies are preformed in the Clinical stage, which is comprised of three phases. Upon completion of Phase III the researchers apply for a New Drug Application seeking FDA approval for the drug candidate. Utilizing *in vitro* PK/PD models in tandem with the *in vivo* animal models during the Preclinical stage, specifically the pharmacology portion would facilitate better decision making therefore eliminate a drug prior to reaching the costly clinical trials.

1.2 General Drug Development Process

The highly complex and intricate drug discovery and development process has several levels, with each subsequent stage adding to expenses and materials. The various stages are pre-discovery, discovery, pre-clinical, and clinical (Figure 1.1). The clinical stage of development, by far the most costly and time consuming, is further broken into Phase I, Phase II and Phase III trials, all of which involve human subjects.^{12,13}

1.2.1 Drug Pre-discovery

The first stage of the drug development process is drug pre-discovery, which involves focus on specific diseases, e.g., cancer, arthritis, cardiovascular, etc. and targeting potentially active therapeutic agents. Often, the influencing factor driving pharmaceutical research is the profit margin associated with a successful target selection, either due to quantity of population affected or a first world concern. Upon understanding the disease, selected drug targets are identified by testing analogues of natural ligands¹³ or targeting genes^{14,15} and such proteins as monoclonal antibodies¹⁶⁻²³, which have been previously associated with a particular disease.^{14,24} High throughput screening, or combinatorial chemistry,^{11,25-27} is another approach that analyzes thousands of compounds in a relatively short timeframe.²⁸⁻³¹ Any compounds that 'hit' are then targeted for further studies. Another pre-discovery targeting approach is

structural-based drug design, i.e., obtaining three dimensional structure through nuclear magnetic resonance or x-ray crystallography.³²⁻³⁷ Early *in vitro* studies are also performed to determine preliminary efficacy.^{12,13}

1.2.2 Drug Discovery

Emerging from the prediscovery stage are approximately 5,000-10,000 target compounds. Upon obtaining a group of lead targets, the compounds are further narrowed by optimization analysis steps identifying such parameters as solubility, toxic effects, genotoxicity, and lack of efficacy. Strategies for optimization include preliminary *in vivo* studies to identify bioavailability, metabolism byproducts, and efficacy. *In vitro* studies are also used to monitor pharmacodynamic properties associated with the lead targets. During drug discovery the initial 10,000 potential targets are reduced to approximately 250 lead targets, before being passed to preclinical stage for further analysis.^{12,13,38}

1.2.3 Drug Development

1.2.3.1 Preclinical

Drug candidates are prepared for human clinical trials during the preclinical stage, which involves additional safety and efficacy studies involving toxicology and pharmacology. Synthesis and formulations are evaluated as the drug target is being investigated for eventual human and animal model dosing. Toxicology studies determine the adverse effects of the drug on *in vivo* models

and how those adverse effects translate to humans. The toxicology studies are conducted based on a single dosing (acute) or repeat dosing (chronic). Overall, toxicology studies, during the preclinical stage, shape the safety parameters and dosing regiment of future clinical studies. During the pharmacology studies, the starting dose for human clinical trials is determined, as well as predicting the effect that the administered drug will have in humans based upon predetermined pharmacokinetic (PK) and pharmacodynamic (PD) profiles obtained with *in vitro* and *in vivo* studies³⁹. There has been a push to supplement costly *in vivo* studies with *in vitro* models,⁴⁰ as well as integrate PK and PD profiles in an effort to increase drug discovery efficiency.⁴¹

1.2.3.2 Pharmacodynamics

PD is the effect that the drug has on the body. Specifically, it is often viewed as drug binding to a receptor to elicit a physiological effect (Figure 1.2).⁴²⁻
⁴⁴ Upon varying concentrations of a drug, while simultaneously monitoring the physiological effect, the maximum response will yield an optimal concentration to dose. PD profiles contain information that can be used to determine such parameters as, potency (E_{50}), efficacy (E_{max}), minimum effective concentration (MEC), and maximum effective concentration. The maximum response or efficacy typically occurs when 100% of the receptors are bound. An exception is when a fraction of the receptors being bound elicit the maximum response, with the remaining receptors being referred to as spare receptors.¹² Potency, or the

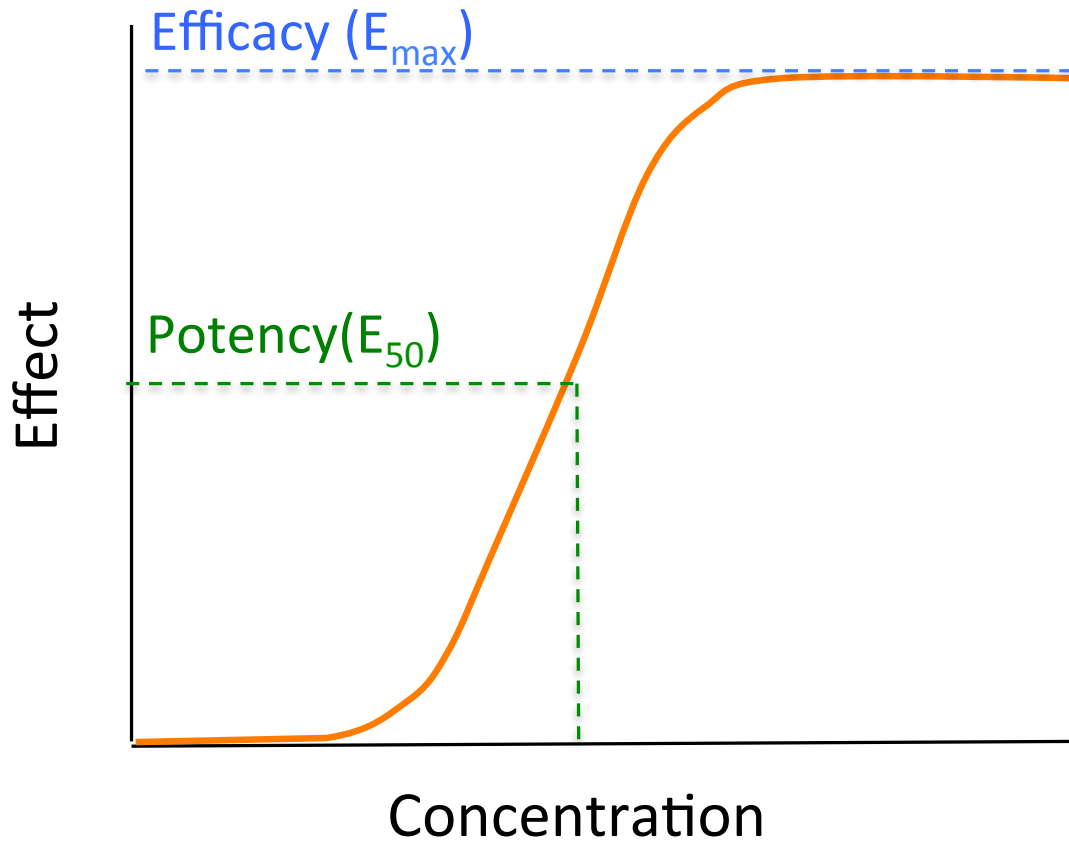


Figure 1.2 Pharmacodynamic Profile and Parameters. A PD profile is obtained by plotting the observed effect with respect concentration. Various parameters such as efficacy and potency are obtained from PD profiles.

drug concentration at which cellular response is 50% of the maximum, is determined at the E_{50} point on the PD profile.

PD profiles are primarily obtained on *in vitro* platforms, utilizing static flow models.⁴⁵⁻⁵³ For example, in a stationary environment, a given bacteria is cultured and administered a specific dose of antibiotic, which is unable to be manipulated. The growth of the bacterial cells in the static model, is limited by available nutrition, space, and produced waste and can be further read about in section 1.2.3.5 under Static Models. However, kinetics of death rate and MEC are vital parameters obtained in PD *in vitro* experiments.⁴⁰

1.2.3.3 Pharmacokinetics

PKs, the effect of the body on the drug,⁵⁴ describe a drug's absorption, and subsequent distribution throughout the system, before the drug is both metabolized and excreted from an individual (ADME; Figure 1.3). Characterization and quantification of the ADME properties are critical for approval of a potential drug or target.^{12,13}

Absorption

There are various routes in which a drug is administered to a patient, including enteral (oral), parenteral (intravenous, subcutaneous, intramuscular), mucus

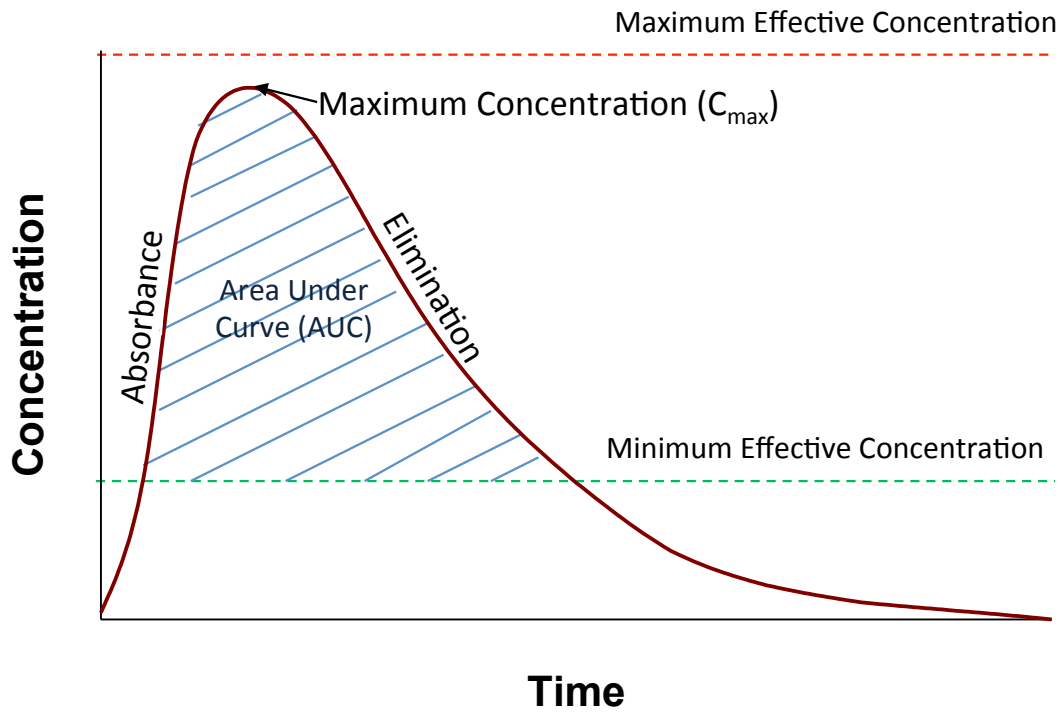


Figure 1.3 Pharmacokinetic Profile and Parameters. A PK profile is obtained by taking the concentration in plasma versus time. Various parameters such as area under the curve, absorbance rates, elimination rate constants, half life, and maximum concentrations can be obtained with PK profiles.

membrane, and transdermal. Each dosing route has advantages and disadvantages, thereby allowing the proper dosage form to be chosen. The oral route is a simple form of dosing that is convenient and painless for the patient to self-administer, although bioavailability (the fraction of drug absorbed into body) may be hindered by the digestive system environment. Absorption into the body is delayed in oral administrations, especially when compared to intravenous (IV) dosing, which bypasses all boundaries and administers the drug directly into the blood stream. IV dosing results in 100% bioavailability, which is defined as:

$$\text{Bioavailability} = \frac{\text{Concentration present in Circulation}}{\text{Concentration Administered}}$$

Subcutaneous dosing has a relatively slow absorption rate compared to the intramuscular injections, however, the injections are much more painful for the patients. Transdermal administrations, are noninvasive, user friendly, and simple, but must contain highly lipophilic properties to allow transport across cellular membranes, which results in a very slow dosing onset.¹² Upon being absorbed, the drug reaches a maximum concentration in the plasma (C_{\max}), a critical parameter obtained during PK studies.

Distribution

Once the absorbed drug reaches the circulation, the drug is may be distributed throughout the body, allowing it to reach the target tissues. Importantly, although

drug concentrations in the body are often reported in the plasma, this does not directly reflect the concentration in the target tissue. Volume of distribution (V_d) is the main parameter characterized during the distribution process. V_d determines the extent that a drug distributes through the body and is described by:

$$V_d = \frac{[\text{Drug}]_{\text{Body}}}{[\text{Drug}]_{\text{Plasma}}}$$

Therefore, the ratio of the concentration of the drug in the body, or dose administered, to the concentration in the plasma yields the extent of distribution. A higher distribution indicates that more of the target tissues have been reached. V_d does not represent a physiologically relevant volume due to values of V_d potentially exceeding the volume of a human body. Thus, when V_d exceed that of the total volume of blood, a greater distribution can be inferred, whereas, if V_d yields a value similar to that of the plasma it can be assumed that very little drug has left the circulation.^{12,55}

The distribution of a drug in the body is divided into various compartments (Figure 1.4). In a one compartment model, the body is viewed as a single entity; therefore, upon administering the drug it is distributed throughout the body instantaneously. In a two compartment model, as implied by the name, the drug is administered to a particular compartment (blood, brain, lungs, kidney, liver), before being distributed to the second compartment(s) such as skin, muscle,

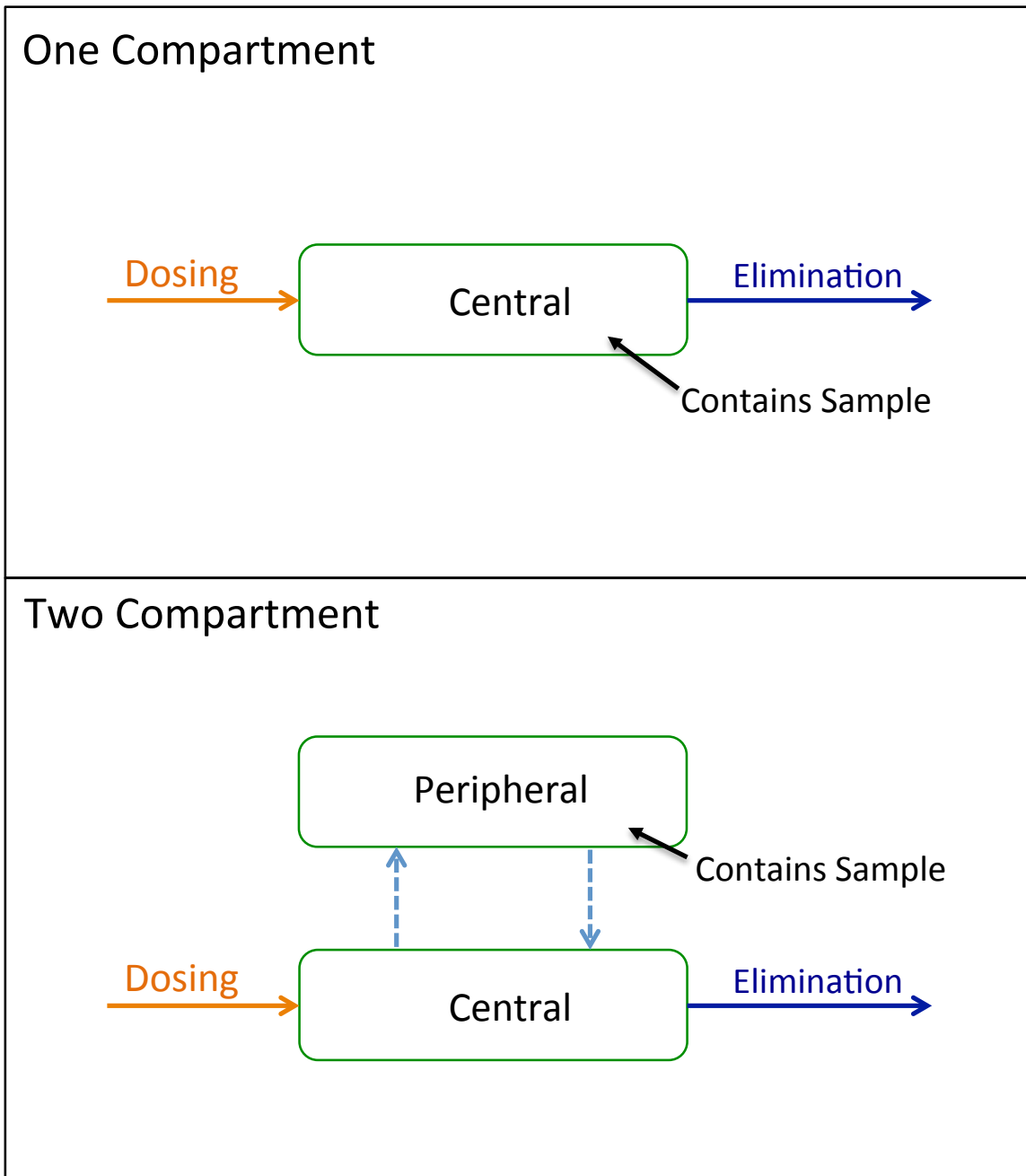


Figure 1.4 Schematic of a One and Two Compartment Model. Top. One compartment model is the simplest model, where uniform, simultaneous absorbance is assumed. Sample is located in the central compartment in direct contact with the flow. Bottom. Two compartment model where drug is flowed through the central compartment and out to waste. Drug transports from the central reservoir to the peripheral compartment, which contains sample.

and/or fat. Additional compartments can be added to the model, however, with each subsequent compartment the complexity of the model significantly increases.⁵⁵

Metabolism

Metabolism of a drug often renders the drug inactive before subsequent elimination by excretion. While several organs such as skin, lungs, kidneys, and the gastrointestinal tract contain metabolizing enzymes, the main organ responsible for metabolism is the liver. In general, the liver modifies the drugs through biotransformation, which is broken down into oxidation/reduction reactions (Phase I) and conjugation/hydrolysis reactions (Phase II).^{12,55} In oxidation/reduction biotransformation the drug is modified by either an oxidation or reduction reaction. Most drugs are oxidized through the cytochrome P450 pathway. Prodrugs such as clopidogrel (Plavix) are administered as biologically inactive molecules, but upon being metabolized in Phase I, either through oxidation or reduction reactions, the active form of the drug is exposed and released back into circulation. Once the drug returns to the liver it is further metabolized (Phase II) to a form that facilitates excretion. Conjugation and hydrolysis reactions are also able to trigger prodrug activation. In general, conjugation/hydrolysis reactions hydrolyze hydrophobic molecules to increase hydrophilicity, thereby increasing solubility and subsequent excretion.^{12,55}

Excretion

Upon metabolism, drugs and their metabolites have an enhanced hydrophilicity compared to their original states. The primary path of elimination is through renal excretion (kidney) although there are other pathways of elimination such as biliary excretion (bile). Elimination rate in the kidneys is contingent upon such parameters as secretion, reabsorption, and drug filtration rates. Reduced kidney function can hinder renal excretion and possibly lead to overdose due to accumulation of drug.^{12,55}

Pharmacokinetic Parameters

The elimination portion of the PK curve, chiefly encompassing metabolism and excretion, contains various parameters including the elimination rate constant, clearance, and half-life. The kinetics, related to the elimination, must first be examined before determining the aforementioned parameters. Most drugs [D] are eliminated under first order kinetics:

$$-k[D] = \frac{d[D]}{dt}$$

Consequently, the concentration of drug that is eliminated, represented by the elimination rate constant (k), is proportional to the concentration in the plasma with respect to time (d[D]/dt). Therefore, graphically, a quadratic relationship is observed for all first order elimination kinetics. The quadratic relationship proves

linear when imposing natural logarithmic association, with the resulting slope being equivalent to the elimination rate constant (k):

$$\ln[D]_t = -kt + \ln [D]_0$$

Derived from the first order reaction equation, the natural log of the drug at a specific time point yields a slope (k) and a y-intercept of the natural log of the original concentration. Although less common, drugs could potentially undergo zero order rate kinetics where the elimination rate is entirely independent of plasma drug concentration, resulting in a linear relationship:^{12,55,56}

$$k[D]_0=k$$

The previously mentioned linear slope of the zero order reaction is equivalent to the elimination rate constant (k). Such zero order rates are seen with alcohol consumption.

The main parameter derived from the elimination rate constant is the half-life ($t_{1/2}$), or the time required for the original concentration to be reduced by 50%:

$$t_{\frac{1}{2}} = -\frac{\ln\left(\frac{1}{2}\right)}{k} = \frac{0.693}{k}$$

The equation for determining the half-life is derived from the natural logarithmic relationship of the first order rate reaction. In first order rate reactions, the half-life is independent of initial concentration; therefore the half-life is constant regardless of the starting dose of the drugs. However, in zero order rate reactions the half-life is halved each consecutive half-life.^{12,55,56}

Another key parameter in defining the elimination of a drug is clearance. Under first order rate kinetics, the clearance of a curve is constant and is related to the volume of distribution and elimination rate constant, which can subsequently be associated with the half-life:^{12,55}

$$t_{\frac{1}{2}} = \frac{0.693}{k} = \frac{0.693 * V_d}{Cl}$$

PK parameters are applied to determine the appropriate concentrations required to reach a steady state for both single and multiple dosing (Figure 1.5). Steady state is achieved when the amount of drug in the system is equivalent to the amount being eliminated, while still maintaining the concentration in a therapeutic range. An example of maintaining steady state is a patient administering an antibiotic daily over a period of 7-10 days. A steady state is achieved after a

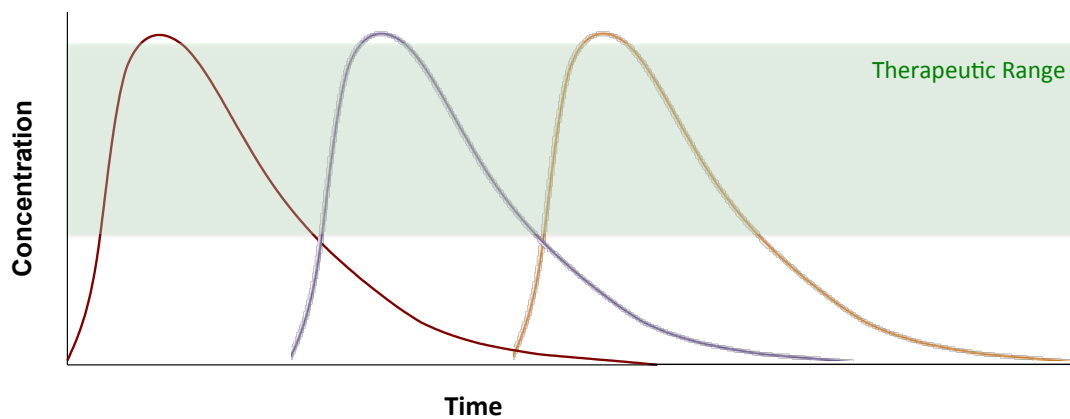


Figure 1.5 Multiple Day Dosing Steady State. Example of a three day dosing PK profiles assuming the dosing has achieved steady state.

specific time point, resulting in the plasma concentration remaining approximately constant. Therefore, prior to administration, a drug must undergo extensive clinical trials to determine the various parameters described above.^{12,55} Traditionally, *in vivo* animal models are used to obtain PK profiles prior to human trials.

1.2.3.4 *In Vivo* Animal Pharmacokinetics

In vivo animal models are crucial in PK studies for predicting potential drug dosing and side effects in humans. The animal models provide a living system that is somewhat comparable to humans. However, PK profiles have the potential and ultimate disadvantage of varying from that of a human due to metabolism differences and scaling issues.^{57,58} Moreover, specific animal models for specific disease types might not be available, or are extremely costly to produce. *In vivo* animal experiments are costly, regardless if the animal models are readily available. Many *in vivo* studies are obtained through composite or parallel sampling, i.e., a different animal sampled at every time point on a PK profile, which consumes large quantities of materials, time and requires high technical skills (Figure 1.6).^{57,59}

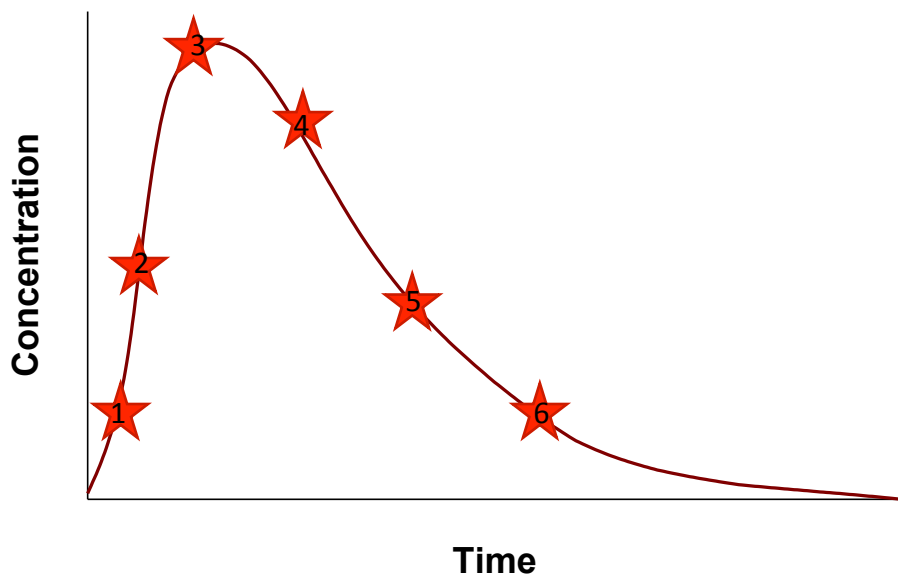
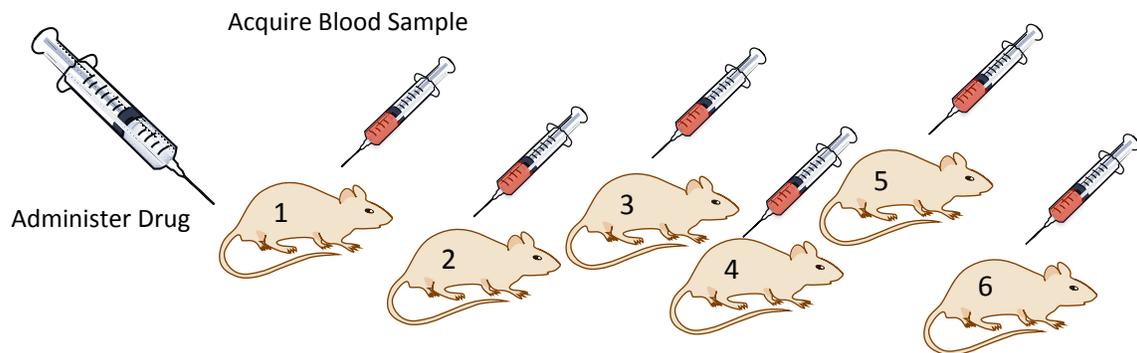


Figure 1.6 Schematic of Parallel or Composite *In Vivo* Sampling. An example of a typical composite *in vivo* sampling. The drug is administered to all animal samples. At specific time points, one animal is sampled and the concentration of drug in the plasma determined, i.e., in the schematic, Animal 1 was sampled for time point 1, Animal 2 was sampled for time point 2, etc.

1.2.3.5 *In Vitro* Pharmacokinetics

Although *in vivo* studies yield valuable PK information, the associated material and costs have resulted in these studies being complimented with *in vitro* studies since the 1960's.^{45,60,61} While *in vivo* studies are irreplaceable, *in vitro* studies have a multitude of advantages, including enhanced control over variables, wider dosing range, and sizeable variety of cellular additions. *In vitro* studies are not without disadvantages though, such as the general design and set-up being an oversimplification of *in vivo* systems. Thus, such *in vitro* systems are often lacking variables present in a living system. These missing variables may include an immune system, dynamic temperatures, cellular growth rate, experimental time versus therapy time, distribution of the drug, and protein binding. Attempting to address the aforementioned limitations of an *in vitro* set-up results in an increasingly complex model. The simplicity of *in vitro* set-ups can be saved when coupling *in vitro* studies with *in vivo* animal models, thereby increasing efficiency while reducing materials and cost. Three *in vitro* models, in increasing complexity are static, dynamic, and diffusion dynamic models. The models are identified based on the environment to which the sample is exposed, as well as how the dosing is achieved.^{40,57,62}

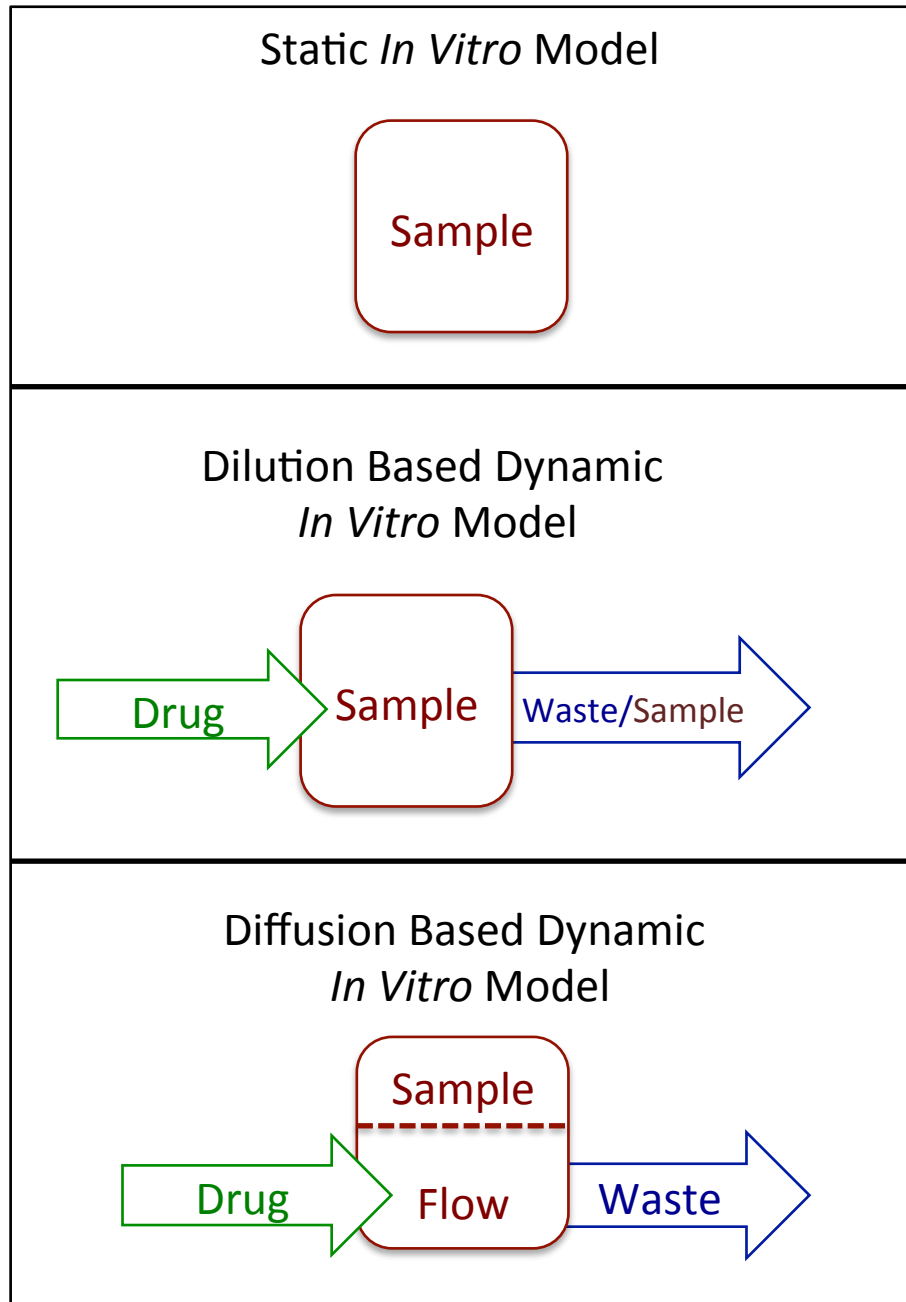


Figure 1.7 Various types of Pharmacokinetic and Pharmacodynamics *In Vitro* Models. *Top.* Static *in vitro* model where a sample is in a constant environment and dosed. Drug concentration is not able to be manipulated. *Middle.* The dilution based *in vitro* model introduces flow into the sample reservoir to manipulate concentration but sample is lost. *Bottom.* In a diffusion based *in vitro* model the sample is conserved by isolating from the flow. Analyte diffuses to the sample compartment from the central compartment while toxic metabolites, produced by the sample simultaneously diffuses into the flow where it goes to waste.

Static Models

Static models are traditionally utilized in PD studies, but will be described here in order to describe *in vitro* classifications together. Static models, the simplest *in vitro* model, are used to describe a constant environment, mimicking that of an intravenous dosing (Figure 1.7). Samples such as bacteria or cells are exposed to a fixed dose of drug administered directly to the sample.⁴⁵⁻⁴⁹ Within static studies, the sample may be constrained in such containers as cell culture flasks,⁶³ spinner flasks,⁶⁴ tubes,^{65,66} and flasks.^{45,61} While valuable parameters, such as minimum effective concentration or minimum bactericidal concentration are obtained, the growth of the bacteria is limited by the media present, build up of waste, aeration, and space. Differentiating the effect of the drug from that of the static environment can be a challenge in these studies. Another limitation of constant dosing that does not mimic the manipulation of dosing observed *in vivo* is the presence of flow that occurs in the circulation.^{57,62,67,68}

Dilution-Based Dynamic Models

The concentration of drug in an *in vitro* system is able to be manipulated with the introduction of flow. Dilution-based dynamic *in vitro* models are a one compartment model (see section 1.2.3.1.2 under *Distribution*), where the sample is in direct contact with flow (Figure 1.7). For example, in a dilution based dynamic *in vitro* model lacking a filter, samples are added to a fixed-volume flask containing concentrated drug. Drug-free media is subsequently added to the

flask, essentially diluting the concentration of drug exposed to the sample, therefore mimicking an elimination of drug from the body.^{57,62} Various models dose the drug in either stepwise or continuous dilutions. Stepwise dilutions result in the dilution of drug and direct loss of sample, as media is removed at the same time fresh media is added.⁶⁹ Continuous dilution models⁷⁰⁻⁸² not only dilute the drug, but also result in a dilution of the sample creating bias. Although this bias can be corrected through mathematical projections, error is still possible due to complexities involved with growth of biofilms⁷⁴ and changes in growth rates.^{57,62}

Dilution-based dynamic *in vitro* models, upon incorporating a filter, allows the conservation of sample, in the reservoir.^{47,64,72,83-88} The filter contains the sample in the flask throughout dilution steps, while a stir bar keeps the sample from clogging the filter membrane. As drug-infused media is added to the flask, sample-free media is continuously drawn out of the flask. PK profiles are obtained through the simple dilution steps, while conserving the sample throughout the dosing and dilutions. Dilution based dynamic models lacking filters can operate in either a stepwise or continuous manner that is dependent upon the setup. A potential limitation with filter dilution based dynamic model is blockage of the filter from sample as flow rates are increased.^{57,62}

Diffusion-Based Dynamic Models

The third type of PK model is a diffusion-based dynamic model, also known as a dialysis model, which is modeled after a closed system, two compartment model (see section 1.2.3.1.2 under *Distribution*). This model houses the sample in a compartment isolated from direct flow by a porous membrane (Figure 1.7). The membranes are classified as either artificial⁸⁹⁻⁹⁷ or natural membranes.⁹⁸⁻¹⁰² Artificial membranes are simply porous filters of synthetic materials such as polycarbonate or polyester, whereas natural membranes have adhered cells cultured on the artificial membranes. Natural membranes study the diffusion of drugs across an intracellular barrier. The general concept of the two membrane varieties are similar with the passive diffusion of drug from the channel into a sample compartment while toxic metabolites produced by the sample can simultaneously diffuse back into the flow compartment and out to waste. The sample is conserved, and due to the diffusion-based dosing the limitation of membrane blockage is averted. Typically, media containing high concentrations of drug, is initially flowed through the central compartment, allowing the drug to diffuse into the sample compartment. The flow of the drug-infused media continues until the sample compartment has reached a concentration similar to those obtained *in vivo*. Once the desired concentration in the sample compartment has been reached, drug-free media is introduced into the flow chamber, essentially reversing the concentration gradient,

and allowing the drug to diffuse back into the flow compartment and subsequently out to waste, thereby mimicking elimination.^{40,62}

An example of a diffusion-based dynamic *in vitro* PK model utilized in industry is the hollow fiber chamber reactor (HFCR).^{97,103-108} The HFCR is comprised of a cartridge containing thousands of porous capillaries. Samples are seeded in the sterile extra capillary space. Drug, fresh media, and nutrients are flowed through the porous capillaries, thereby allowing diffusion into the extra capillary space to dose the samples, while waste created by the samples diffuses into the capillaries. While this model conserves sample during the dosing process, large volumes of drug and media are consumed in the process. The large volume of drug becomes problematic when the drug has a challenging or costly synthesis. Also, samples seeded in the extra capillary space are not able to be accessed once the cartridges have been sealed, resulting in the cartridges being essentially single use due to the sterilization concerns and reductions in. This lack of reusability, and the low throughput significantly add to the expensive set up. Other limiting factors are drugs binding to the porous capillaries, membrane blockage, and sampling from the sampling chamber containing sample to determine actual concentrations.^{40,62}

PK and PD detection are able to be coupled, on an *in vitro* platform, in order determine the efficacy in response to a specific dosage scheme. Monitoring

these two pharmacological factors would increase efficiency by allowing more informed decisions toward the target in question.

Upon completion of the preclinical stage, an Investigational New Drug Application (IND) is submitted to the FDA for approval for the drug to continue on to clinical trials. The IND is essentially a summary of all preceding stages and studies.^{12,13} Without approval of the IND, a drug is not able to proceed to clinical trials.

1.2.3.6 Clinical Trials

At the point that a drug is approved for clinical trials, i.e., the first time humans are dosed, the target compounds have been further reduced to approximately five. Clinical trials encompass 50-70% of the drug discovery and development cost, while the timeframe associated with clinical trials is on the order of 6-7 years. The drug discovery and preclinical steps, combined, are approximately 3-6 years before being passed to the clinical stage (Figure 1.1).^{12,13,109}

Phase I

A small group consisting of 20-100 healthy patients are dosed in Phase I trials to observe potential side effects with dose. The dose administered to humans will have been previously determined with *in vivo* animal models during the preclinical stage.¹² Safety due to toxicity, adverse effects, and kinetics in the

human body are the main focus points in Phase I trials. Approximately 40% of drugs that enter phase I end up undergoing attrition.⁶

Phase II

Phase II involves a larger study group, typically exceeding 200 participants, in which patients with the disease are dosed at random with placebos or actual dosing determined in Phase I. Studies can be single (patient does not know if they have been given the actual drug or a placebo) or double blinded (the patient and doctor are both unaware). Additional information on safety, efficacy, and side effects obtained in Phase II assists in designing future Phase III trials.¹² Approximately 62% of drugs that passed Phase I do not pass Phase II.⁶

Phase III

Phase III trials are very similar to Phase II trials, but a patient population between 1000-5000 individuals is studied. Similar concepts involving placebos, dosing, and double-blinded studies are employed with various parameters being monitored. Dosing used in Phase III is determined from observations made in Phase II, as a result of the safety and efficacy studies. The failure rate in Phase III is 40%.⁶ Upon completion of Phase III studies, a drug can be submitted for approval as a New Drug Application (NDA) to the FDA where all results from preceding stages are reviewed. The review process could potentially take up to two years. Additional studies involving a “Phase IV” and Post Market

Surveillance, could possibly be needed and is dependent upon reviews from the NDA.^{12,13} A fourth of the drugs that reach the review process undergo attrition.⁶

1.3 Microfluidic Applications

Thus far the drug discovery and development process has been examined in depth. Specifically highlighted is the inefficiency, and high cost associated with bringing a drug to market.²⁻⁴ Research improvements, such as high throughput screening, have the potential to increase efficiency in identifying potential targets, although increased number of drug approvals has yet to be realized. Downsizing and developing high throughput dynamic diffusion *in vitro* PK models, based on the concept of existing *in vitro* setups, is another area in which efficiency can be increased. Microfluidics offer an attractive downsizing platform to reduce volume consumption of the diffusion based dynamic *in vitro* platforms.^{110,111} The terms ‘Body on a Chip’ and ‘Organ on a Chip’ have been frequently used to describe microfluidic devices that merge varying cell types in different compartments, similar to the multi-compartment model, which more closely represents an *in vivo* environment.¹¹²⁻¹¹⁷ The aforementioned models utilized PK and PD profiling (PK/PD) monitored in tandem. However, as the models include additional compartments, the complexity increases significantly.

1.3.1 Pharmacokinetic/Pharmacodynamic Microfluidic Platforms

Multiple microfluidic platforms have been reported in pharmacological models comprised of various materials such as, Plexiglass,¹¹⁸ polydimethyl siloxane (PDMS),^{115,119-122} polystyrene,^{123,124} three dimensional printed acrylates^{125,126} or combinations of the aforementioned materials.¹¹² Specifically, Sung *et al.* fabricated a PK/PD microfluidic model, containing multiple layers of PDMS, Plexiglass and polystyrene, which incorporated multiple compartments consisting of tissue representing liver, tumor, and marrow.^{112,127} Another 'organ on a chip' PDMS based PK/PD microfluidic device fabricated by Huh *et al.* was modeled after alveolar-capillary interface of a human lung.¹¹⁵ Lockwood *et al.*, although not marketed as a PK/PD device, used a two compartment PDMS based microfluidic device which, upon dosing red blood cells with the sickle cell drug hydroxyurea, enabled the monitoring of the PD response of endothelial cells adhered to a detection well.¹²⁰ The microfluidic scale offers the unique opportunity to observe and monitor various cell types in spatially relevant proximities. However, as in all cases of microfluidic PK/PD devices, such drastic reductions in volume are not necessary. Even reducing volumes to a milifluidic scale would result in significant improvements in volume consumption. Potential limitations associated with microfluidics are a lack of automation, skilled technicians for fabrication and use, impact of materials on adhered cells, as well as, subsequent shear forces.^{111,112,128,129} The lack of automation is one of many reasons microfluidics have not been regularly employed by the pharmaceutical

industry. Established and existing automated infrastructure, e.g., auto samplers, plate readers, and robotics, demands that any new technologies conform to such equipment. Pharmaceutical companies would have to make a significant commitment financially to utilize microfluidics in their current state.¹¹¹

Polystyrene/PDMS based microfluidic devices have been reported to be amenable to automation and are more rigid than PDMS based devices; however, fabrication was still highly technical and labor intensive.^{123,124} Furthermore, the polystyrene/PDMS device was not specifically utilized for PK/PD experimentation. The devices were modeled after a 96 well plate, thereby adding amenability to automation, such as a conventional plate reader. However, the trained technical skills required, as well as the high risk of device failure make the gap associated with the jump to industry challenging.

3D printing has the potential to bridge the aforementioned gap into industry.¹³⁰ 3D printed devices, Anderson *et al.*, offer a rigid, reusable two compartment PK/PD platforms that would alleviate limitations associated with traditional microfluidics, i.e., lack of automation, skilled technicians, and reusability.¹²⁵ 3D printing allows flexibility with device design, thereby integration with commercial fittings, as well as, modeling after 96 or 24 well plates merges microfluidic technologies with automation such as plate readers, auto samplers, robotics, etc. Again, limitations such as material biocompatibility also plague 3D

printed fabricated devices. Also, current resolutions hinder the channel sizes to the millifluidic scale however although the scale size is larger than the microfluidic models the change in volume scale is not a deterring factor.

In the following chapters, both PDMS and 3D printed devices will be explored and utilized for two compartment PK/PD modeling. Chapter 2 describes the experimental design and set up of the aforementioned Lockwood *et al.* device that was not marketed toward a PK/PD model, however in hindsight, the device is a rudimentary two compartment PK/PD set up. The dosing of the sickle cell drug, hydroxyurea to the red blood cell, a PK response, and the subsequent release of ATP in response to mechanical deformation while flowing through the microfluidic device channels, stimulates a nitric oxide production, a PD response, in endothelial cells, which is detected using an intracellular probe. The third chapter uses a prototype, comparable to the PDMS device used in Chapter 2, for specific PK characterization. While limitations previously mentioned, corresponding to PDMS based microfluidics, ultimately compromised this device layout and lead to the 3D printed diffusion based dynamic PK/PD device characterized in Chapter 4. Chapter 5 explores future uses, e.g., dosing spheroids with for chemotherapeutic agents, dosing *E. coli* over multiple days, with the 3D printed diffusion based dynamic in vitro PK/PD device with capabilities of natural or artificial membranes.

REFERENCES

REFERENCES

- (1) DiMasi, J. A.; Grabowski, H. G.: The cost of biopharmaceutical R&D: is biotech different? *Managerial and Decision Economics* **2007**, *28*, 469-479.
- (2) Kaitin, K.: Deconstructing the drug development process: the new face of innovation. *Clinical pharmacology and therapeutics* **2010**, *87*, 356.
- (3) Adams, C. P.; Brantner, V. V.: Estimating The Cost Of New Drug Development: Is It Really \$802 Million? *Health Affairs* **2006**, *25*, 420-428.
- (4) Dickson, M.; Gagnon, J. P.: Key factors in the rising cost of new drug discovery and development. *Nat Rev Drug Discov* **2004**, *3*, 417-429.
- (5) Grabowski, H.; Vernon, J.; DiMasi, J. A.: Returns on research and development for 1990s new drug introductions. *Pharmacoeconomics* **2002**, *20*, 11-29.
- (6) Kola, I.; Landis, J.: Can the pharmaceutical industry reduce attrition rates? *Nat Rev Drug Discov* **2004**, *3*, 711-716.
- (7) FDA Amendments Act. *Public Law No. 110-85, 121 STAT. 823*
- (8) Innovation or stagnation: challenges and opportunity on the critical path to new medical products. *Food and Drug Administration* **2004**.
- (9) Mervis, J.: Productivity Counts--But the Definition Is Key. *Science* **2005**, *309*, 726.
- (10) Lilly sells its Greenfield, Indiana, operations to Covance; expands existing collaboration between the two companies. **2008**.
- (11) Ohlstein, E. H.; Ruffolo Jr, R. R.; Elliott, J. D.: Drug discovery in the next millennium. *Annual review of pharmacology and toxicology* **2000**, *40*, 177-191.
- (12) Golan, D. E.; Tashjian, A. H.; Armstrong, E. J.: *Principles of pharmacology: the pathophysiologic basis of drug therapy*; Lippincott Williams & Wilkins, 2011.
- (13) Levine, R. R.; Walsh, C. T.; Schwartz-Bloom, R. D.: *Pharmacology: drug actions and reactions*; CRC Press, 2000.

- (14) Drews, J.: Drug discovery: a historical perspective. *Science* **2000**, *287*, 1960-1964.
- (15) Debouck, C.; Metcalf, B.: The impact of genomics on drug discovery. *Annual review of pharmacology and toxicology* **2000**, *40*, 193-208.
- (16) Cragg, M. S.; French, R. R.; Glennie, M. J.: Signaling antibodies in cancer therapy. *Current opinion in immunology* **1999**, *11*, 541-547.
- (17) Köhler, G.; Milstein, C.: Continuous cultures of fused cells secreting antibody of predefined specificity. *Nature* **1975**, *256*, 495-497.
- (18) Winter, G.; Harris, W. J.: Humanized antibodies. *Immunology today* **1993**, *14*, 243-246.
- (19) Queen, C.; Schneider, W. P.; Selick, H. E.; Payne, P. W.; Landolfi, N. F.; Duncan, J. F.; Avdalovic, N. M.; Levitt, M.; Junghans, R. P.; Waldmann, T. A.: A humanized antibody that binds to the interleukin 2 receptor. *Proceedings of the National Academy of Sciences* **1989**, *86*, 10029-10033.
- (20) Brüggemann, M.; Neuberger, M. S.: Strategies for expressing human antibody repertoires in transgenic mice. *Immunology today* **1996**, *17*, 391-397.
- (21) Huse, W.; Sastry, L.; Iverson, S.; Kang, A.; Alting-Mees, M.; Burton, D.; Benkovic, S.; Lerner, R.: Generation of a large combinatorial library of the immunoglobulin repertoire in phage lambda. *Science* **1989**, *246*, 1275-1281.
- (22) Hoogenboom, H. R.; de Bruïne, A. P.; Hufton, S. E.; Hoet, R. M.; Arends, J.-W.; Roovers, R. C.: Antibody phage display technology and its applications. *Immunotechnology* **1998**, *4*, 1-20.
- (23) Rodi, D. J.; Makowski, L.: Phage-display technology-finding a needle in a vast molecular haystack. *Current opinion in biotechnology* **1999**, *10*, 87-93.
- (24) Burke, M. D.; Schreiber, S. L.: A Planning Strategy for Diversity-Oriented Synthesis. *Angewandte Chemie International Edition* **2004**, *43*, 46-58.
- (25) Fenniri, H.: Combinatorial Chemistry. *Combinatorial Chemistry* **2000**.

- (26) Rademann, J.; Jung, G.: Integrating combinatorial synthesis and bioassays. *Science* **2000**, *287*, 1947-1948.
- (27) White, R. E.: High-throughput screening in drug metabolism and pharmacokinetic support of drug discovery. *Annual review of pharmacology and toxicology* **2000**, *40*, 133-157.
- (28) Kauvar, L. M.; Higgins, D. L.; Villar, H. O.; Sportsman, J. R.; Engqvist-Goldstein, Å.; Bukar, R.; Bauer, K. E.; Dilley, H.; Rocke, D. M.: Predicting ligand binding to proteins by affinity fingerprinting. *Chemistry & biology* **1995**, *2*, 107-118.
- (29) Burley, S. K.; Almo, S. C.; Bonanno, J. B.; Capel, M.; Chance, M. R.; Gaasterland, T.; Lin, D.; Šali, A.; Studier, F. W.; Swaminathan, S.: Structural genomics: beyond the human genome project. *Nature genetics* **1999**, *23*, 151-157.
- (30) Lindley, P. F.: Macromolecular crystallography with a third-generation synchrotron source. *Acta Crystallographica Section D: Biological Crystallography* **1999**, *55*, 1654-1662.
- (31) Dixon, S. L.; Villar, H. O.: Bioactive diversity and screening library selection via affinity fingerprinting. *Journal of chemical information and computer sciences* **1998**, *38*, 1192-1203.
- (32) Kindt, T.; Morse, S.; Gotschlich, E.; Lyons, K.: Structure-based strategies for drug design and discovery. *Nature* **1991**, *352*, 581.
- (33) Bohacek, R. S.; McMartin, C.; Guida, W. C.: The art and practice of structure-based drug design: A molecular modeling perspective. *Medicinal research reviews* **1996**, *16*, 3-50.
- (34) Colman, P. M.: Structure-based drug design. *Current opinion in structural biology* **1994**, *4*, 868-874.
- (35) Murcko, M. A.; Caron, P. R.; Charifson, P. S.: Structure-based drug design. *Annu. Rep. Med. Chem* **1999**, *34*, 297-306.
- (36) Amzel, L. M.: Structure-based drug design. *Current opinion in biotechnology* **1998**, *9*, 366-369.
- (37) Blundell, T. L.: Structure-based drug design. *Nature* **1996**, *384*, 23-26.

(38) Pritchard, J. F.; Jurima-Romet, M.; Reimer, M. L.; Mortimer, E.; Rolfe, B.; Cayen, M. N.: Making better drugs: Decision gates in non-clinical drug development. *Nature Reviews Drug Discovery* **2003**, *2*, 542-553.

(39) Sams-Dodd, F.: Strategies to optimize the validity of disease models in the drug discovery process. *Drug discovery today* **2006**, *11*, 355-363.

(40) Vaddady, P. K.; Lee, R. E.; Meibohm, B.: In vitro pharmacokinetic/pharmacodynamic models in anti-infective drug development: focus on TB. *Future medicinal chemistry* **2010**, *2*, 1355-1369.

(41) Derendorf, H.; Lesko, L. J.; Chaikin, P.; Colburn, W. A.; Lee, P.; Miller, R.; Powell, R.; Rhodes, G.; Stanski, D.; Venitz, J.: Pharmacokinetic/Pharmacodynamic Modeling in Drug Research and Development. *The Journal of Clinical Pharmacology* **2000**, *40*, 1399-1418.

(42) Levy, G.: Relationship between elimination rate of drugs and rate of decline of their pharmacologic effects. *Journal of pharmaceutical sciences* **1964**, *53*, 342-343.

(43) Levy, G.: Kinetics of pharmacologic effects. *Clinical pharmacology and therapeutics* **1966**, *7*, 362.

(44) Mager, D. E.; Wyska, E.; Jusko, W. J.: Diversity of Mechanism-Based Pharmacodynamic Models. *Drug Metabolism and Disposition* **2003**, *31*, 510-518.

(45) Garrett, E. R.; Wright, O. K.; Miller, G. H.; Smith, K. L.: Quantification and Prediction of the Biological Activities of Chloramphenicol Analogs by Microbial Kinetics¹. *Journal of medicinal chemistry* **1966**, *9*, 203-208.

(46) Li, R. C.; Zhu, M.; Schentag, J. J.: Achieving an optimal outcome in the treatment of infections. *Clinical pharmacokinetics* **1999**, *37*, 1-16.

(47) Nolting, A.; Dalla Costa, T.; Rand, K. H.; Derendorf, H.: Pharmacokinetic-pharmacodynamic modeling of the antibiotic effect of piperacillin in vitro. *Pharmaceutical research* **1996**, *13*, 91-96.

(48) Schentag, J. J.: Pharmacokinetic and pharmacodynamic surrogate markers: studies with fluoroquinolones in patients. *American journal of health-system pharmacy* **1999**, *56*, S21-S24.

(49) Schentag, J.: Antimicrobial action and pharmacokinetics/pharmacodynamics: the use of AUC to improve efficacy and avoid resistance. *Journal of chemotherapy* **1999**, *11*, 426-439.

(50) Jayaram, R.; Gaonkar, S.; Kaur, P.; Suresh, B.; Mahesh, B.; Jayashree, R.; Nandi, V.; Bharat, S.; Shandil, R.; Kantharaj, E.: Pharmacokinetics-pharmacodynamics of rifampin in an aerosol infection model of tuberculosis. *Antimicrobial agents and chemotherapy* **2003**, *47*, 2118-2124.

(51) Jayaram, R.; Shandil, R. K.; Gaonkar, S.; Kaur, P.; Suresh, B.; Mahesh, B.; Jayashree, R.; Nandi, V.; Bharath, S.; Kantharaj, E.: Isoniazid pharmacokinetics-pharmacodynamics in an aerosol infection model of tuberculosis. *Antimicrobial agents and chemotherapy* **2004**, *48*, 2951-2957.

(52) Shandil, R. K.; Jayaram, R.; Kaur, P.; Gaonkar, S.; Suresh, B.; Mahesh, B.; Jayashree, R.; Nandi, V.; Bharath, S.; Balasubramanian, V.: Moxifloxacin, ofloxacin, sparfloxacin, and ciprofloxacin against Mycobacterium tuberculosis: evaluation of in vitro and pharmacodynamic indices that best predict in vivo efficacy. *Antimicrobial agents and chemotherapy* **2007**, *51*, 576-582.

(53) Andes, D.; Craig, W. A.: Animal model pharmacokinetics and pharmacodynamics: a critical review. *International Journal of Antimicrobial Agents* **2002**, *19*, 261-268.

(54) Gerlowski, L. E.; Jain, R. K.: Physiologically based pharmacokinetic modeling: principles and applications. *Journal of pharmaceutical sciences* **1983**, *72*, 1103-1127.

(55) Dhillon, S.; Gill, K.: Basic pharmacokinetics. *Clinical pharmacokinetics* **2006**, 1-44.

(56) Hunter, P. W. W.; Pollock, A.: *Chemistry*; 8 ed.; Cengage, 2010; Vol. 2.

(57) Gloede, J.; Scheerans, C.; Derendorf, H.; Kloft, C.: In vitro pharmacodynamic models to determine the effect of antibacterial drugs. *Journal of antimicrobial chemotherapy* **2010**, *65*, 186-201.

(58) Boshoff, H. I. M.; Barry, C. E.: Tuberculosis [mdash] metabolism and respiration in the absence of growth. *Nat Rev Micro* **2005**, *3*, 70-80.

(59) Dudley, M. N.; Griffith, D.: Animal models of infection for the study of antibiotic pharmacodynamics. *Antimicrobial pharmacodynamics in theory and clinical practice*. Marcel Dekker, New York, NY **2001**, 67-97.

(60) Garrett, E.; Nolte, H.: Kinetics and mechanisms of drug action on microorganisms. XIV. The action of fluorouracil, other uracils and derived nucleosides on the microbial kinetics of *Escherichia coli*. *Chemotherapy* **1971**, *17*, 81-108.

(61) Garrett, E. R.; Miller, G. H.; Brown, M.: Kinetics and mechanisms of action of antibiotics on microorganisms V chloramphenicol and tetracycline affected *Escherichia coli* generation rates. *Journal of pharmaceutical sciences* **1966**, *55*, 593-600.

(62) White, R. L.: What in vitro models of infection can and cannot do. *Pharmacotherapy: The Journal of Human Pharmacology and Drug Therapy* **2001**, *21*, 292S-301S.

(63) Treyaprasert, W.; Schmidt, S.; Rand, K. H.; Suvanakoot, U.; Derendorf, H.: Pharmacokinetic/pharmacodynamic modeling of in vitro activity of azithromycin against four different bacterial strains. *International Journal of Antimicrobial Agents* **2007**, *29*, 263-270.

(64) Löwdin, E.; Odenholt, I.; Bengtsson, S.; Cars, O.: Pharmacodynamic effects of sub-MICs of benzylpenicillin against *Streptococcus pyogenes* in a newly developed in vitro kinetic model. *Antimicrobial agents and chemotherapy* **1996**, *40*, 2478-2482.

(65) Scaglione, F.; Demartini, G.; Dugnani, S.; Frascini, F.: A new model examining intracellular and extracellular activity of amoxicillin, azithromycin, and clarithromycin in infected cells. *Chemotherapy* **1993**, *39*, 416-423.

(66) Darouiche, R. O.; Dhir, A.; Miller, A. J.; Landon, G. C.; Raad, I. I.; Musher, D. M.: Vancomycin Penetration Into Biofilm Covering Infected Prostheses And Effect On Bacteria. *Journal of Infectious Diseases* **1994**, *170*, 720-723.

(67) Mueller, M.; de la Pena, A.; Derendorf, H.: Issues in pharmacokinetics and pharmacodynamics of anti-infective agents: kill curves versus MIC. *Antimicrobial agents and chemotherapy* **2004**, *48*, 369-377.

(68) Katsube, T.; Yano, Y.; Yamano, Y.; Munekage, T.; Kuroda, N.; Takano, M.: Pharmacokinetic–pharmacodynamic modeling and simulation for bactericidal effect in an in vitro dynamic model. *Journal of pharmaceutical sciences* **2008**, *97*, 4108-4117.

(69) Nishida, M.; Murakawa, T.; Kamimura, T.; Okada, N.; Sakamoto, H.: Laboratory evaluation of FR10612, a new oral cephalosporin derivative. *The Journal of antibiotics* **1976**, *29*, 444-459.

(70) Bergan, T.; Carlsen, M. I.; Fuglesang, J.: An in vitro model for monitoring bacterial responses to antibiotic agents under simulated in vivo conditions. *Infection* **1980**, *8*, S96-S102.

(71) Nies, B.: Comparative activity of cefixime and cefaclor in an in vitro model simulating human pharmacokinetics. *European Journal of Clinical Microbiology and Infectious Diseases* **1989**, *8*, 558-561.

(72) Haller, I.: Combined action of decreasing concentrations of azlocillin and sisomicin on *Pseudomonas aeruginosa* as assessed in a dynamic in vitro model. *Infection* **1982**, *10*, S229-S233.

(73) Grasso, S.; Meinardi, G.; De Carneri, I.; Tamassia, V.: New in vitro model to study the effect of antibiotic concentration and rate of elimination on antibacterial activity. *Antimicrobial agents and chemotherapy* **1978**, *13*, 570-576.

(74) Haag, R.; Lexa, P.; Werkhäuser, I.: Artifacts in dilution pharmacokinetic models caused by adherent bacteria. *Antimicrobial agents and chemotherapy* **1986**, *29*, 765-768.

(75) Gerber, A. U.; Wiprachtiger, P.; Stettler-Spichiger, U.; Lebek, G.: Constant infusions vs. intermittent doses of gentamicin against *Pseudomonas aeruginosa* in vitro. *Journal of Infectious Diseases* **1982**, *145*, 554-560.

(76) Satta, G.; Cornaglia, G.; Foddìs, G.; Pompei, R.: Evaluation of ceftriaxone and other antibiotics against *Escherichia coli*, *Pseudomonas aeruginosa*, and *Streptococcus pneumoniae* under in vitro conditions simulating those of serious infections. *Antimicrobial agents and chemotherapy* **1988**, *32*, 552-560.

(77) Firsov, A.; Chernykh, V.; Kuznetsova, S.; Navashin, S.: [A dynamic system for the in vitro study of the kinetics of the antimicrobial effect of antibiotics in pharmacokinetic changes in their concentration]. *Antibiotiki i meditsinskaia biotekhnologiya= Antibiotics and medical biotechnology/Ministerstvo meditsinskoi promyshlennosti SSSR* **1985**, *30*, 36-43.

(78) Firsov, A. A.; Nazarov, A. D.; Chernykh, V. M.; Navashin, S. M.: Validation of optimal ampicillin/sulbactam ratio in dosage forms using in-vitro dynamic model. *Drug Development and Industrial Pharmacy* **1988**, *14*, 2425-2442.

(79) MacGowan, A. P.; Bowker, K. E.; Noel, A. R.: Pharmacodynamics of the antibacterial effect and emergence of resistance to tomopenem, formerly RO4908463/CS-023, in an in vitro pharmacokinetic model of *Staphylococcus aureus* infection. *Antimicrobial agents and chemotherapy* **2008**, *52*, 1401-1406.

(80) MacGowan, A. P.; Bowker, K. E.; Wootton, M.; Holt, H. A.: Activity of moxifloxacin, administered once a day, against *Streptococcus pneumoniae* in an in vitro pharmacodynamic model of infection. *Antimicrobial agents and chemotherapy* **1999**, *43*, 1560-1564.

(81) MacGowan, A. P.; Rogers, C. A.; Holt, H. A.; Bowker, K. E.: Activities of moxifloxacin against, and emergence of resistance in, *Streptococcus pneumoniae* and *Pseudomonas aeruginosa* in an in vitro pharmacokinetic model. *Antimicrobial agents and chemotherapy* **2003**, *47*, 1088-1095.

(82) Allen, G. P.; Kaatz, G. W.; Rybak, M. J.: Activities of mutant prevention concentration-targeted moxifloxacin and levofloxacin against *Streptococcus pneumoniae* in an in vitro pharmacodynamic model. *Antimicrobial agents and chemotherapy* **2003**, *47*, 2606-2614.

(83) Greenwood, D.; Tupper, H.: New in vitro device for examining the response of bacteria to changing drug concentrations. In *Current chemotherapy and immunotherapy: proceedings of the 12th international congress of chemotherapy, Florence, 1981*; pp 100-102.

(84) Schneider, P.; Tosch, W.; Maurer, M.; Zak, O.: Antibacterial effects of cefroxadine, cephalexin and cephradine in a new in vitro pharmacokinetic model. *The Journal of antibiotics* **1982**, *35*, 843-849.

(85) Shah, P.: An improved method to study antibacterial activity of antibiotics in an in vitro model simulating serum levels. *Methods and findings in experimental and clinical pharmacology* **1980**, *2*, 171-176.

(86) Shah, P. M.: Bactericidal activity of ampicillin and amoxicillin. *Journal of antimicrobial chemotherapy* **1981**, *8*, 93-99.

(87) Löwdin, E.; Odenholt, I.; Cars, O.: In Vitro Studies of Pharmacodynamic Properties of Vancomycin against *Staphylococcus aureus* and *Staphylococcus epidermidis*. *Antimicrobial agents and chemotherapy* **1998**, *42*, 2739-2744.

(88) Odenholt, I.; Cars, O.; Löwdin, E.: Pharmacodynamic studies of amoxicillin against *Streptococcus pneumoniae*: comparison of a new

pharmacokinetically enhanced formulation (2000 mg twice daily) with standard dosage regimens. *Journal of antimicrobial chemotherapy* **2004**, *54*, 1062-1066.

(89) Toothaker, R. D.; Welling, P. G.; Craig, W. A.: An in vitro model for the study of antibacterial dosage regimen design. *Journal of pharmaceutical sciences* **1982**, *71*, 861-864.

(90) Drugeon, H.; Maurisset, B.; Chung, S.; Courtieu, A.: [Bactericidal activity of antibiotics as a function of pharmacokinetic constants. I. Experimental dynamic model simulating variations in the concentrations of antibiotics]. *Pathologie-biologie* **1982**, *30*, 837-839.

(91) Guggenbichler, J. P.; Semenitz, E.; König, P.: Kill kinetics and regrowth pattern of bacteria exposed to antibiotic concentrations simulating those observed in vivo. *Journal of antimicrobial chemotherapy* **1985**, *15*, 139-146.

(92) König, P.; Guggenbichler, J.; Semenitz, E.: Kill kinetics of bacteria under fluctuating concentrations of various antibiotics. II: Description of experiments. *Chemotherapy* **1986**, *32*, 44-58.

(93) König, P.; Guggenbichler, J.; Semenitz, E.; Foisner, W.: Kill kinetics of bacteria under fluctuating concentrations of various antibiotics. I: Description of the model. *Chemotherapy* **1986**, *32*, 37-43.

(94) Vance-Bryan, K.; Larson, T. A.; Garrison, M. W.; Toscano, J. P.; Canafax, D. M.; Rotschafer, J. C.: An in vitro pharmacodynamic model to simulate antibiotic behavior of acute otitis media with effusion. *Pharmaceutical research* **1992**, *9*, 920-924.

(95) Shah, P. M.: Activity of imipenem in an in-vitro model simulating pharmacokinetic parameters in human blood. *Journal of antimicrobial chemotherapy* **1985**, *15*, 153-157.

(96) Garrison, M.; Vance-Bryan, K.; Larson, T.; Toscano, J.; Rotschafer, J.: Assessment of effects of protein binding on daptomycin and vancomycin killing of *Staphylococcus aureus* by using an in vitro pharmacodynamic model. *Antimicrobial agents and chemotherapy* **1990**, *34*, 1925-1931.

(97) Zinner, S. H.; Husson, M.; Klastersky, J.: An artificial capillary in vitro kinetic model of antibiotic bactericidal activity. *Journal of Infectious Diseases* **1981**, *144*, 583-587.

(98) Hulten, K.; Rigo, R.; Gustafsson, I.; Engstrand, L.: New pharmacokinetic in vitro model for studies of antibiotic activity against intracellular microorganisms. *Antimicrobial agents and chemotherapy* **1996**, *40*, 2727-2731.

(99) Birkness, K.; Deslauriers, M.; Bartlett, J.; White, E.; King, C.; Quinn, F.: An In Vitro Tissue Culture Bilayer Model To Examine Early Events in Mycobacterium tuberculosis Infection. *Infection and immunity* **1999**, *67*, 653-658.

(100) Birkness, K. A.; Swisher, B. L.; White, E. H.; Long, E. G.; Ewing, E.; Quinn, F. D.: A tissue culture bilayer model to study the passage of Neisseria meningitidis. *Infection and immunity* **1995**, *63*, 402-409.

(101) Shaw, J.; Falkow, S.: Model for invasion of human tissue culture cells by Neisseria gonorrhoeae. *Infection and immunity* **1988**, *56*, 1625-1632.

(102) Shaw, J.; Hayes, F.; Brooks, G.; Falkow, S.: Development of a tissue culture model for gonococcal invasion. In *Gonococci and Meningococci*; Springer, 1988; pp 441-447.

(103) Blaser, J.; Stone, B.; Zinner, S.: Efficacy of intermittent versus continuous administration of netilmicin in a two-compartment in vitro model. *Antimicrobial agents and chemotherapy* **1985**, *27*, 343-349.

(104) Blaser, J.; Stone, B. B.; Groner, M. C.; Zinner, S. H.: Comparative study with enoxacin and netilmicin in a pharmacodynamic model to determine importance of ratio of antibiotic peak concentration to MIC for bactericidal activity and emergence of resistance. *Antimicrobial agents and chemotherapy* **1987**, *31*, 1054-1060.

(105) Blaser, J.; Vergères, P.; Widmer, A. F.; Zimmerli, W.: In vivo verification of in vitro model of antibiotic treatment of device-related infection. *Antimicrobial agents and chemotherapy* **1995**, *39*, 1134-1139.

(106) Ba, B. B.; Bernard, A.; Iliadis, A.; Quentin, C.; Ducint, D.; Etienne, R.; Fourtillan, M.; Maachi-Guillot, I.; Saux, M.-C.: New approach for accurate simulation of human pharmacokinetics in an in vitro pharmacodynamic model: application to ciprofloxacin. *Journal of antimicrobial chemotherapy* **2001**, *47*, 223-227.

(107) Dudley, M.; Mandler, H.; Gilbert, D.; Ericson, J.; Mayer, K.; Zinner, S.: Pharmacokinetics and pharmacodynamics of intravenous ciprofloxacin. Studies in vivo and in an in vitro dynamic model. *The American journal of medicine* **1987**, *82*, 363-368.

(108) Haller, I.: Penetration of antibiotics through cell culture monolayers. *Journal of antimicrobial chemotherapy* **1985**, *15*, 197-199.

(109) Kato, G. J.; Gladwin, M. T.; Steinberg, M. H.: Deconstructing sickle cell disease: reappraisal of the role of hemolysis in the development of clinical subphenotypes. *Blood reviews* **2007**, *21*, 37-47.

(110) Kang, L.; Chung, B. G.; Langer, R.; Khademhosseini, A.: Microfluidics for drug discovery and development: From target selection to product lifecycle management. *Drug discovery today* **2008**, *13*, 1-13.

(111) Neuži, P.; Giselbrecht, S.; Länge, K.; Huang, T. J.; Manz, A.: Revisiting lab-on-a-chip technology for drug discovery. *Nature Reviews Drug Discovery* **2012**, *11*, 620-632.

(112) Sung, J. H.; Kam, C.; Shuler, M. L.: A microfluidic device for a pharmacokinetic–pharmacodynamic (PK–PD) model on a chip. *Lab on a Chip* **2010**, *10*, 446-455.

(113) Huh, D.; Hamilton, G. A.; Ingber, D. E.: From 3D cell culture to organs-on-chips. *Trends in cell biology* **2011**, *21*, 745-754.

(114) Esch, M.; King, T.; Shuler, M.: The role of body-on-a-chip devices in drug and toxicity studies. *Annual review of biomedical engineering* **2011**, *13*, 55-72.

(115) Huh, D.; Matthews, B. D.; Mammoto, A.; Montoya-Zavala, M.; Hsin, H. Y.; Ingber, D. E.: Reconstituting organ-level lung functions on a chip. *Science* **2010**, *328*, 1662-1668.

(116) Baker, M.: Tissue models: A living system on a chip. *Nature* **2011**, *471*, 661-665.

(117) van Midwoud, P. M.; Verpoorte, E.; Groothuis, G. M.: Microfluidic devices for in vitro studies on liver drug metabolism and toxicity. *Integrative Biology* **2011**, *3*, 509-521.

(118) Sin, A.; Chin, K. C.; Jamil, M. F.; Kostov, Y.; Rao, G.; Shuler, M. L.: The Design and Fabrication of Three-Chamber Microscale Cell Culture Analog Devices with Integrated Dissolved Oxygen Sensors. *Biotechnology Progress* **2004**, *20*, 338-345.

(119) Ma, B.; Zhang, G.; Qin, J.; Lin, B.: Characterization of drug metabolites and cytotoxicity assay simultaneously using an integrated microfluidic device. *Lab on a Chip* **2009**, *9*, 232-238.

(120) Lockwood, S. Y.; Erkal, J. L.; Spence, D. M.: Endothelium-derived nitric oxide production is increased by ATP released from red blood cells incubated with hydroxyurea. *Nitric Oxide* **2014**, *38*, 1-7.

(121) van Midwoud, P. M.; Merema, M. T.; Verpoorte, E.; Groothuis, G. M.: A microfluidic approach for in vitro assessment of interorgan interactions in drug metabolism using intestinal and liver slices. *Lab on a Chip* **2010**, *10*, 2778-2786.

(122) Gunther, A.; Yasotharan, S.; Vagaon, A.; Lochovsky, C.; Pinto, S.; Yang, J.; Lau, C.; Voigtlaender-Bolz, J.; Bolz, S.-S.: A microfluidic platform for probing small artery structure and function. *Lab on a Chip* **2010**, *10*, 2341-2349.

(123) Anderson, K. B.; Halpin, S. T.; Johnson, A. S.; Martin, R. S.; Spence, D. M.: *Analyst (Cambridge, United Kingdom)* **2013**, *138*, 137.

(124) Johnson, A. S.; Anderson, K. B.; Halpin, S. T.; Kirkpatrick, D. C.; Spence, D. M.; Martin, R. S.: *Analyst (Cambridge, United Kingdom)* **2013**, *138*, 129.

(125) Anderson, K. B.; Lockwood, S. Y.; Martin, R. S.; Spence, D. M.: A 3D Printed Fluidic Device that Enables Integrated Features. *Analytical Chemistry* **2013**.

(126) Chen, C.; Wang, Y.; Lockwood, S. Y.; Spence, D. M.: 3D-printed fluidic devices enable quantitative evaluation of blood components in modified storage solutions for use in transfusion medicine. *Analyst* **2014**, *139*, 3219-3226.

(127) Shuler, M. L.; Sung, J. H.: Microfluidic device for pharmacokinetic-pharmacodynamic study of drugs and uses thereof. Google Patents, 2010.

(128) Kim, L.; Toh, Y.-C.; Voldman, J.; Yu, H.: A practical guide to microfluidic perfusion culture of adherent mammalian cells. *Lab on a Chip* **2007**, *7*, 681-694.

(129) Meyvantsson, I.; Warrick, J. W.; Hayes, S.; Skoien, A.; Beebe, D. J.: Automated cell culture in high density tubeless microfluidic device arrays. *Lab on a Chip* **2008**, *8*, 717-724.

(130) Gross, B. C.; Erkal, J. L.; Lockwood, S. Y.; Chen, C.; Spence, D. M.: Evaluation of 3d printing and its potential impact on biotechnology and the chemical sciences. *Analytical Chemistry* **2014**, *86*, 3240-3253.

CHAPTER 2

**UTILIZING POLYDIMETHYL-SILOXANE BASED MICROFLUIDIC DEVICES
FOR ANALYSIS OF ENDOTHELIUM-DERIVED NITRIC OXIDE PRODUCTION
STIMULATED BY ADENOSINE TRIPHOSPHATE RELEASED FROM RED
BLOOD CELLS INCUBATED WITH HYDROXYUREA**

2.1 Red Blood Cells and the Vascular System

Red blood cells (RBCs) are the oxygen delivery component of the whole blood matrix, which comprise approximately 5-6 L in an adult human. The matrix consists of approximately 45% RBCs, platelets, and leukocytes. The remaining 55% of matrix is made up of the plasma, which contains water, glucose, proteins, electrolytes, clotting factors and hormones.¹ The biconcave disc shape (6-8 μm diameter) of the RBC allows the maximum surface area per volume, thereby reducing the time required for oxygen to leave the cell by diffusion. The absence of nuclei and organelles in RBCs is yet another modification that enhances the efficiency of the RBC to carry oxygen, by allowing large quantities of hemoglobin (2.7×10^5 hemoglobin/RBC), an oxygen carrying protein. In humans, hemoglobin is comprised of 4 subunits (2 α globin and 2 β globin chains), which bind up to four oxygen molecules in the lungs and delivers the oxygen throughout the vascular system to tissues.² Resistance vessels (capillaries, arterioles) that ferry the oxygen-laden RBCs throughout the body are lined with a monolayer of

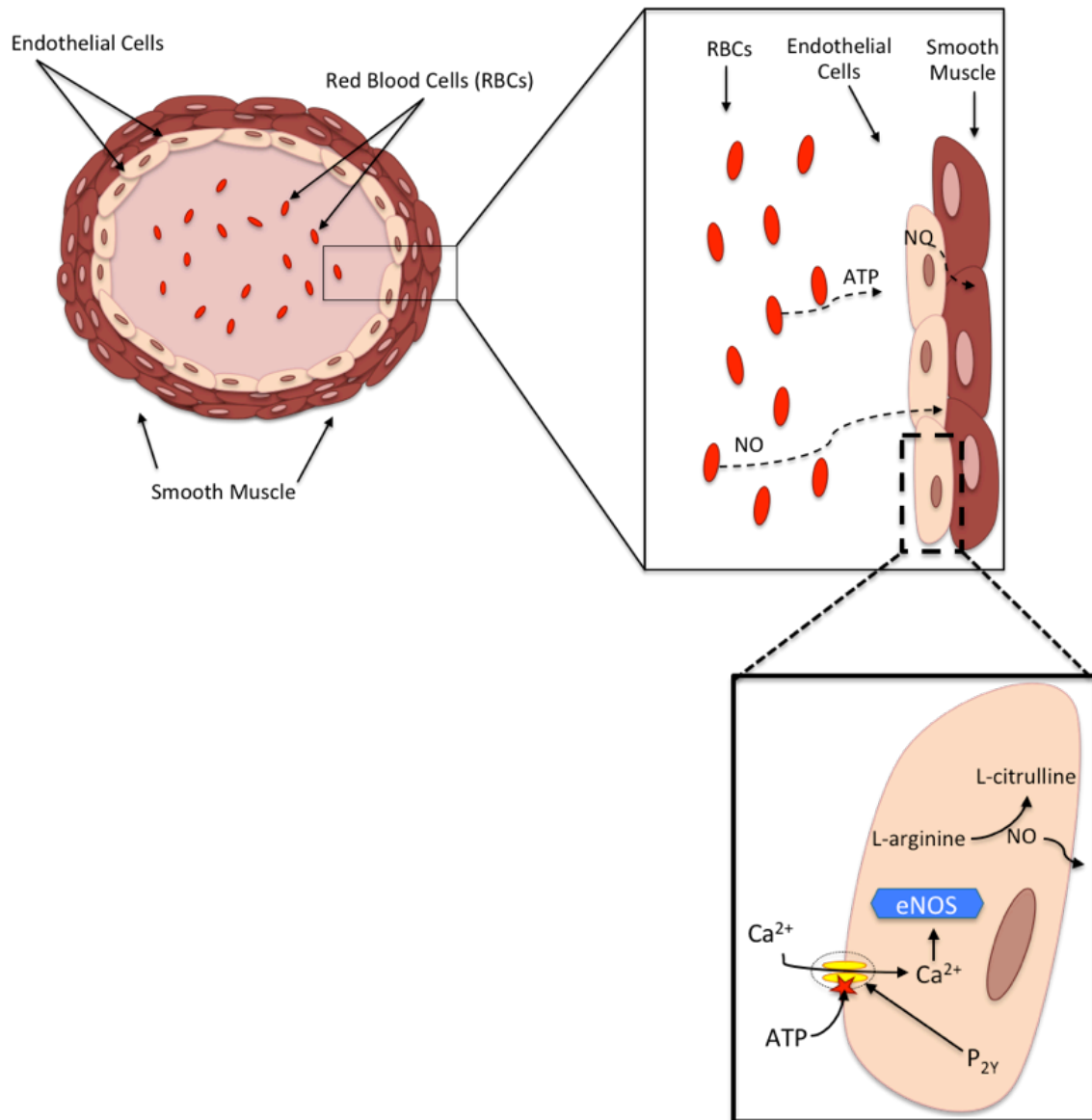


Figure 2.1 Proposed Sources of Nitric Oxide in Resistance Vessels, as well as, Adenosine Triphosphate Elicited Nitric Oxide Production in Endothelial Cells. Cross section of a resistance vessel (Left), showing only endothelial cells, RBC, and smooth muscle cells. Zoomed in version (Top Right) shows potential sources of NO in the vascular system; NO produced from RBC or the subsequent RBC derived ATP stimulation of NO production in endothelial cells. The ATP elicited NO synthesis is further depicted on bottom left. ATP binds to the purinergic receptor, P_{2Y}, which allows an influx of calcium ion into the cell, thereby stimulating e-NOS to convert L-arginine to L-citrulline.

endothelial cells. Surrounding this endothelial layer are the smooth muscle cells, which act to mediate resistance vessel diameter upon stimulation by the endothelium derived relaxation factor, nitric oxide (NO; Figure 2.1). NO has several potential sources, but RBC-derived adenosine triphosphate (ATP) is a main stimulus.

2.1.1 Red Blood Cell-Derived Adenosine Triphosphate

RBCs produce millimolar concentrations of adenosine triphosphate (ATP)³ through anaerobic glycolysis, due to the absence of mitochondria, thus impairing oxidative glycolysis.⁴ ATP can be released from RBCs in response to a variety of different factors such as hypoxia,^{5,6} pH,⁷ mechanical deformation (shear stress),⁸⁻¹² or small peptides,¹³ and pharmaceutical agents (hydroxyurea,^{14,15} iloprost,¹⁶). Shear stress has been linked to endothelium NO production,¹⁷ and the ensuing vasodilation, although Sprague *et al.* made the first connection requiring RBCs to be present for NO production.¹⁸ Subsequent data supported the role of RBC-derived ATP in stimulating the P_{2Y} purinergic receptor on endothelial cells.⁸

When the RBC encounters mechanical deformation, the ATP release mechanism begins with the receptor-mediated activation of G protein.¹⁹ The protein subtypes, G_{as} and G_{ai} then stimulate adenylyl cyclase, which converts ATP to 3'-5' cyclic adenosine monophosphate (cAMP).^{20,21} The cascade

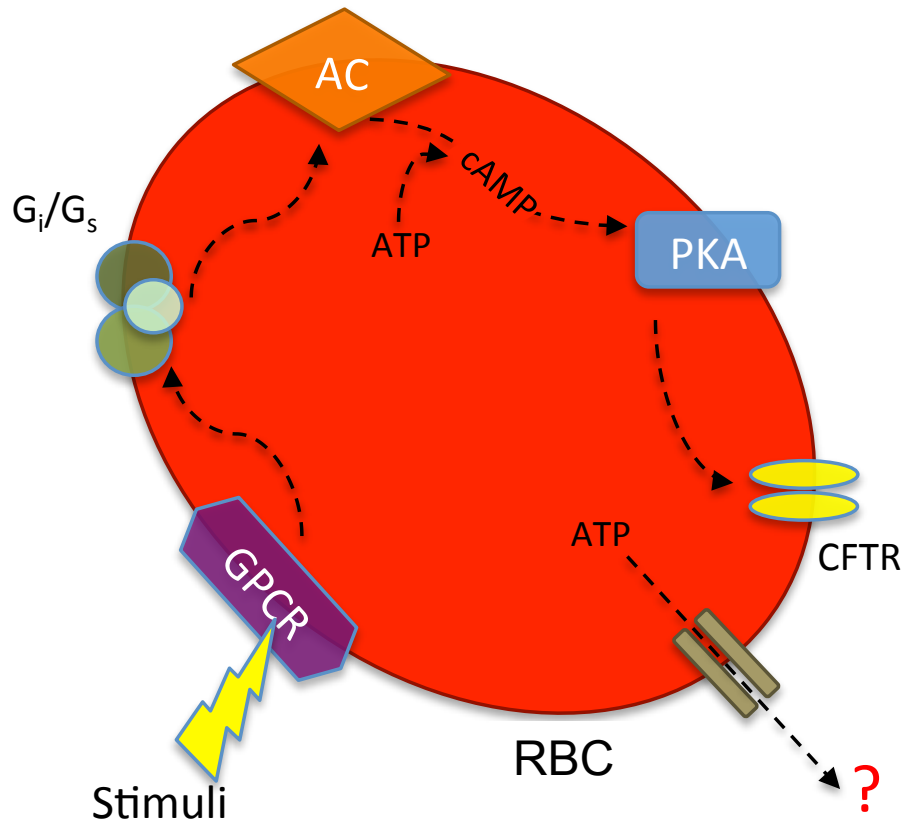


Figure 2.2 Proposed Signal Transduction Mechanism for Red Blood Cell Release of Adenosine Triphosphate in Response to Stimuli. GPCR activates the G protein in response to a conformation. The G protein subsequently triggers AC, which produces cAMP. PKA is activated by cAMP, which then phosphorylates the CFTR. ATP is then release but the remainder of the mechanism, whether the CFTR or another unidentified channel is responsible, is unknown

continues with protein kinase A (PKA) activation and subsequent phosphorylation of the cystic fibrosis transmembrane conductance regulator protein (CTFR).^{19,20,22} Upon phosphorylation of CTFR, ATP is released, although the exact mechanism is still unknown (Figure 2.2).

2.1.2 Mechanism of Nitric Oxide Stimulation

The aforementioned RBC-derived ATP, upon release, diffuses to the endothelium monolayer lining the resistance vessels, where it binds to P_{2Y} purinergic receptors. Once activated, the receptor allows an influx of calcium ions into the endothelial cell. Calcium, along with oxygen and NADPH, are cofactors needed for NO production by the endothelial nitric oxide synthase (e-NOS) enzyme. NO is formed upon the conversion of L-arginine to L-citrulline, where due to the small molecule's rapid diffusion (3,300-3,800 $\mu\text{m}^2/\text{s}$) and hydrophobicity, it easily passes through endothelial cell membranes to the smooth muscle layer, thus affecting vascular tone.

RBCs also contain e-NOS and are thus capable of producing NO. RBCs are capable of releasing NO in response to hypoxic conditions, however there exists conflicting hypotheses as to the source of the NO, primarily due to the relatively short half-life²³ of NO.²⁴⁻²⁷ For RBC-elicited NO to play a role in vasodilation, it must first diffuse to and cross the endothelial layer to reach the smooth muscle cells. The environment, through which it is diffusing, contains

hemoglobin and other oxidizing agents that would likely scavenge NO or change its form through redox chemistry.

2.2 Sickle Cell Disease

Sickle cell disease (SCD) is an autosomal recessive genetic blood disorder that primarily affects individuals of African descent.²⁸ While the exact number of infected individuals in the United States is unknown, it is estimated that 100,000 people have SCD.²⁹ This disease is caused by a single polymorphism mutation of an adenine to a thymine, subsequently resulting in the substitution of a glutamate to a valine on the B subunit of the new hemoglobin (HbSS).³⁰⁻³² Upon deoxygenation, the mutated hemoglobin will begin to polymerize. Polymerization is reversible if the RBC is reoxygenated before a crucial threshold time.³³ The polymerization of HbSS into long fibers causes the affected RBC to become rigid and deform into a 'sickled' shape. It is this rigid shape and ensuing lack of deformation in RBCs that result in vaso-occlusive crises for patients with SCD. Vaso-occlusive crises have a multitude of effects ranging from pain, organ damage, stroke, and acute chest syndrome.³⁴ Anemia is an added symptom of SCD patients, owing to the reduced life span of sickled RBCs from 120 days for healthy RBCs to 16 days for sickled cells. These cells experience premature lysis due to decreased deformation.^{35,36} Additionally, the sickled RBCs accumulate along the endothelium due to increased adhesiveness of the RBCs. The aforementioned accumulation can cause damage to the endothelial layers of

the vascular system, which subsequently activates platelets and potentially leads to such medical complications as stroke, clotting, or pulmonary hypertension.³⁷

2.2.1 Use of Hydroxyurea as a Sickle Cell Disease Treatment

The only FDA approved drug for the treatment of SCD is hydroxyurea (HU). While the mechanism of action is still unknown, it is generally accepted that HU, a ribonucleotide reductase inhibitor,³⁸⁻⁴⁰ results in an increase in fetal hemoglobin (HbF) in RBCs.⁴¹⁻⁴⁵ The sickle hemoglobin has shown increased polymerization delay time (a reduction in sickling) in the presence of elevated levels of HbF.⁴⁶⁻⁴⁸ However, increased levels of HbF are not observed in patients who take HU for at least 4 weeks to 6 months after dosing, which does not explain the immediate relief reported by patients. Also, the beneficial effects are not uniformly reported through the adult population.⁴⁹ HU has been reported to result in overall improved blood flow, in accordance with the well-documented relationship of HU and the vasodilator, NO.⁵⁰⁻⁵⁶ The endothelial derived relaxation factor,⁵⁷ NO, potentially works to dilate blood vessels in SCD patients to allow the sickling RBCs to return to the lungs faster, thus becoming oxygenated before the polymerization of the deoxygenated hemoglobin becomes permanent.

HU's impact on the deformability of RBCs has been the focus of several conflicting reports, although the studies in question should not have been

controversial when considering that each study used varying concentrations of HU per RBC.^{35,36} Previously, our group reported that incubation of rabbit RBCs over a wide range of HU concentrations resulted in an increase in the amount of ATP release. Furthermore, the response to mechanical deformation was dependent upon the concentration of HU. As the concentration of HU increased, the ATP increased until it reached a maximum before a subsequent decrease in ATP as the HU concentrations continued to increase. Moreover, inhibiting e-NOS in RBCs resulted in the return of ATP release to basal levels, indicating a link between ATP release and the e-NOS stimulated NO.¹⁴

2.3 Utilizing Microfluidics for Investigating *In Vitro* Cell to Cell Interactions

Microfluidics offer the unique ability to spatially represent such *in vivo* conditions such as dynamic flow in channels that approximate blood vessels. Assays analyzing single cell types on microfluidic platforms have been well documented,⁵⁸⁻⁶³ however, the incorporation of a detection well isolated from a channel by a porous membrane has been limited.⁶⁴⁻⁶⁷ The detection well has the added benefit of separating the analyte of interest from the complex matrix in the channel (RBC containing hemoglobin).

A drawback of traditional microfluidics is the lack of integration with high throughput automation equipment such as plate readers, robotics, and auto samplers, ultimately limiting microfluidics expansion into industrial settings. Two

polydimethyl siloxane (PDMS) based microfluidic devices, used to facilitate the assay of endothelium derived NO release, are compared in this chapter. The experimental set up and reagents are identical for both designs with the difference lying in the detection schemes. The first is a conventional, time intensive, microscope-fluorescence detection scheme where each individual detection well is imaged several times for cellular count, background, and NO signal. The second microfluidic device was modeled after a 96 well plate, therefore all detection wells were able to be simultaneously detected using a high throughput plate reader, resulting in a significant reduction in time of analysis.¹⁵

2.4 Adenosine Triphosphate Release in Hydroxyurea Incubated Human Red Blood Cells

ATP release from human RBCs, incubated in various concentrations of HU, has been reported using the exact PDMS based microfluidic device design used in the plate reader set up described later in section 2.5.4.2. The results for ATP release from human RBCs incubated in HU were similar to those reported for rabbit RBCs incubated in similar concentrations of HU. A concentration of 100 μ M HU resulted in the highest ATP release from the RBCs (2.06 ± 0.37 fold). Concentrations less than or greater than 100 mM resulted in less RBC released ATP.

The use of ATP release inhibitors such as diamide and glybenclamide provided evidence that measured extracellular ATP was not due to cell lysis. The role of RBC-derived NO was found to play a critical role in the ATP release. Incubation of RBCs with L-N^G-Nitroarginine methyl ester (L-NAME), an e-NOS inhibitor, reduced ATP release to basal levels. ATP, when released in the vascular system, stimulates the endothelium to produce NO.

The cell to cell communication, i.e., RBC-derived ATP stimulating NO produced from endothelial cells, is mimicked in the *in vitro* microfluidic device. In short, RBCs, upon being incubated with the optimal concentration of HU, release ATP through mechanical deformation. The aforementioned ATP diffuses from the channel, through a porous polycarbonate membrane where it stimulates NO production in the endothelial cells.

2.5 Experimental

2.5.1 Materials and Methods

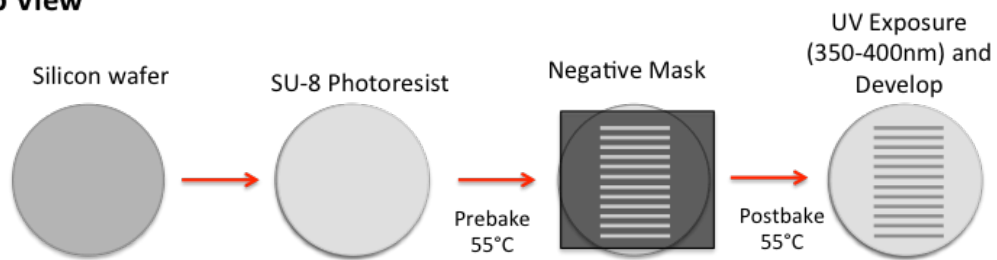
2.5.1.1 Fabrication of Master

The silicon wafers used in master fabrication have photocured resin that serve as molds for the polydimethyl siloxane (PDMS) devices. Before photocuring, the silicon wafers are cleaned with acetone, isopropanol and water, respectively. A piranha solution (2:1 sulfuric acid, 30% (w/w) hydrogen peroxide) was prepared to soak the silicon wafer overnight at 95 °C for a thorough clean.

Upon cooling to room temperature, the silicon wafer was removed from the corrosive acid before rinsing with deionized water and isopropanol.

Once cleaned, the wafer was ready to be prepared for fabrication of the master (Figure 2.3). The wafer was heated for 1 hour at 200 °C to allow for dehydration of the silanol groups. After the wafer had cooled, it was spin coated with SU-8-50 photoresist. A 50 mL syringe was filled with SU-8-50 and allowed to rest overnight to allow for degassing. The height of the features is dependent upon the uniformity of the layer of SU-8-50 achieved during the spin coat process. For example, to achieve 100 μm features, the wafer is accelerated at 100 rpm/s to 500 rpm for 15 seconds before being further accelerated at 300 rpm/s until ultimately reaching 1000 rpm, where the rpm were held for 30 seconds. Post spin coating, the SU-8-50 coated wafer is prebaked at 95 °C for 15 minutes to evaporate excess solvent. Once cooled, a transparent mask also referred to as a negative, which contains the desired features, is positioned above the wafer prior to curing by exposure to UV light. Current masks used for fabrication of masters are printed on conventional plastic transparencies by a laser printer. The ease and cost associated with using the laser printed transparencies are a significant enhancement over the time consuming and costly traditional masks. However, a critical limitation when using the laser printers for mask fabrication is reduced resolution of the mask features. Also, the printed portion of the transparency

Top View



Side View

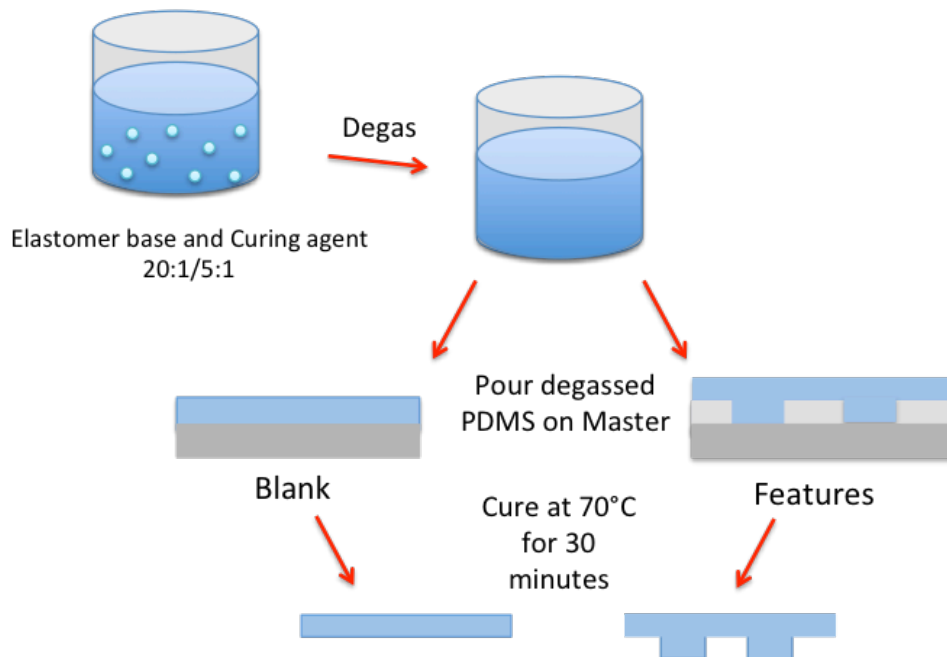
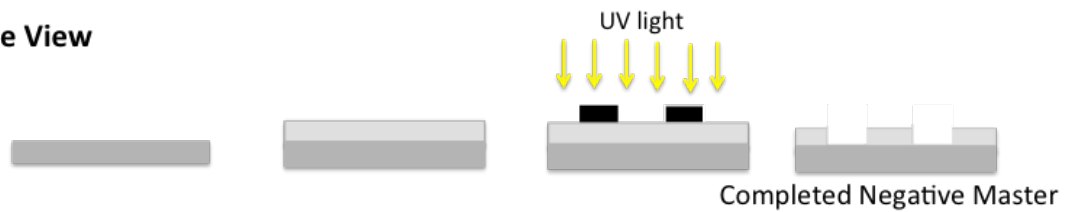


Figure 2.3 Silicon Master and Polydimethyl Siloxane based device Fabrication. Silicon master fabrication (Top) involves spin coating SU-8 photoresist, applying a transparent mask with printed features and exposing a UV light source for an allotted amount of time. Upon removing the excess photoresist cured features are revealed. The completed master is then covered with degassed (Bottom) PDMS and baked to cure, before being peeled off the master.

must be traced with a black marker to guarantee further blockage of UV light. CorelDraw was used to create the precise designs for the transparency masks. Upon laying the mask over the uncured photoresist, a mercury arc lamp (< 375 nm) was used to expose the mask/wafer to UV light. Any photoresist exposed to the UV light was cured by activation of a polymerized crosslinking process. An exposure control system, which has a detector in the light source, controls the exact UV dosing received by the wafer through an automatic shutter. Once the UV source was automatically turned off, the mask was removed from the wafer and the wafer returned to the hot plate for a post baking step for 15 min at 90 °C to complete the crosslinking process. A developing step, soaking the wafer in propylene glycol monomethyl ether acetate, follows the post baking step to remove any excess or uncured photoresist. If a laser jet printed transparency is used, additional developing steps could be required, such as using a fine brush to scrub the master with the solvent in SU-8-50 gamma-butyrolactone (GBR). Upon removing all excess photoresist, a final washing step of acetone and isopropanol was performed to complete the master fabrication.

2.5.1.2 Polydimethyl Siloxane (PDMS) Device Fabrication

Using the master fabricated in section 2.5.1.1, PDMS slabs were prepared for both sides of a microfluidic device (Figure 2.3). Both PDMS based devices, utilized for the macroscope detection platform (Figure 2.4), as well as the plate

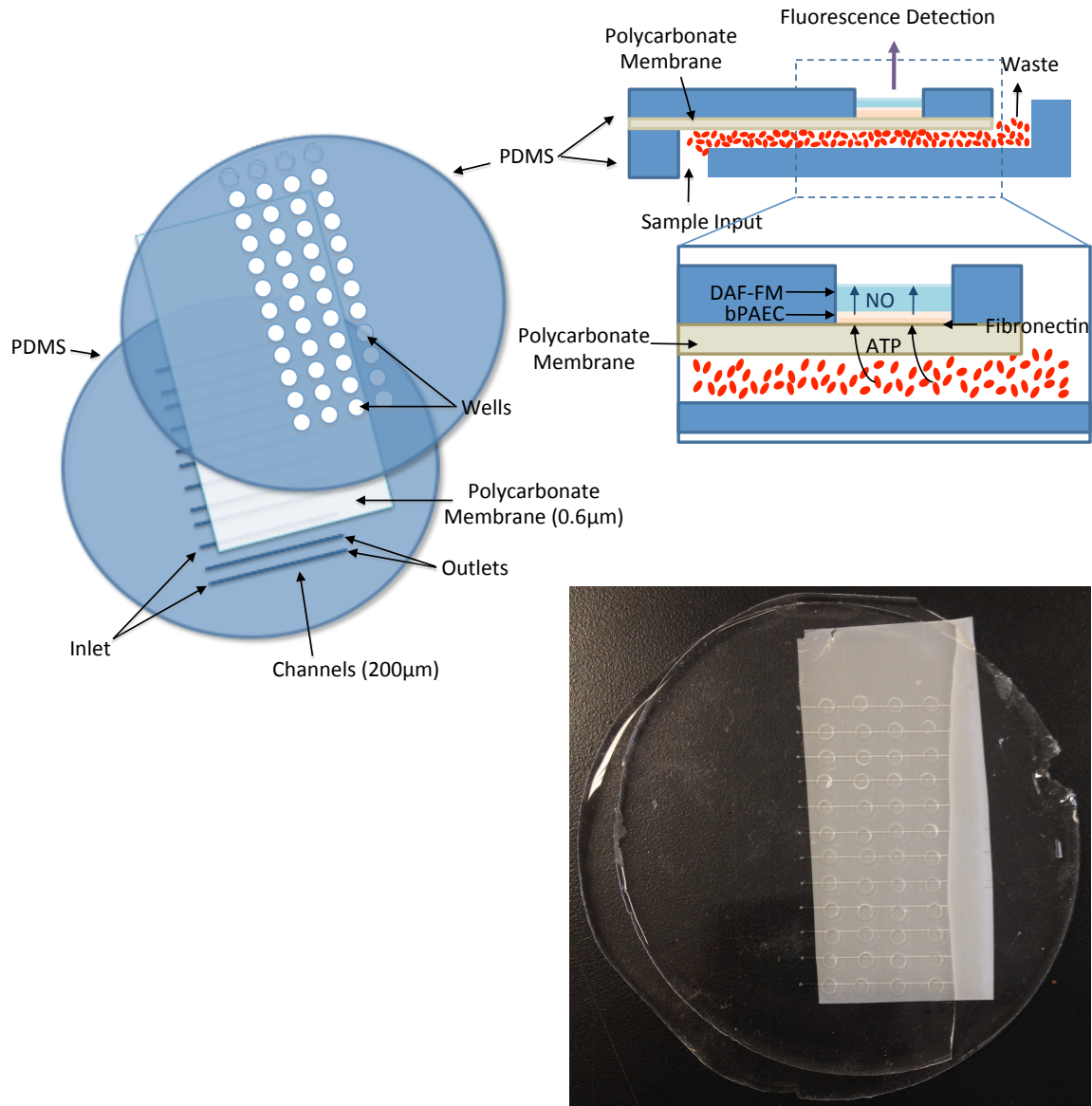


Figure 2.4 Macroscopic Fluorescence Microfluidic Device Schematic, Cross Section and Actual Image. Schematic (Top) shows the layout for the PDMS based microfluidic device as well as a cross section of the device with RBCs flowing through the channel and endothelial cells culturing in the detection well. ATP, released from the RBCs, diffuses across the porous polycarbonate layer where it stimulated NO production from the endothelial cells. Subsequent fluorescence detection was observed using a macroscope. An actual image of the PDMS based microfluidic device (Bottom, 4 inch diameter) utilized.

reader detection scheme (Figure 2.5) were fabricated in the following manner. PDMS, Dow Corning's Sylgard 184 Elastomer (Ellsworth Adhesives, Germantown, WI) can be prepared in a variety of different concentrations to elicit the desired the rigidity of cured PDMS. In this study, 10 g each of 5:1 and 20:1 PDMS (w/w) to curing agent were prepared, thoroughly mixed, and degassed. The 20:1 mixture was poured over the channels of the positive feature master, as well as the center of a blank master. The masters were heated for 11 min at 75 °C to allow for the PDMS to cure. Once removed from the heat, the 5:1 mixture was then poured over the entire wafer. A 5:1 mixture is much more rigid than the 20:1 mixture, thereby offering stability to the PDMS slabs. The curing process was then repeated at 75 °C for 11 min. Post curing, the PDMS was removed from the silicon masters and inlets were made in the PDMS slabs containing features by punching the ends of channels with 20 gauge steel tubing. Excess PDMS plugs were removed from the inlets using forceps. Wells were produced into the blank slab of PDMS using a ¼ inch hollow punch with a channel guide to allow for proper alignment. After both slabs were prepared, a piece of porous polycarbonate membrane having 0.6 μm diameter pores, was carefully flattened over the channels (20:1 face up). The well slab was then positioned above the channel/polycarbonate (20:1 face down) to allow for alignment of wells and channels. The device, as a whole, was then reversibly sealed together at 75 °C for 15 min.

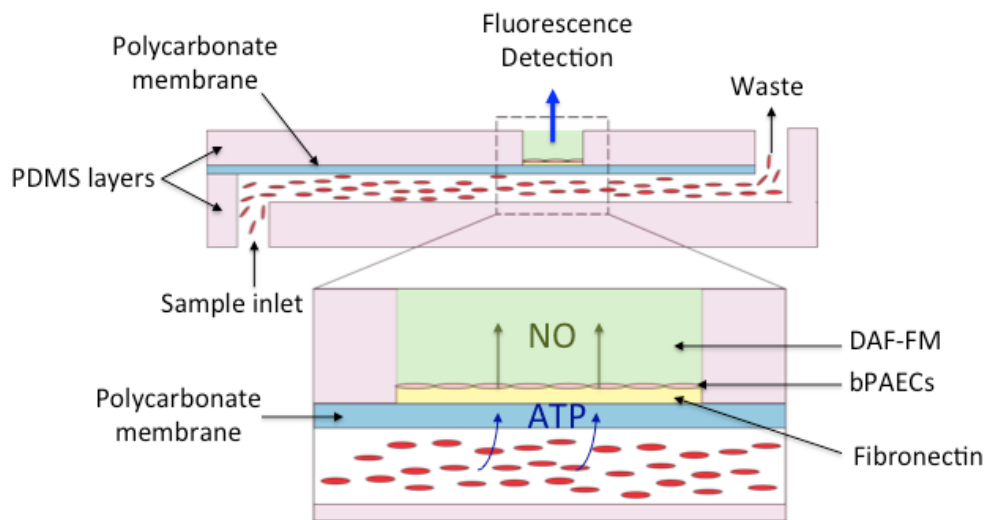
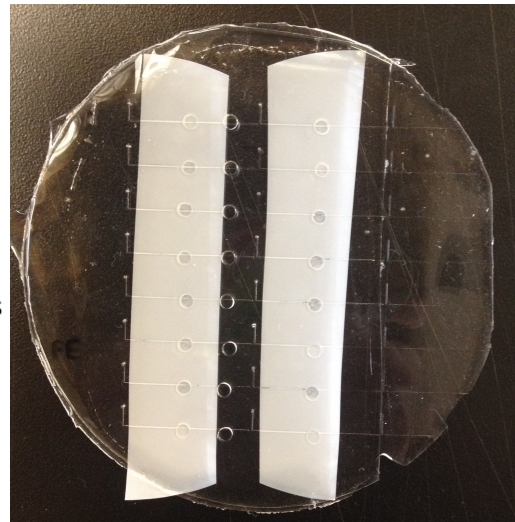
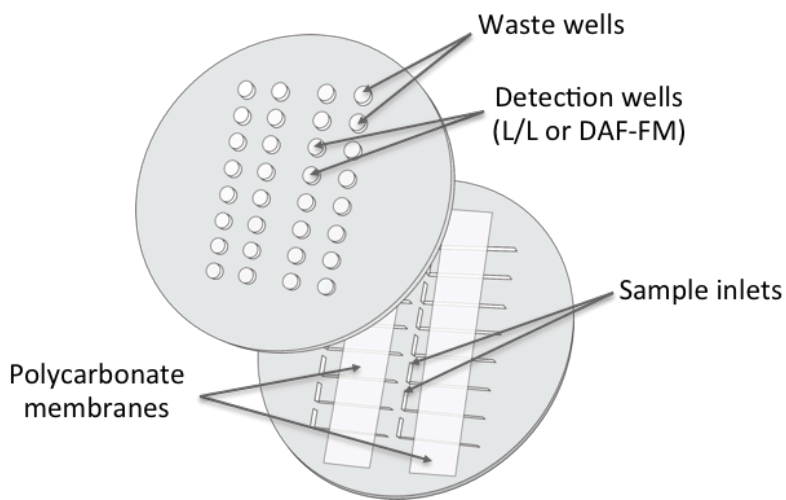


Figure 2.5 Plate Reader Fluorescence Microfluidic Device Schematic, Cross Section and Actual Image. Schematic (Top Right) shows the layout for the PDMS based microfluidic device. An actual image of the PDMS based microfluidic device (Bottom, 4 inch diameter) utilized. Cross section of the device (Bottom) showing ERYs flowing through the channel and endothelial cells culturing in the detection well. ATP, released from the ERYs, diffuses across the porous polycarbonate layer where NO production is stimulated from the endothelial cells. Subsequent fluorescence detection was observed using a plate reader and a modified 96 well plate.

2.5.1.3 Preparation of Regents

Collection and Purification of Human Red Blood Cells

Human whole blood was collected by venipuncture and RBCs were isolated by centrifuging the whole blood at 500g for 10 min at 20 °C. The plasma and buffy coat were removed by aspiration and the remaining RBCs were washed multiple times in a physiological salt solution (PSS; 1.2 mM magnesium sulfate, 2.0 mM calcium chloride, 4.7 mM potassium chloride, 5.6 mM glucose, 21.0 mM tris (hydroxymethyl) aminomethane, 140.5 mM sodium chloride in 5% bovine serum albumin, adjusted to a pH of 7.4). All samples were measured within 8 hours of harvesting from consenting donors. The hematocrit of the washed RBCs was determined to allow samples to be diluted to 7% RBCs with the PSS. For certain studies, calcium²⁺ free PSS was used during the RBC washing steps and diluted to a 7% RBC-containing solution.

Immobilizing Endothelial Cells in Wells

A 10 µL solution of fibronectin (100 µM, Sigma, St. Louis, MO) was added to the detector well and allowed to evaporate. Upon evaporation, the device was exposed to a UV light (15 min) to sterilize the well contents. A 10 µL suspension of bovine pulmonary artery endothelial cells (bPAECs) in endothelial growth media (EGM, Caisson Laboratories Inc., North Logan, UT) was added to wells and the device was incubated at 37 °C. The EGM was replaced in the detector

wells every 2 h. After 12 h, confluent cells could be observed in the wells using a Hoechst 33342 DNA and nuclei stain (excitation 346/emission 497).

2.5.2 Fluorescence Determination of Nitric Oxide Released from Endothelial Cells

2.5.2.1 Macroscopy Fluorescence Detection

The HU incubated RBCs were flowed through the device at 6 $\mu\text{L}/\text{min}$ for 30 minutes at 37 ° using fused silica capillaries to connect the syringes to the microfluidic device (Figure 2.6). First, confluency of bPAECs in the microfluidic device was validated by observing fluorescence from bPAECs, which were incubated with Hoechst 33342 stain, using a DAPI filter (ex: 340-380 nm/em: 435-485 nm) on an Olympus MVX10 macroscopy (Olympus America, Melville, NY). Fluorescence intensities in the wells were averaged using MicroSuite Biological Suite software (Olympus America, Melville, NY). Due to the variation in number of cells per well, the fluorescence measured for Hoechst 33342 stain is required to enable NO analysis to be normalized per cell (Figure 2.7).

NO was detected with the extracellular fluorescent probe diaminodifluorofluorescein (DAF-FM, excitation: 495 nm/emission: 515 nm, Invitrogen, Eugene, OR). A 10 μL aliquot of 50 μM DAF-FM was pipetted into the wells, followed by the initiation of flow through the device channels. The amount

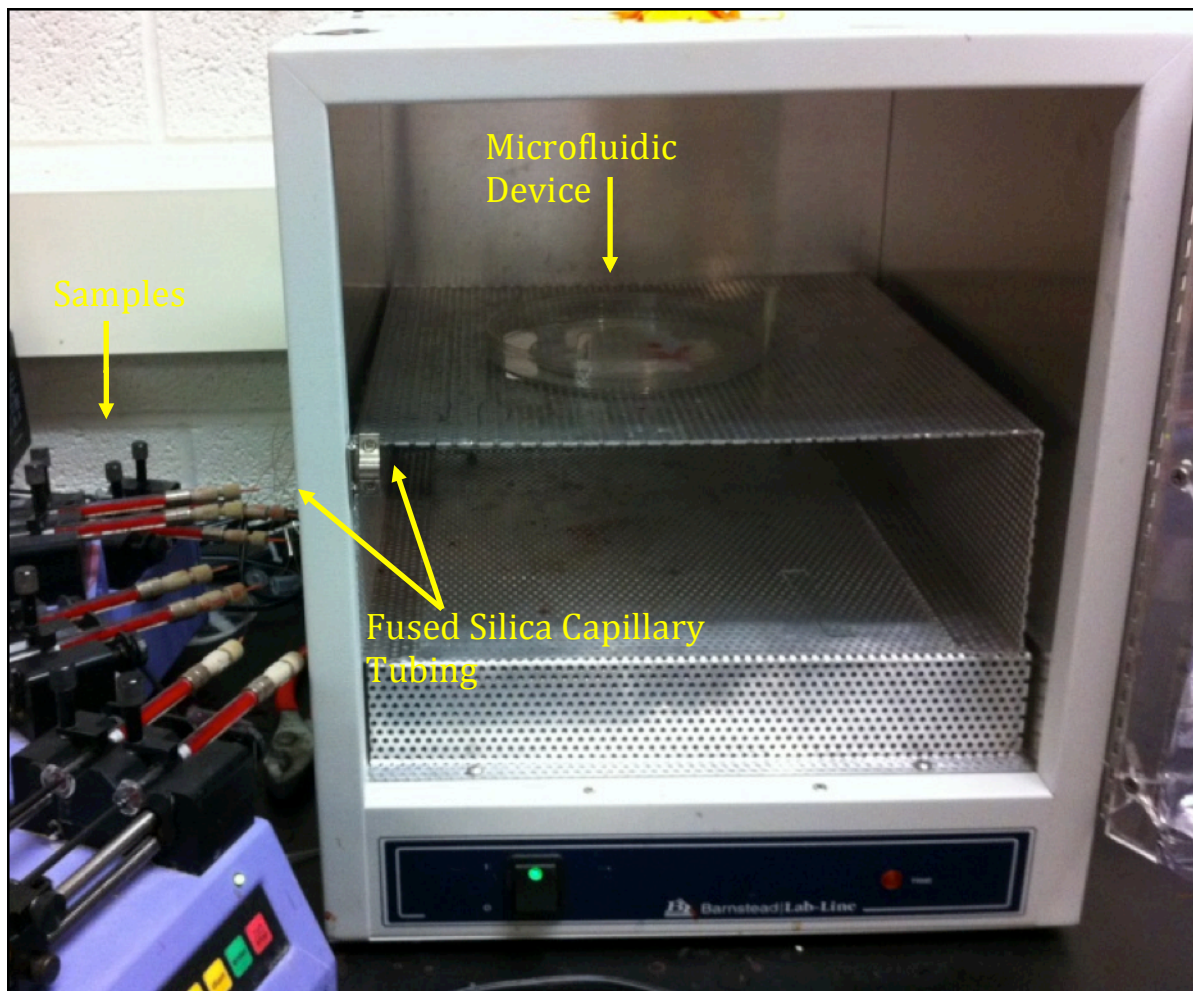


Figure 2.6 Experimental Set Up for All Microfluidic Devices. RBC samples were delivered to the devices by syringe pumps (6 $\mu\text{L}/\text{min}$) and fused silica capillary tubing (50 μm i.d.). Oven was kept at 37 $^{\circ}\text{C}$ throughout the duration of the experiment.

of NO released from the endothelial cells is proportional to the measured fluorescence signal. Fluorescence images of wells loaded with DAF-FM prior to flowing samples were obtained using a FITC filter cube (ex: 465-495 nm/em: 515-555 nm). The RBC samples were incubated for 30 minutes with various concentrations of HU and introduced to the channels of the microfluidic device at a flow rate of 6 μ L/min (Figure 2.6).

A 2 mM hydroxyurea working solution was prepared by adding 10 mL of PSS to 1.6 mg of HU. During the incubation, inhibitors such as pyridoxal phosphate 6-azo (benzene – 2',4' – disulfonic acid) (PPADS, Sigma, St. Louis, MO) and L-N^G-Nitroarginine methyl ester (L-NAME, Cayman Chemical Company, Ann Arbor, MI) could be added to the wells of the microfluidic device or to the RBCs. PPADS, a purinergic receptor inhibitor used to inhibit ATP binding to the bPAECs, was added (10 μ L) only to the wells containing the bPAECs; a 10 mM solution of PPADS was used as the working concentration. A 5 mM L-NAME stock solution was prepared by adding 5 mL of DDW to 6.7 mg of L-NAME with 10 μ L aliquots being added to the detection well.

After 30 minutes of flow through the device channels, the final fluorescence intensity was obtained, allowing calculation of change in fluorescence (Figure 2.7). Specific wells were assigned to be control wells, where no sample was

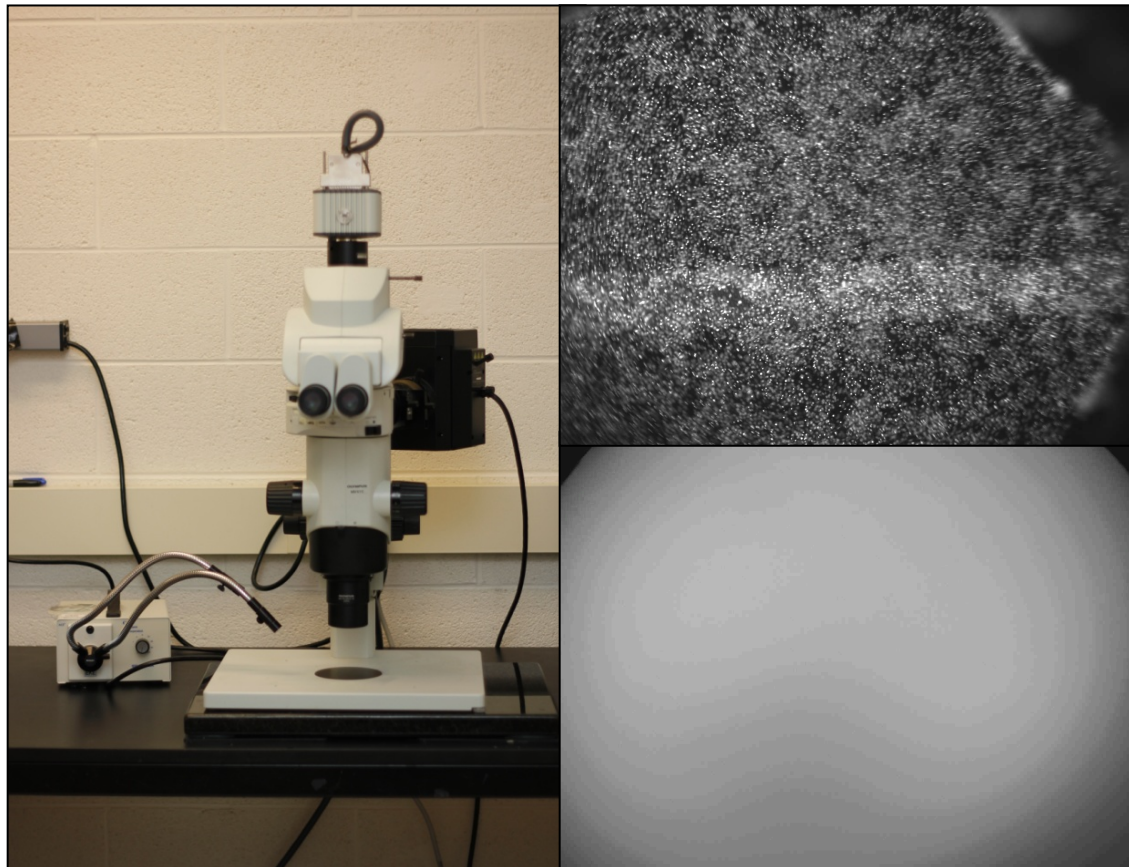


Figure 2.7 Macroscope and Florescent Images of Confluent Cells and DAF-FM. Image of macroscope (Left) used for fluorescence detection. Confluent cells (Top Right) stained with Hoechst 33342 dye. Fluorescence of DAF-FM in same detection well, post RBC flow.

introduced to the channels. The change in fluorescence from the control wells was averaged and added to the final fluorescence intensity to act as a correction factor. The change in fluorescence for each sample was normalized to the change in fluorescence for the 7% RBC control sample. There were three total fluorescence images taken per well, to account for cell count, background, and experimental fluorescence. There were 48 wells per device, thus totaling 144 images. As surmised, the detection procedure becomes timely (approximately 5 hours) and tedious, thus providing motivation for alternative methods of detection.

2.5.4.2 Plate Reader Fluorescence Detection

Procedures and reagents were prepared as described in section 2.3.4.2. The RBC samples were incubated for 30 minutes at 37 °C and subsequently, through the use of syringes and fused silica capillaries, the samples were introduced to the channels of the microfluidic device at a flow rate of 6 $\mu\text{L}/\text{min}$ (Figure 2.6). As previously described (section 2.5.4.1) inhibitors could be added to either the microfluidic device or the RBCs during the incubation period. Throughout the 30 minutes of sample flow through the capillaries and device, the microfluidic chip was maintained in a closed 37 °C environment. A 10 μL solution of 50 μM DAF-FM was pipetted onto the detection well and sample flow was started. The amount of NO released from the bPAEC cells is proportional to the fluorescence signal measured in the plate reader. A 96 well plate was modified by removing

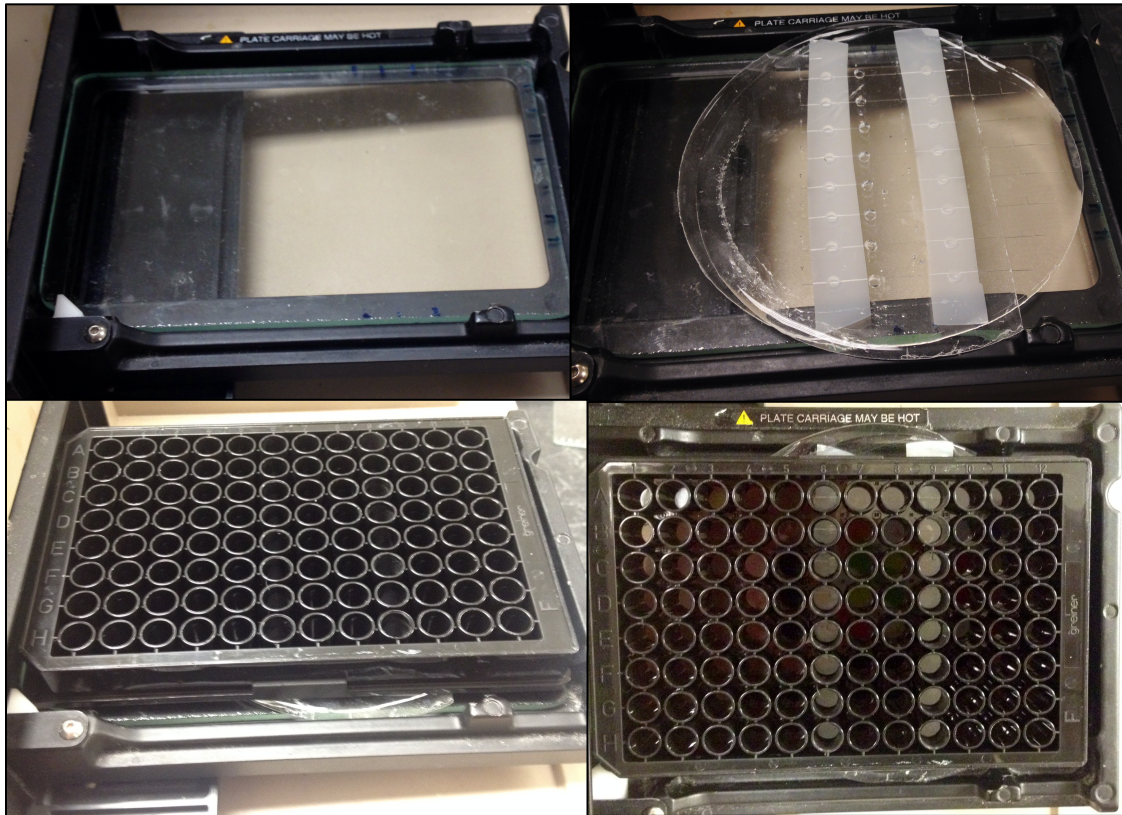


Figure 2.8 Progression of Layout for Integrating the PDMS Microfluidic Device with a High Throughput Plate Reader. Top Right: Glass Plate, notched at the top by the glass shop, filled bottom of plate reader 96 well plate holder. Top Left: Post flow, device is lined up on glass plate. Bottom Left: Modified 96 well plate is positioned above microfluidic device. The bottoms of wells in row 6 and 9 were removed to allow for fluorescence measurements. Bottom Right: Top view of the modified plate with microfluidic device positioned underneath.

the bottoms on select rows and positioned above the detector wells. The device was mounted on a glass plate whose dimensions were that of a 96 well plate. In a matter of seconds the fluorescence was determined for the all 16 detection wells (Figure 2.8). A background correction was performed to negate any native fluorescence from the DAF-FM.

2.6 Results and Discussion

2.6.1 Macroscope Fluorescence Detection of Endothelium Nitric Oxide Stimulated from Red Blood Cell-Derived Adenosine Triphosphate

Initial studies confirmed that RBCs, when exposed to flow conditions in fused silica capillary tubing, release micromolar concentrations of ATP.⁶⁸ The aforementioned release of ATP from rabbit RBCs was increased when incubated with HU prior to flowing.¹⁴ Microfluidics offer a unique opportunity to mesh spatially relevant dimensions as well as approximating the dimensions of *in vivo* vascular resistance vessels. RBCs were pumped (0.6 $\mu\text{L}/\text{min}$) through fused silica capillaries (50 μm) that were connected to PDMS channels (200 μm ; Figure 2.6). The channels are separated from detection wells, which contain adhered endothelial cells, by a polycarbonate membrane (0.6 μm pore diameter; Figure 2.4). The RBCs release ATP in response to both pharmaceutical and mechanical deformation stimuli. The ATP then diffuses across the polycarbonate membrane where it stimulates NO production in the endothelial cells. The

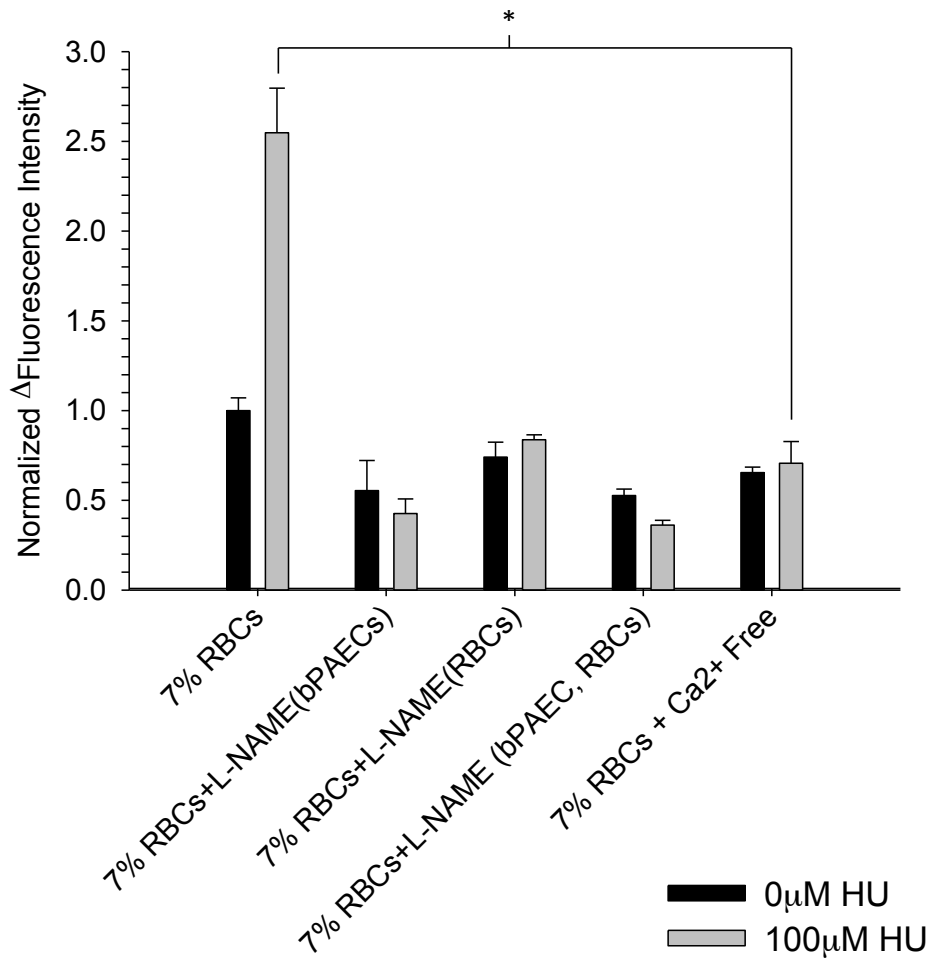


Figure 2.9 Fluorescence Detection of HU Incubated RBC derived ATP Elicited NO Production in bPAECs (Macroscopic). Here, bPAECs were cultured in the detection wells and DAF-FM probe was loaded into the wells prior to pumping. Fluorescence was detected using a fluorescence microscope. NO release from bPAECs was observed after pumping 7% solutions of RBCs incubated with various conditions (HU, L-NAME, Ca²⁺ free buffer). The NO release from bPAECs increased significantly (*) when RBCs incubated with HU were flowed, confirming that HU can increase NO release from bPAECs. When NO release is inhibited in bPAECs using L-NAME, the difference in NO release between HU incubated and the control is statistically insignificant, suggesting only NOS produced from bPAECs is responsible for observed NO. Moreover, when RBC NOS was inhibited by L-NAME, the RBC sample incubated with HU has NO production statistically similar to basal levels. This suggests that RBC derived NO can affect bPAEC NO production, potentially indirectly through the mechanism of HU induced RBC ATP release. Further confirming the role of RBC derived NO, when RBC samples are prepared in calcium free buffer any previously observed increases are negated. n ≥ 3 devices and p < 0.0001. Error = S.E.M.

detection well contains DAF-FM, an intracellular NO fluorescent probe, therefore the actual production of NO is monitored. Prior to flow being introduced to the device, the bPAEC cells were incubated with Hoechst 33342 dye and the subsequent fluorescence, based on amount of pixels, allows calculations to be normalized to a per cell basis. DAF-FM emits in the absence of NO, therefore it is critical to obtain background fluorescence for every individual well. The fluorescence is recorded again for individual wells following the delivery of RBCs through the channels (30 min) while incubating the device at 37 °C (Figure 2.9). RBC samples incubated with 100 μ M HU had NO levels that were 2.54 ± 0.25 fold higher than control RBC samples lacking HU. To verify that the NO being observed was produced from the endothelial cells, L-NAME was used to inhibit e-NOS with the resulting wells having NO concentrations well below basal levels. Moreover, when L-NAME was added to the RBCs, the NO production in bPAECs was significantly reduced, therefore suggesting that RBC derived NO plays a role in the HU mechanism. NO concentrations remained below basal levels when both the bPAECs and RBCs were incubated with L-NAME, further suggesting the importance of RBC derived NO. When a calcium free buffer was used to wash the RBCs, NO production in HU incubated RBCs mirrored that of the control samples. Calcium is needed in the e-NOS mechanism for NO production. There were 48 sample wells per device, hence when taking three fluorescence images per well, for a total of 144 images, the highly time consuming (approximately 5 hours), inefficient data collection should be emphasized.

2.6.2 Plate Reader Fluorescence Detection of Endothelium Nitric Oxide Stimulated from Red Blood Cell Derived Adenosine Triphosphate

Due to the time consuming nature of the initial microfluidic design, a simpler version was modeled after a 96 well plate to allow for amenability to automation (Figure 2.5). Two sets of eight detection wells were lined up with the 6 and 9 rows of the 96 well plate allowing for integration with a high throughput plate reader. Subsequently the bottoms of wells in rows 6 and 9 were removed to allow fluorescence analysis of the microfluidic device. Samples were treated and introduced to the device in the same manor and set up as in section 2.6.1, the only differences pertaining to the device layout and detection scheme. Background measurements were obtained to correct for any auto fluorescence. Following in the same pattern as with the microscope detection scheme, RBC samples incubated with 100 μ M HU had a significant increase in endothelial derived NO (1.34 ± 0.03 ; Figure 2.10). When the bPAEC cells were incubated with L-NAME to inhibit e-NOS both the RBC samples, with and without HU, reported levels of NO significantly lower than the control. L-NAME, when incubated with the RBCs, also reduced levels of NO to below basal. Moreover, when the purinergic receptors on the bPAECs are inhibited using PPADS, NO levels are significantly reduced, which indicates that ATP is responsible for the stimulated levels of endothelial derived NO that is observed and not NO released from RBCs.

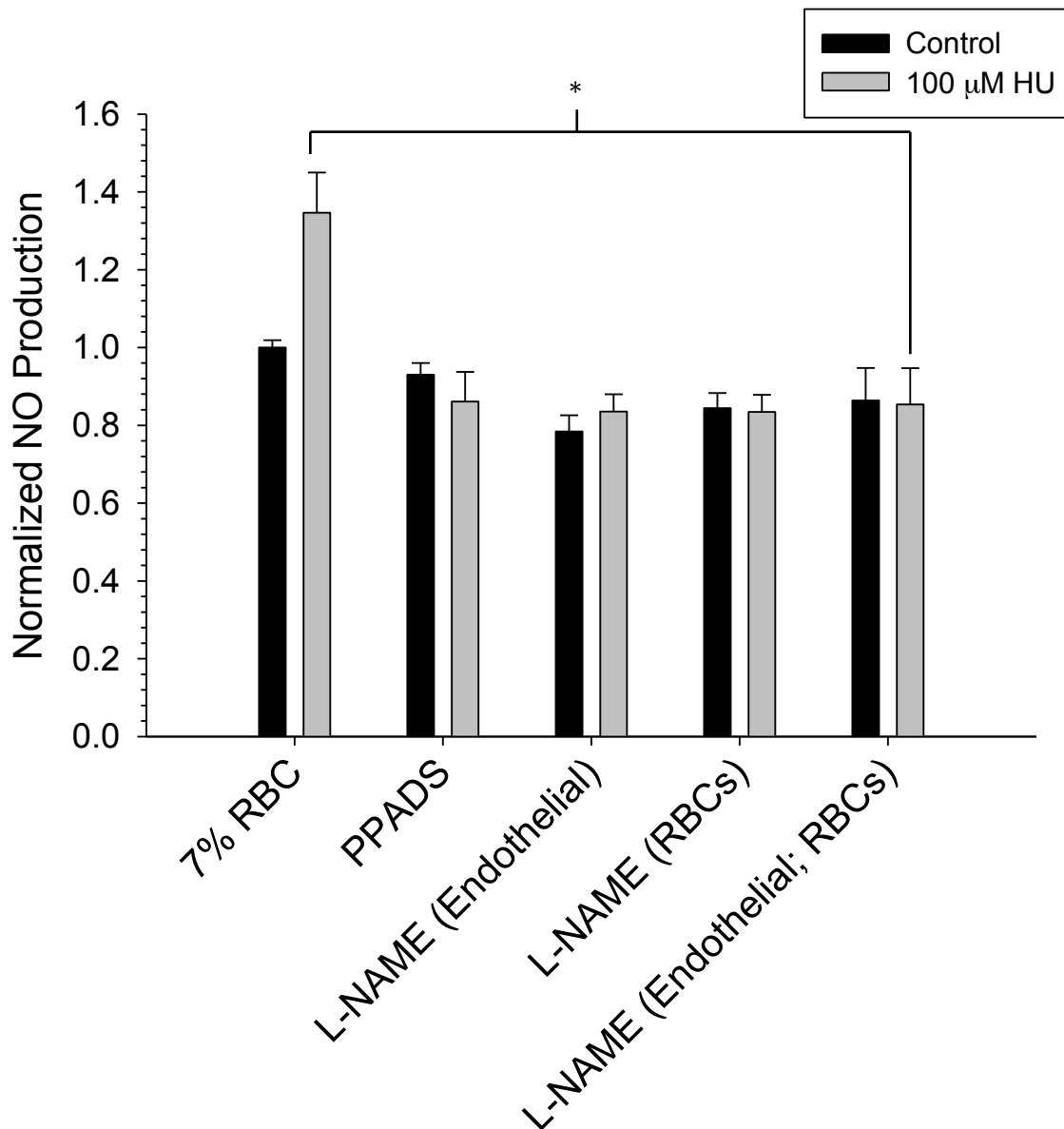


Figure 2.10 Fluorescence Detection of HU Incubated RBC derived ATP Elicited NO Production in bPAECs (Plate Reader). Although the experimental set up was identical to Figure 2.9, the detection platform for this experiment was measured using a commercial plate reader. As in Figure 4, when 7% RBCs are incubated with HU, a significant increase in NO is observed. Upon incubation of the bPAECs and RBCs with L-NAME the increases of NO production in the HU incubated samples were reduced to below basal levels. When bPAECs are incubated for 30 minutes with PPADS, a purinergic receptor antagonist, prior to flowing 7% RBCs no significant increase in NO release is observed, suggesting that RBC derived ATP is necessary to observe an increase in NO release from bPAECs. $n \geq 3$ devices and $p < 0.005$. Error = S.E.M.

The PDMS-based microfluidic device allowed the integration of two unique cell types on the same platform, thereby monitoring cell-to-cell communications. Specifically, ATP, which was released from HU incubated RBCs undergoing mechanical deformation, diffused across a polycarbonate membrane. Upon crossing the polycarbonate membrane, the ATP stimulated NO production from a monolayer of endothelial cells seeded in the detection well. Moreover, the PDMS device allows specific dosing of the RBCs (a pharmacokinetic parameter), along with the monitoring of the subsequent, elicited effect on the endothelial cells (a pharmacodynamic parameter) on a single platform. The merging pharmacokinetics and pharmacodynamics on the same microfluidic *in vitro* diffusion-based device would prove to be a beneficial tool for the pharmaceutical industry.

REFERENCES

REFERENCES

- (1) Krebs, H.: Chemical composition of blood plasma and serum. *Annual review of biochemistry* **1950**, *19*, 409-430.
- (2) Harmening, D. M.: *Clinical hematology and fundamentals of hemostasis*; FA Davis, 1997.
- (3) Dean, B. M.; Perrett, D.: Studies on adenine and adenosine metabolism by intact human erythrocytes using high performance liquid chromatography. *Biochimica et Biophysica Acta (BBA)-General Subjects* **1976**, *437*, 1-15.
- (4) Rose, I. A.; Warms, J. V.: Control of glycolysis in the human red blood cell. *Journal of Biological Chemistry* **1966**, *241*, 4848-4854.
- (5) Bergfeld, G. R.; Forrester, T.: Release of ATP from human erythrocytes in response to a brief period of hypoxia and hypercapnia. *Cardiovasc Res* **1992**, *26*, 40-7.
- (6) Faris, A.; Spence, D. M.: Measuring the simultaneous effects of hypoxia and deformation on ATP release from erythrocytes. *Analyst* **2008**, *133*, 678-82.
- (7) Ellsworth, M. L.; Forrester, T.; Ellis, C. G.; Dietrich, H. H.: The erythrocyte as a regulator of vascular tone. *Am J Physiol* **1995**, *269*, H2155-61.
- (8) Sprague, R. S.; Ellsworth, M. L.; Stephenson, A. H.; Lonigro, A. J.: ATP: the red blood cell link to NO and local control of the pulmonary circulation. *Am J Physiol* **1996**, *271*, H2717-22.
- (9) Edwards, J.; Sprung, R.; Sprague, R.; Spence, D.: Chemiluminescence detection of ATP release from red blood cells upon passage through microbore tubing. *Analyst* **2001**, *126*, 1257-60.
- (10) Adak, S.; Chowdhury, S.; Bhattacharyya, M.: Dynamic and electrokinetic behavior of erythrocyte membrane in diabetes mellitus and diabetic cardiovascular disease. *Biochimica et Biophysica Acta (BBA)-General Subjects* **2008**, *1780*, 108-115.
- (11) Price, A. K.; Fischer, D. J.; Martin, R. S.; Spence, D. M.: Deformation-induced release of ATP from erythrocytes in a

poly(dimethylsiloxane)-based microchip with channels that mimic resistance vessels. *Analytical chemistry* **2004**, *76*, 4849-55.

(12) Pries, A. R.; Secomb, T. W.: Microvascular blood viscosity in vivo and the endothelial surface layer. *American Journal of Physiology-Heart and Circulatory Physiology* **2005**, *289*, H2657-H2664.

(13) Meyer, J. A.; Froelich, J. M.; Reid, G. E.; Karunaratne, W. K.; Spence, D. M.: Metal-activated C-peptide facilitates glucose clearance and the release of a nitric oxide stimulus via the GLUT1 transporter. *Diabetologia* **2008**, *51*, 175-182.

(14) Raththagala, M.; Karunaratne, W.; Kryziniak, M.; McCracken, J.; Spence, D. M.: Hydroxyurea stimulates the release of ATP from rabbit erythrocytes through an increase in calcium and nitric oxide production. *European journal of pharmacology* **2010**, *645*, 32-38.

(15) Lockwood, S. Y.; Erkal, J. L.; Spence, D. M.: Endothelium-derived nitric oxide production is increased by ATP released from red blood cells incubated with hydroxyurea. *Nitric Oxide* **2014**, *38*, 1-7.

(16) Carroll, J.; Raththagala, M.; Subasinghe, W.; Baguzis, S.; D'Amico Oblak, T.; Root, P.; Spence, D.: An altered oxidant defense system in red blood cells affects their ability to release nitric oxide-stimulating ATP. *Mol Biosyst* **2006**, *2*, 305-11.

(17) Rubanyi, G. M.; Romero, J. C.; Vanhoutte, P. M.: Flow-induced release of endothelium-derived relaxing factor. *Am J Physiol* **1986**, *250*, H1145-9.

(18) Sprague, R. S.; Stephenson, A. H.; Dimmitt, R. A.; Weintraub, N. A.; Branch, C. A.; McMurdo, L.; Lonigro, A. J.; Weintraub, N.: Effect of L-NAME on pressure-flow relationships in isolated rabbit lungs: role of red blood cells. *American Journal of Physiology-Heart and Circulatory Physiology* **1995**, *38*, H1941.

(19) Olearczyk, J. J.; Stephenson, A. H.; Lonigro, A. J.; Sprague, R. S.: Heterotrimeric G protein Gi is involved in a signal transduction pathway for ATP release from erythrocytes. *Am J Physiol Heart Circ Physiol* **2004**, *286*, H940-5.

(20) Sprague, R. S.; Ellsworth, M. L.; Stephenson, A. H.; Lonigro, A. J.: Participation of cAMP in a signal-transduction pathway relating erythrocyte deformation to ATP release. *American Journal of Physiology-Cell Physiology* **2001**, *281*, C1158-C1164.

- (21) Sprague, R.; Stephenson, A.; Bowles, E.; Stumpf, M.; Ricketts, G.; Lonigro, A.: Expression of the heterotrimeric G protein G_i and ATP release are impaired in erythrocytes of humans with diabetes mellitus. In *Hypoxia and Exercise*; Springer, 2007; pp 207-216.
- (22) Sprague, R.; Bowles, E.; Olearczyk, J.; Stephenson, A.; Lonigro, A.: THE ROLE OF G PROTEIN B SUBUNITS IN THE RELEASE OF ATP. *Journal of physiology and pharmacology* **2002**, *53*, 667-674.
- (23) Hakim, T.; Sugimori, K.; Camporesi, E.; Anderson, G.: Half-life of nitric oxide in aqueous solutions with and without haemoglobin. *Physiological measurement* **1996**, *17*, 267.
- (24) Gow, A. J.; Luchsinger, B. P.; Pawloski, J. R.; Singel, D. J.; Stamler, J. S.: The oxyhemoglobin reaction of nitric oxide. *Proceedings of the National Academy of Sciences* **1999**, *96*, 9027-9032.
- (25) Gow, A. J.; Stamler, J. S.: Reactions between nitric oxide and haemoglobin under physiological conditions. *Nature* **1998**, *391*, 169-173.
- (26) Jia, L.; Bonaventura, C.; Bonaventura, J.; Stamler, J. S.: S-nitrosohaemoglobin: a dynamic activity of blood involved in vascular control. **1996**.
- (27) Gladwin, M. T.; Shelhamer, J. H.; Schechter, A. N.; Pease-Fye, M. E.; Waclawiw, M. A.; Panza, J. A.; Ognibene, F. P.; Cannon, R. O.: Role of circulating nitrite and S-nitrosohemoglobin in the regulation of regional blood flow in humans. *Proceedings of the National Academy of Sciences* **2000**, *97*, 11482-11487.
- (28) Kyle Mack, A.; Kato, G. J.: Sick cell disease and nitric oxide: a paradigm shift? *The international journal of biochemistry & cell biology* **2006**, *38*, 1237-1243.
- (29) Hassell, K. L.: Population estimates of sickle cell disease in the US. *American journal of preventive medicine* **2010**, *38*, S512-S521.
- (30) Ashley-Koch, A.; Yang, Q.; Olney, R. S.: Sick cell hemoglobin (Hb S) allele and sickle cell disease: a HuGE review. *American Journal of Epidemiology* **2000**, *151*, 839-845.
- (31) Kaul, D. K.; Liu, X.-D.; Fabry, M. E.; Nagel, R. L.: Impaired nitric oxide-mediated vasodilation in transgenic sickle mouse. *American Journal of Physiology-Heart and Circulatory Physiology* **2000**, *278*, H1799-H1806.

(32) Pawloski, J. R.; Hess, D. T.; Stamler, J. S.: Impaired vasodilation by red blood cells in sickle cell disease. *Proceedings of the National Academy of Sciences of the United States of America* **2005**, *102*, 2531-2536.

(33) Wang, J. C.; Kwong, S.; Ferrone, F. A.; Turner, M. S.; Briehl, R. W.: Fiber depolymerization: fracture, fragments, vanishing times, and stochastics in sickle hemoglobin. *Biophysical journal* **2009**, *96*, 655-670.

(34) Kato, G. J.; Gladwin, M. T.; Steinberg, M. H.: Deconstructing sickle cell disease: reappraisal of the role of hemolysis in the development of clinical subphenotypes. *Blood reviews* **2007**, *21*, 37-47.

(35) Huang, Z.; Louderback, J. G.; King, S. B.; Ballas, S. K.; Kim-Shapiro, D. B.: In vitro exposure to hydroxyurea reduces sickle red blood cell deformability. *Am J Hematol* **2001**, *67*, 151-6.

(36) Athanassiou, G.; Moutzouri, A.; Kourakli, A.; Zoumbos, N.: Effect of hydroxyurea on the deformability of the red blood cell membrane in patients with sickle cell anemia. *Clin Hemorheol Microcirc* **2006**, *35*, 291-5.

(37) Platt, O. S.: Hydroxyurea for the treatment of sickle cell anemia. *New England Journal of Medicine* **2008**, *358*, 1362-1369.

(38) Young, C. W.; Hodas, S.: Hydroxyurea: inhibitory effect on DNA metabolism. *Science* **1964**, *146*, 1172-1174.

(39) Krakoff, I. H.; Brown, N. C.; Reichard, P.: Inhibition of ribonucleoside diphosphate reductase by hydroxyurea. *Cancer research* **1968**, *28*, 1559-1565.

(40) Fishbein, W. N.; Carbone, P. P.: Hydroxyurea: mechanism of action. *Science* **1963**, *142*, 1069-1070.

(41) Charache, S.; Dover, G. J.; Moore, R. D.; Eckert, S.; Ballas, S. K.; Koshy, M.; Milner, P.; Orringer, E.; Phillips, G. J.; Platt, O.: Hydroxyurea: effects on hemoglobin F production in patients with sickle cell anemia [see comments]. *Blood* **1992**, *79*, 2555-2565.

(42) Ferster, A.; Tahriri, P.; Vermylen, C.; Sturbois, G.; Corazza, F.; Fondu, P.; Devalck, C.; Dresse, M. F.; Feremans, W.; Hunninck, K.: Five years of experience with hydroxyurea in children and young adults with sickle cell disease. *Blood* **2001**, *97*, 3628-3632.

(43) Hankins, J. S.; Ware, R. E.; Rogers, Z. R.; Wynn, L. W.; Lane, P. A.; Scott, J. P.; Wang, W. C.: Long-term hydroxyurea therapy for infants with sickle cell anemia: the HUSOFT extension study. *Blood* **2005**, *106*, 2269-2275.

(44) Zimmerman, S. A.; Schultz, W. H.; Davis, J. S.; Pickens, C. V.; Mortier, N. A.; Howard, T. A.; Ware, R. E.: Sustained long-term hematologic efficacy of hydroxyurea at maximum tolerated dose in children with sickle cell disease. *Blood* **2004**, *103*, 2039-2045.

(45) Kinney, T. R.; Helms, R. W.; O'Branski, E. E.; Ohene-Frempong, K.; Wang, W.; Daeschner, C.; Vichinsky, E.; Redding-Lallinger, R.; Gee, B.; Platt, O. S.: Safety of hydroxyurea in children with sickle cell anemia: results of the HUG-KIDS study, a phase I/II trial. *Blood* **1999**, *94*, 1550-1554.

(46) El-Hazmi, M.; Warsy, A.; Al-Momen, A.; Harakati, M.: Hydroxyurea for the treatment of sickle cell disease. *Acta Haematol* **1992**, *88*, 170-174.

(47) Bridges, K.; Barabino, G.; Brugnara, C.; Cho, M.; Christoph, G.; Dover, G.; Ewenstein, B.; Golan, D.; Guttmann, C.; Hofrichter, J.: A multiparameter analysis of sickle erythrocytes in patients undergoing hydroxyurea therapy. *Blood* **1996**, *88*, 4701-4710.

(48) Steinberg, M. H.: Hydroxyurea treatment for sickle cell disease. *The Scientific World Journal* **2002**, *2*, 1706-1728.

(49) Ware, R. E.: How I use hydroxyurea to treat young patients with sickle cell anemia. *Blood* **2010**, *115*, 5300-5311.

(50) Cokic, V. P.; Beleslin-Cokic, B. B.; Tomic, M.; Stojilkovic, S. S.; Noguchi, C. T.; Schechter, A. N.: Hydroxyurea induces the eNOS-cGMP pathway in endothelial cells. *Blood* **2006**, *108*, 184-91.

(51) Glover, R. E.; Ivy, E. D.; Orringer, E. P.; Maeda, H.; Mason, R. P.: Detection of nitrosyl hemoglobin in venous blood in the treatment of sickle cell anemia with hydroxyurea. *Molecular pharmacology* **1999**, *55*, 1006-1010.

(52) Nahavandi, M.; Wyche, M.; Perlin, E.; Tavakkoli, F.; Castro, O.: Nitric Oxide Metabolites in Sickle Cell Anemia Patients after Oral Administration of Hydroxyurea; Hemoglobinopathy. *Hematology (Amsterdam, Netherlands)* **1999**, *5*, 335-339.

(53) Jiang, J.; Jordan, S. J.; Barr, D. P.; Gunther, M. R.; Maeda, H.; Mason, R. P.: In vivo production of nitric oxide in rats after administration of hydroxyurea. *Molecular pharmacology* **1997**, *52*, 1081-1086.

(54) Huang, J.; Yakubu, M.; Kim-Shapiro, D. B.; King, S. B.: Rat liver-mediated metabolism of hydroxyurea to nitric oxide. *Free Radical Biology and Medicine* **2006**, *40*, 1675-1681.

(55) King, S.: The nitric oxide producing reactions of hydroxyurea. *Current medicinal chemistry* **2003**, *10*, 437-452.

(56) King, S. B.: Nitric oxide production from hydroxyurea. *Free Radical Biology and Medicine* **2004**, *37*, 737-744.

(57) Ignarro, L. J.; Buga, G. M.; Wood, K. S.; Byrns, R. E.; Chaudhuri, G.: Endothelium-derived relaxing factor produced and released from artery and vein is nitric oxide. *Proceedings of the National Academy of Sciences* **1987**, *84*, 9265-9269.

(58) Kotsis, D. H.; Spence, D. M.: Detection of ATP-induced nitric oxide in a biomimetic circulatory vessel containing an immobilized endothelium. *Analytical Chemistry* **2003**, *75*, 145-151.

(59) Spence, D. M.; Torrence, N. J.; Kovarik, M. L.; Martin, R. S.: Amperometric determination of nitric oxide derived from pulmonary artery endothelial cells immobilized in a microchip channel. *Analyst* **2004**, *129*, 995-1000.

(60) D'Amico Oblak, T.; Root, P.; Spence, D. M.: Fluorescence monitoring of ATP-stimulated, endothelium-derived nitric oxide production in channels of a poly (dimethylsiloxane)-based microfluidic device. *Analytical Chemistry* **2006**, *78*, 3193-3197.

(61) Halpin, S. T.; Spence, D. M.: Direct Plate-Reader Measurement of Nitric Oxide Released from Hypoxic Erythrocytes Flowing through a Microfluidic Device. *Anal. Chem. (Washington, DC, U. S.)* **2010**, *82*, 7492-7497.

(62) Hediger, S.; Sayah, A.; Horisberger, J.; Gijs, M.: Modular microsystem for epithelial cell culture and electrical characterisation. *Biosensors and Bioelectronics* **2001**, *16*, 689-694.

(63) Tolan, N. V.; Genes, L. I.; Subasinghe, W.; Raththagala, M.; Spence, D. M.: Personalized metabolic assessment of erythrocytes using microfluidic delivery to an array of luminescent wells. *Analytical Chemistry* **2009**, *81*, 3102-3108.

(64) Genes, L. I.; N, V. T.; Hulvey, M. K.; Martin, R. S.; Spence, D. M.: Addressing a vascular endothelium array with blood components using underlying microfluidic channels. *Lab on a chip* **2007**, *7*, 1256-9.

(65) Ku, C.-J.; D'Amico Oblak, T.; Spence, D. M.: Interactions between multiple cell types in parallel microfluidic channels: monitoring platelet adhesion to an endothelium in the presence of an anti-adhesion drug. *Analytical Chemistry* **2008**, *80*, 7543-7548.

(66) Letourneau, S.; Hernandez, L.; Faris, A. N.; Spence, D. M.: Evaluating the effects of estradiol on endothelial nitric oxide stimulated by erythrocyte-derived ATP using a microfluidic approach. *Analytical and Bioanalytical Chemistry* **2010**, *397*, 3369-3375.

(67) Vogel, P. A.; Halpin, S. T.; Martin, R. S.; Spence, D. M.: Microfluidic transendothelial electrical resistance measurement device that enables blood flow and postgrowth experiments. *Analytical Chemistry* **2011**, *83*, 4296-4301.

(68) Sprague, R. S.; Ellsworth, M. L.; Stephenson, A. H.; Kleinhenz, M. E.; Lonigro, A. J.: Deformation-induced ATP release from red blood cells requires CFTR activity. *Am J Physiol* **1998**, *275*, H1726-32.

CHAPTER 3

POLYDIMETHYL SILOXANE BASED MICROFLUIDIC DEVICES FOR THE ANALYSIS OF DRUG DIFFUSION ACROSS A POROUS POLYCARBONATE MEMBRANE

3.1 *In Vitro* Pharmacokinetics

As the cost of bringing a drug to market in the pharmaceutical industry continues to rise, there is an increasing need to revise current drug discovery methods, along with existing procedures to emphasize efficiency in both time and materials.^{1,2} pharmacokinetic PK profiles (Figure 3.1), a gold standard in the pharmaceutical industry, yield information about the absorbance rate, maximum concentrations (C_{max}), elimination rate constant (K_{EL}), half lives ($t_{1/2}$), area under the curve (AUC), bioavailability, and volume of distribution.³ *In vitro* (PK) models, when working in tandem with animal models, are an appealing area to dramatically influence the reduction in materials and the subsequent cost. Initial PK profiles, obtained through animal models, can be further characterized using high throughput *in vitro* PK models, replacing the need for additional animal model studies.^{4,5}

Several, established *in vitro* models are currently employed in industry. For example, pharmacodynamic (PD) profiles are typically monitored using static

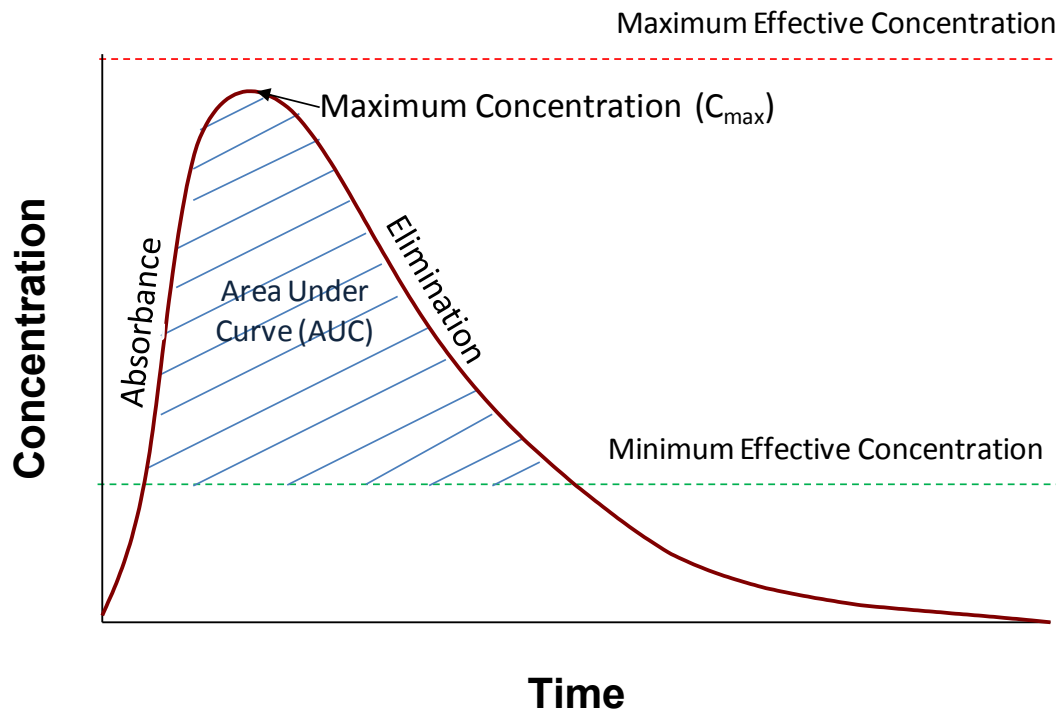


Figure 3.1 Conventional Pharmacokinetic Profile and Corresponding Parameters. Schematic of a typical oral administered pharmacokinetic curve and the various parameters, e.g., absorbance rate, C_{\max} , elimination rate constant, half-life, AUC, that can be obtained from the aforementioned curve.

in vitro PK models. Static models are the most basic of the *in vitro* models. The sample is housed in a stagnant environment, where a fixed concentration of drug is directly added.^{6,7} While the stationary environment and fixed drug concentration are ideal for PD studies, PK studies require the drug concentration to be manipulated, thereby representing the various stages of drug concentration in the body, specifically, absorbance, distribution, metabolism, and elimination. The manipulation of drug is achieved through the introduction of flow to the *in vitro* design. Dynamic *in vitro* models allow the concentration of the drug sample to be altered based on flow of new media, potentially drug infused, into a sample cell.^{7,8} A caveat of the dynamic *in vitro* model setup lies with the compromised integrity of the actual sample due to dilution or waste flow. This limitation is eliminated in diffusion-based dynamic *in vitro* models, which employ a membrane filter to separate direct flow of drug and nutrients from the actual sample.^{7,9} Diffusion delivers the nutrients, drugs and oxygen across the porous membrane to the samples. Waste, created by the samples, simultaneously diffuses back across the aforementioned membrane into the direct flow where it exits to the waste, thereby allowing for conservation of the sample.

3.1.1 Hollow Fiber Chamber Reactor

The hollow fiber chamber reactor (HFCR) is an industry-established, diffusion-based dynamic *in vitro* model (Figure 3.2) that produces PK profiles and

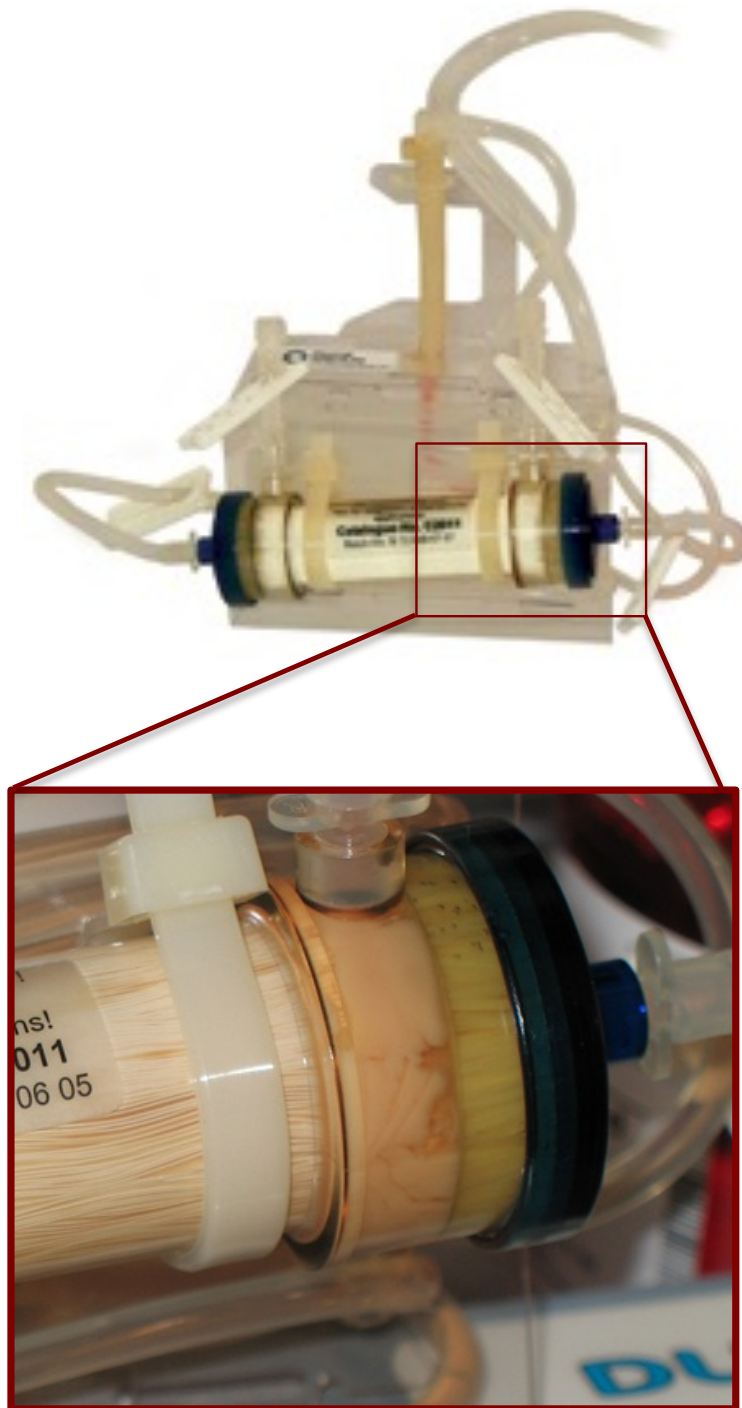


Figure 3.2 Hollow Fiber Chamber Reactor. HFCR set up with a zoomed in image of the closed cartridge containing porous capillaries and cells. Image reproduced with permission from Fiber Cell Systems.

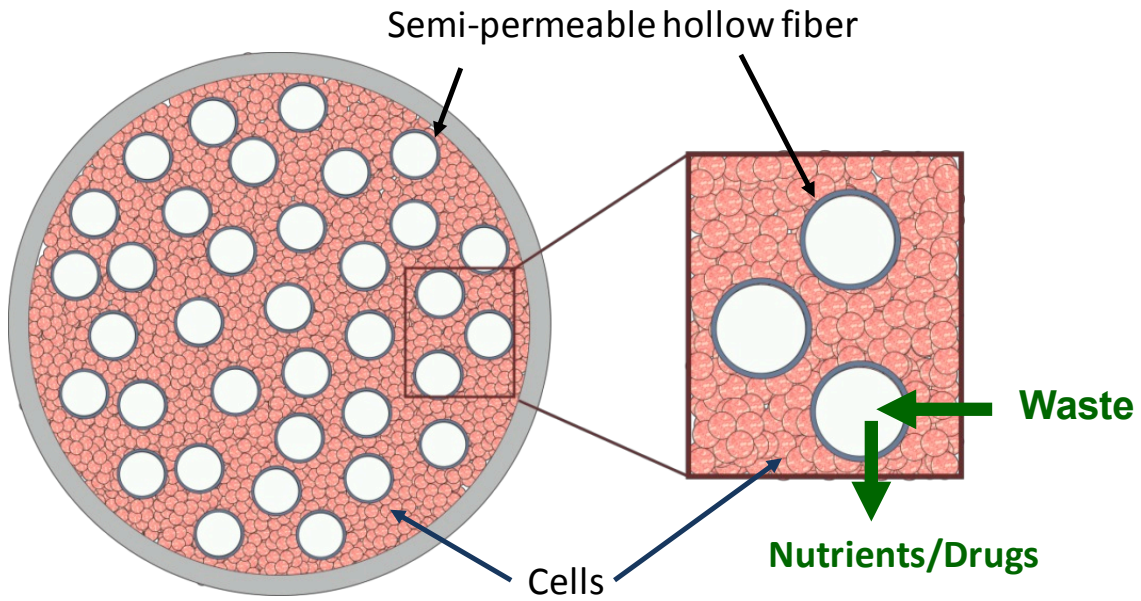


Figure 3.3 Hollow Fiber Chamber Reactor Cross Section Schematic and Image. Schematic of HFCR cross section (Top) showing diffusion action of nutrients and drug from the capillaries to the extra capillary space, with the simultaneous removal of waste. An image of a open HFCR cartridge showing porous capillaries (Bottom). Image reproduced with permission from Fiber Cell Systems.

mimics those obtained *in vivo*.¹⁰⁻¹² A HFCR consists of a hollow chamber containing thousands of porous capillaries along with cells seeded in the extra capillary space (Figure 3.3). Porous capillaries have nutrients and drug-infused media constantly flowing and diffusing into the extra capillary space, while toxic metabolites simultaneously diffuses back into the capillaries and out to waste (Figure 3.3). A major limitation of HFCR lies with the large quantities of drug-infused media consumed while obtaining a PK profile. The large volume used during the constant perfusion through the cartridge can be quite costly and taxing for synthetic chemists due to the quantity of drug required. Moreover, due to the HFCR setup, the cells seeded in the extra capillary space are unable to be sampled during analysis for post-exposure testing. Further drawbacks of HFCRs include the labor intensive and overall low throughput, as well as a lack of automation. While diffusion-based dynamic *in vitro* PK models are appealing options for enhancing research efficiency in drug discovery, the limitations associated with HFCRs provide motivation for alternative diffusion-based dynamic *in vitro* models, specifically those on a milli- or micro scale to reduce consumed volumes.⁷

Microfluidics are a viable option to miniaturize the diffusion-based concept of the HFCR, thereby alleviating some of the aforementioned limitations associated with HFCRs, such as volume consumption and accessibility to cells during experimentation. A polydimethyl siloxane (PDMS) platform was utilized to design a diffusion-based dynamic *in vitro* PK/PD device. Note the purely PK

capabilities of the HFCR design are improved upon in the PDMS platform by integrating a PD model in the layout, a direct result of allowing the harvest of cells at any point during analysis. However, the lack of reusability, as well as fragility of the porous membrane results in challenges regarding reproducibility and lengthy analysis times.

3.2 Experimental

3.2.1 Preparation of Reagents

Fluorescein Stock and Working Solutions

A stock solution of 100 ppm fluorescein was prepared by diluting the appropriate amount of weighed fluorescein and diluting with deionized (DI) water. Appropriate working concentrations were prepared from the initial stock solution with further dilutions in DI water.

Levofloxacin, Linezolid, Raltegravir, Ciprofloxacin Stock and Working Solutions

Levofloxacin was prepared by dissolving in 50% DI water and methanol solution for a final stock solution (10 mL) of 1 mg/mL. Raltegravir stock solution of (1 mg/mL) was prepared by dissolving 1 mg in 1 mL of dimethyl sulfoxide (DMSO). Linezolid stock (mg/mL) was prepared by dissolving linezolid in DI water (10 mL). Ciprofloxacin stock solution was prepared (1 mg/mL) by dissolving in DI water (10 mL). A ciprofloxacin working solution, prepared daily,

was made by mixing acetonitrile (5 mL) with the ciprofloxacin stock solution (550 μL) to prepare the internal standard. Working solutions were prepared daily by combining the appropriate quantity of stock solutions and diluting with PSS lacking BSA. Samples were taken from the detection well (5 μL) and diluted with 100 μL of BSA free PSS. The diluted samples (5 μL) were then diluted with 200 μL of the working internal standard solution.

3.2.2 Preparation of Microfluidic Device

Master and general PDMS device fabrication were previously described, in depth, in section 2.5.1.1; briefly, masters were fabricated on 6 inch silicon wafers, which differs by 2 inches from the 4 inch wafers previously used for the device design in Chapter 2. Quantity of PDMS base and curing agent prepared was 20 g for both 5:1 and 20:1 mixtures, which covered 2, 6-inch silicon wafers, a blank and one with positive features. Upon curing the PDMS slabs and removing them from their silicon masters, a piece of porous polycarbonate membrane (0.2 μm pore diameter) was positioned between the two layers, and the entire device was reversibly cured (30 min at 75 $^{\circ}\text{C}$) (Figure 3.4).

3.2.3 HUH-7 Cell Storage, Preparation, and Immobilization

HUH-7 cells are an immortal cell line from hepatocyte derived carcinoma, that typically grows in monolayers, akin to endothelial cells.¹⁴ HUH-7 cells were first harvested in 1982 from a liver tumor of a Japanese male.

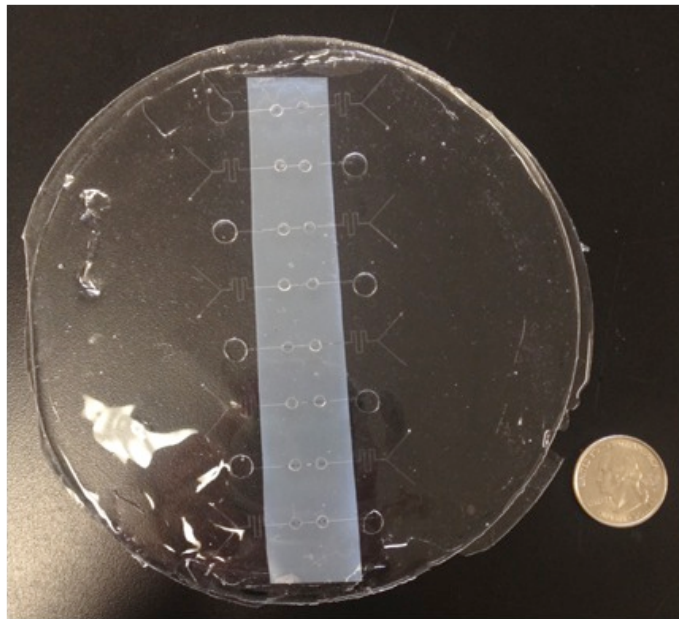
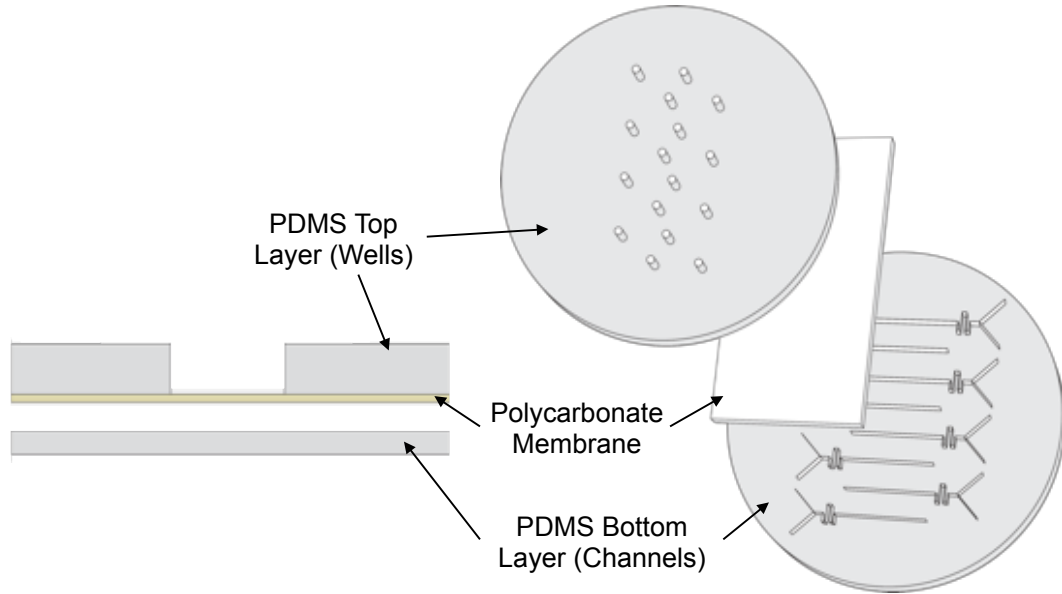


Figure 3.4 Schematic and Image of a Polydimethyl Siloxane Diffusion-based Dynamic *In Vitro* Microfluidic Pharmacokinetic Model. Schematic of the microfluidic PDMS device used for *in vitro* PK studies, which consists of two PDMS slabs separated by a porous polycarbonate membrane (Top). An image of an actual PDMS device (Bottom).

Thawing from Cryostorage

Upon removing from cryostorage, samples were immediately placed in a water bath (37 °C). Media containing high glucose Dulbecco's Modified Eagle Medium (1000 mL, with sodium bicarbonate and glutamine), fetal bovine serum (100 mL), penicillin/streptomycin (10 mL, 10 kU/mL), MEM nonessential amino acids (10 mL) and HEPES (10 mL, 1 M). Growth media was stored at 20 °C until use. Once the frozen cell pellet was completely thawed, the total volume was added to 10 mL of warmed (37 °C) cell media. Cells were then centrifuged (1000 *g* for 5 min) before the supernatant was removed, leaving behind the cell pellet. The pellet was resuspended with cell media (5 mL) and added to a T-75 flask containing 25 mL of media and incubated at 37 °C and 5% CO₂.

Cell Splitting and Maintenance

HUH-7 cells should be split approximately 2 times a week or until 90% confluency. To subculture the confluent cells, the excess growth media must first be aspirated from the T-75 flask before washing the cells several times with 5 mL of Dulbecco's Phosphate-Buffered Saline (DPBS). After washing, approximately 3 mL of 0.05% trypsin/EDTA (37 °C) were added to the flask and incubated at

Drug	Linezolid	Levofloxacin	Raltegravir	Ciprofloxacin
Molecular Weight (g/mol)	337.346	361.368	444.42	331.346
Parent Ion (m/z)	338.13	362.11	445.14	332.11
Daughter Ion (m/z)	296.11	234.05	72.73	231.06
Retention Time (min)	1.71	1.48	1.27	1.51
Cone Voltage (V)	28	28	50	34
Collisional Energy (eV)	50	50	34	22
Collision Gas (Torr)	1.96 x 10 ⁻³			

Table 3.1 LC/MS/MS Parameters for Levofloxacin, Linezolid, Raltegravir, and Clopidogrel. Table depicting LC/MS/MS parameters, e.g., molecular weight, parent ion, retention time, cone voltage, collisional energy and collisional gas.

37 °C for 5 min. Excess trypsin was aspirated and approximately 10 mL of fresh media were added to the cells for resuspension. Aliquots of 2-5 mL of cell suspension were added (dependent upon desired growth time) to new T-75 flasks containing fresh 25 mL of media before being returned to the incubator (37 °C, 5% CO₂).

Immobilization of HUH-7 in PDMS Microfluidic Device

The HUH-7 cells were added to the microfluidic device in a manner similar to that described in section 2.5.1.3 for the bPAECs. Briefly, excess media was drained from a confluent T-75 flask of HUH-7 cells. The cells were then washed several times with 5 mL of DPBS. Upon removing the DPBS, 3 mL of 0.05% trypsin/EDTA were added to the flask and incubated at 37 °C for 5 min. Excess trypsin was removed by aspiration and 10 mL of fresh media were added to the flask and the cells resuspended. The suspended cells were centrifuged (1000 *g* for 5 min) before excess supernatant was removed. Media (600 µL) was used to resuspend the resulting cell pellet. Each detection well of the microfluidic device had 10 µL of fibronectin, allowed to dry, and then sterilized by placement under a UV light for approximately 15 min. The concentrated suspension of cells was aliquoted (15 µL) into each detection well and allowed to incubate for two hours. After two hours, once the cells settled, the supernatant was removed and replaced with fresh media. The media replacement was repeated for four hours, until the device could be incubated over 12 hours while cells became confluent.

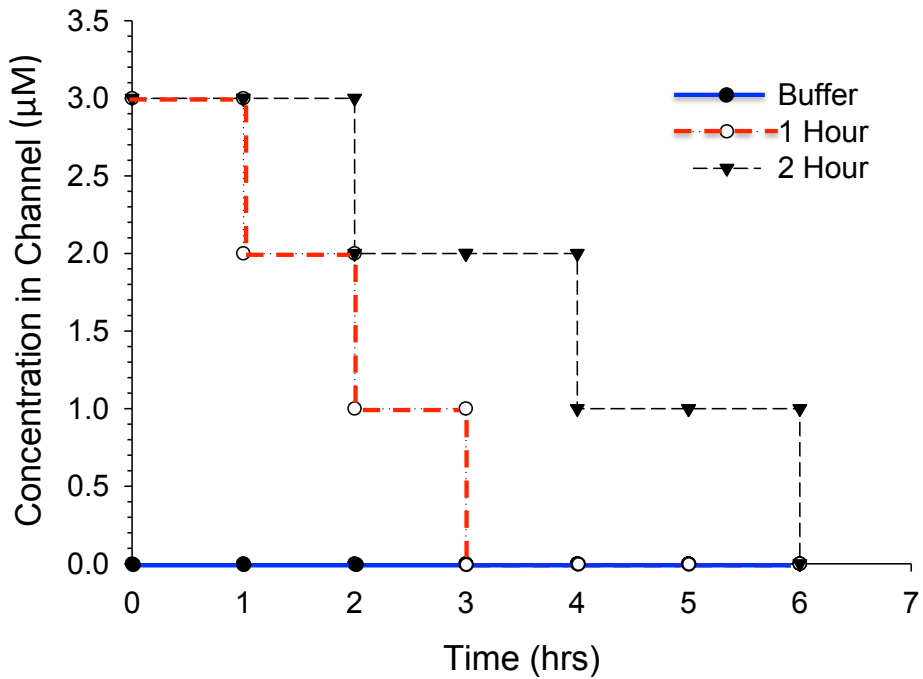


Figure 3.5 Graphical Representations of the Concentrations in the Channel during the Various Gradients. While flowing just buffer (Blue Line) there is no drug being flowed through the channel. However, during the 1 hour gradient, 75% of the concentrated drug added to the detection well is flowed for 1 hour before being reduced to 50% of the concentrated drug, which is flowed for the subsequent hour. The concentration in the channel is further reduced to 25% drug, which is flowed for an hour before being flowing buffer the remainder of the time. A similar, stepwise reduction in concentration concept is followed for the 2 hour gradient, where 75% of the concentration in the detection well is flowed through the channel for 2 hours before switching to 50% drug. The concentration is further reduced every 2 hours before just buffer is flowing through the channel.

3.2.4 Pumping and Gradient System

Syringe pumps, used in tandem with Hamilton Gastight syringes (500 μL), were linked to the microfluidic device using Tygon tubing fitted with 20-gauge stainless steel tubing (New England Small Tube Company). Gradients were implemented by varying syringe pump flow rates, thereby delivering different concentrations. For example, if a 75% drug concentration was desired, a Y-channel would combine a syringe pump (delivering a concentrated drug solution) was pumped at 0.6 $\mu\text{L}/\text{min}$, while a secondary syringe pump containing buffer being pumped at 0.2 $\mu\text{L}/\text{min}$. The resulting in an overall concentration entering the device channel would be of 75% drug the original drug concentration. Similar methods were followed to create gradients of 0, 25, 50, and 100% drug. Figure 3.5 is a graphical representation of the gradients, specifically the concentrations in the channel during the buffer, 1 hour gradient, and 2 hour gradient.

3.2.5 Multiple Reaction Monitoring Ultra Performance Liquid Chromatography Mass Spectrometry (MRM-LC/MS/MS) for Analysis of Drug Transport

A 5 μL sample taken from the detection well was diluted with 100 μL of BSA-free PSS before being further diluted with an internal standard working solution (5 μL diluted into 200 μL). The diluted solutions were then added to a polycarbonate PCR plate and sealed with a RapidEPS seal (Bio Chromato, Fujisawa, Japan). Next, 10 μL aliquots of sample were injected by auto sampler

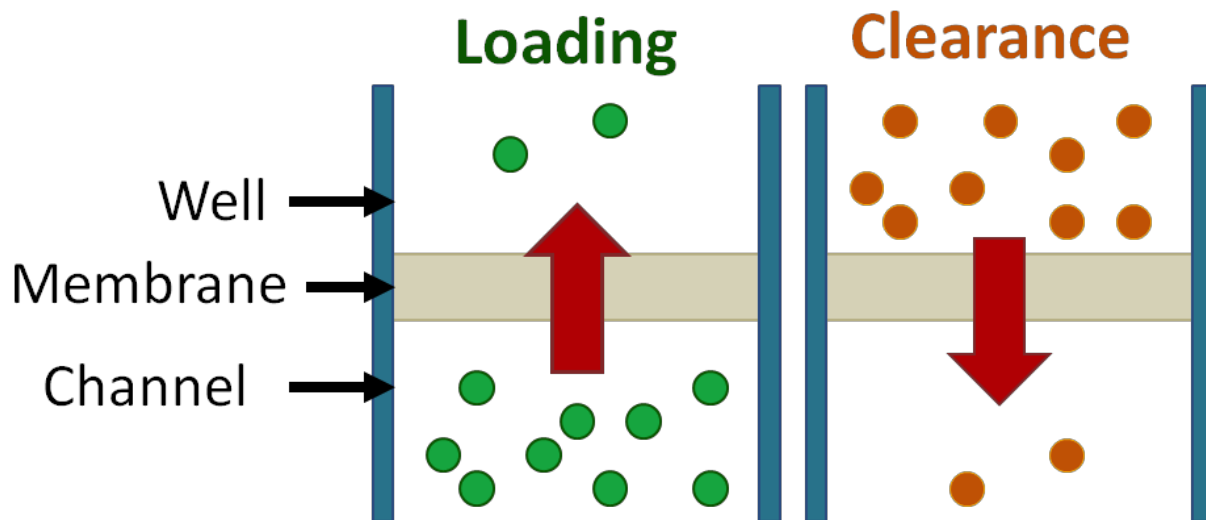


Figure 3.6 Schematic of a Cross Section at the Detection Well, Polycarbonate Membrane and Channel Interface. Loading, or absorbance, of drug is achieved by flowing concentrated drug through channel while adding buffer to the detection well. Drug diffuses from the channel to the membrane (Left). Clearance or elimination, of a drug is attained by reversing the concentration gradient. Buffer is flowed through the channel, thereby allowing the diffusion of drug from the well to the channel (Right).

and separated using Ultra Performance Liquid Chromatography (LC). The solvents methanol (A), acetonitrile (B), and 1% formic acid in water (C), were administered in the corresponding gradient, 95% A, 0% B at 0.25 min; 2%A, 0%B at 1.00 min; 2% A, 0% B at 1.25 min; 30% A, 15% B at 1.75 min; 30% A, 15% B at 1.90 min; 95% A, 0%B at 2.00 min.

Upon separation, the samples were introduced to the mass spectrometer by electrospray ionization (ESI). Through a process called multiple reaction monitoring (MRM), a parent ion was selected from the ions produced through ESI and further fragmented to produce daughter ions, which were subsequently detected. MRM allows the analysis of multiple analytes simultaneously. In the following profiles, levofloxacin, linezolid, raltegravir, and ciprofloxacin were all monitored simultaneously. Specific parameters for each analyte can be found in Table 3.1. Calibration curves were obtained by diluting the prepared standards (0-2000 nM) in the same manner as samples. Samples exceeding the maximum concentration can be further diluted such that all signals fall within the linear range of the calibration curve.

3.3 Results and Discussion

The microfluidic-based dynamic *in vitro* PK platform was used to mimic the absorption and elimination of a drug into the body. Figure 3.6 shows a cross section of the microfluidic device where loading is achieved by pumping

concentrated drug in the channel buffer is added to the detection well. The concentration gradient results in drug diffusion from the channel, across the porous membrane, to the detection well. The elimination portion of the PK curve was obtained by reversing the previously described concentration gradient. Upon loading the detection well with concentrated analyte, buffer was flowed through the channel resulting in diffusion from the well into the channel.

3.3.1 Validate Drug Loading Profiles

In the microfluidic device, the loading effect was mimicked by flowing concentrated drug through the channels, while adding 12 μL of buffer to the detection well, thereby creating a concentration gradient. Driven by the concentration gradient, drug diffuses from the channel, across the polycarbonate membrane, to the detection well. The concentration in the insert was monitored after 1 hour of pumping various concentrations (1, 2, 3, and 4 μM) through the channels. Aliquots (6 μL) were taken from detection wells and diluted with 100 μL of buffer followed by removal of a 5 μL sample that was diluted with the internal standard, ciprofloxacin. MRM-LC/MS/MS allowed the simultaneous detection of the three drugs and the internal standard. As the concentration of the drug flowing through the channels was increased, the concentration of the drug in the detection well also increased, thereby successfully mimicking the front half of a PK curve (Figure 3.6).

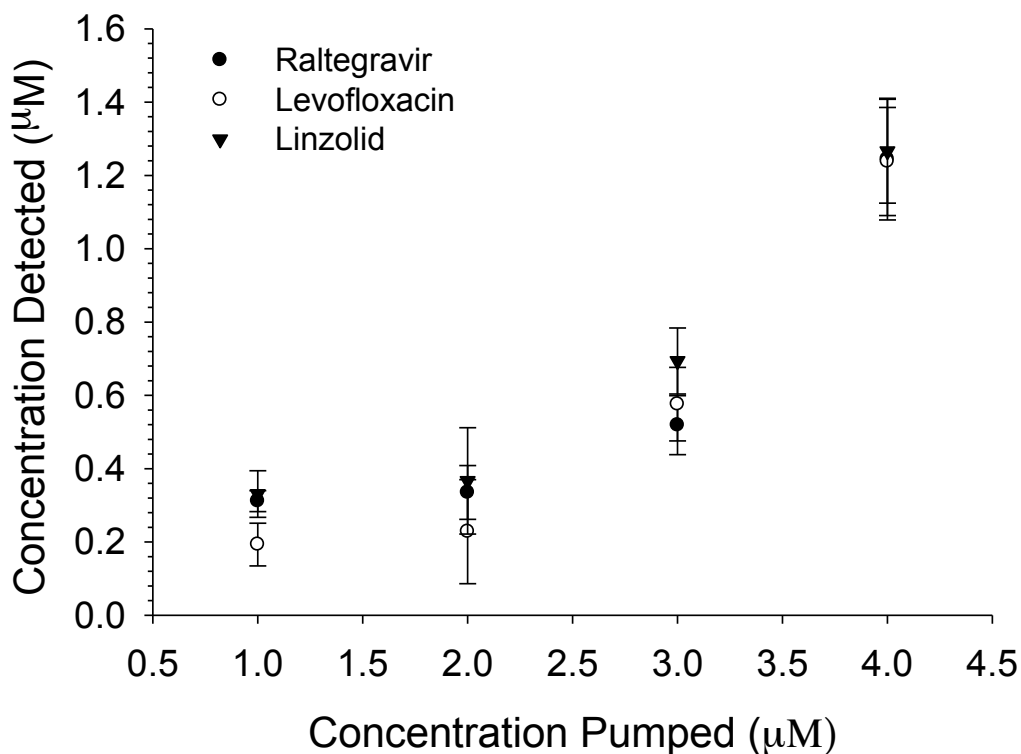


Figure 3.7 Validation of the Loading of the Detection Well with Various Concentrations of Linezolid, Levofloxacin, and Raltegravir. Various concentrations (1, 2, 3, 4 µM) of linezolid, levofloxacin, and raltegravir were pumped through the channels with 12 µL of PSS lacking BSA. After 1 hour, 5 µL was sampled from the detection well, diluted with 200 µL buffer, before further dilution with the internal standard working solution. $n \geq 3$; error: standard deviation

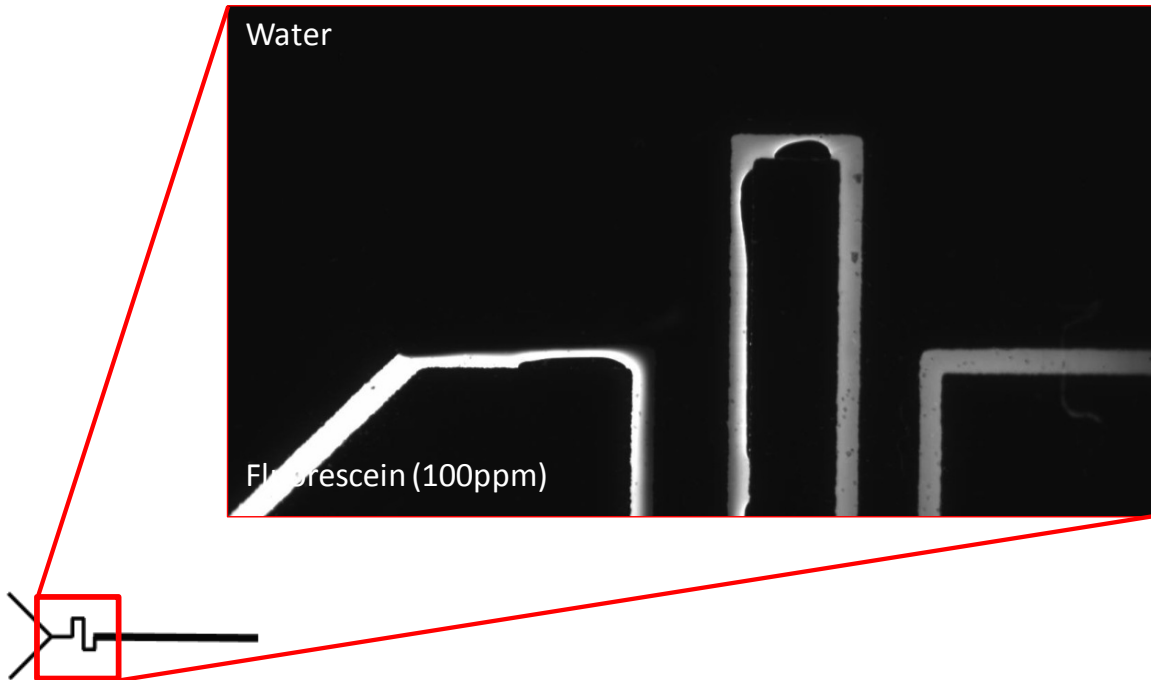


Figure 3.8 Validation of Mixing in Serpentine Channels by Fluorescence. A solution of 100 μM fluorescein was flowed through the bottom of the Y channel while water was flowed through the top of the Y channel. Using a macroscope, the mixing of the two solutions in the serpentine channels is monitored. At the completion of the serpentine the solutions are successfully and completely mixed.

3.3.2 Verification of Complete Mixing in Channel

The decay portion of a PK curve represents the elimination and metabolism of a drug from the body. This phenomenon is achieved in the microfluidic device by reversing the concentration gradient created in section 3.3.1. Therefore, the detection well is filled with 12 μL of 2 μM concentrated drug, while buffer or a concentration of drug lower than that of the well is delivered through the channel. It is imperative that the serpentine channel completely mixes the concentrated drug and buffer to achieve the desired concentration from the gradient approach. To validate the mixing, fluorescein was pumped through the bottom half of the Y-channel, while water was flowed through the top half of the Y-channel (Figure 3.7). Mixing was observed throughout the serpentine until a uniform mixture exits the serpentine, and where the flow encounters the detection well. Upon validating the complete mixing of the two solutions in the serpentine channel, the manipulation of the concentration in the channel for future studies, specifically those concerning the half-life can be assured.

3.3.3 Validation of Drug Elimination Profiles and Manipulation of Elimination Half-Lives

In section 3.3.1, the absorption portion of the PK curve was validated. The decay portion of the curve is shown for three different drugs, levofloxacin (Figure 3.8), linezolid (Figure 3.9), and raltegravir (Figure 3.10). Each of the three

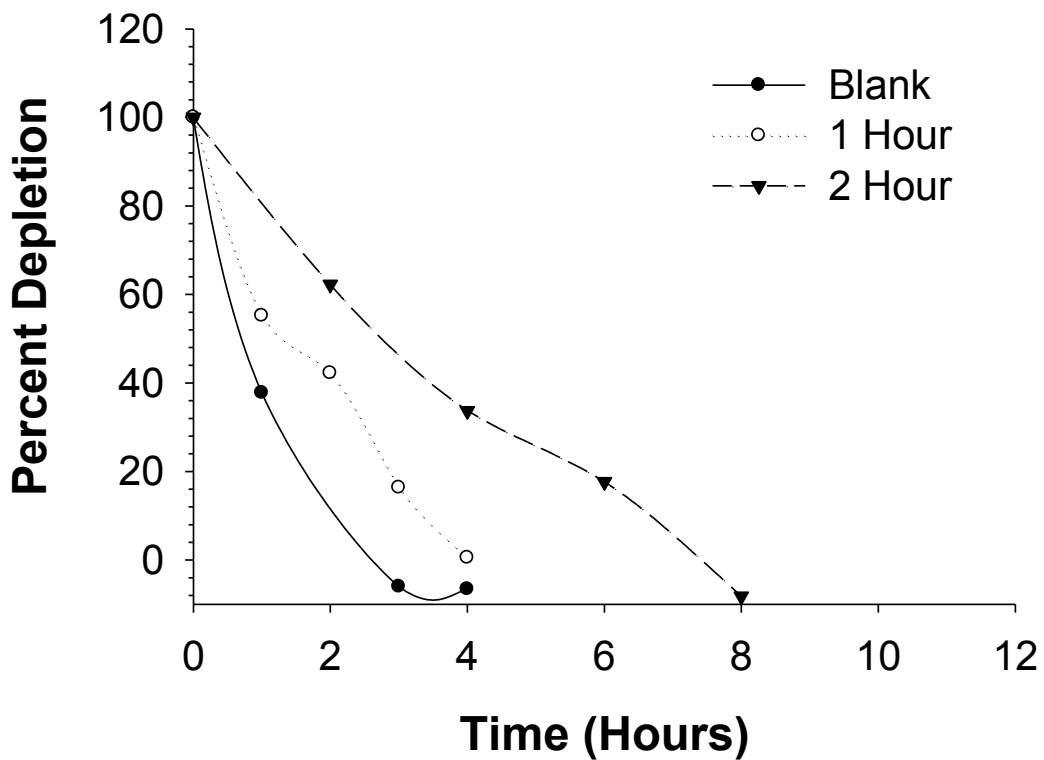


Figure 3.9 Various Elimination Profiles for Linezolid. The solid black line with black circles represents the quickest elimination with buffer flowing through the channel and concentrated drug ($2 \mu\text{M}$) in the detection well. The gray dotted lines with white circles represents a manipulation of the concentration of drug in the channel to alter the half-life. The half-life is further increased when the gradient is increased to 2 hours increments. The general trend was apparent but lacked quantitation reproducibility therefore the curves shown are an example of an n of 1.

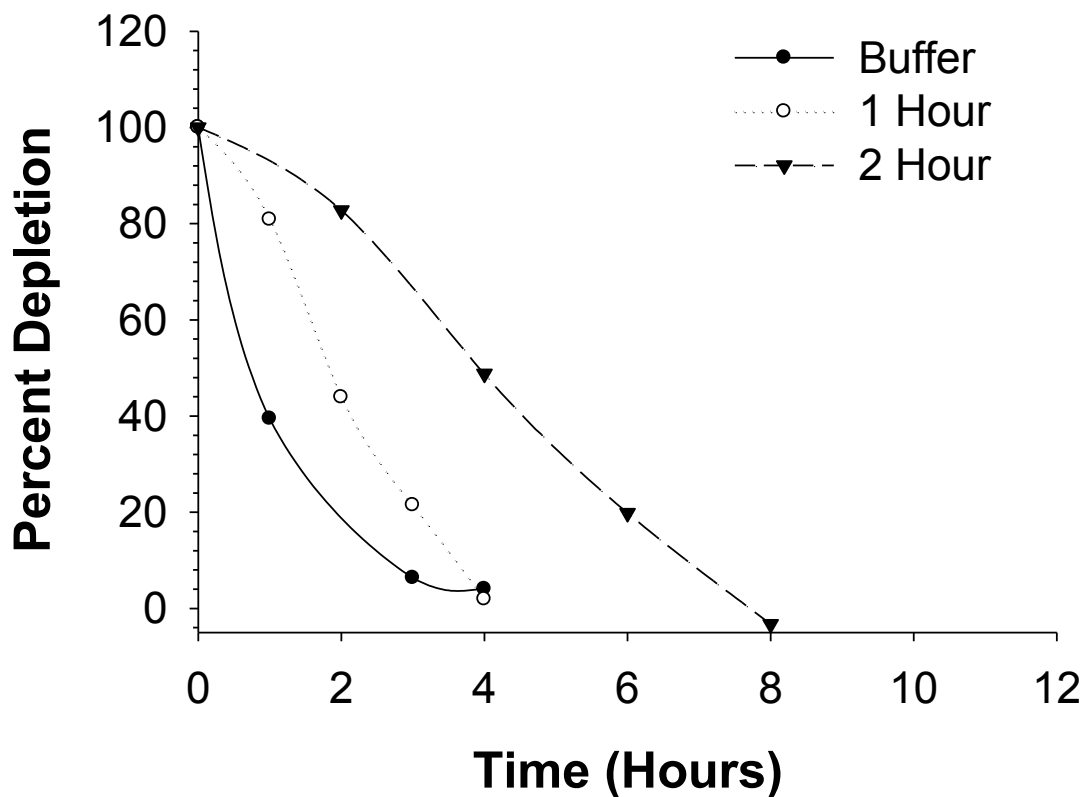


Figure 3.10 Various Elimination Profiles for Levofloxacin. The solid black line with black circles represents the quickest elimination with buffer flowing through the channel and concentrated drug ($2 \mu\text{M}$) in the detection well. The gray dotted lines with white circles represents a manipulation of the concentration of drug in the channel to alter the half-life. The half-life is further increased when the gradient is increased to 2 hours increments. The general trend was apparent but lacked quantitation reproducibility therefore the curves shown are an example of an n of 1.

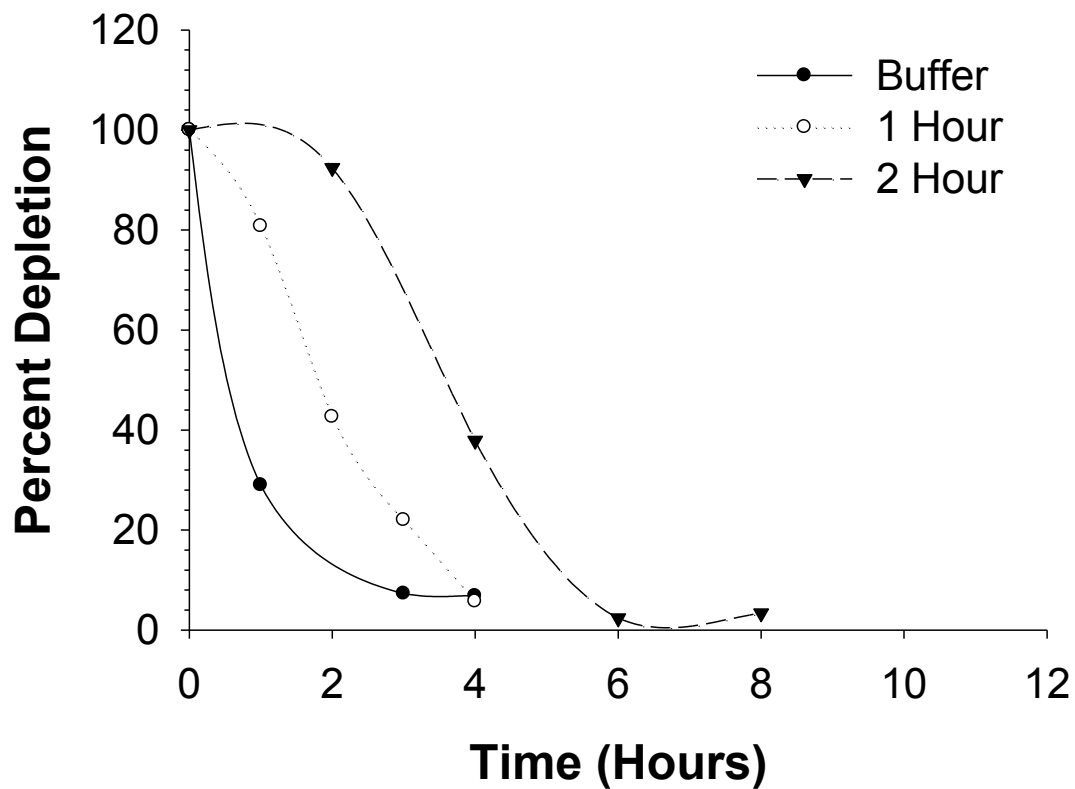


Figure 3.11 Various Elimination Profiles for Raltegravir. The solid black line with black circles represents the quickest elimination with buffer flowing through the channel and concentrated drug ($2 \mu\text{M}$) in the detection well. The gray dotted lines with white circles represents a manipulation of the concentration of drug in the channel to alter the half-life. The half-life is further increased when the gradient is increased to 2 hours increments. The general trend was apparent but lacked quantitation reproducibility therefore the curves shown are an example of an n of 1.

figures contains a buffer depletion curve, in which the detection well initially contained drug at 2 μM with drug-free buffer flowing through the channel. The figures contain an additional two curves, which had varying gradients flowing through the channel. The additional gradients are achieved by changing the concentration of drug flowing through the channel at different time points, with the overarching goal manipulation of the half-lives. For example, the 1 hour gradient was achieved by initially flowing 75% of the original concentration of the drug for one hour, before changing the concentration to 50%. The concentrations were again lowered to 25% an hour later until just buffer is flowing through the channel in the subsequent hour. The overall aim is to gradually reduce the concentration gradient experienced by the drug in the concentration well, thereby slowing the diffusion from the detection well and ultimately manipulating the half-life. The half-life was obtained by plotting the natural log of the concentration in the detection well versus time flowed. A linear relationship in the curve is indicative of a first order process, with the slope pertaining to the elimination reaction rate constant (K_{EL}). Utilizing this rate constant in the following equation allows for the mathematical determination of the half-life ($t_{1/2}$):

$$t_{\frac{1}{2}} = \frac{0.693}{K_{EL}}$$

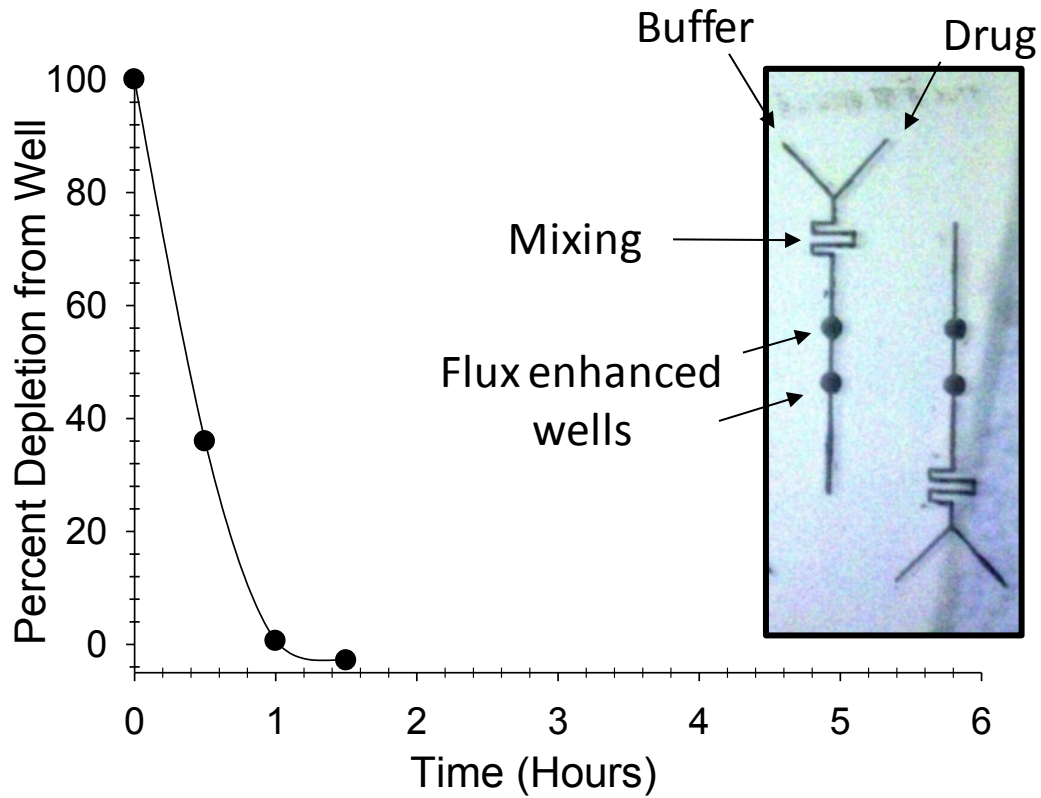


Figure 3.12 Manipulating the Physical Design of the Microfluidic Device to Influence Elimination. Initial designs of the microfluidic device had channel diameters of 200 μm . Upon increasing the channel diameter under the wells (see inset) the half life decreased to approximately 30 min. $n = 1$

The various gradients of buffer, 1 hour and 2 hour, successfully altered the half-lives at approximately 1, 2, and 4 hours, respectively. One limitation of PDMS microfluidic PK profiles is the overall lack of reproducibility, which could owe to single use nature of the devices. The general elimination trend is reproducible, although quantitative results were difficult to obtain, especially for longer duration half-lives. These drawbacks led us to seek other platforms for device fabrication. The fragility of the polycarbonate membrane ultimately leads to leaking and this bulk fluid transport from the channel to the membrane limits the experimental time of the device before failure. The maximum overall flow time was 8 h but was difficult to achieve due to device fragility.

3.3.4 Physical Manipulation of Device Design to Decrease the Half Life.

Through utilizing gradients, the half-life was lengthened; however, there was interest in shortening the half-life. With buffer flowing through the original device design, the shortest possible half-life was approximately 1 hour. The device design was initially altered (Figure 3.11 and Figure 3.12A) to have two wells opened up along the channel, with the detection wells positioned above the channel wells, to increase the surface area, thereby, allowing a larger area for diffusion. The half-life was reduced to less than a half hour, however, the membrane failure and subsequent leaking resulted in new design considerations that included a large serpentine (Figure 3.12B), two small serpentine (Figure 3.12C), or subtly increasing surface area with a small two channel serpentine

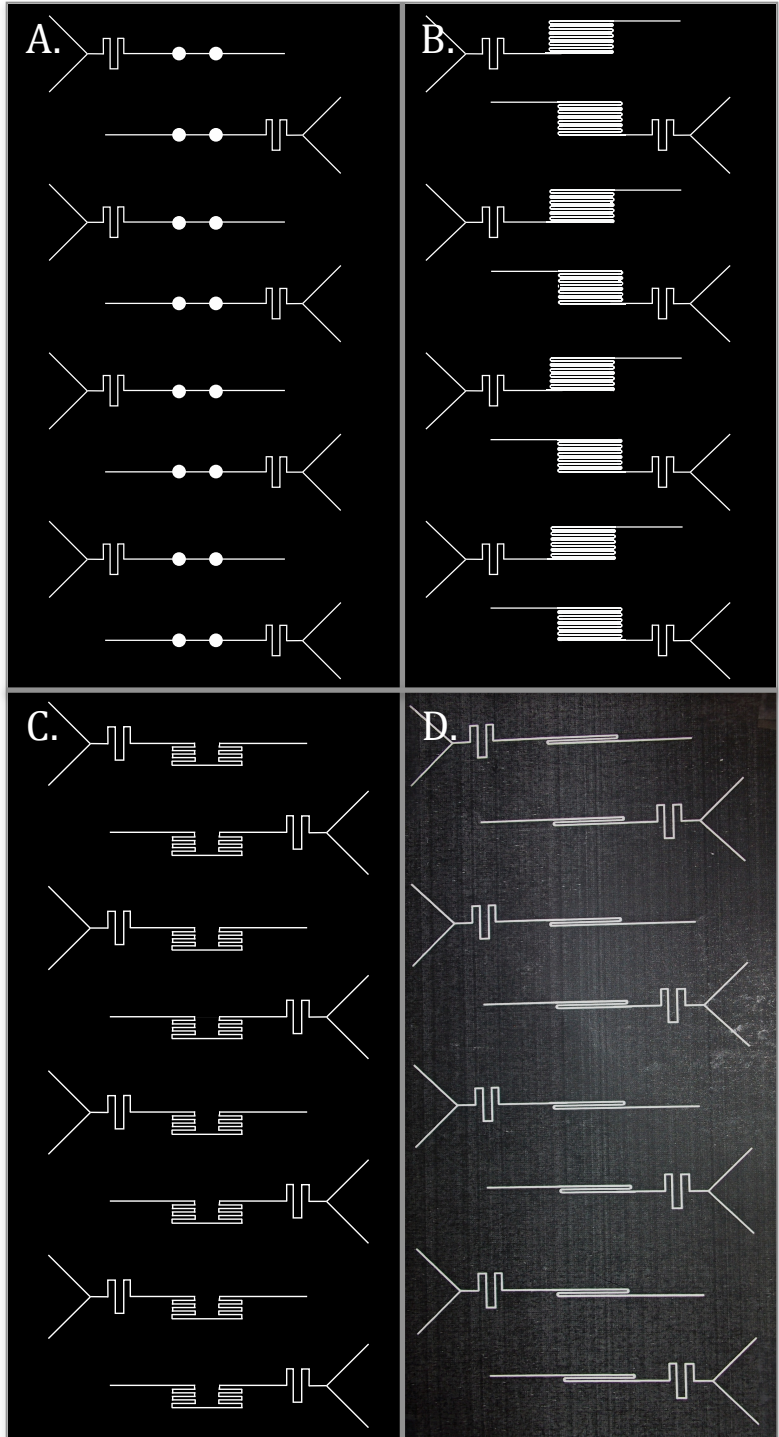


Figure 3.13 Various Alterations to the Physical Design of the Microfluidic Device to Influence Elimination. As seen in Figure 3.11, mask A is the full mask design with the increased surface area. Due to leaking, mask B was temporarily employed before it was also subject to membrane failure. Both masks C and D were also designs used that resulted in bulk fluid transport.

(Figure 3.12D). Alas, all of the aforementioned designs had substantial bulk fluid transport problems making lengthy experiments, or combining both the front half and back half of a PK curve nigh impossible.

3.3.5 Effect of Culturing Cells in the Loading Well on Overall Drug Transport

A key feature and perceived drawback of the HFCR is the inability to harvest the cells after dosing. The design of the PDMS based device allows cells to be cultured in the detection well and collected throughout the experimentation. It is critical to monitor the effect that cells, in the detection well, pose to the both the loading and elimination portions of the PK curve.

3.3.5.1 Effect of adhered HUH-7 Cells on Drug Loading Profiles

Upon adhering the HUH-7 cells in the detection wells, buffer (12 μL) was added to the wells, while various concentrations (0-7 μM) of drug are flowed under different channels (Figures 3.13 and 3.14). At the lower concentrations there is no significant effect on hindered diffusion, however, at higher concentrations (6 and 7 μM) the effect becomes more pronounced, with the concentrations in the detection well being significantly higher for wells lacking HUH-7 cells versus wells containing adhered cells. Therefore, any characterization that will be performed on this device would need to be performed with cells adhered in the wells to correct for any diffusion obstruction.

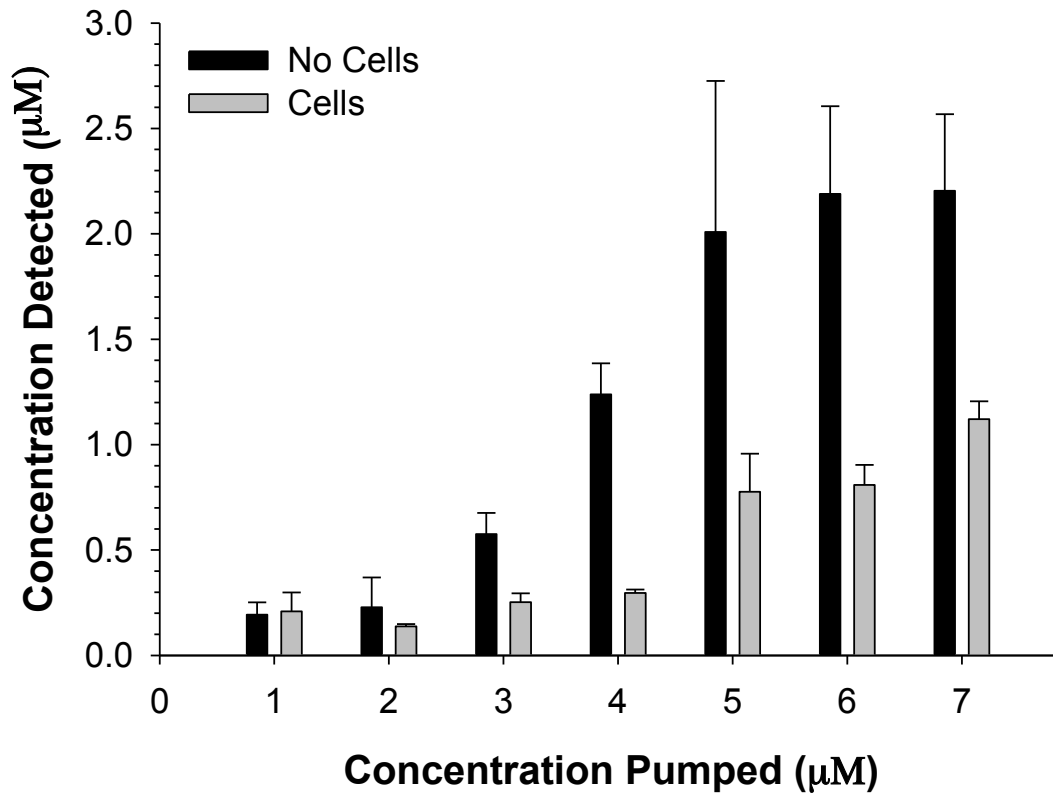


Figure 3.14 Impact on Loading Diffusion of Levofloxacin upon Adherence of HUH-7 cells in the Detection Well. HUH-7 cells were seeded in the detection well and various concentrations of drug (0, 1, 2, 3, 4, 5, 6, 7 µM). A significant impact on diffusion was not observed until the more concentrated samples (6 and 7 µM). $n \geq 3$; $p < 0.005$; Error: SEM

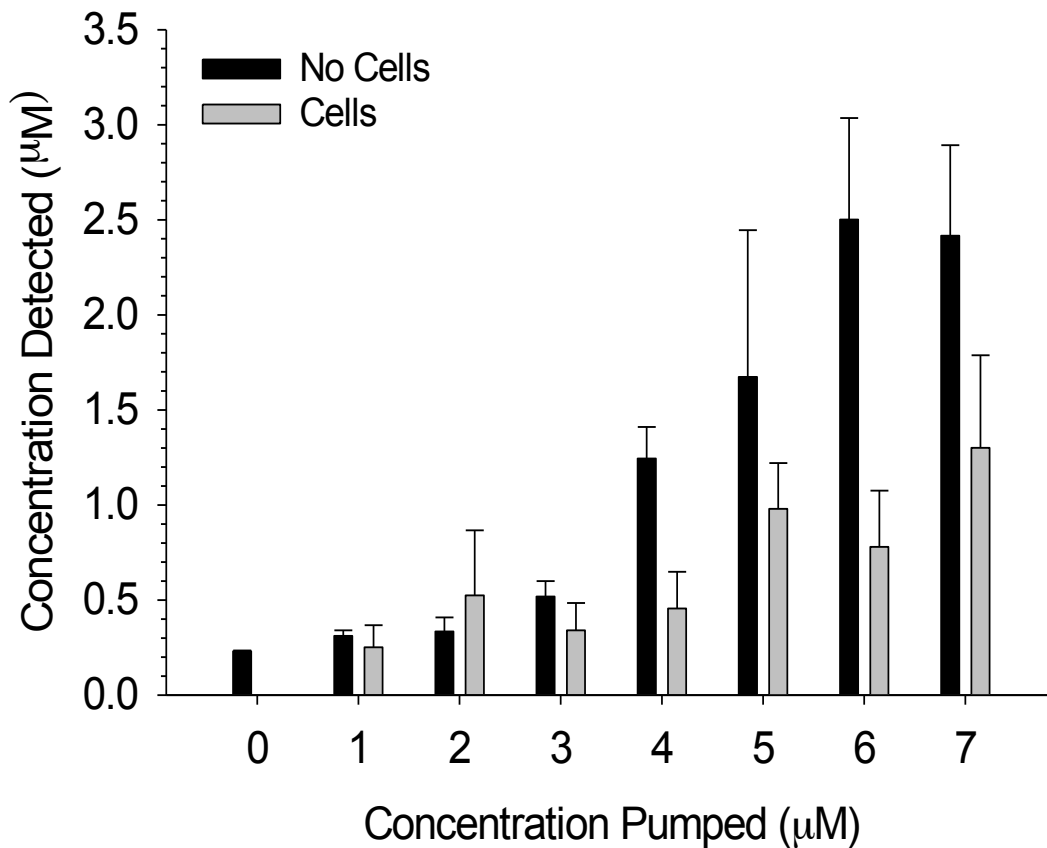


Figure 3.15 Impact on Loading Diffusion of Raltegravir upon Adherence of HUH-7 cells in the Detection Well. HUH-7 cells were seeded in the detection well and various concentrations of drug (0, 1, 2, 3, 4, 5, 6, 7 μM). A significant impact on diffusion was not observed until the more concentrated samples (6 and 7 μM). $n \geq 3$; $p < 0.005$; Error: SEM

3.3.5.2 Effect of Adhered HUH-7 Cells on Drug Elimination Profiles

The influence of the adhered HUH-7 cells on the elimination portion of the PK curve was monitored by adding concentrated drug (2 μM) to the detection well while flowing buffer or gradients (40 min and 60 min) through the channel (Figure 3.15, Figure 3.16, and Figure 3.17). The half-lives were similar to those previously observed with regard to lack of precision, moreover bulk fluid transport was still a major concern with flow times exceeding 3 or 4 hours. Additionally, the primary goal of this device is to make the setup amenable to industry, which would find the fabrication time, failure rate of the membrane, irreproducibility, or the lack of integration to automation inconvenient, therefore would not implement such a tool into their program despite the ability to harvest cells during or post analysis and the savings associated with material consumption. A platform is needed that will integrate automation and reusability, minimize sample and reagent consumption, and enable cell harvest post-dosing.

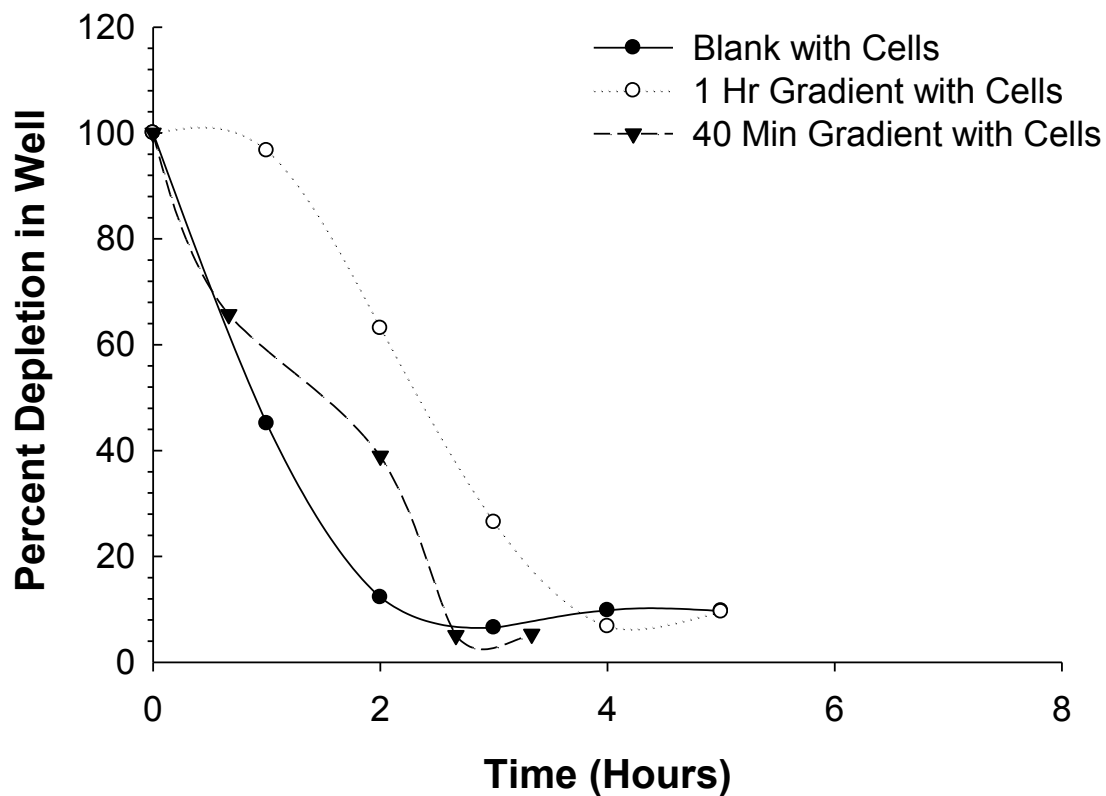


Figure 3.16 Impact on Elimination Diffusion of Linezolid upon Adherence of HUH-7 cells in the Detection Well. HUH-7 cells were seeded in the detection well and 2 μM of concentrated drug was added. Buffer alone was flowed through the channel for the fastest elimination (Black line/circles). Various gradients of drug concentrations were also flowed under the well (40 min: Black dashes/triangles; 1 hour: Gray dashed/white circles). The general trend was apparent but lacked quantitation reproducibility therefore the curves shown are an example of an n of 1.

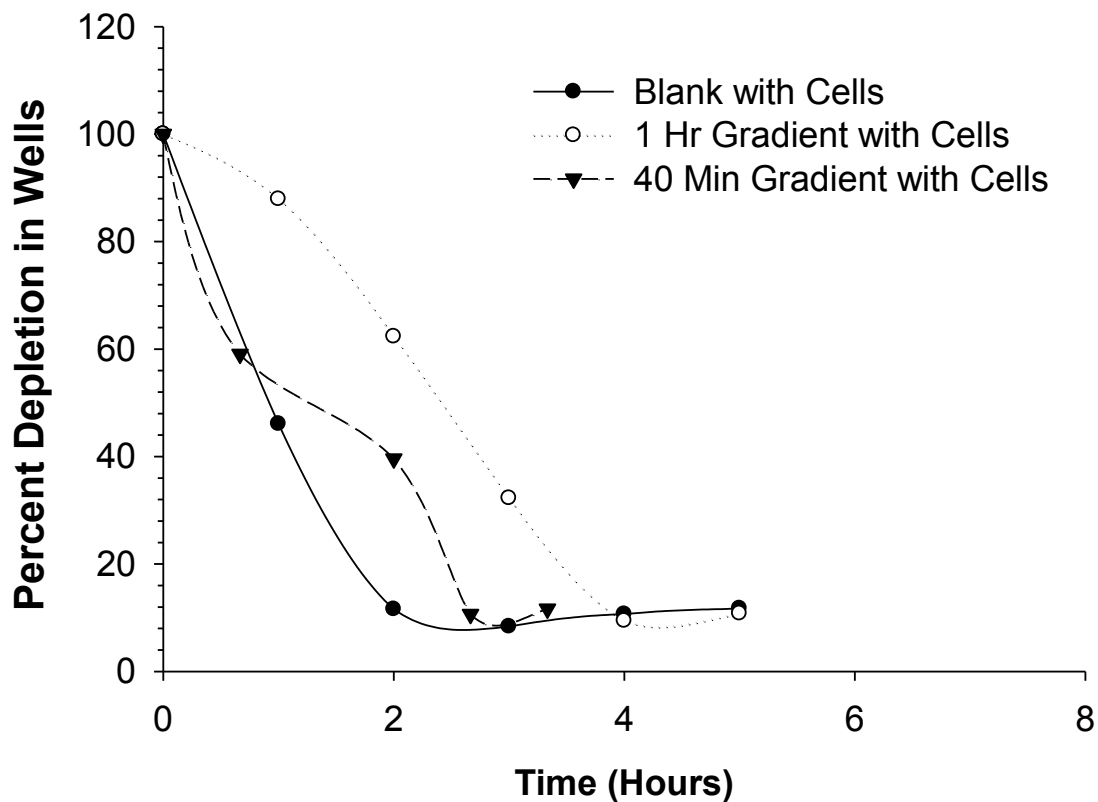


Figure 3.17 Impact on Elimination Diffusion of Levofloxacin upon Adherence of HUH-7 cells in the Detection Well. HUH-7 cells were seeded in the detection well and 2 μ M of concentrated drug was added. Buffer alone was flowed through the channel for the fastest elimination (Black line/circles). Various gradients of drug concentrations were also flowed under the well (40 min: Black dashes/triangles; 1 hour: Gray dashed/white circles). The general trend was apparent but lacked quantitation reproducibility therefore the curves shown are an example of an n of 1.

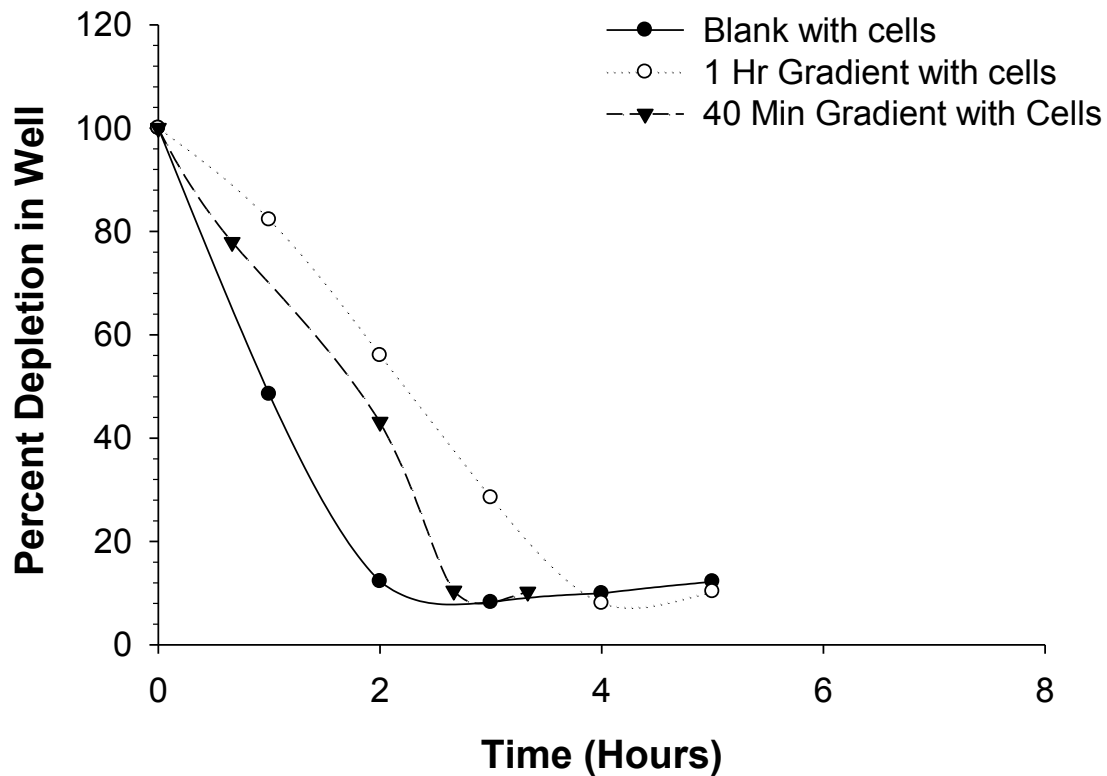


Figure 3.18 Impact on Elimination Diffusion of Raltegravir upon Adherence of HUH-7 cells in the Detection Well. HUH-7 cells were seeded in the detection well and 2 μM of concentrated drug was added. Buffer alone was flowed through the channel for the fastest elimination (Black line/circles). Various gradients of drug concentrations were also flowed under the well (40 min: Black dashes/triangles; 1 hour: Gray dashed/white circles). The general trend was apparent but lacked quantitation reproducibility therefore the curves shown are an example of an n of 1.

REFERENCES

REFERENCES

(1) Paul, S. M.; Mytelka, D. S.; Dunwiddie, C. T.; Persinger, C. C.; Munos, B. H.; Lindborg, S. R.; Schacht, A. L.: How to improve R&D productivity: the pharmaceutical industry's grand challenge. *Nature reviews Drug discovery* **2010**, *9*, 203-214.

(2) PhRMA: 2013 Biopharmaceutical Research Industry Profile **2013**.

(3) Golan, D. E.; Tashjian, A. H.; Armstrong, E. J.: *Principles of pharmacology: the pathophysiologic basis of drug therapy*, Lippincott Williams & Wilkins, 2011.

(4) Adams, C. P.; Brantner, V. V.: Estimating The Cost Of New Drug Development: Is It Really \$802 Million? *Health Affairs* **2006**, *25*, 420-428.

(5) Holford, N. H. G.; Sheiner, L. B.: Kinetics of pharmacologic response. *Pharmacology & Therapeutics* **1982**, *16*, 143-166.

(6) Mueller, M.; de la Peña, A.; Derendorf, H.: Issues in pharmacokinetics and pharmacodynamics of anti-infective agents: kill curves versus MIC. *Antimicrobial agents and chemotherapy* **2004**, *48*, 369-377.

(7) Vaddady, P. K.; Lee, R. E.; Meibohm, B.: In vitro pharmacokinetic/pharmacodynamic models in anti-infective drug development: focus on TB. *Future medicinal chemistry* **2010**, *2*, 1355-1369.

(8) White, R. L.: What in vitro models of infection can and cannot do. *Pharmacotherapy: The Journal of Human Pharmacology and Drug Therapy* **2001**, *21*, 292S-301S.

(9) Löwdin, E.; Odenholt, I.; Bengtsson, S.; Cars, O.: Pharmacodynamic effects of sub-MICs of benzylpenicillin against *Streptococcus pyogenes* in a newly developed in vitro kinetic model. *Antimicrobial agents and chemotherapy* **1996**, *40*, 2478-2482.

(10) Blaser, J.; Stone, B. B.; Zinner, S. H.: Two compartment kinetic model with multiple artificial capillary units. *Journal of Antimicrobial Chemotherapy* **1985**, *15*, 131-137.

(11) Garrison, M.; Vance-Bryan, K.; Larson, T.; Toscano, J.; Rotschafer, J.: Assessment of effects of protein binding on daptomycin and vancomycin

killing of *Staphylococcus aureus* by using an in vitro pharmacodynamic model. *Antimicrobial agents and chemotherapy* **1990**, *34*, 1925-1931.

(12) Reeves, D.: Advantages and disadvantages of an in-vitro model with two compartments connected by a dialyser: results of experiments with ciprofloxacin. *Journal of Antimicrobial Chemotherapy* **1985**, *15*, 159-167.

(13) FiberCellSystems: Advantages of Hollow Fiber Cell Culture.

(14) Sainz, B.; TenCate, V.; Uprichard, S. L.: Three-dimensional Huh7 cell culture system for the study of Hepatitis C virus infection. *Virology journal* **2009**, *6*, 103.

CHAPTER 4

A THREE DIMENSIONAL PRINTING PLATFORM FOR THE DEVELOPMENT AND CHARACTERIZATION OF A DIFFUSION-BASED DYNAMIC *IN VITRO* MILLIFLUIDIC PHARMACOKINETIC MODEL

4.1 Introduction

In Chapter 3, a traditional microfluidic PDMS platform was used for the development of a diffusion-based dynamic *in vitro* PK device. While certain aspects of the device such as reduction in volume consumption are improvements on industry established diffusion-based dynamic *in vitro* PK models, the irreproducibility of the device and fragility of the membrane are fatal flaws for long-term use of the PDMS platform. Lack of reusability, compatibility with automation, and ease of operator use were other limitations shared by both HFCRs and the PDMS model. Three Dimensional (3D) printing offers flexibility in device design and a rigid base platform, thus making it an appealing option for *in vitro* PK platform development.

4.1.1 Three Dimensional Printing

3D printing, i.e., additive manufacturing, rapid prototyping, or solid-free form technology, has recently been garnering attention in the research communities in a variety of fields.^{1,2} Advances in tissue growth,³⁻⁶ prototyping,^{7,8} electrochemistry,⁹ electronics,¹⁰ microfluidics,^{11,12} mass spectrometry,¹³ and pneumatics¹⁴ have all been reported. Applications in microfluidics have been

only recently explored due to limitations related to the printing resolution of currently available 3D printers. As 3D printers continue to develop, and reduce in price, the field will continue to grow and expand into new avenues with creativity and imagination being the main limitation.

4.1.2 History and Concepts

3D printing was first conceived by Charles Hull in 1986, with his patent for stereolithography.¹⁵ His accomplishments over the years included a multitude of patents,¹⁶⁻²² which led to the creation of his own company, 3D Systems, and the development of the stereolithography file (.STL).²³ An .STL file uses the 3D modeled image created by computer aided design (CAD) software and breaks it into triangles. A high resolution image is broken into smaller triangles, in contrast to a low resolution image having larger triangles.²⁴ Figure 1 shows a CAD file broken into a low resolution .STL file, as well as a high resolution .STL file. The .STL file is read by any 3D printer, thereby allowing universal communication between all printers. This communication is a unique and special tool when applied to scientific fields. For example, in traditional microfluidics, the fabrication of a specific device is described in detail when published, but this description is the only instruction other laboratories have when wanting to reproduce the aforementioned device. Therefore, any nuances important to proper fabrication

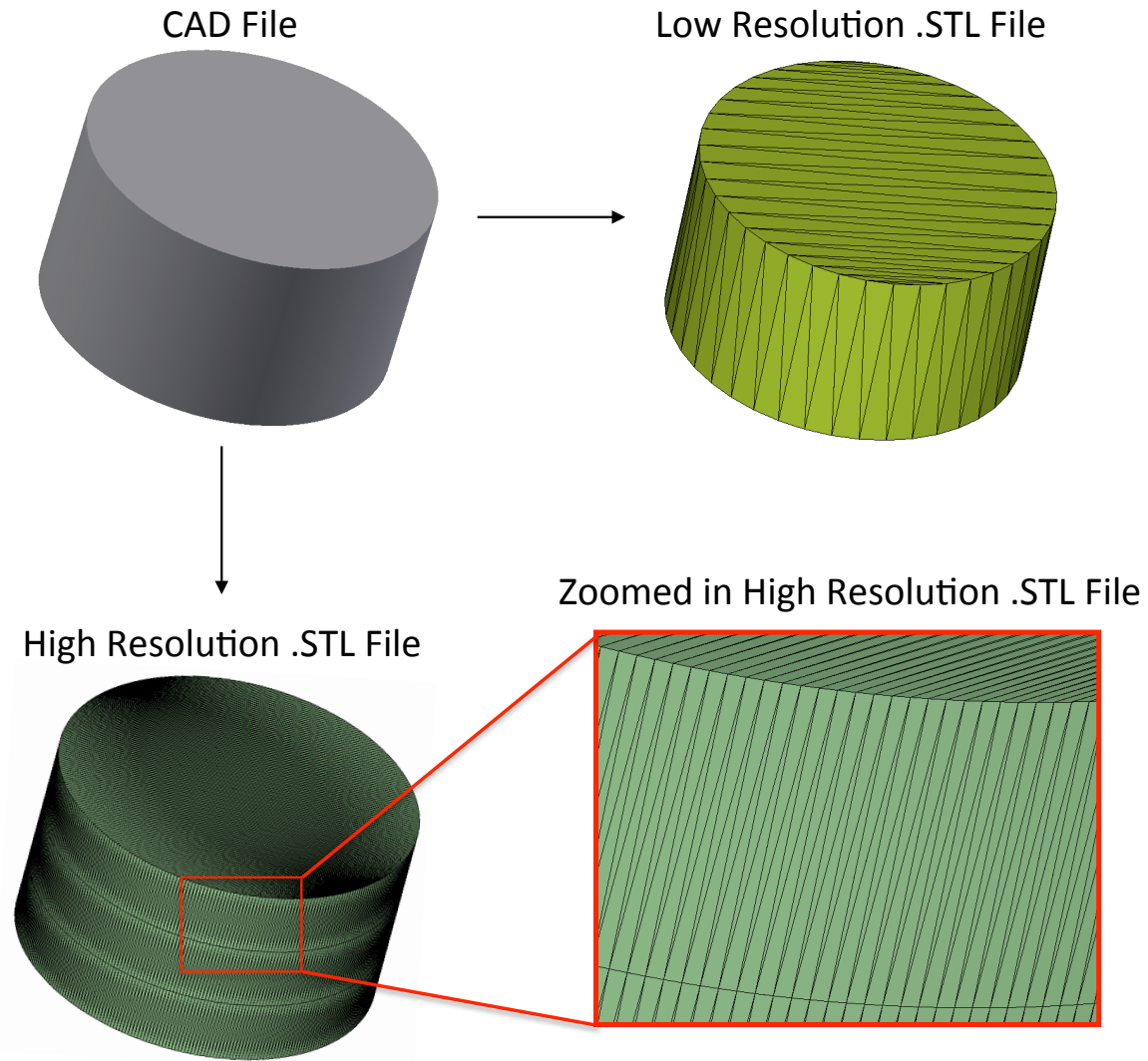


Figure 4.1 Examples of a CAD File, Low Resolution .STL File and a High Resolution .STL File with a Zoomed in Cutout. CAD files (Top Left) are 3D models that are able to be saved as .STL files, thereby breaking the 3D images into a series of triangles. A low resolution .STL (Top Right) contains less triangles than a high resolution (Bottom Left) .STL file. In the high resolution cylinder showed, the triangles in such close proximity they are hard to individually depict, therefore a zoomed in cutout is shown on the bottom right, in which the triangles can be depicted.

that did not appear in a published report will most certainly hinder production of the device. In 3D printing, the .STL file of the device is able to be uploaded into open source file sharing, where other researchers are able to download and print exact replicas of the original device used, but on their own printers. There are a variety of 3D printers, ranging from highly developed and commercialized to early in development. Some of the more common techniques are stereolithography, inkjet printing, selective laser sintering, Polyjet, fused silica deposition modeling and laminate object manufacturing. Each technique is unique with regard to curing source, layout, base materials, and resolution. The devices made in the research reported here were fabricated through photocuring, using Polyjet technologies.

4.2 Experimental

4.2.1 Fabrication of 3D Printed Device

The fabrication of 3D printed devices is very different than the labor intensive fabrication of conventional microfluidics.^{25,26} 3D model prototypes are created in engineering based CAD software. The files are subsequently saved as an .STL file, which is compatible with all 3D printers.

4.2.1.1 Initial Design

Prototypes were designed, in house, using AutoDesk Inventor Professional

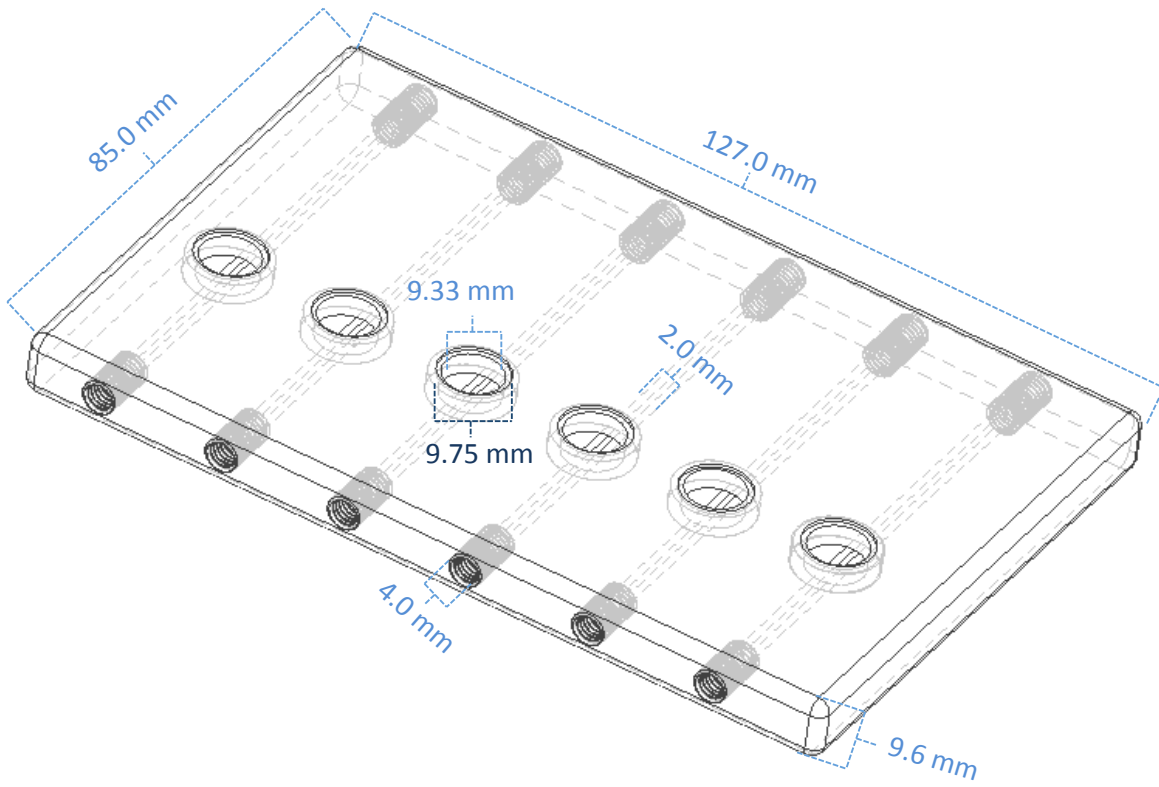


Figure 4.2 Image of the Computer Aided Design File for the 3D Printed Base. CAD file of the 3D printed base with corresponding dimensions.

Student Edition (AutoDesk, San Rafael, CA, USA). The overall device design mirrored that of a 24 well plate to allow compatibility with automation, i.e., 6 channels with wells lining up to those of a 24 well plate. The channels were 2 mm in diameter. Threads modeled after a 10-32 coned fitting, in initial prototypes had to be manually tapped,¹¹ but in current prototypes the threads can be printed with the use of an add-in for the CAD software. A wireframe view of the CAD file with the indicated dimensions is shown in Figure 4.2. The CAD files were then saved as .STL files and sent to the 3D printer for production. If modifications to the original prototype are necessary, the original CAD file can be opened and adjusted before submitting to reprint, a much simpler process than the soft lithography of traditional microfluidics where a new mask would need to be fabricated to make a new master. The process of fabricating a new master requires a day or two, compared to the 3D printing process that can produce a new finished prototype in a matter of hours.

4.2.1.2 3D Printed Fabrication

The College of Engineering at Michigan State University houses an Objet Connex 350 printer. The sophisticated printer is capable of printing multiple materials simultaneously, as well as creating alloys of the two materials to create desired properties, such as flexibility versus rigidity. The Objet Connex 350 is a Polyjet printer that relies on the photocurable properties of its materials to create

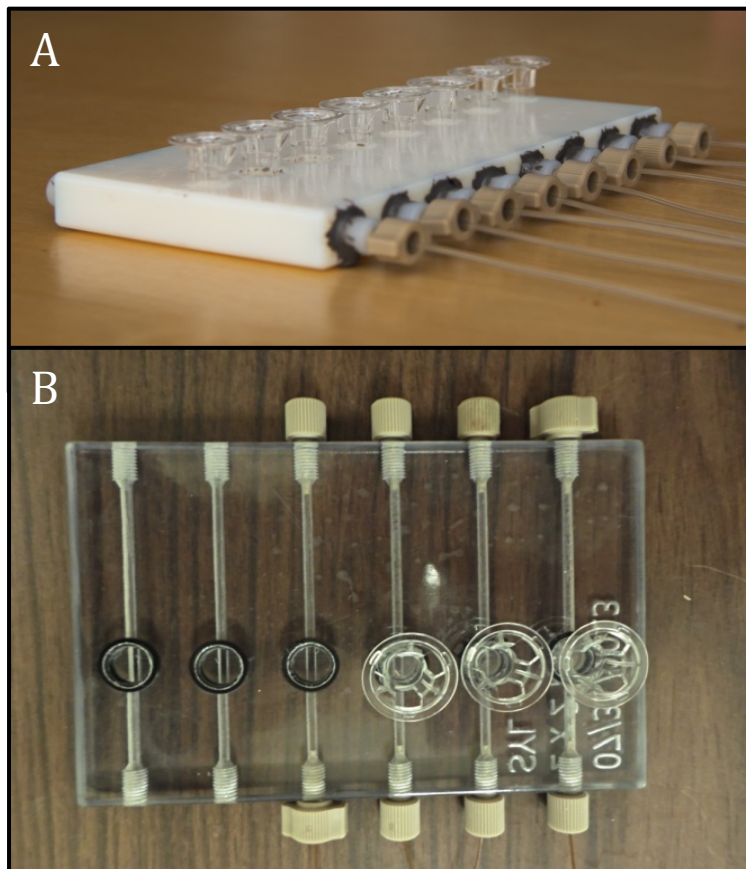
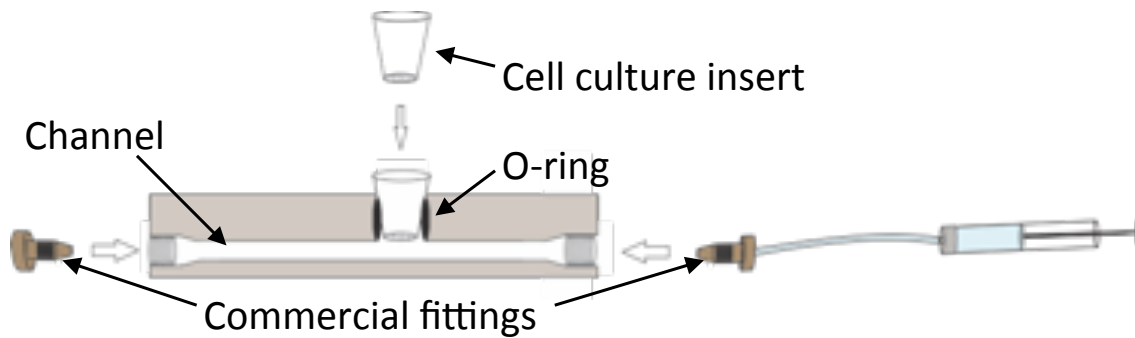


Figure 4.3 Schematic of a Cross Section of a 3D printed Device and Actual Images of Several Prototypes. A schematic depicting a cross section of the 3D printed device (Top) is shown with commercial fittings, syringe, and disposable membrane insert. An early prototype (A) has 8 channels and is fabricated in TangoWhite material. Also, female commercial fittings were affixed by epoxy to the device to allow for integration of the male commercial fittings. In the current prototype (B), threads could directly be printed into the device, thereby simplifying the setup. Current devices, modeled after 24 well plates, are fabricated with an optically clear, VeroClear material with O-rings simultaneously printed with the rubbery TangoBlack.

a rigid product. In short, a layer of the photocurable liquid polymer was printed (resolution: 100 μm x 100 μm x 16 μm) before it was rolled flat, and photocured by exposure to UV light. Subsequent layers were printed and cured in the same manner, therefore, building the device in an additive process. The materials used were Fullcure 810 VeroClear (Objet Geometries Ltd., Rehovot, Israel), which comprise the body of the device, and Fullcure 980 TangoBlackPlus (Objet Geometries Ltd., Rehovot, Israel) that makes up the O-ring lining the detection wells that host the disposable membrane inserts (Figure 4.3). The composition of Fullcure 810 VeroClear, while proprietary, is approximately isobornyl acrylate (15-30%), acrylic monomer (15-30%), urethane acrylate (10-30%), acrylic monomer (5-10; 10-15%), epoxy acrylate (5-10; 10-15%) and a photoinitiator (0.1-2%). Fullcure 980 TangoBlackPlus also has a proprietary composition but contains urethane acrylate oligomer (30-60%), exo-1,7,7-trimethylbicyclo[2.2.1]hept-2-yl acrylate (1-20%), methacrylate oligomer (1-20%), resin-polyurethane (1-20%), and a photoinitiator (0.1-1%). Post printing, the devices are translucent. To obtain an optically clear finish device, the exterior is finely sanded (600-2000 grain sandpaper) and rigorously polished. An alternative to achieving a clear device involves coating with a clear lacquer (RUST-OLEUM, Vernon Hills, IL, USA) after sanding. The clear lacquer finish will become opaque if cleaned with isopropyl alcohol. The inlets and outlets contained either manually tapped or printed threads, allowing the integration of

commercial fittings, thereby streamlining the design when compared to conventional microfluidics.

4.2.2 Preparation of Reagents

4.2.2.1 Fluorescein Stock and Working Solutions

Fluorescein (332.31 g/mol, Sigma Aldrich, St. Louis, MO, USA) was used to characterize the 3D printed *in vitro* PK models due to ease of analysis and detection. A stock solution of fluorescein (100 ppm) was prepared and diluted with deionized (DI) water to make the appropriate working solutions of 5, 10, and 15 μM .

4.2.2.2 Levofloxacin Stock and Working Solutions

Levofloxacin was chosen to characterize the 3D printed *in vitro* PK model due to similar molecular weight as fluorescein. Levofloxacin stock and working solution preparation was initially described in section 3.2.1. Briefly, levofloxacin (361.37 g/mol; Sigma Aldrich, St. Louis, MO, USA) was dissolved with 50% methanol and DI water to prepare a 1 mg/mL stock solution. Working solutions were subsequently diluted from the concentrated stock solution with BSA free PSS.

4.2.2.3 Ciprofloxacin Stock and Working Internal Standard Solutions

Ciprofloxacin was chosen as the internal standard and prepared as described in section 3.2.1. In short, ciprofloxacin was dissolved in DI water to prepare a stock solution of 1 mg/mL. The working solution was prepared by dilution of 550 μ L of the stock solution with 5 mL of acetonitrile. This solution was placed in an ice bath until mixing the sample with 200 μ L of the internal standard prior to analysis. Proteins were precipitated out in the cold internal standard solution and upon centrifugation (500 *g* for 5 min), the supernatant was added to a 96 well polycarbonate PCR plate (Denville, Metuchen, NJ, USA). Once the PCR plate was sealed with a RapidEPS seal, the polycarbonate plate was ready for MRM-LC/MS/MS analysis.

4.2.3. Pumping System

Sample was introduced to the 3D printed devices by standard syringe pumps. Hamilton Gastight syringes (5.00 mL; Hamilton Company, Reno, NV, USA) were filled with sample and flowed at 10 μ L/min for all experiments, with the exception of the flow rate characterization, which involved fluctuating the flow rate from 2.5 to 25 μ L/min. The syringes were fastened to fused silica capillary tubing (i.d. 536 μ m; o.d. 669.7 μ m; Polymico Technologies, Phoenix, AZ, USA) by a commercial male leur syringe fitting (F-120, IDEX Health and Science, Oak Harbor, WA, USA), which was connected to a 10-32 female compression fitting (P-659, IDEX Health and Science, Oak Harbor, WA, USA). The female

compression fitting snugly sheaths the capillary tubing when coupled with a tube sleeve (i.d. 685 μm ; 1.58 mm o.d.; F-234, IDEX Health and Science, Oak Harbor, WA, USA). The 10-32 coned female fitting and tube sheath were also on the opposite end of the fused silica capillary tubing to allow integration into the 3D printed device's 10-32 printed threads. A useful plugin for the AutoDesk software allows for threads of various parameters to be added and subsequently printed into designs, thereby integrating commercial fittings. Initial 3D printed prototypes had 10-32 threads manually tapped, thus adding an additional fabrication step. A key limitation of traditional microfluidic devices is the lack of amenability between PDMS platforms and the commercial fittings, see section 3.2.4, which is rectified in the setup for the 3D printed device. All experiments were completed at room temperature.

4.2.4 Plate Reader Analysis of Fluorescein

The sampling process from the membrane inserts was intended to mirror that of a conventional auto sampler, with 5 μL being sampled from each insert at specific time points. This process allowed up to 6 samples per time point, per device, whereas sampling from an HFCR allowed for one sample per time point per cartridge. The 5 μL sample was subsequently diluted with 100 μL of DI water and added to a 96 well plate. Standards encompassing the concentrations of the samples were prepared and diluted to the same ratios as the samples to obtain a linear calibration curve and determine unknown concentrations of the samples.

Upon completion of the allotted time frame, the 96 well plate containing diluted sample and standards was placed in a plate reader. Fluorescence detection (ex. 480/em. 520; Spectromax M4, Molecular Devices, Sonnyvale, CA) was obtained in a matter of seconds.

4.2.5 Mass Spectrometry Analysis of Levofloxacin

As described in section 3.2.5, the sealed polycarbonate plate was added to an auto sampler and 10 μ L aliquots were injected into the Shimadzu ultra performance liquid chromatograph (UPLC) to be separated using reverse chromatography, (retention times: ciprofloxacin: 1.51 min; levofloxacin: 1.48 min). A Supelco Ascentis precolumn preceded a Supelco Ascentis Express C18 column (length: 3 cm; i.d.: 2.1 mm; particles: 2.7 μ L; Supelco, Bellefonte, PA, USA). Solvents A (methanol), B (acetonitrile) and C (1% formic acid in water) were used in the following gradient at 0.45 mL/min; 95% A, 0% B for 0.25 min; 2% A, 0% B at 1.00 min; Hold 2% A, 0% B until 1.25 min; 30% A, 15% B at 1.75 min; Hold 30% A, 15% B until 1.90 min; 95% A, 0% B at 2.00 min.

The samples were subsequently subjected to electrospray ionization before entering the Waters Quatro Micro triple quadrupole mass spectrometer for analysis using MRM. Specific parameters for levofloxacin and ciprofloxacin can be found in Table 3.1. Waters MassLynx software (Millford, MA, USA) was used to produce peak information. For calibration and measurement, a ratio of the

analyte peak area to the internal standard peak area was used to generate a calibration curve. The regression statistics from this curve were then used for quantitative determination of standards and samples.

4.3 Results and Discussion

4.3.1 Characterization of the Loading Profile

The front half of a typical oral dosing PK curve represents the absorbance of the drug into the body. Important parameters such as the maximum concentration (C_{max}), flow rate, loading volume and loading times are factored into the device characterization of the PK absorbance profile. The loading volume is related to the amount of solution added to the disposable cell culture insert at the beginning of experimentation. The loading time refers to the amount of time that concentrated analyte is pumped through the channel before delivery of drug-free buffer in the channel.

4.3.1.1 Impact of Flow Rate

The rate of flow through the channels of the device was varied to determine its impact on analyte diffusion across the membrane into the insert (Figure 4.4). Parameters such as loading volume (75 μL), loading time (1 hr), and initial channel concentrations (15 μM) were held constant, with the flow rate (2.5, 5.0, 10.0, 15.0 $\mu\text{L}/\text{min}$) being the only variable altered. The experimental

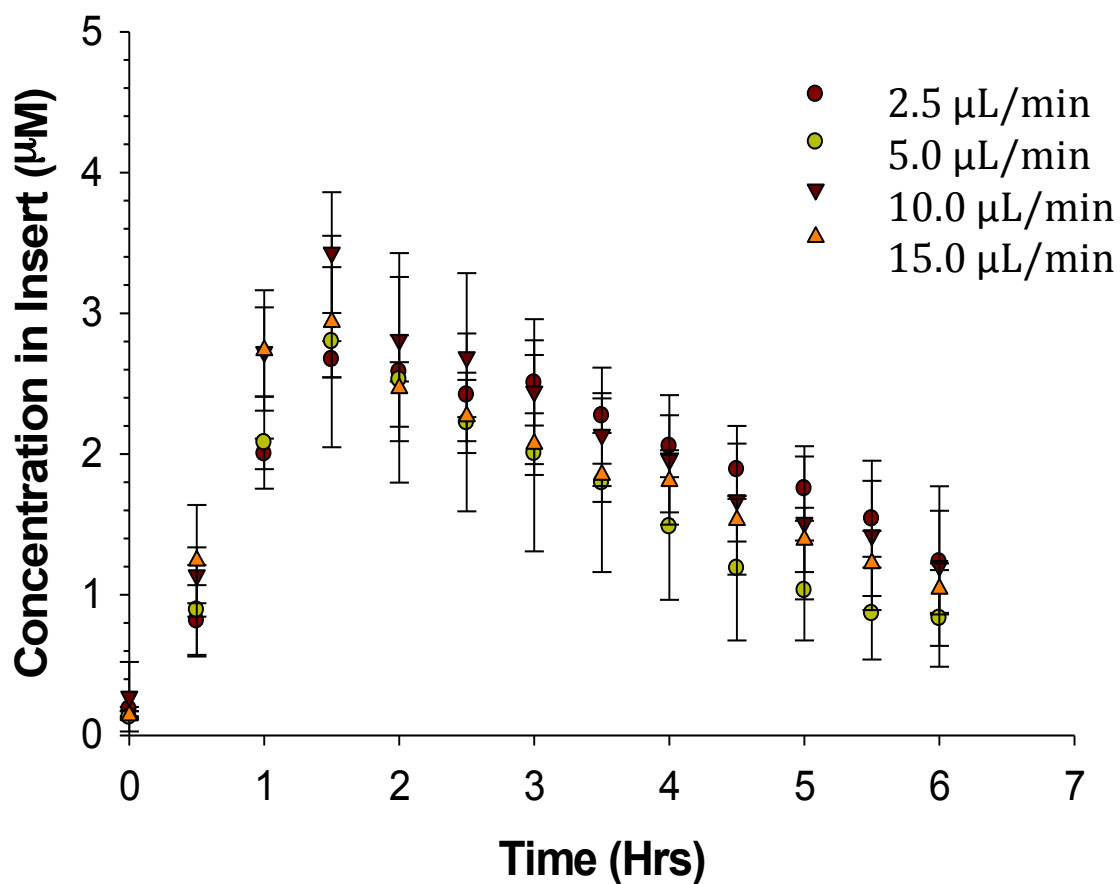


Figure 4.4 Characterization of the Flow Rate in the 3D Printed *In Vitro* PK device. While holding other parameters constant, i.e., insert volume (75 µL), initial concentration (15 µM), and loading time (1 hour), the flow rate was varied to see the impact on diffusion, specifically the C_{max} . The flow rates (2.5, 5.0 7.5, 10.0, 15.0 µL/min) yielded PK profiles that were statistically the similar. $n \geq 4$; $p > 0.05$; error: standard deviation

procedure consisted of pumping a 15 μM fluorescein solution through a channel at the aforementioned flow rates, while 75 μL of DI water were added to the membrane insert. After an hour, the concentrated fluorescein solution was replaced with DI water, flowing at the same rate as the previous fluorescein-containing solution, for a total of 6 hours. Aliquots of sample (5 μL) were taken from the membrane inserts every 30 min, diluted with 100 μL of DI water and added to a 96 well plate. Upon completion of sample collection, the plate was analyzed using a commercial plate reader. The fluorescence intensities were statistically equal for all flow rates ($p < 0.05$, $n \geq 4$) The average C_{max} was $2.96 \pm 0.33 \mu\text{M}$. The lack of flow rate effect on the diffusion was expected when considering Fick's Law of Diffusion:

$$J = -D \frac{\delta\theta}{\delta x}$$

Fick's Law of Diffusion lacks a flow component (flux of diffusion (J); diffusion coefficient (D); concentration gradient ($\delta\theta/\delta x$)), therefore an *in vitro* PK device that relies solely on diffusion would not be influenced by relatively minor changes in the flow rate.

4.3.1.2 Impact on Loading Volume

The initial volume of solution in the membrane insert is crucial to the characterization of the device because it directly influences the resultant loading

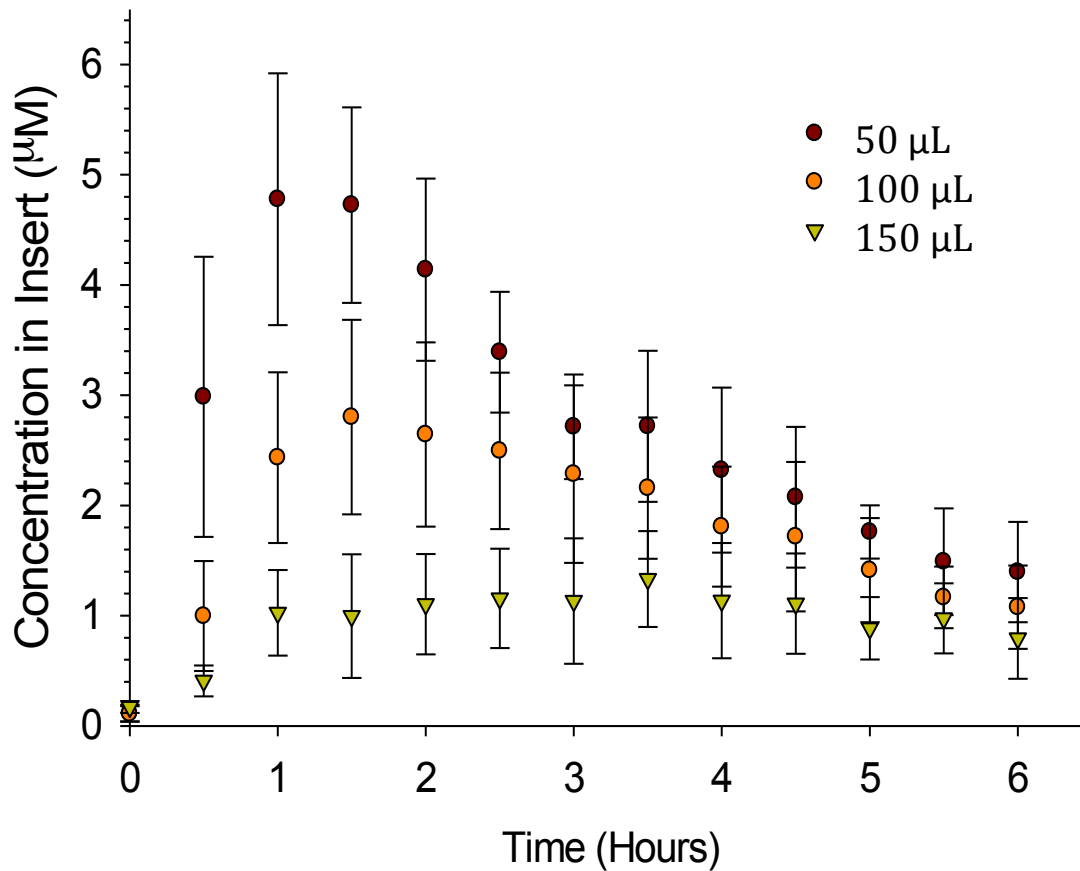


Figure 4.5 Characterization of the Loading Volume in the 3D Printed *In Vitro* PK device. As seen in Figure 4.4, to characterize the loading volume, parameters, such as, flow rate (10 $\mu\text{L}/\text{min}$), initial concentration (15 μM), and loading time (1 hour), were held constant while the loading volume was varied to see the impact on diffusion, specifically the C_{max} . The loading volumes, i.e., 50, 100, 150 μL , yielded PK profiles that indicated the lower the initial volume had a more concentrated C_{max} , while the larger volume was a more diluted sample. $n \geq 4$; $p < 0.01$; error: standard deviation

concentrations (Figure 4.5). Similar to section 4.3.1.1, flow rate (10 $\mu\text{L}/\text{min}$), initial channel concentration (15 μM), and loading time (1 hour), were held constant while the volume in the insert was varied (50, 100, 150 μL). A 15 μM fluorescein solution was delivered through the channel at 10 $\mu\text{L}/\text{min}$ for an hour with the various volumes of DI water in the disposable membrane insert. After an hour, the concentrated solution in the channel was replaced with DI water to reverse the concentration gradient. Aliquots of 5 μL were taken every 30 minutes from the membrane insert and diluted with 100 μL of DI water. Upon completion of sampling, all diluted samples were added to a 96 well plate and analyzed with a plate reader. When the insert contained a decreased volume (50 μL), the concentrated fluorescein diffusing from the channel into the insert was entering into a smaller volume and therefore resulted in a higher concentration ($4.78 \pm 1.14 \mu\text{M}$) when compared to the larger volumes. For example, as the volume in the insert increases to 150 μL , the resulting concentration was significantly decreased ($p < 0.01$, $n \geq 4$) to $1.02 \pm 0.38 \mu\text{M}$.

4.3.1.3 Impact of Loading Time

The loading time was analyzed by holding the loading volume (75 μL), initial concentration (15 μM), and flow rate (10 $\mu\text{L}/\text{min}$) constant, while varying the time allotted for flowing concentrated fluorescein (30, 60, and 90 min) (Figure 4.6) through the system. The experiential setup involves 75 μL of DI water in the

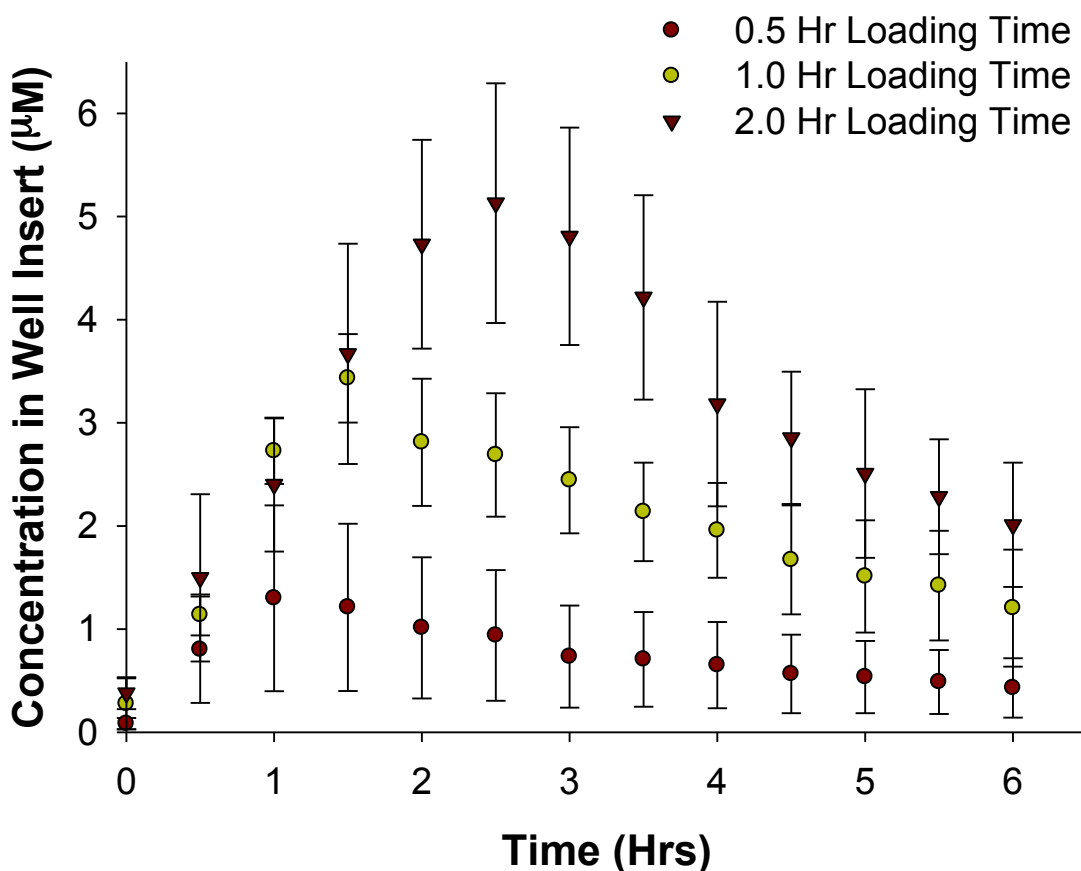


Figure 4.6 Characterization of the Loading Volume in the 3D Printed *In Vitro* PK device. As seen in Figure 4.4, to characterize the loading volume, parameters, such as, flow rate (10 µL/min), initial concentration (15 µM), and loading time (1 hour), were held constant while the loading volume was varied to see the impact on diffusion, specifically the C_{max} . The loading volumes, i.e., 50, 100, 150 µL, yielded PK profiles that indicated the lower the initial volume had a more concentrated C_{max} , while the larger volume was a more diluted sample. $n \geq 4$; $p < 0.01$; error: standard deviation

membrane insert, with 15 μM fluorescein flowing through the channel at 10 $\mu\text{L}/\text{min}$. The variation involves adjusting the time that the concentrated fluorescein is flowing. Increasing the duration of the concentration gradient enables increased time for diffusion of the analyte into the insert. Therefore, the 30 min loading time yielded the shortest time until C_{max} is reached (t_{max}), as well as the lowest C_{max} , $1.29 \pm 0.90 \mu\text{M}$, while the longest loading time, 90 min, resulted in the longest t_{max} , with the most concentrated C_{max} , $5.12 \pm 1.16 \mu\text{M}$.

4.3.1.4 Impact of Initial Concentration

Arguably, the most influential parameter being characterized was the influence of the initial concentration in the channel on the overall C_{max} . Upon changing the concentration of fluorescein flowing through the channels, a direct impact was made on the resulting concentration in the membrane insert (Figure 4.7). In this validation study the loading volume (75 μL), loading time (1 hour), and flow rate (10 $\mu\text{L}/\text{min}$) were held constant, while the initial concentration in the channel was varied (7.5, 15, 30 μM). The detection well contained 75 μL of DI water, while various concentrations of fluorescein were pumped through the channels for an hour before being replaced with DI water. Sampling was identical to previous setups with 5 μL sampled every 30 minutes and diluted with 100 μL of DI water prior to analysis in a plate reader. Upon flowing 7.5 μM fluorescein for an hour, the C_{max} was $1.53 \pm 1.02 \mu\text{M}$, whereas after increasing the channel concentration

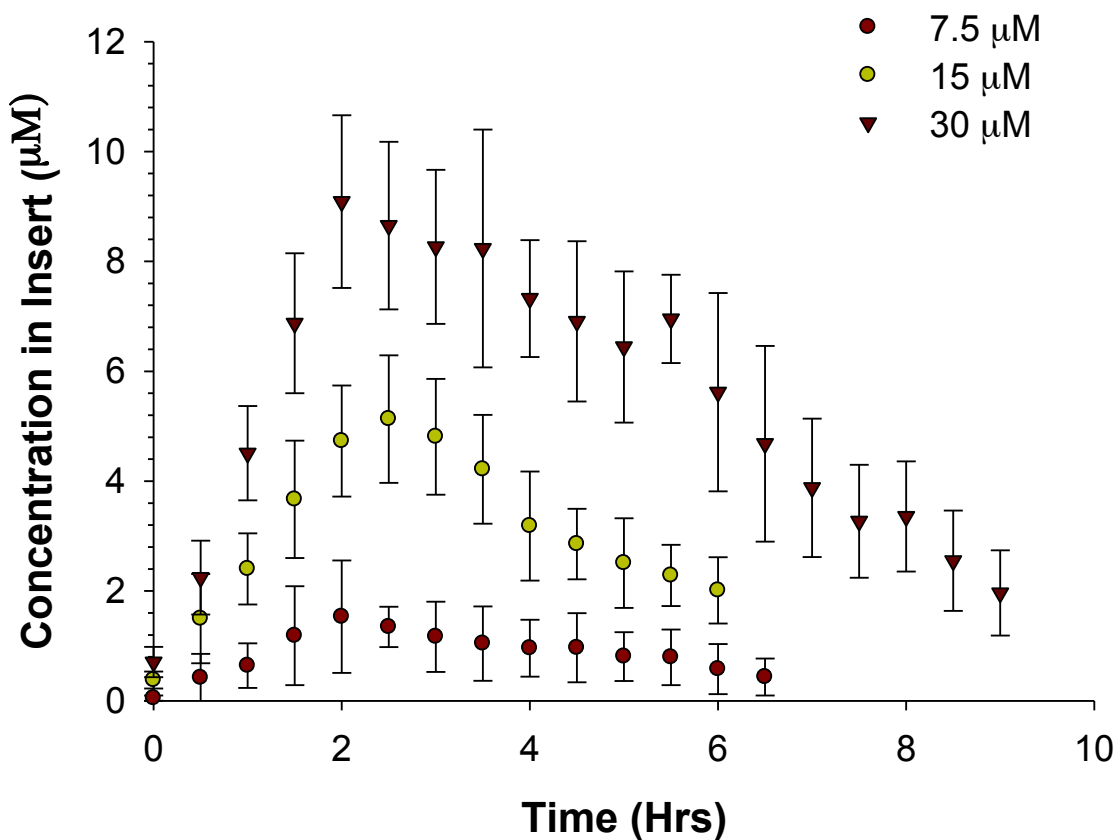


Figure 4.7 Characterization of the Initial Channel Concentration in the 3D Printed *In Vitro* PK Device. To characterize the initial concentration's effect on the C_{max} when various parameters, such as, flow rate (10 $\mu\text{L}/\text{min}$), loading volume (75 μL), and loading time (1 hour), were held constant, the initial volume was varied. The initial concentrations used were 7.5, 15, 30 μM , which resulted in the higher concentration yielding the highest C_{max} and vice versa. $n \geq 3$; $p < 0.01$; error: standard deviation

to 30 μM , the increase in C_{max} was almost 6 fold ($9.09 \pm 1.57 \mu\text{M}$). In section 4.3.1.5, a C_{max} prediction model was formulated using the PK curves obtained in the validation of the initial channel concentration.

4.3.1.5 Prediction Model of Loading Concentration

A prediction model for the concentration along any portion of the loading profile, at a specific time point, was generated by further analysis of the front half of the PK profile in Figure 4.7. The linear slopes correlating to the loading rate of the PK profile were plotted against the initial concentrations (Figure 4.8) with a best fit linear line slope (0.1533) yielding the following prediction model:

$$\text{Initial Concentration} = \frac{\text{Expected Concentration}}{(\text{Loading Time} * \text{Slope})}$$

The initial concentration in the syringe is calculated based on a theoretical expected concentration in the membrane insert at a specific time point. The prediction model was validated in Figure 4.9 by selecting a theoretical expected concentration in the membrane insert of 6.5 μM and varying the loading time (Figure 4.9; Table 4.1). Throughout the loading times (5, 10, 15, 20, 25 μM), samples (5 μL) were taken from the inserts and diluted with 100 μL of DI water. At the completion of the specified loading times, the inserts all contained values that were statistically equivalent to 6.5 μM . Numerical values representing Figure

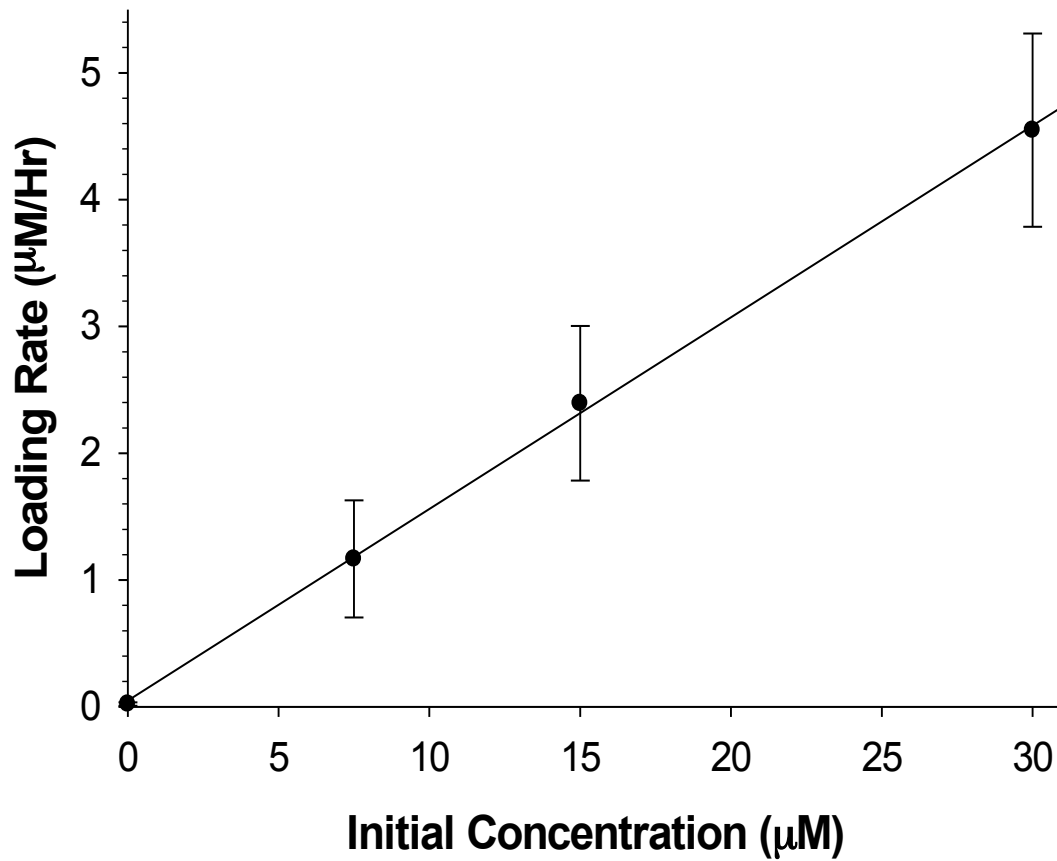


Figure 4.8 Prediction Model for the Concentration along the Loading Portion of the PK Curve. A prediction model was obtained by taking the slope of the loading portion of Figure 4.7 and plotting it against the initial concentration flowed through the channel. The slope of the linear line can be used for a prediction model predicting concentrations at specific time points. $n \geq 3$; error: standard deviation

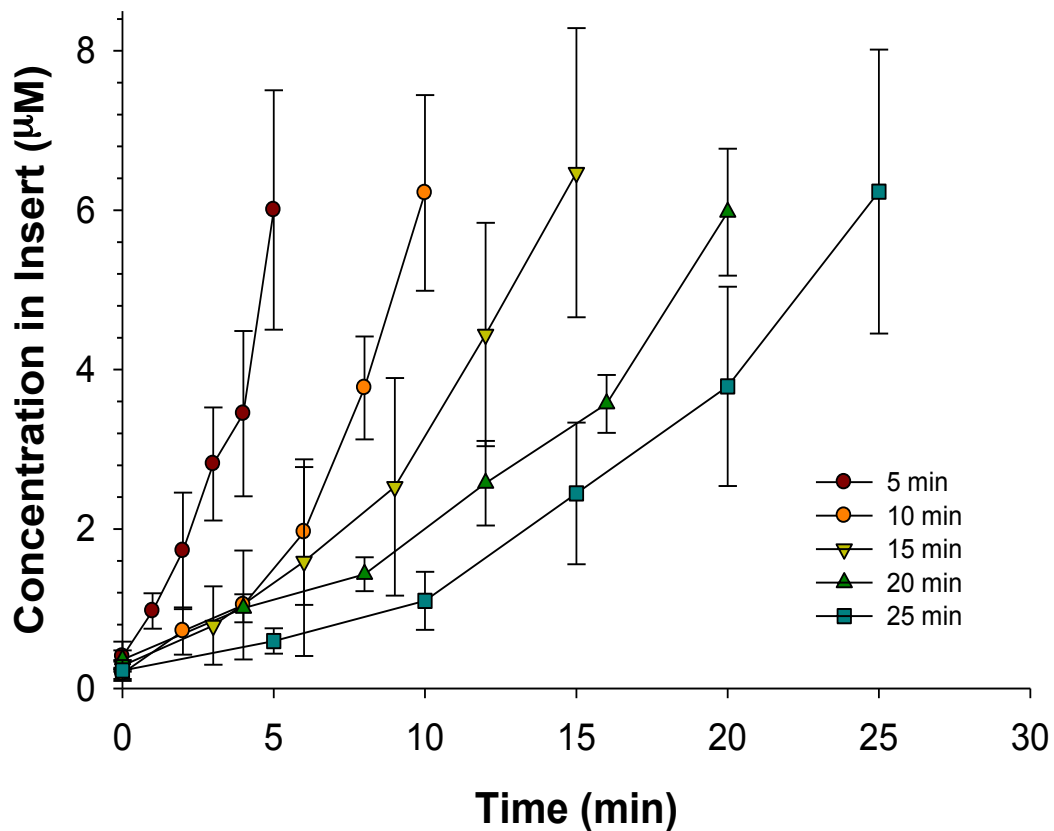


Figure 4.9 Prediction Model for the Concentration along the Loading Portion of the PK Curve Validation. To validate the prediction model, a theoretical C_{max} was set to 6.5 μM and the loading time was varied (5, 10, 15, 20, 25 min) to obtain the initial concentration that will be flowed through the channel. At the specified loading time, the resulting C_{max} was statistically within the theoretical C_{max} . Note, the prediction model was based off of a linear correlation but the curves have a quadratic relationship. $n \geq 4$; $p > 0.05$; error: standard deviation

Loading Time (min)	Initial Conc. (μM)	Exp. C_{max} (μM)	% Error
5	508.8	6.0 ± 1.5	7.6
10	254.4	6.2 ± 1.2	4.3
15	169.3	6.5 ± 1.8	0.8
20	127.3	6.0 ± 0.8	8.1
25	101.8	6.2 ± 1.8	4.0

Table 4.1 Numerical Representation of Parameters Associated with Figure 4.9; Prediction Model Validation. Table is color coded for equation for the concentration based prediction model. Based upon the loading time and a maximum desired concentration the concentration at a certain point can be determine within error. $n \geq 4$; error: standard deviation

4.9 can be found in Table 4.1, as well as the table headings being color coded with the prediction model equation. An interesting observation was the quadratic loading rate relationship observed in Figure 4.9, due to the prediction model being based on a linear relationship.

4.3.1.6 Proof of Concept for Loading Prediction Model

Fluorescein is an ideal molecule for characterization, although to have broad, practical applications for the 3D printed device in the pharmaceutical field, the prediction model needs to be validated with established drugs. Here, an antibiotic, levofloxacin, of similar molecular weight (361.37 g/mol) to fluorescein was utilized to monitor the rugged nature of the prediction model. In Figure 4.10, the desired concentration of fluorescein and levofloxacin was set to 25.6 μM with a loading time of 1 hour, loading volume of 75 μL and a loading concentration of 167.27 μM , which was derived from the prediction model. After 1 hour, the concentrated fluorescein or levofloxacin solutions in the channel were exchanged with water or buffer, respectively. Samples (5 μL) were taken ever 30 minutes from the detection well and prepared in the appropriate manor for either plate reader or mass spectrometry analysis. At 1 hour, the concentrations of both solutions in the membrane insert were within error of the desired concentration, 25.6 μM (fluorescein: $29.23 \pm 5.20 \mu\text{M}$; levofloxacin: $28.26 \pm 7.56 \mu\text{M}$). After the concentrated solution in the channels was replaced with water or buffer the concentration in the insert continued to increase (fluorescein: $36.14 \pm 5.35 \mu\text{M}$;

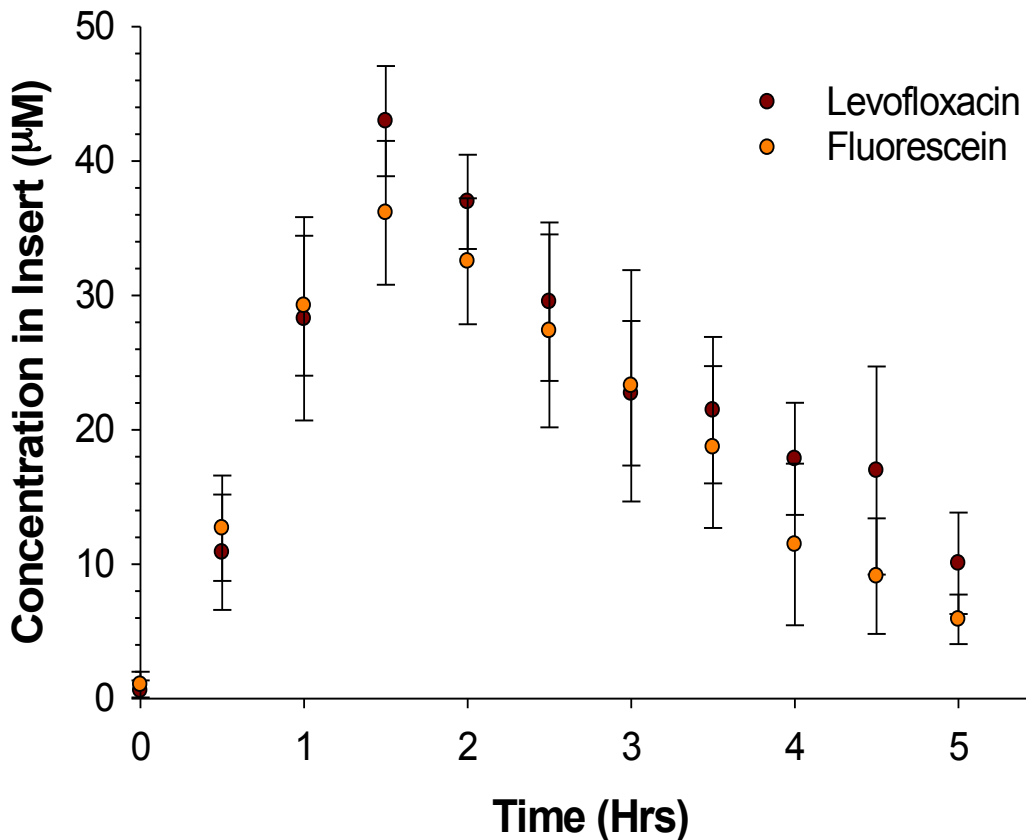


Figure 4.10 Proof of Concept for the Prediction Model for the Concentration along the Loading Portion of the PK Curve. The proof of concept of the prediction model is tested by choosing a drug, which has a molecular mass comparable to that of fluorescein, e.g., levofloxacin. The desired concentration was 25.6 μM with a loading time of 1 hr. The concentration in the syringes, derived from the prediction model for 1 hour of flow was 167.27 μM . The desired concentration was 25.6 μM with a loading time of 1 hr. Experimentally, the fluorescein and levofloxacin were statistically the same and at 1 hour the concentration was within error as the theoretical concentration. Importantly, the experimental C_{max} is $43.0 \pm 4.1 \mu\text{M}$; $n \geq 4$; $p > 0.05$; error: standard deviation

levofloxacin: $42.96 \pm 4.10 \mu\text{M}$), a result of the concentrated solutions absorbing into the sides on the channels within the device. Upon switching to the buffer or water, the concentration gradient reverses. Therefore, the analyte absorbed into the material diffuses back into the channel, thus creating a concentrated solution that continues to add to the concentration in the insert. Therefore, a prediction model based upon the C_{max} was needed to account for the absorbance of the concentrated solutions into the device material.

4.3.1.7 C_{max} Prediction Model

The C_{max} prediction model was formulated by revisiting Figure 4.9. Figure 4.9 was reexamined with emphasis on the quadratic relationship observed in contrast to the initial linear prediction model employed. The concentration in the insert was reassessed by taking the square root of the concentration and plotting the resulting values versus time (Figure 4.11). The resulting lines were indicative of the quadratic relationship, and therefore the slopes of the lines were plotted versus the original concentrations in the syringes (Figure 4.12) to yield a prediction model for the C_{max} of a PK profile.

4.3.1.8 C_{max} Prediction Model Proof of Concept

As a proof of concept, similar to Figure 4.10, levofloxacin was chosen as a comparison to fluorescein (Figure 4.13). The theoretical C_{max} was selected again

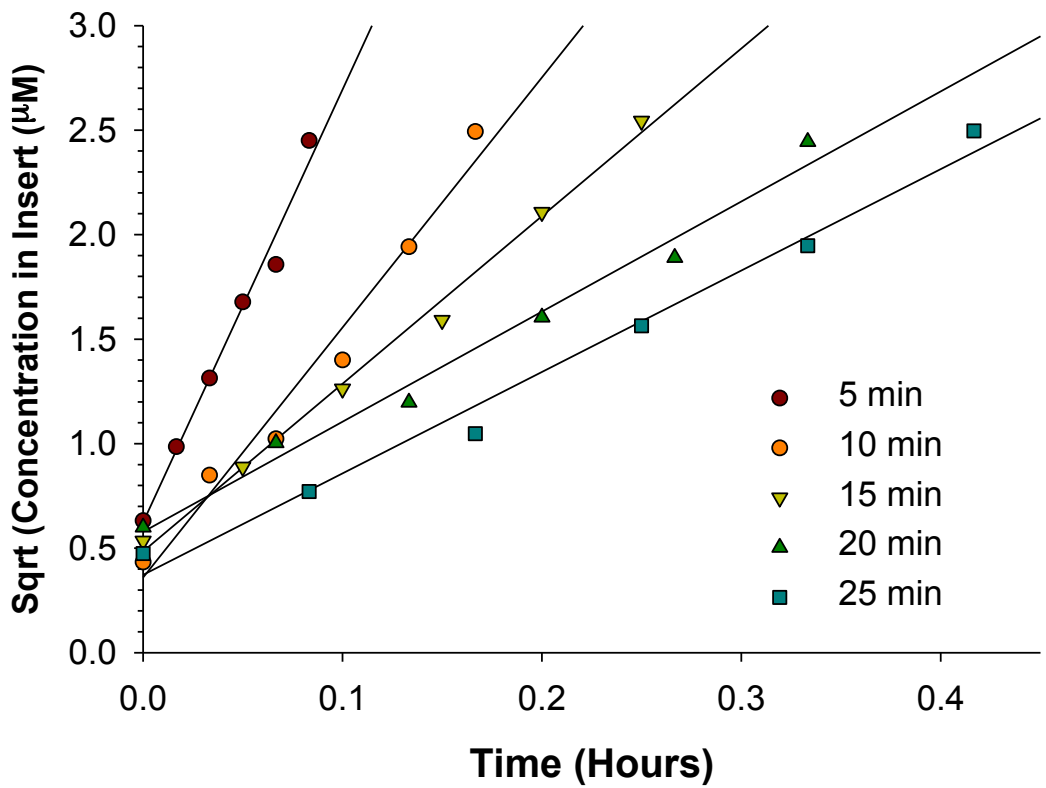


Figure 4.11 Reworking Figure 4.9 to Explore a Quadratic Relationship. The concentrations in the insert, from Figure 4.9, were analyzed for a quadratic relationship by taking the square root of the concentration. The resulting linear lines were indicative of a quadratic relationship and a new prediction model based off this correlation. $n \geq 4$

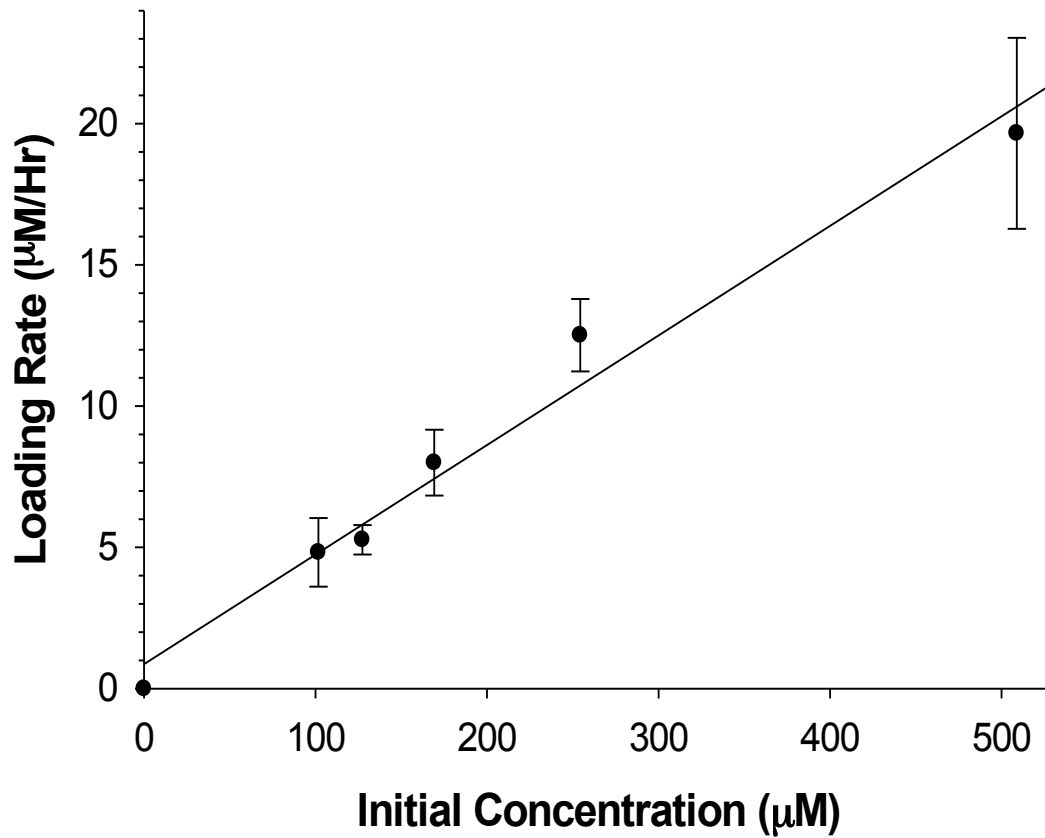


Figure 4.12 Prediction Model for the C_{\max} after a Specific Loading Time. A prediction model was obtained by taking the slope of the linear lines, after taking the square root of the concentration in the insert, in Figure 4.9 and plotting it against the initial concentration flowed through the channel. The resulting slope of the linear line can be used for a prediction model predicting concentrations at specific time points. $n \geq 4$; error: standard deviation

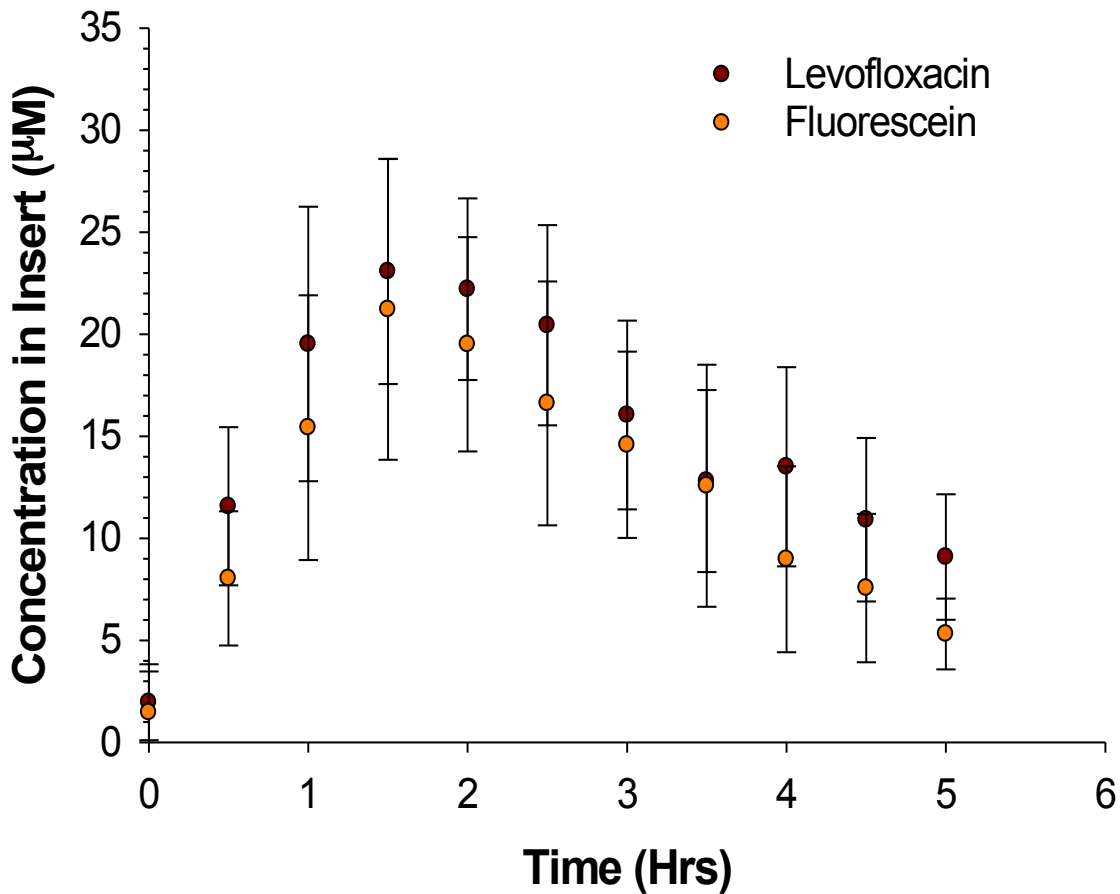


Figure 4.13 Proof of Concept of the Prediction Model for the C_{max} for Specific Loading Times. The proof of concept of the prediction model, similar to that seen in Figure 4.10, used levofloxacin as a comparable molecule to fluorescein. The desired C_{max} was 25.6 μM with a loading time of 1 hr. The concentration in the syringes, derived from the prediction model was 119.28 μM . Experimentally, the fluorescein ($21.21 \pm 7.37 \mu\text{M}$) and levofloxacin ($23.07 \pm 5.42 \mu\text{M}$) were statistically the same as the desired C_{max} . $n \geq 3$; $p > 0.05$. error: standard deviation

to be 25.6 μM with a flow time of 1 hour at 10 $\mu\text{L}/\text{min}$. Derived from the prediction model, the initial loading concentration, in the syringe was 119.28 μM . Both solutions yielded C_{max} concentrations (fluorescein: $21.21 \pm 7.37 \mu\text{M}$; levofloxacin: $23.07 \pm 5.42 \mu\text{M}$) that were within error of the theoretical C_{max} . Interestingly, although both the C_{max} occurred at the target concentration, they reached t_{max} at 1.5 hours despite the concentrated solutions in the channel being swapped with either water or buffer at a loading time of 1 hour.

4.3.2 Characterization of the Elimination Profile

The back half of a PK curve represents the removal of a drug from the body, whether through metabolism or elimination. Almost all drugs represent first order elimination rate kinetics, hence it is crucial that the 3D printed diffusion-based dynamic *in vitro* PK model also mimics this same depletion model. The *in vitro* 3D printed PK model was characterized to validate first order rate kinetics, as well as determination and prediction of the elimination half-life.

4.3.2.1 First Order Rate Kinetic Studies

There are various ways to confirm that the observed elimination follows first order kinetics. The validation involves a slight manipulation of the depletion portion of a PK profile. The natural log of the concentration of the insert is taken

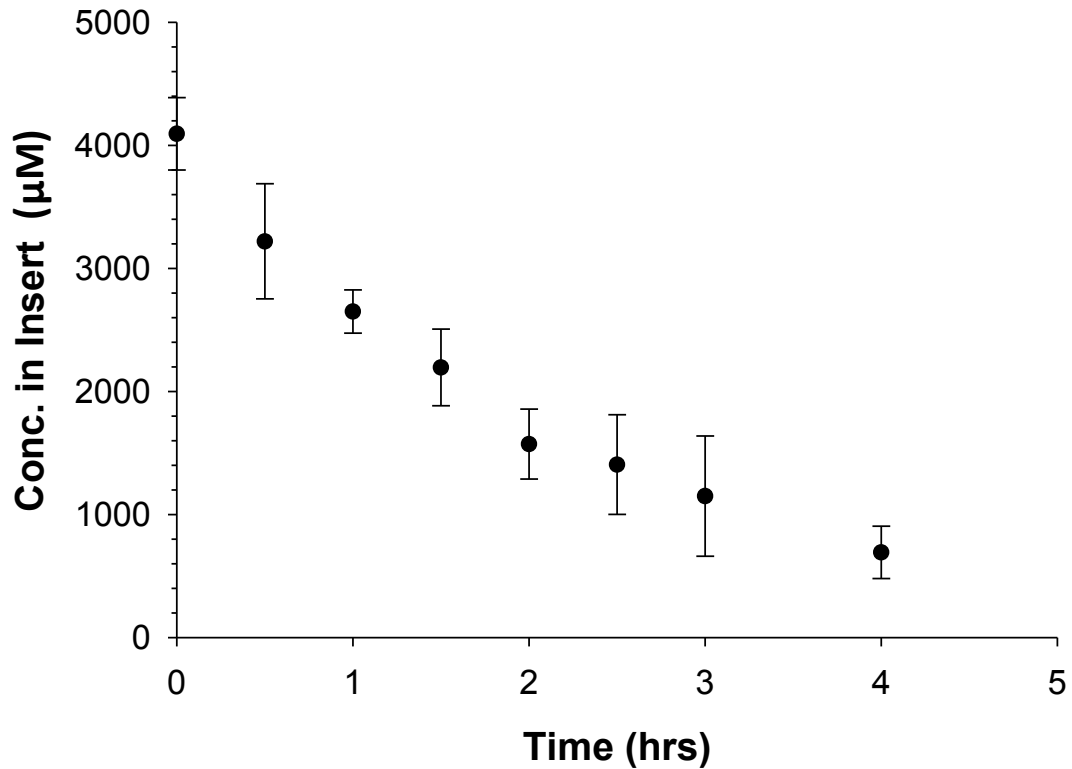


Figure 4.14 Mimicking an IV Dosing PK Profile to Characterize the Elimination Parameters. Loading the insert with 4 µM of fluorescein while flowing DI water through the channel. Every 30 min 5 µL was sampled from the insert, diluted with 100 µL DI water, and analyzed with a plate reader after all samples were taken. n = 4; error: standard deviation

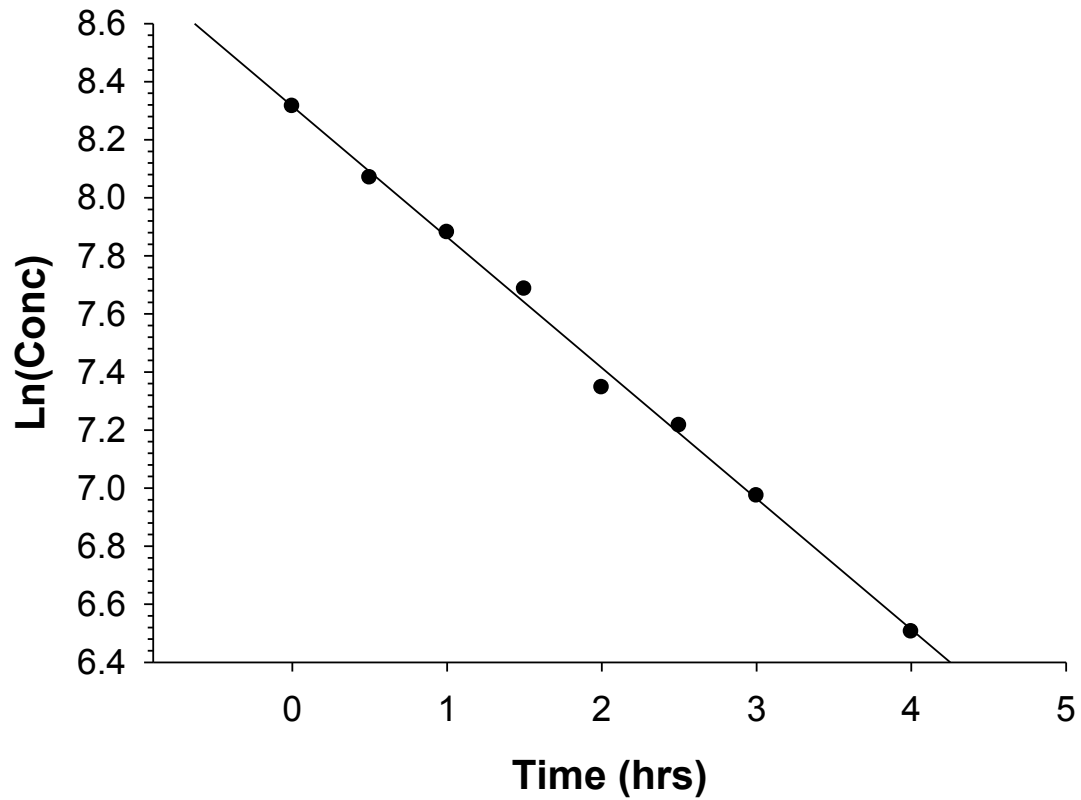


Figure 4.15 Manipulating Figure 4.14 to show First Order Kinetics and Obtain Elimination Rate Constant and Half Life. The natural log was taken of the concentrations in the insert obtained in Figure 4.14 and plotted with respect to time. A linear line is indicative of first order rate kinetics. The slope of the linear line is equivalent to the elimination rate constant (K_{EL}). The half-life is obtained by: $0.693/K_{EL}$. $r^2 = 0.9548$

and plotted against time. A linear curve is indicative of first order kinetics. The slope of the line is equivalent to the elimination rate constant (K_{EL}), which is used to find the half-life ($t_{1/2}$) of the depletion:

$$t_{\frac{1}{2}} = \frac{0.693}{K_{EL}}$$

The half-life denotes the amount of time for a drug to reach half of its C_{max} during elimination. Figure 4.14 shows a representation of an *in vitro* mimic of an intravenous (IV) dosing PK curve obtained on the 3D printed *in vitro* device. A 4 μ M solution of fluorescein (75 μ L) was added to the disposable membrane insert, while DI water was pumped through the channels. Samples (5 μ L) were taken from the membrane insert every 30 minutes for 4 hours and diluted (100 μ L) with DI water and analyzed with a plate reader. The natural log of the concentration in the insert plotted with respect to the time (Figure 4.15) displays a linear line ($r^2 = 0.955$), thus first order kinetics.

The second method for validating first order kinetics involves varying the concentration while monitoring the half-life because it is independent of the initial dosing concentration. As previously described, concentrated fluorescein (2.5, 5.0, 7.5, 10, 15 μ M) was added to the membrane insert (75 μ M), with DI water flowing through the channel. The inserts were sampled every 30 minutes and the

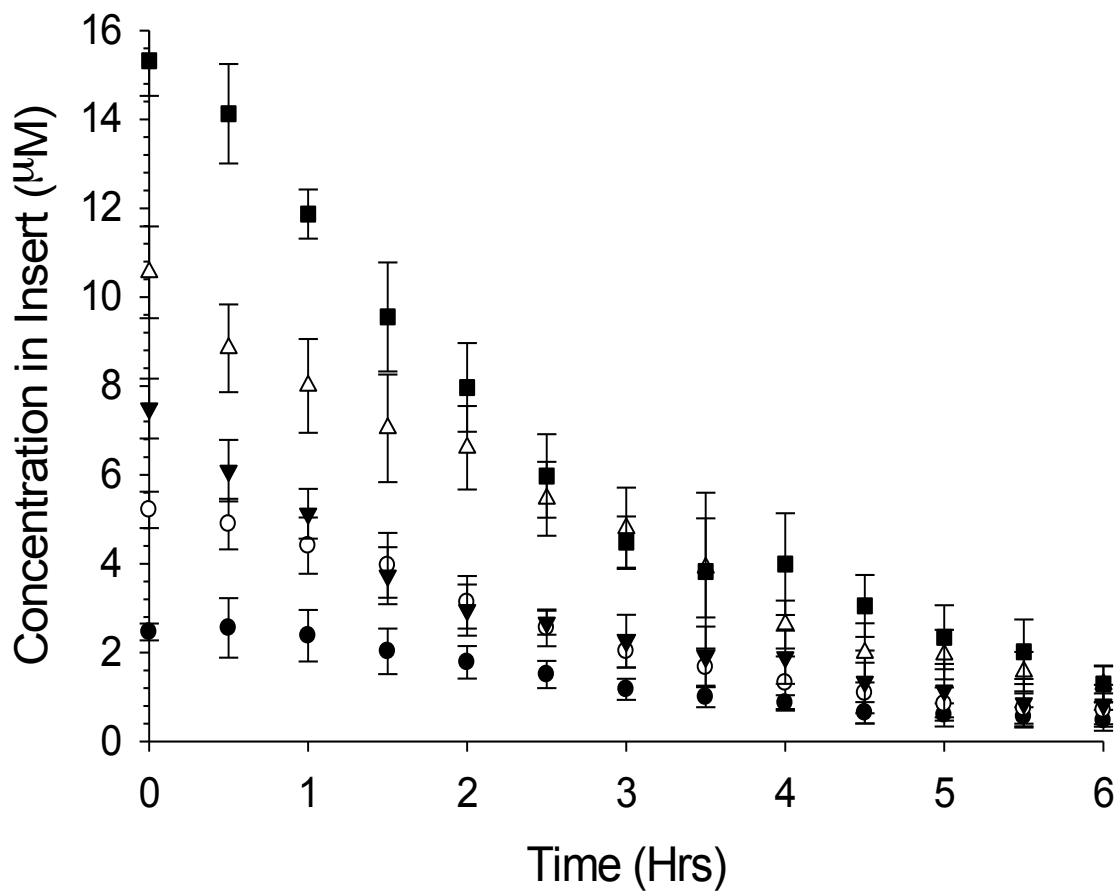


Figure 4.16 Depletion Profiles when Manipulating the Concentration in the Membrane. Various concentrations (2.5, 5.0, 7.5, 10, 15 μM) were added to the membrane insert in the same quantity (75 μL). DI water is flowed at 10 $\mu\text{L}/\text{min}$ through the channel while 5 μL is sampled from the insert every 30 min over 6 hours. $n \geq 4$; error: standard deviation

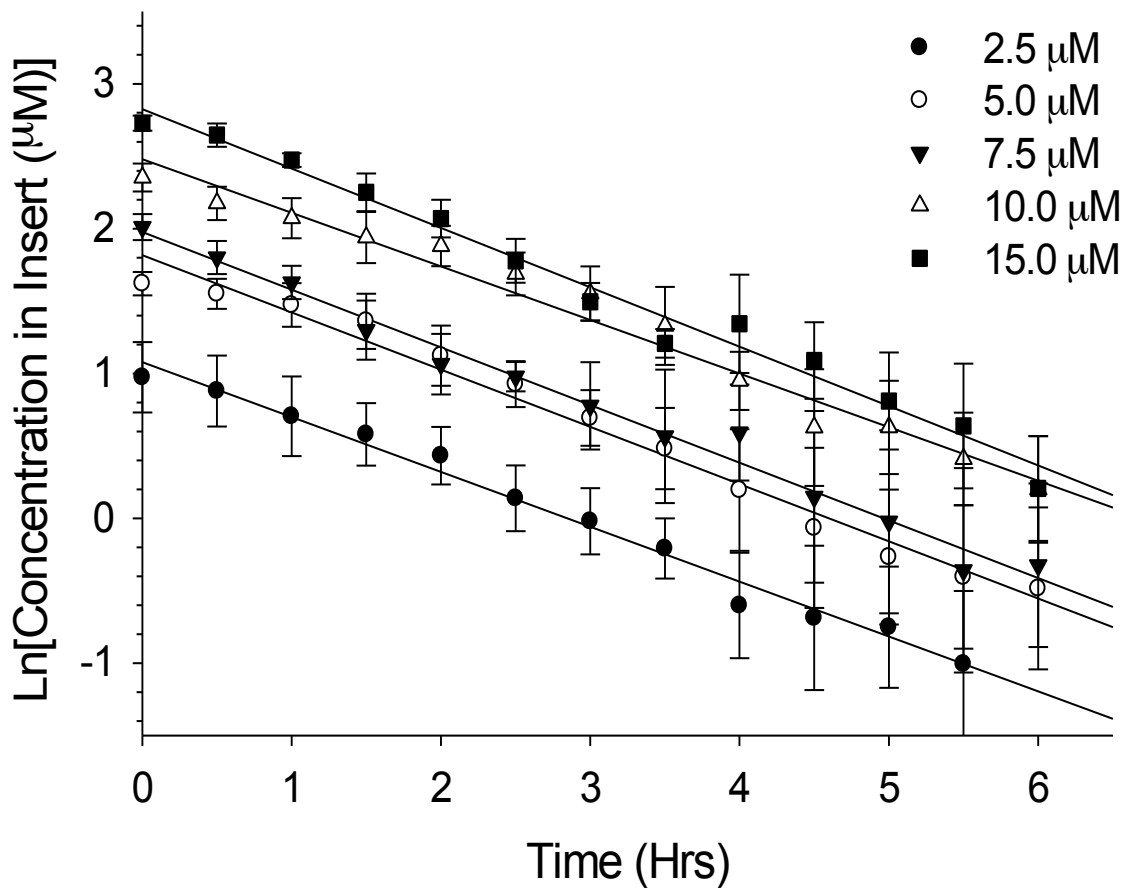


Figure 4.17 Determining the Half-Lives of the Elimination Profiles in Figure 4.16. The natural log is taken of the concentrations in the insert reported in Figure 4.16 and plotted against the time. The slopes of the resulting linear lines is equivalent the elimination rate constant (K_{EL}), from which, the half life can be determined. The half-lives are all statistically the same (numerical representation can be found in Table 4.2), despite having different initial concentrations, which is indicative of first order rate kinetics. $n \geq 4$; $p > 0.05$; error: standard deviation

Concentration in Insert (μM)	$t_{1/2}$ (hrs)*	R ² Value	Slope
2.5	2.23 \pm 0.83	0.9872	-0.351 \pm 0.123
5.0	1.89 \pm 0.77	0.9833	-0.414 \pm 0.132
7.5	1.86 \pm 0.53	0.9866	-0.399 \pm 0.102
10.0	1.91 \pm 0.33	0.9739	-0.376 \pm 0.070
15.0	1.73 \pm 0.27	0.9832	-0.410 \pm 0.074

Table 4.2 Numerical Representation of Figure 4.17. The determination of the half-lives in Figure 4.17 is numerically represented. Information and values relating to the statistically similar half lives, the linear lines (r^2), and the slope of the linear lines used to calculate the half-lives can be found in the table. $n \geq 4$; $p > 0.05$; error: standard deviation.

samples diluted with DI water (100 μL) before analyzing using a plate reader (Figure 4.16). Figure 4.17 is the natural log of the concentrations in the insert from Figure 4.16 with respect to time. All elimination profiles resulted in linear curves, which is indicative of first order kinetics. Moreover, the half-lives obtained from all five concentrations were statistically the same (Table 4.2; $p > 0.05$), i.e., 2.5 μM : 2.23 ± 0.83 hours; 5.0 μM : 1.89 ± 0.77 hours; 7.5 μM : 1.86 ± 0.53 hours; 10.0 μM : 1.91 ± 0.33 hours; 15.0 μM : 1.73 ± 0.27 hours, further indicating first order elimination kinetics occurring within the 3D printed *in vitro* PK model.

4.3.2.2 Manipulation of Half-Lives

Similar to section 3.4.2, the half-life was manipulated in the 3D printed device through the use of gradients, such as mixing the concentrated analyte and DI water in a T-junction to vary the concentration under the membrane insert. Figure 4.17 depicts the gradient set up with 12 syringes, either containing concentrated analyte or DI water, fused silica capillaries, T-junctions and the 3D printed device. Note, the black T-junctions were commercially purchased (approximately \$50 each), while the clear T-junctions were 3D printed for under \$2 each. The gradients incorporated deionized water with concentrated fluorescein (5 μM), which was also added to the membrane insert (75 μL). The beginning gradients were 75% fluorescein, which was achieved by flowing water

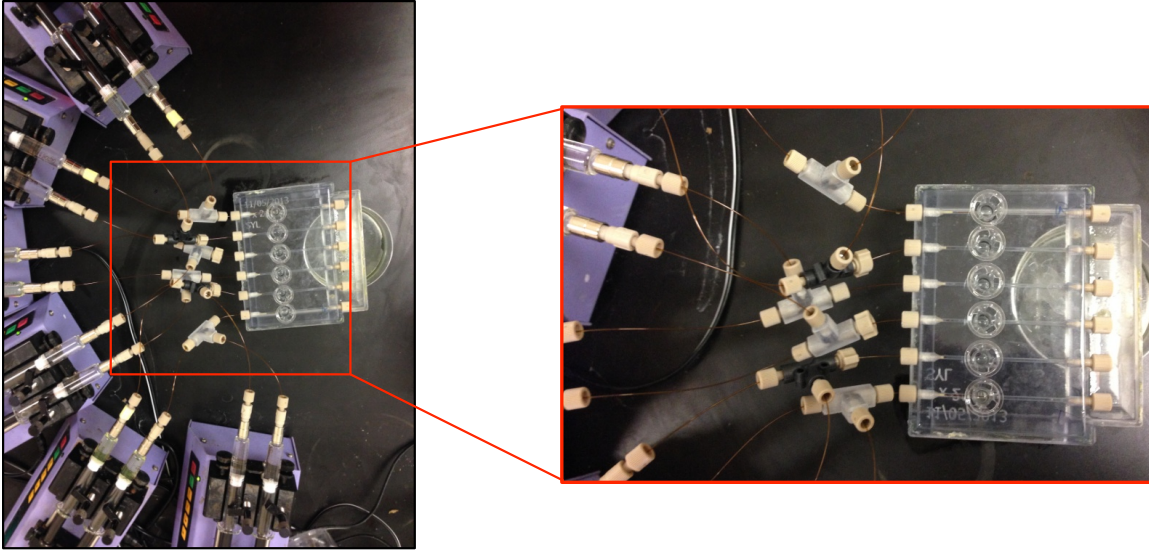


Figure 4.18 Images of Gradient Setup with T-junctions. Left. Image of experimental set up using T-junctions to merge concentrated fluorescein solutions with DI water. Right. Zoomed in image of complex setup of capillaries, T-junctions, and 3D printed device.

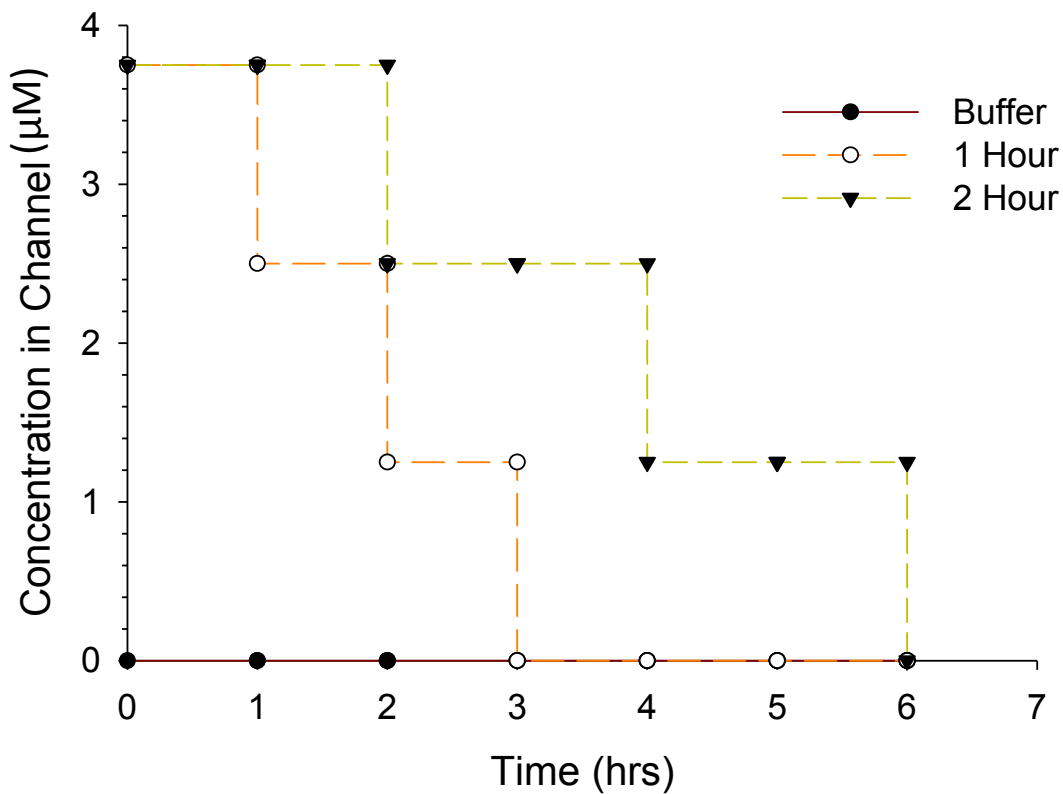


Figure 4.19 Manipulation of Half Life using Gradients Introduced through T-Junction. Using a concentrated fluorescein concentration of 5 μM and deionized water various gradients were achieved through the used of flow rates, e.g., 75%: fluorescein (0.6 $\mu\text{L}/\text{min}$), water (0.2 $\mu\text{L}/\text{min}$); 50%: fluorescein (7.5 $\mu\text{L}/\text{min}$), water (2.5 $\mu\text{L}/\text{min}$); 25%: fluorescein (5.0 $\mu\text{L}/\text{min}$), water (5.0 $\mu\text{L}/\text{min}$); 0%: fluorescein (0 $\mu\text{L}/\text{min}$), water (10 $\mu\text{L}/\text{min}$). The membrane insert contains 75 μL of 5 μM fluorescein. Only buffer is flowed under the membrane insert under the blank depletion. The gradient is changed every hour or every 2 hours in order to manipulate the concentration gradient experienced by the membrane insert. $n \geq 6$; error: standard deviation

at 2.5 $\mu\text{L}/\text{min}$ and fluorescein at 7.5 $\mu\text{L}/\text{min}$. The gradient was held for either a 1 hour or 2 hour segment before being switch to a 50% drug (water: 5.0 $\mu\text{L}/\text{min}$; fluorescein: 5.0 $\mu\text{L}/\text{min}$) for the same allotted time period. The reductions in gradient continue until 0% analyte is reached and held for the duration of the experiment. A graphical representation of the buffer, 1 hour and 2 hour gradients can be seen in Figure 4.19. Throughout the experiment, samples (5 μL) are taken from the insert every half hour, diluted with DI water (100 μL) before being analyzed in a plate reader. The PK profile for blank, 1 hour and 2 hour gradients is found in Figure 4.20. In order to obtain parameters, such as validating first order rate kinetics, elimination rate constants, and half-lives, the natural log of the concentration in the insert versus time (Figure 4.21), is obtained from Figure 4.20. The resulting lines had $r^2 = 0.9707$, 0.9176, and 0.9645 for blank, 1 hour and 2 hour gradients, respectively and were indicative of first order rate kinetics, while the slopes of the aforementioned lines yield the half-lives. The half-life of the blank gradient (1.69 ± 0.45 hours) was significantly different ($p < 0.001$) than the half-lives of the 1 hour (5.55 ± 1.99 hours) and 2 hour (6.11 ± 2.34 hours) gradients. Moreover, the half-lives of the 1 and 2 hour gradients were statistically the same ($p > 0.05$).

Before additional studies were done to attempt to further influence the half-life on this experimental setup the device design was altered. The capillaries

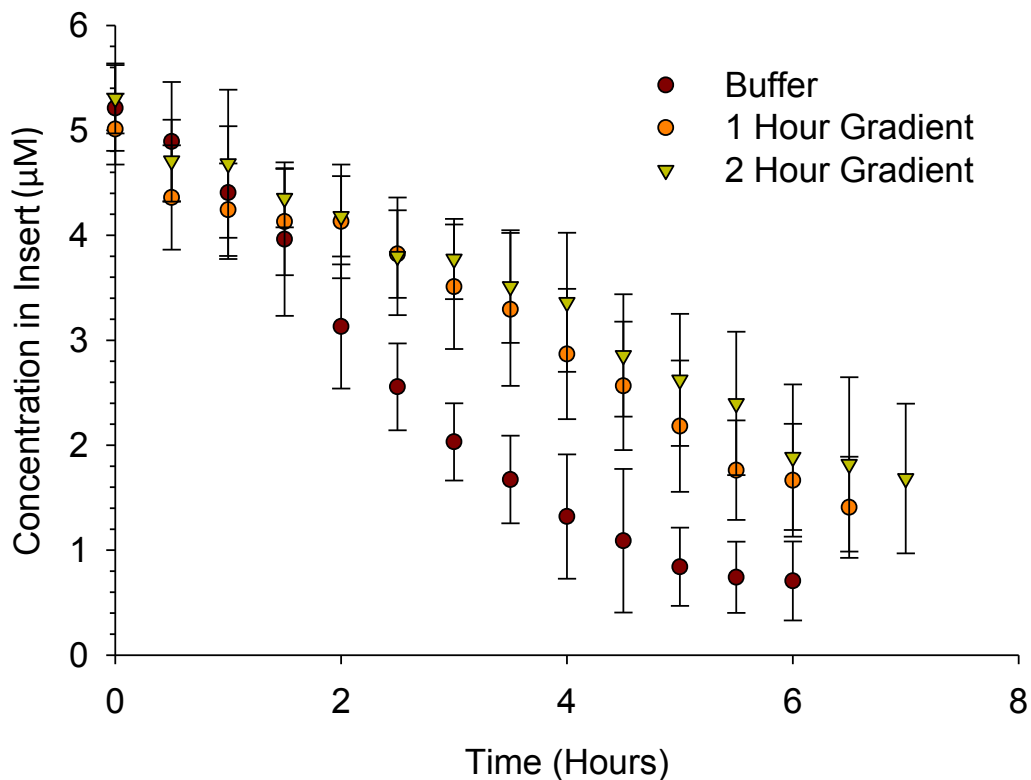


Figure 4.20 Manipulation of Half Life using Gradients Introduced through T-Junction. Using a concentrated fluorescein concentration of 5 µM and deionized water various gradients were achieved through the use of flow rates, e.g., 75%: fluorescein (0.6 µL/min), water (0.2 µL/min); 50%: fluorescein (7.5 µL/min), water (2.5 µL/min); 25%: fluorescein (5.0 µL/min), water (5.0 µL/min); 0%: fluorescein (0 µL/min), water (10 µL/min). The membrane insert contains 75 µL of 5 µM fluorescein. Only buffer is flowed under the membrane insert under the blank depletion. The gradient is changed every hour or every 2 hours in order to manipulate the concentration gradient experienced by the membrane insert. $n \geq 6$; error: standard deviation

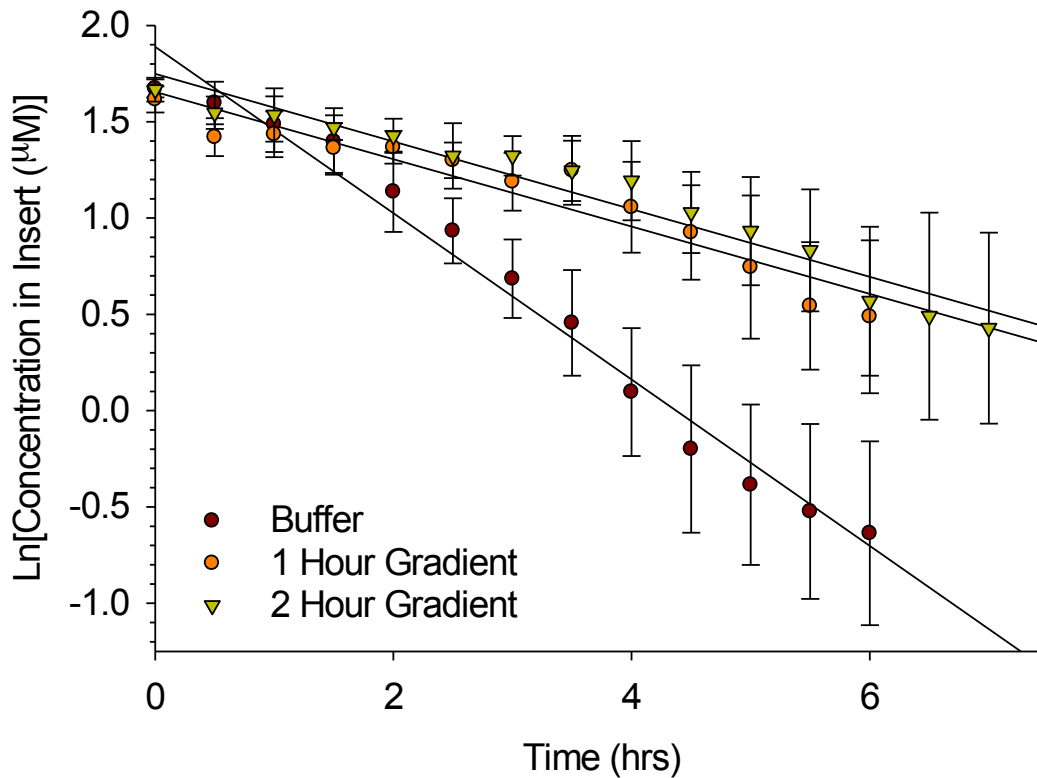


Figure 4.21 Natural Log of Concentration in Insert verse Time Derived from 4.20. The natural log of the concentration in the insert obtained in Figure 4.20, with respect to time yields information such as elimination rate constant, half life, and kinetic order. The three gradients still were first order rate kinetics with linear relationships, i.e., $r^2 = 0.9707$, 0.9176 , and 0.9645 for blank, 1 hour and 2 hour gradients, respectively. A significant difference ($p < 0.001$) in half life was observed between the blank (1.69 ± 0.45 hours) and the 1 (5.55 ± 1.99 hours) and 2 hour (6.11 ± 2.34 hours) gradients, however there was no statistical difference between the 1 and 2 hour gradients ($p > 0.05$). $n \geq 6$; error: standard deviation

used to link the syringes to the T-junction, and then to the 3D printed device were very fragile and would easily break. The new design, featured in Figure 4.22, Figure 2.23 and Figure 4.24, was comprised of a 3D printed Y-channel fabricated in VeroClear with a layer of TangoBlack printed on the end to enhance sealing. Figure 4.23 and Figure 2.24 are schematics of the CAD file illustrating the dimensions of Y-channel. Specifically, Figure 4.23 shows the alterations to the base device to allow the incorporation of the Y-channel at the inlets and outlets. The Y-channel, the CAD schematic shown in Figure 4.24, and fitting holder contains two knobs which fit snugly into notches in the inlets and outlets of the 3D printed devices. The simpler set up allows for easy and quick disassembly of the device from the flow setup that was lacking in previous prototypes.

The first depletion study performed on the locking mechanism device was an exact replication of the depletion study of 5 μM fluorescein performed on the original set up. Figure 4.25 depicts the resulting PK profile when 5 μM fluorescein was added in the membrane insert and exposed to various concentration gradients through the use of manipulating the concentration of fluorescein in the channel. The natural log of the concentration in the insert derived in Figure 4.25 with respect to time (Figure 4.26) portrays a linear relationship for the blank ($r^2 = 0.9067$), 1 hour ($r^2 = 0.9406$), and 2 hour ($r^2 = 0.9877$) gradients. The corresponding half-lives were statistically different

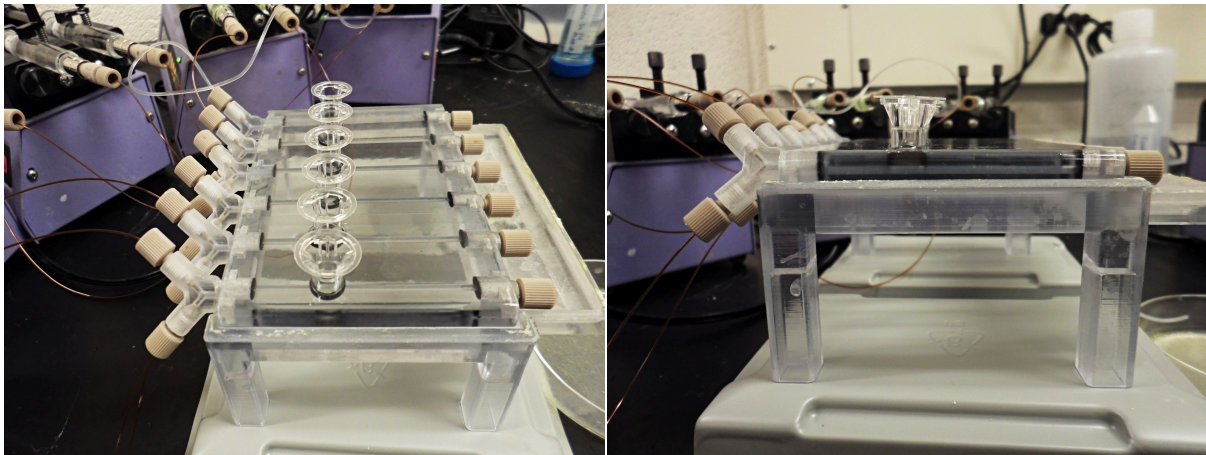
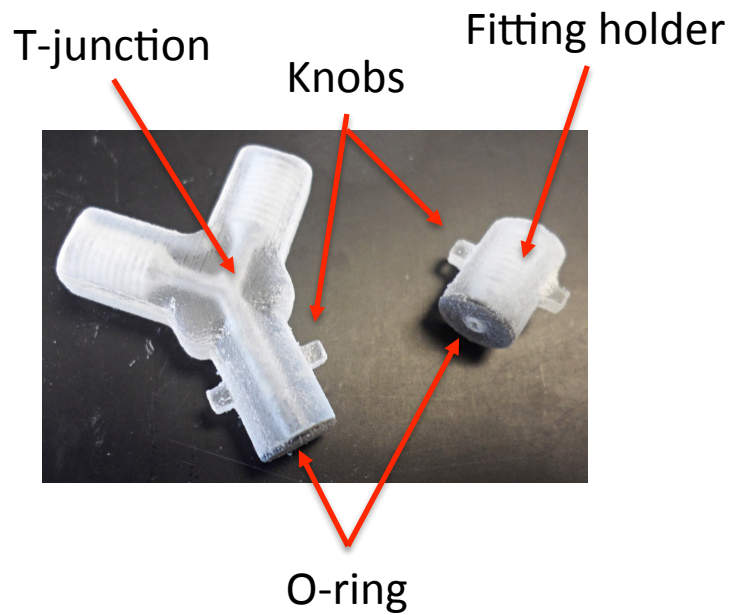


Figure 4.22 Images of 3D Printed T-Junction with Locking Mechanism in 3D Printed Device. Top. 3D printed T-junction and single fitting comprised of VeroClear. Bottom. Images of setup with locking mechanisms, resulting in an overall simplified setup.

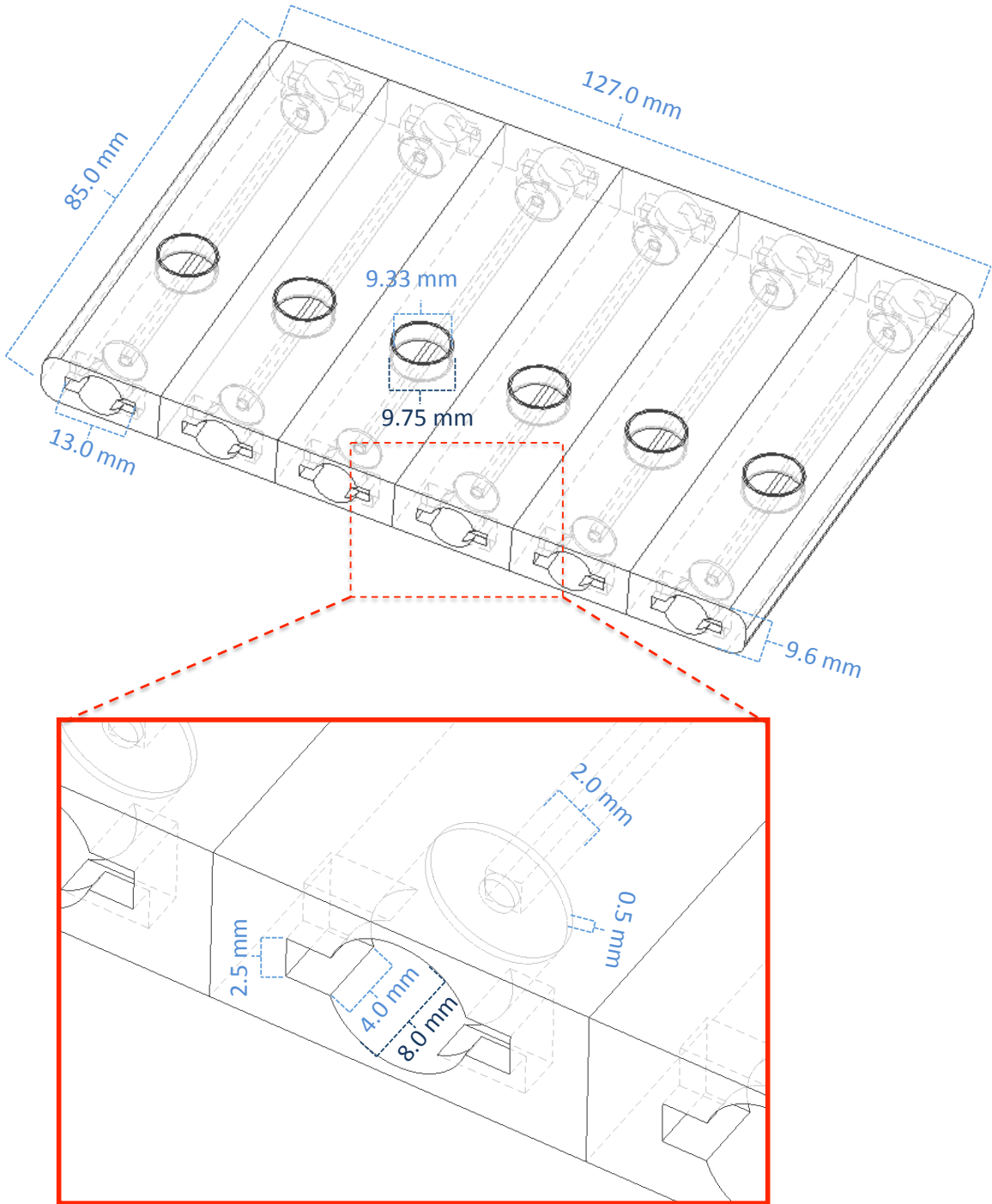


Figure 4.23 Image of the Computer Aided Design File for the Base 3D Printed Device. Schematic of the CAD file for the 3D printed base, along with dimensions. The bottom image is a zoomed in portion of the inlet/outlets of the locking mechanism, with the corresponding dimensions.

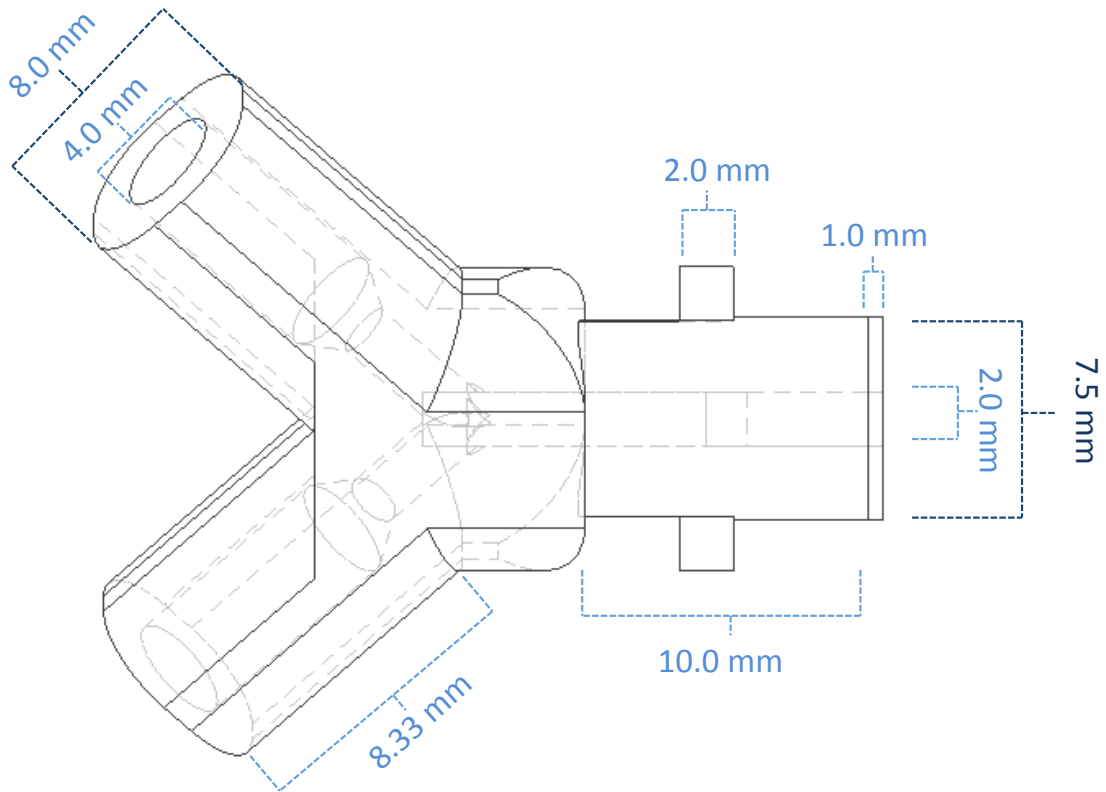


Figure 4.24 Image of the Computer Design File for the 3D Printed Y-Junction. Schematic of the CAD file for the 3D printed Y-junction, along with dimensions.

($p < 0.001$) for the blank (1.78 ± 0.45 hours), 1 hour (3.42 ± 0.79 hours) and 2 hour (6.01 ± 1.44 hours) gradients. The impact on PK profiles in the locking 3D printed device upon increasing the concentration in the insert ($10 \mu\text{M}$) and syringes ($10 \mu\text{M}$) observed in Figure 4.27, with the corresponding natural log of the concentration in the gradient versus time (Figure 2.28) yielding the half-lives of the PK studies. Linear relationships for the three PK profiles were again observed, i.e., blank: 0.9108, 1 hour: 0.9860, and 2 hour gradients: 0.9699. The blank gradient half-life (1.81 ± 0.25 hours), 1 hour gradient (2.73 ± 0.90 hours), and 2 hour gradient (3.30 ± 1.99 hours) were all statistically equal ($p > 0.05$). At this point, it is evident the concentrations in the channel were not as expected, for example, in Figure 4.27 during the 2 hour gradient at the 2 hour mark the concentration in the channel should be $8 \mu\text{M}$, therefore the concentration in the insert should be similar to that of the channel, however, the concentration in the membrane insert at 2 hours is approximately $7 \mu\text{M}$. The absorption of analyte in the channel needs further characterized to obtain a correction factor to account for the missing concentration.

4.3.2.3 Characterization of Analyte Absorption into 3D Printed Material

During the characterization of the loading portion of a PK curve, the actual concentration in the channel is not a significant factor due to the prediction model automatically correcting for any analyte absorption into the device as a result of

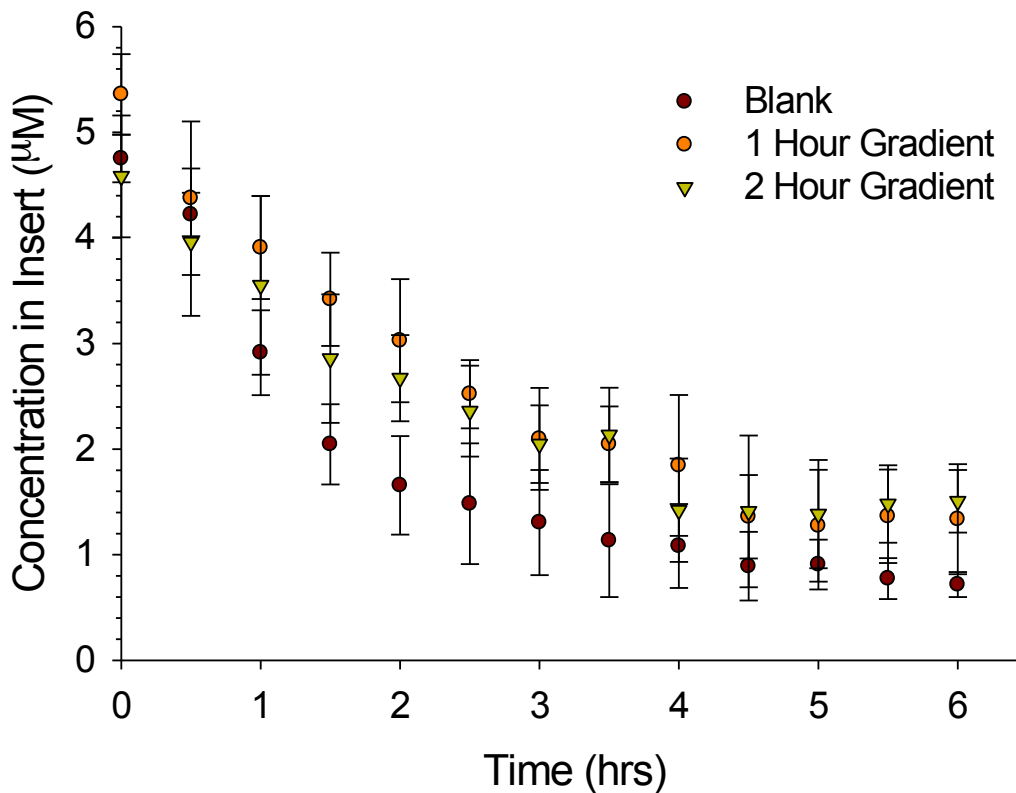


Figure 4.25 Manipulation of Half Life using Gradients Introduced through Locking Mechanism T-Junction (5 µM). Similar to the original set up, however, t-junctions were directly incorporated into the 3D printed devices using a locking mechanism. The same concentrated fluorescein (5 µM) was used in the membrane insert (75 µL), as well as in the syringes with deionized water to introduce various gradients achieved through the used of flow rates, e.g., 75%: fluorescein (0.6 µL/min), water (0.2 µL/min); 50%: fluorescein (7.5 µL/min), water (2.5 µL/min); 25%: fluorescein (5.0 µL/min), water (5.0 µL/min); 0%: fluorescein (0 µL/min), water (10 µL/min). Only buffer is flowed under the membrane insert under the blank depletion. The gradient is changed every hour or every 2 hours in order to manipulate the concentration gradient experienced by the membrane insert. $n \geq 6$; error: standard deviation

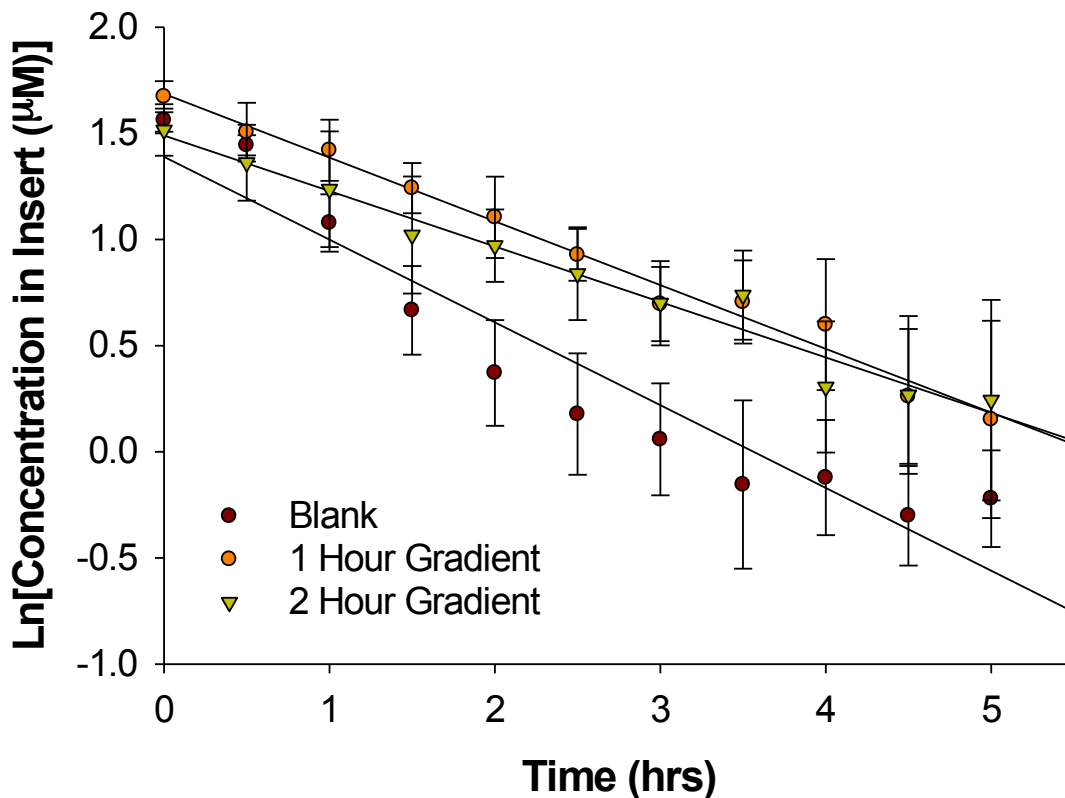


Figure 4.26 Natural Log of Concentration in Insert versus Time Derived from 4.25 (5 μM). Similar to Figure 4.21, the natural log of the concentration in the insert obtained in Figure 4.25, with respect to time yields information such as elimination rate constant, half life, and kinetic order. The three gradients still were first order rate kinetics with linear relationships, i.e., $r^2 = 0.9067, 0.9406, \text{ and } 0.9877$ for blank, 1 hour and 2 hour gradients, respectively. A significant difference ($p < 0.001$) in half-life was observed between the blank (1.78 ± 0.45 hours), 1 hour (3.42 ± 0.79 hours) and 2 hour (6.01 ± 1.44 hours) gradients. $n \geq 6$; error: standard deviation

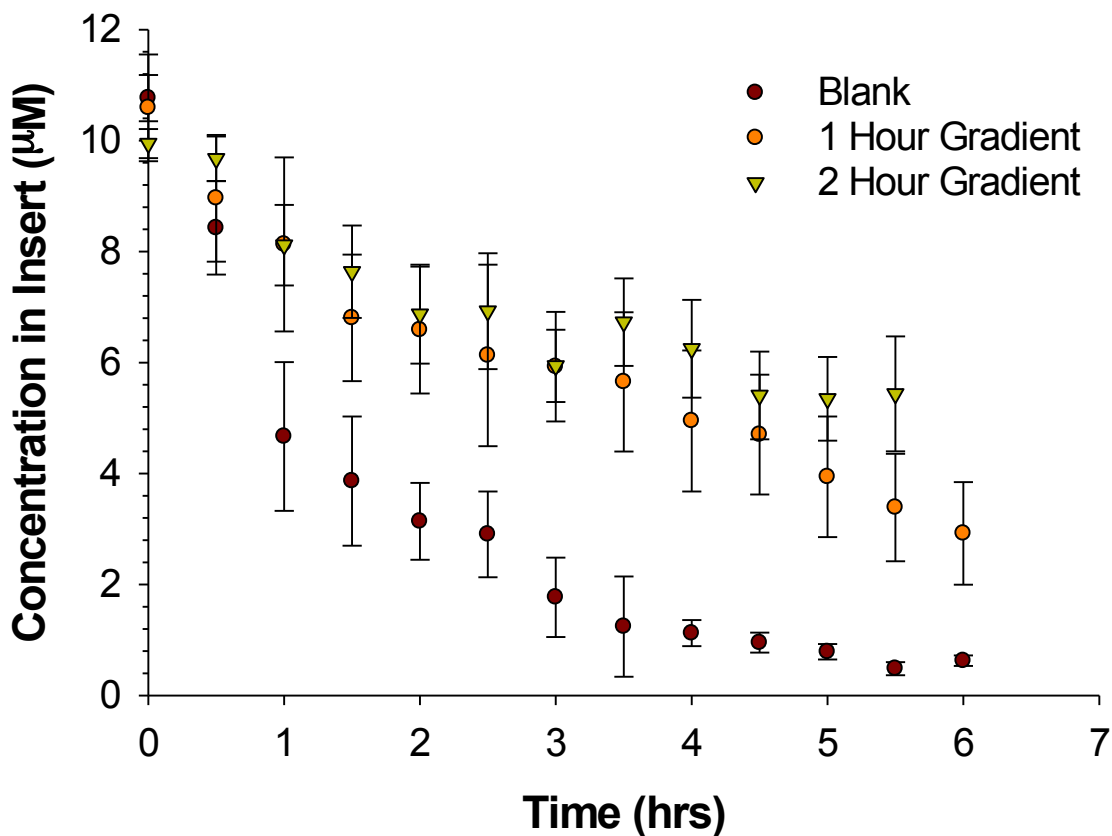


Figure 4.27 Manipulation of Half Life using Gradients Introduced through Locking Mechanism T-Junction (10 µM). Similar to the experimental set up with the t-junctions being directly incorporated into the 3D printed devices using a locking mechanism. An increased concentrated fluorescein (10 µM) was used in the membrane insert (75 µL), as well as in the syringes with deionized water to introduce various gradients achieved through the used of flow rates, e.g., 75%: fluorescein (0.6 µL/min), water (0.2 µL/min); 50%: fluorescein (7.5 µL/min), water (2.5 µL/min); 25%: fluorescein (5.0 µL/min), water (5.0 µL/min); 0%: fluorescein (0 µL/min), water (10 µL/min). Only buffer is flowed under the membrane insert under the blank depletion. The gradient is changed every hour or every 2 hours in order to manipulate the concentration gradient experienced by the membrane insert.

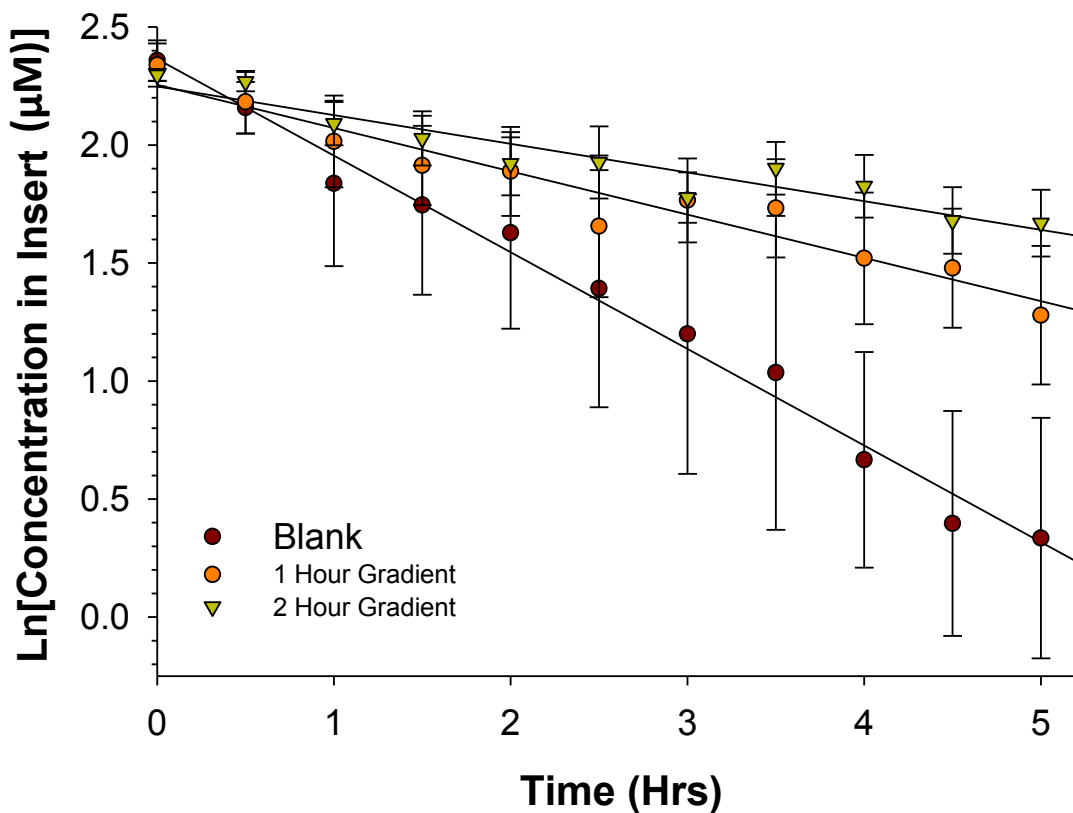


Figure 4.28 Natural Log of Concentration in Insert verse Time Derived from 4.27 (10 μM). Similar to Figure 4.21, the natural log of the concentration in the insert obtained in Figure 4.27, with respect to time yields information such as elimination rate constant, half-life, and kinetic order. The three gradients still were first order rate kinetics with linear relationships, i.e., $r^2 = 0.9108, 0.9860,$ and 0.9699 for blank, 1 hour and 2 hour gradients, respectively. No significant difference ($p > 0.05$) in half-life was observed between the blank (1.81 ± 0.25 hours), 1 hour (2.73 ± 0.90 hours) and 2 hour (3.30 ± 1.99 hours) gradients. $n \geq 6$; error: standard deviation

the absorption being uniform throughout and as such is factored into the calibration basis of the prediction models. However, the actual concentration in the channel under the detection well is critical for the depletion portion. When manipulating the half-life, the actual concentration directly below the membrane plays a pertinent role in the rate of diffusion. As mentioned in section 4.3.2.1, half-lives are independent of initial concentration, therefore as discussed in section 3.2.4, the concentration of analyte in the channel is varied in a gradient to directly affect the concentration gradient and subsequent diffusion rate.

In Figure 4.29, various concentrations of fluorescein (2.5, 5.0, 7.5, 25, 50, 75, 100 μM) were flowed at 10 $\mu\text{L}/\text{min}$ for 1 hour and sampled directly from the open well lacking the membrane insert. The concentrations of fluorescein in the well were 45-60% less than the initial concentration in the syringe, thereby signifying that the fluorescein was partially absorbing into the channel walls. The concentrations in the well were plotted against the initial concentration in the syringe to form a linear relationship ($r^2 = 0.9975$). The resulting slope (0.5772) was used to formulate the following correction factor to account for loss of fluorescein due to absorption into the device:

$$\textit{Desired Concentration in Well} = \textit{Slope} * \textit{Initial Concentration in Insert}$$

A proof of concept for the correction model was shown in Table 4.3. Initially, concentrations of 2.5, 5.0 and 7.5 μM were pumped through the channels and

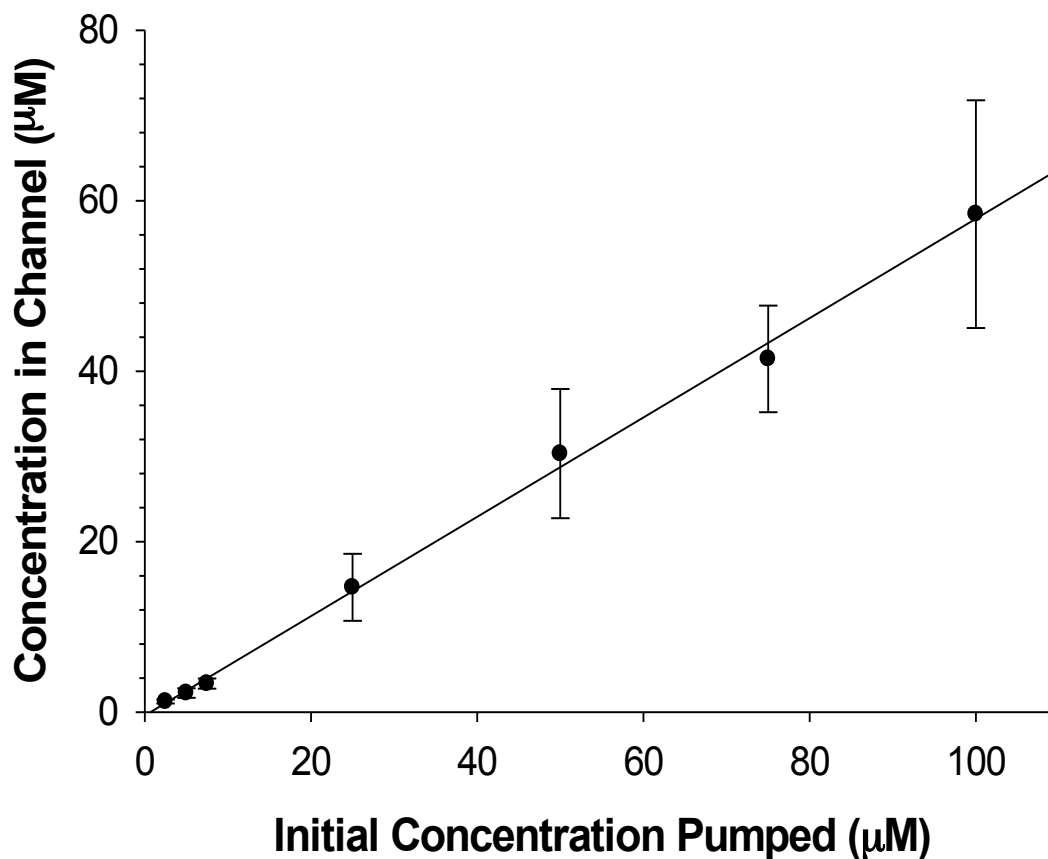


Figure 4.29 Absorbance of Fluorescein into the Device Channels and Correction Factor for Expected Concentration. Various concentrations of fluorescein (2.5-100 μM) were flowed through the channels for an hour and sampled (5 μL). Samples were diluted with 100 μL of DI water analyzed in a plate reader. The resulting concentrations were plotted against the initial concentrations and a best fit linear line drawn through the lines ($r^2= 0.9975$; slope = 0.5772). From the aforementioned line a concentration correction factor can be made from the resulting slope (Concentration in Well = Slope*Initial Concentration), therefore, if a concentration of 2.5 μM was desired in the well a concentration of 4.33 μM would need to the initial concentration. $n \geq 3$; error: standard deviation

Concentrations (μM)			
Desired	Previous Experimental	Corrected Initial	Corrected Experimental
2.5	1.25 ± 0.22	4.33	2.97 ± 0.50
5.0	2.24 ± 0.56	8.66	4.66 ± 0.45
7.5	3.35 ± 0.60	12.99	7.89 ± 1.42

Table 4.3 Absorbance of Fluorescein into the Channel Correction Factor Proof of Concept. Based on the correction factor correcting the concentration of fluorescein in the channel to account for absorption into the channel, derived in Figure 4.17, specific concentrations are flowed through the channel and sampled (5 μL) in the open well. The original initial concentrations (2.5, 5.0, 7.5 μM) fluorescein yielded concentrations under the well of 1.25 ± 0.22 , 2.24 ± 0.56 , and 3.35 ± 0.60 , respectively. The loss of concentration from the syringe to the well indicates that fluorescein is absorbing into the walls of the channel. From Figure 4.17, the initial concentrations were corrected (4.33, 8.66, 12.99 μM) to result in theoretical concentrations under the well of 2.5, 5.0, 7.5 μM , respectively. The resulting values were statistically the same as the theoretical values (2.97 ± 0.50 , 4.66 ± 0.45 , 7.98 ± 1.42). $n \geq 4$; $p > 0.05$; error: standard deviation

the resulting concentration in the wells were 1.25 ± 0.22 , 2.24 ± 0.56 , 3.35 ± 0.60 μM , respectively. After the correction model was implemented for desired well concentrations of 2.5, 5.0, and 7.5 μM , the initial concentrations in the syringes were 4.33, 8.66, and 12.99 μM , respectively. After flowing the previously mentioned concentrations for 1 hour at 10 $\mu\text{L}/\text{min}$, samples (5 μL) were taken from the well, diluted with 100 μL of DI water, and analyzed in a plate reader. The resulting concentrations (2.97 ± 0.50 , 4.66 ± 0.45 , and 7.89 ± 1.42 μM , respectively) were, within error, the same as the desired concentrations. The correction model allows the concentration in the channel and subsequently the gradients to be precisely controlled, therefore the manipulation of the half-lives is able to be better regulated. Upon varying the half-lives, potential mathematical relationships would need to be explored to formulate a prediction model for the half-lives.

Thus far, various parameters of the 3D printed diffusion-based dynamic *in vitro* PK model were studied, such as the impact of the flow rate, loading volume, loading time, and initial volume. Prediction models were formulated for the concentration along the loading portion of the PK profile, as well as for the C_{max} , based upon the PK profiles obtained during the characterization of the initial volume in the channels. Due to half-lives being independent to initial dosing, first order rate elimination in the device was confirmed during the elimination portion of the PK profile. Upon characterizing a correction factor to account for the

amount of analyte absorbed by the device material, accurate gradient are able to be employed to manipulate the half life. Furthermore, a prediction model for the half-life, obtained from the gradient studies, will complete the characterization of the reusable, 3D printed *in vitro* model.

REFERENCES

REFERENCES

- (1) Gross, B. C.; Erkal, J. L.; Lockwood, S. Y.; Chen, C.; Spence, D. M.: An Evaluation of 3D Printing and its Potential Impact on Biotechnology and the Chemical Sciences. *Analytical chemistry* **2014**.
- (2) Waldbaur, A.; Rapp, H.; Lange, K.; Rapp, B. E.: Let there be chip-towards rapid prototyping of microfluidic devices: one-step manufacturing processes. *Analytical Methods* **2011**, *3*, 2681-2716.
- (3) Shepherd, J. N. H.; Parker, S. T.; Shepherd, R. F.; Gillette, M. U.; Lewis, J. A.; Nuzzo, R. G.: 3D microperiodic hydrogel scaffolds for robust neuronal cultures. *Adv. Funct. Mater.* **2011**, *21*, 47.
- (4) Lee, W.; Lee, V.; Polio, S.; Keegan, P.; Lee, J. H.; Fischer, K.; Park, J. K.; Yoo, S. S.: On-demand three-dimensional freeform fabrication of multi-layered hydrogel scaffold with fluidic channels. *Biotechnol. Bioeng.* **2010**, *105*, 1178.
- (5) Lee, Y. B.; Polio, S.; Lee, W.; Dai, G. H.; Menon, L.; Carroll, R. S.; Yoo, S. S.: Bio-printing of collagen and VEGF-releasing fibrin gel scaffolds for neural stem cell culture. *Exp. Neurol.* **2010**, *223*, 645.
- (6) Butscher, A.; Bohner, M.; Hofmann, S.; Gauckler, L.; Muller, R.: Structural and material approaches to bone tissue engineering in powder-based three-dimensional printing. *Acta Biomater.* **2011**, *7*, 907.
- (7) Stampfl, J.; Liska, R.: New materials for rapid prototyping applications. *Macromol. Chem. Phys.* **2005**, *206*, 1253.
- (8) Rangel, D. P.; Superak, C.; Bielschowsky, M.; Farris, K.; Falconer, R. E.; Baveye, P. C.: Rapid Prototyping and 3-D Printing of Experimental Equipment in Soil Science Research. *Soil Sci. Soc. Am. J.* **2012**, *77*, 54.
- (9) Erkal, J. L.; Selimovic, A.; Gross, B. C.; Lockwood, S. Y.; Walton, E. L.; McNamara, S.; Martin, R. S.; Spence, D. M.: 3D printed microfluidic devices with integrated versatile and reusable electrodes. *Lab on a Chip* **2014**, *14*, 2023-2032.
- (10) Ahn, B. Y.; Duoss, E. B.; Motala, M. J.; Guo, X. Y.; Park, S. I.; Xiong, Y. J.; Yoon, J.; Nuzzo, R. G.; Rogers, J. A.; Lewis, J. A.: Omnidirectional printing of flexible, stretchable, and spanning silver microelectrodes. *Science* **2009**, *323*, 1590.

(11) Anderson, K. B.; Lockwood, S. Y.; Martin, R. S.; Spence, D. M.: A 3D Printed Fluidic Device that Enables Integrated Features. *Analytical Chemistry* **2013**.

(12) Kitson, P. J.; Rosnes, M. H.; Sans, V.; Dragone, V.; Cronin, L.: Configurable 3D-printed millifluidic and microfluidic 'lab on a chip' reactionware devices. *Lab on a Chip* **2012**, *12*, 3267-3271.

(13) Mathieson, J. S.; Rosnes, M. H.; Sans, V.; Kitson, P. J.; Cronin, L.: Continuous parallel ESI-MS analysis of reactions carried out in a bespoke 3D printed device. *Beilstein Journal of Nanotechnology* **2013**, *4*, 285-291.

(14) Ilievski, F.; Mazzeo, A. D.; Shepherd, R. E.; Chen, X.; Whitesides, G. M.: Soft robotics for chemists. *Angew. Chem., Int. Ed.* **2011**, *50*, 1890.

(15) Hull, C. W.: Apparatus for production of three-dimensional objects by stereolithography. Patent, U. S., Ed.; UVP Inc. San Gabriel Calif.: United States, 1986; Vol. 4575330.

(16) Hull, C. W.: Method for production of three-dimensional objects by stereolithography. US, 1990; Vol. 07340894.

(17) Charles W. Hull, S. T. S., Charles W. Lewis, Wayne A. Vinson, Raymond S. Freed, Dennis R. Smalley: Method of and apparatus for production of three-dimensional objects by stereolithography with reduced curl. US, 1992; Vol. 07339246.

(18) Hull, C. W.: Method of and apparatus for production of three dimensional objects by stereolithography. US, 1993; Vol. 07840630.

(19) Hull, C. W.; Spence, S. T.; Albert, D. J.; Smalley, D. R.; Harlow, R. A.; Stinebaugh, P.; Tarnoff, H. L.; Nguyen, H. D.; Lewis, C. W.; Vorgitch, T. J.; Remba, D. Z.: Method and apparatus for production of high resolution three-dimensional objects by stereolithography. US, 1993; Vol. 07331644.

(20) Hull, C. W.; Spence, S. T.; Lewis, C. W.; Vinson, W.; Freed, R. S.; Smalley, D. R.: Stereolithographic curl reduction. US, 1993; Vol. 07868462.

(21) Hull, C. W.; Leyden, R. N.; Sekowski, M.: Methods of coating stereolithographic parts. US, 1993; Vol. 07929463.

(22) Hull, C. W.; Jacobs, P. F.; Schmidt, K. A.; Smalley, D. R.; Vinson, W. A.: Apparatus for building three-dimensional objects with sheets. US, 1993; Vol. 07803681.

(23) 3DSystems: 30 Years of Innovation. 2013; Vol. September 27, 2013.

(24) Dolenc, A.; Mäkelä, I.: Slicing procedures for layered manufacturing techniques. *Computer-Aided Design* **1994**, *26*, 119-126.

(25) Duffy, D. C.; McDonald, J. C.; Schueller, O. J.; Whitesides, G. M.: Rapid Prototyping of Microfluidic Systems in Poly(dimethylsiloxane). *Analytical chemistry* **1998**, *70*, 4974-84.

(26) McDonald, J. C.; Duffy, D. C.; Anderson, J. R.; Chiu, D. T.; Wu, H.; Schueller, O. J. A.; Whitesides, G. M.: Fabrication of topologically complex three-dimensional microfluidic systems in PDMS by rapid prototyping. *Electrophoresis* **2000**, *21*, 27.

CHAPTER 5

FUTURE DIRECTIONS

5.1 Applications for Diffusion Based Dynamic *In Vitro* Pharmacokinetic Model

Thus far, the 3D printed diffusion based dynamic *in vitro* PK/PD model has had various parameters characterized, such as loading time, initial volume, maximum concentration, flow rate, and establishment of first order kinetics. Prediction models regarding magnitude and timing of the maximum concentrations have been formulated, as well as, proof of concepts obtained through the use of an antibiotic of similar molecular weight. However, during the characterization studies, no living samples were introduced into the membrane insert on the device. Upon completion of the device characterization, there is opportunity for the device to be utilized in new research avenues, such as utilizing 3D cell culture technology to be seeded in the membrane insert to allow the monitoring of tissue like spheroids to further mimic *in vivo* environments, specifically the effect on tumors upon dosing with the chemotherapeutic agent irinotecan. Also, exploring multiple day dosing of bacteria with antibiotics within the confines of the device would yield information regarding bacteria resistance. The simplicity of the device design allows a wide variety of cell types to be cultured in the cell culture inserts, while simultaneously flowing a multitude of solutions through the channel, thereby allowing the experimental setup to be very flexible. The solutions flowing through the channel can include drugs, buffers,

even other cell types like red blood cells. In Chapter 5, several projects will be discussed that utilized the 3D printed diffusion based dynamic *in vitro* PK/PD model for applications in various research fields.

5.2 Further Characterization

The last characterization of the device monitored the amount of fluorescein absorbed into the device channels, which will factor into attempting to manipulate the half-life through gradients. With the empirical determination of the correction factor, which accounts for the concentration of analyte absorbed into the channel, thereby allows the manipulation of the half-life and subsequent determination of a prediction model for the half-life. A future prediction model for half-lives would include pumping various gradients of analyte through the channel for specific time points. For example, the concentration of the drug flowed under the channel, upon being varied in a gradient fashion, for example, the concentrated drug is added to the insert, while 75% drug was flowed through the channel for the first hour, 50% of the concentrated drug the second hour, 25% the following hour, before flowing pure buffer, with the actual concentrations being varied over time. By varying the concentration of drug under the membrane insert, the concentrated drug in the insert experiences different concentration gradients, thus allowing manipulation of the diffusion of drug from the insert. Integrating an automated gradient pump would also be an added improvement over the stepwise varying of concentration in the channel currently

used during gradient studies. The programmable gradient pump would allow for smooth concentration transitions to be employed during flow. A prediction model for the half-life can be determined by varying the aforementioned gradient over various time points. By predicting the half-life, the *in vitro* studies are better able to mimic actual *in vivo* studies. Another parameter worth exploring is further reducing the half-life, however this could ultimately require a new device design.

5.3 3D Cell Culture Incorporation in the 3D Printed *In Vivo* Device

3D cell culture, or more commonly called spheroids, utilizing various cell types,¹⁻⁴ has been used with the overarching goal of mimicking actual tissues.⁵⁻⁷ For example, Li *et al.* showed the effect of administering irinotecan, a chemotherapeutic agent, to 3D cultured HCT 116 colon carcinoma multicellular spheroids in a stagnant environment.⁸ The statically dosed spheroids were then sliced into cross sections and analyzed using matrix aided laser desorption ionization (MALDI) imaging mass spectrometry to measure the depth at which irinotecan penetrated the cellular tissue and effectively damaged or killed the cells. This dosing was performed in a static environment, therefore in order to further model *in vivo* studies the dosing of irinotecan should be manipulated under various rates, concentrations and eliminates as achieved in patients, as can be achieved in the 3D printed PK/PD device. Incorporation of 3D cell culture tissue only aids in mimicking *in vivo* PK profiles and as such would make the

diffusion based dynamic *in vitro* 3D printed device a more powerful tool when used in tandem with animal models.

5.3.1 Experimental Method

5.3.1.1 Preparations of Solutions

Fluorescein Stock and Working Solutions

Fluorescein stock solutions (332.31 g/mol, Sigma Aldrich, St. Louis, MO, USA) were prepared as described in section 4.2.2. In short, a stock solution of 100 ppm was prepared by weighing out the appropriate amount of fluorescein and diluting with deionized water. Further diluting the stock with deionized water made the appropriate working solutions.

Irinotecan Stock and Working Solutions

Irinotecan stock solutions were prepared by dissolving the compound in deionized water for a final concentration of 0.5 mg/mL. Further dilutions, for the working solutions, were made by diluting the stock solutions in PSS.

Camptothecin Stock and Working Internal Standard Solutions

The internal standard, camptothecin, stock solution was dissolved in water for a concentration of 0.5 mg/mL. The stock solution was diluted with of acetonitrile (550 nM) and was kept on ice. The working solution of the internal standard (200 μ L) was added to 5 μ L of the diluted sample solution.

5.3.1.2 Analysis of Irinotecan using Multiple Reaction Monitoring Liquid Chromatography-Mass Spectrometry

The detection of irinotecan was similar to that of levofloxacin as described in section 3.2.5. Again, the 96 well polycarbonate PCR plate containing samples was placed in the autosampler, which injects 10 μ L of sample into the Shimadzu ultra performance liquid chromatography (UPLC) instrument. Using a reverse phase chromatography column, i.e., Supelco Ascentis Express C18 column (length: 3 cm; i.d.: 2.1 mm; particles: 2.7 μ m; Supelco, Bellefonte, PA, USA), irinotecan and camptothecin were separated with the following retention times: 1.10 min and 1.22 min, respectively. The following solvents, 1% formic acid in water (A), acetonitrile (B) and methanol (C) were used in the corresponding gradient, 95% A, 0% B for 0.25 min; 2% A, 0% B at 1.00 min; hold 2% A, 0% B until 1.25 min; 30% A, 15% B at 1.75 min; Hold 30% A, 15% B until 1.90 min; 95% A, 0% B at 2.00 min. Upon exiting the UPLC system, the sample is vaporized and ionized using electrospray ionization before being introduced to the Waters Quatro Micro triple quadrupole mass spectrometer and analyzed using Waters MassLynx software. Specific parameters such as cone voltages, collisional energy, parent ions, daughter ions, can be found in Table 5.1.

Drug	Irinotecan	Camptothecin
Molecular Weight (g/mol)	586.67	348.52
Parent Ion (m/z)	587.24	349.23
Daughter Ion (m/z)	167.12	305.18
Retention Time (min)	1.10	1.22
Cone Voltage (V)	46	40
Collisional Energy (eV)	34	22
Collision Gas (Torr)	1.96 x 10 ⁻³	

Table 5.1 LC/MS/MS Parameters for Irinotecan and Camptothecin.
Table depicting LC/MS/MS parameters, e.g., molecular weight, parent ion, retention time, cone voltage, collisional energy and collisional gas.

5.3.2 Results and Discussion

5.3.2.1 Validating Existing Prediction Model

The prediction model described in Chapter 4 had only been tested and validated with molecules of similar molecular weight, i.e., levofloxacin and fluorescein. The molecule of interest, irinotecan (586.68 g/mol), has a significantly larger molecular weight than fluorescein (332.31 g/mol). To validate the existing prediction model for the larger molecule, identical concentrations (52.6 μM) of both molecules were flowed through the channels of the device for 1 hour before being swapped for buffer (irinotecan) or for water (fluorescein, Figure 5.1). Samples (5 μL) were taken every 30 minutes and diluted with the respective buffer or water (100 μL). Samples taken of fluorescein were analyzed in a plate reader while the irinotecan samples were analyzed using MRM-LC/MS/MS. The irinotecan saw a significantly lower C_{max} ($9.97 \pm 0.67 \mu\text{M}$) than fluorescein ($13.82 \pm 1.09 \mu\text{M}$; $p < 0.001$), therefore a new prediction model would be needed for irinotecan. A full PK curve was not completed in Figure 5.1, due to only requiring the C_{max} for a comparison the two analytes in the prediction model. A new prediction model would only entail flowing various concentrations of irinotecan for approximately an hour with sampling every 15 minutes. The slope pertaining to the concentration in the insert with respect to time is plotted versus

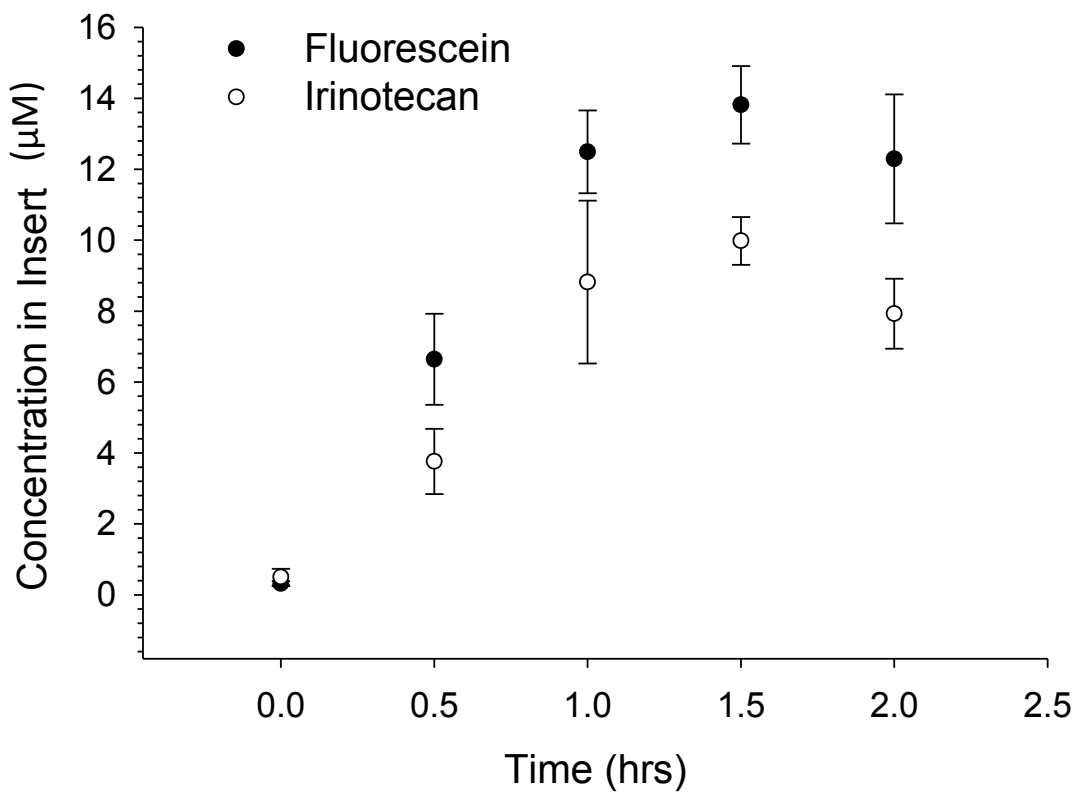


Figure 5.1 Validating Irinotecan Loading Profile with Prediction Model. Irinotecan (586.68 g/mol) is a larger molecule than fluorescein (332.31 g/mol), which was the molecule, originally used to formulate the prediction model. Both analytes were flowed at initial concentrations 52.6 µM with irinotecan resulting in a C_{max} of 9.97 ± 0.67 µM, which is significantly less than fluorescein's C_{max} (13.82 ± 1.09 µM; $p < 0.001$). Therefore irinotecan needs a specific prediction model characterized. $n \geq 4$, error = standard deviation

the original concentration of drug flowed. A prediction model for C_{\max} is obtained from the resulting slope, i.e., rate of loading versus original concentration. Overall, obtaining a new prediction model would entail a day of flowing and analysis thus does not require an excess of time or materials.

5.3.2.2 Elimination Profile

In section 5.3.2.1, prediction models established for fluorescein and levofloxacin were validated for irinotecan. The prediction model mimics an oral dosing, however irinotecan is typically administered through IV dosing. To mimic the IV dosing, concentrated irinotecan (5.78 μM) was directly added to the membrane insert (75 μL), while PSS was flowed through the channel. Samples (5 μL) were taken from the cell culture insert over a period of 5 hours and analyzed using MRM-LC/MS/MS (Figure 5.2). Validating that the depletion followed first order rate kinetics was determined by taking the natural log of the concentrations in the insert, obtained in Figure 5.2, with respect to time (Figure 5.3). The resulting line ($r^2 = 0.9742$) is indicative of first order rate kinetics, and the half-life, obtained from the slope of the line, was 1.69 hours. Furthermore, the first order elimination relationship is crucial due to a majority of drugs being eliminated through first order rate kinetics.

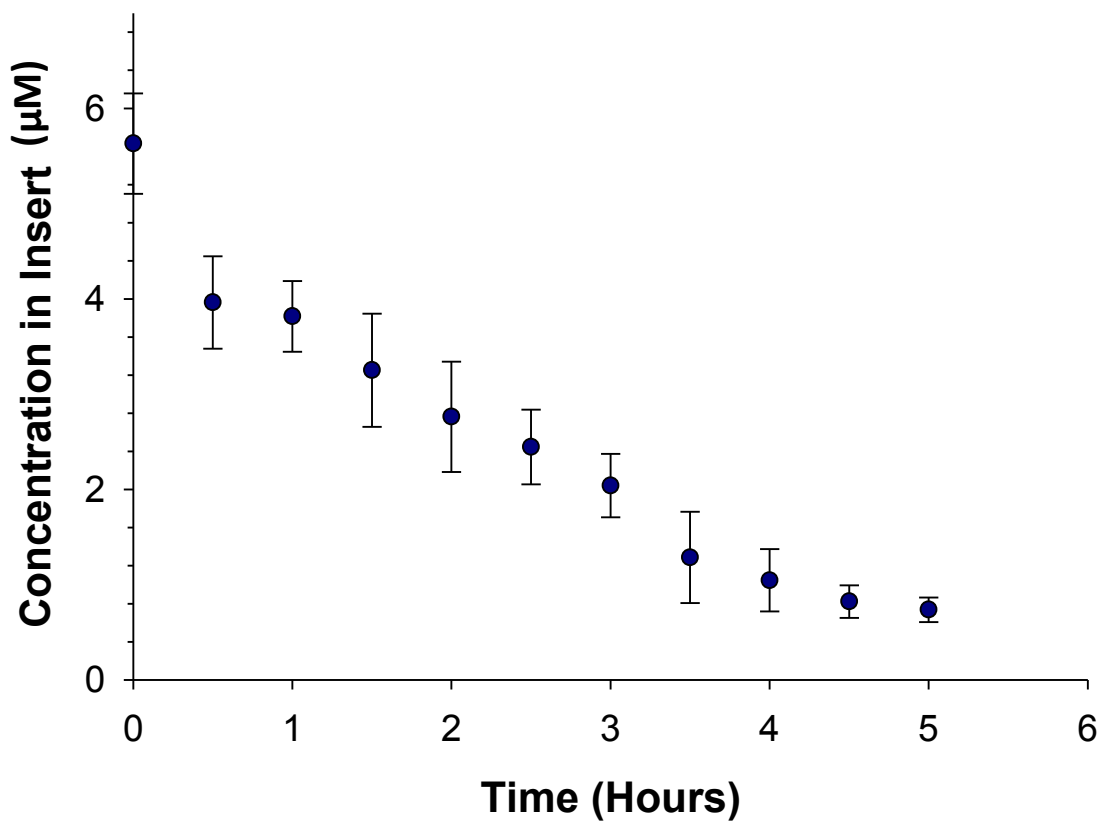


Figure 5.2 Elimination Profile for Irinotecan. Irinotecan (5.78 µM) was added to the membrane insert (75 µL) while deionized water was flowed through the channel. Samples (5 µL) were taken every 30 minutes. $n \geq 4$, error = standard deviation

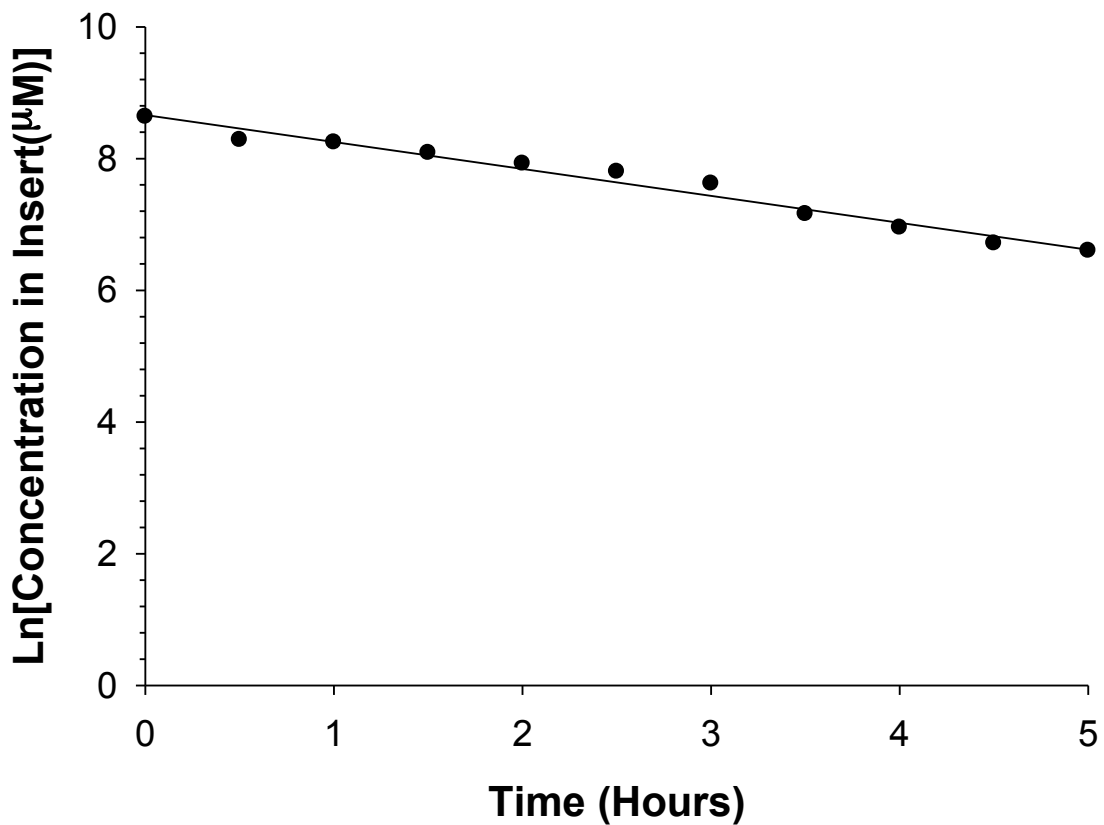


Figure 5.3 Validating First Order Rate Elimination. The natural log of the concentration in the insert with respect to time derived from Figure 5.2 resulted in a linear relationship ($r^2 = 0.9742$). The linear relationship is indicative of first order rate kinetics. The half-life, obtained from the slope of the line was 1.96 hours.

5.4 Multiple Day Dosing of Bacteria for Future Antibacterial Resistance Studies

Sir Alexander Fleming discovered the first antibiotic, penicillin, in 1929. Since then antibiotics have become an integral part of our society resulting in an overall longer life expectancy.⁹ However, an increasingly alarming number of bacteria, e.g. 70%, have become resistant to at least one of the commonly used antibiotics. The first resistances were reported as early as 1946, in the same year that penicillin was first marketed. For example, 450,000 multi-resistance cases of tuberculosis were reported in 2012. Resistances have also been reported in malaria, influenza, and HIV cases. Perhaps more alarming is the developing resistance to bacteria responsible for common infections such as urinary tract, pneumonia, and ear.¹⁰ These resistances are fueled, in part, due to misuse of patient adherence, antibiotics being prescribed inappropriately, as well as, antibiotics being used as growth stimulants in livestock.¹¹ The latter cause was recently the target of a Food and Drug administration guidance for industry urging the practice of incorporating antibiotics in feed as growth stimulants to end.¹² The World Health Organization (WHO) has recently addressed the concerns of bacterial resistance by making the theme of World Health Day 2011 antibacterial resistance.¹³ Also in 2014, the WHO published a report concerning a surveillance of antibacterial resistance that called for increasing research efforts to find new antibiotic drugs needed to treat the resistant bacteria as well as new strains of infectious bacteria.¹⁰ Driving the

search for new antibiotics stems from the fact that a new class of antibiotics has not been discovered since 1987.¹¹ The Center for Disease Control (CDC) published a threat report, *Antibiotic Resistance Threats in the United States: 2013*, addressing the current state of antibiotic resistance, impact, and effect.¹⁴ Overall, antibacterial resistance is a global concern that could plunge us into a post antibacterial age, in which, common infections could prove difficult or even impossible treat unless new practices and research are implemented.¹⁵ The 3D printed diffusion based dynamic *in vitro* device offers to ability to monitor bacterial kill rates while mimicking *in vivo* dosing. The device design allows flexible experimental designs for personalized set ups.

5.4.1 Experimental Method

5.4.1.1 Preparation of Solutions

Levofloxacin Stock and Working Solutions

Levofloxacin stock and working solutions were prepared as previously described in section 3.2.1. In short, the stock solution (1 mg/mL) was prepared by diluting levofloxacin in 50% methanol and water. Working solutions were prepared by further diluting the stock solution with PSS until the desired concentrations are reached.

Ciprofloxacin Stock and Working Internal Standard Solutions

Ciprofloxacin stock and working solutions were prepared as previously described in sections 3.2.1. Briefly, stock solutions of ciprofloxacin were prepared by diluting ciprofloxacin in deionized water until a 1 mg/mL concentration is reached. A working internal standard solution was prepared by taking 550 μ L of the stock solution and diluting with 5 mL of acetonitrile before placing in an ice bath until needed. Samples taken from the sample insert were diluted with 100 μ L of buffer before a 5 μ L aliquot was further diluted with the working internal standard solution.

5.4.1.2 Bacteria Culture Growth, Purification, and Viability Assay

Kanamycin-resistant *Escherichia coli* (*E. coli*) (BL21DE3, Novagen) was prepared by adding 1 mL of thawed stock (1:1 in 50% glycerol) to sterilized Lysogeny Broth (LB Lennox, EMD) with 50 μ g/mL kanamycin added. The solution, i.e., media, antibiotic, and bacteria, was subsequently shaken for 14 hours at 180 RPM at 37°C. After 14 hours, 30 mL of culture was transferred to a 50 mL polypropylene centrifuge tube (Greiner Bio-One). The sample was centrifuged for 15 minutes at 3000 x g to obtain a pellet. The supernatant was removed by aspiration, and two milliliters of BSA Free PSS was added. The pellet was resuspended using a vortex mixer (Fisher Scientific), and 1 mL of the suspension was added to 30 mL of BSA Free PSS. The sample was centrifuged 2x more at 3000 x g for 15 minutes and supernatant was aspirated off each time.

The resulting pellet was resuspended in 10 mL BSA Free PSS, and the optical density was adjusted to 0.06 OD_{670nm} using a commercial plate reader (SpectraMax) and a 96-well clear polycarbonate plate (Greiner).

Agar plates for bacteria plating was prepared by autoclaving LB (20g/L) with added agar (15g/L, VWR) for 45 minutes. After autoclaving, the solution was allowed to cool to 50°C before 50 µg/mL of kanamycin was added to the solution. Agar was immediately added to polycarbonate plates and allowed to cool before storing in refrigerator for up to 1 month.

The viability assessment of bacteria after dosing was performed using the BacLight Kit (Invitrogen). The kit contains the two nuclear dyes, SYTO9 and propidium iodide (PI). SYTO9 enters all cells regardless of membrane permeability, and PI only enters cells with compromised membranes. Using this principle, standards containing ratios of dead (fixed with 70% ethanol) and live bacteria were mixed. The standards were added in triplicate to a 96 well plate and an equal volume of SYTO9/PI mix (5 µM and 30 µM working concentrations, respectively) was added to the wells and incubated for 15 minutes. Signal from both fluorophores (ex: 488 nm), SYTO9 (em: 530 nm) and PI (em: 630 nm) and were read using the plate reader. The ratio of SYTO9 to PI fluorescence was plotted against % bacteria live to yield a calibration curve. Subsequent samples were analyzed using the obtained calibration curve.

5.4.2 Results and Discussion

5.4.2.1 Multiple Day Dosing of *Escherichia coli* with Levofloxacin

A multiple day dosing of *E. Coli* with the antibiotic levofloxacin was performed on the 3D printed device (Figure 5.4). Each day, *E. coli* suspended in BSA free PSS buffer was added to the membrane insert (75 μL) and concentrated levofloxacin (119.28 μM) was flowed through the channel for one hour before being switched with BSA free PSS buffer. The target C_{max} was 25.6 μM , which mimics the internal concentration of a urinary tract infection dosing of 250 mg levofloxacin over 3 days.^{16,17} The buffer is allowed to flow for 5 hours before the bacteria is collected, sampled, and incubated overnight for recovery. A second dosing was repeated the following morning, thereby mimicking the administration of a second 250 mg levofloxacin dosing, followed by a third dosing on the subsequent day. At the completion of each day the bacteria sample is collected and analyzed using viability staining and a plate reader. As the dosing was preliminary, conventional plating procedures will be done to validate plate reader and flow cytometry findings for future studies. As seen in Figure 5.4, the prediction model worked as expected with all C_{max} values, i.e., Day 1: 18.66 ± 6.48 μM ; Day 2: 25.64 ± 4.23 μM ; Day 3: 20.01 ± 5.27 μM , being within error of the expected C_{max} of 25.6 μM . The actual dosing represents a PK profile. The effect of the drug on the bacteria is a PD parameter, and as such, after Day 1 there was $83.4 \pm 12.4\%$ of bacteria remaining alive as obtained by the viability

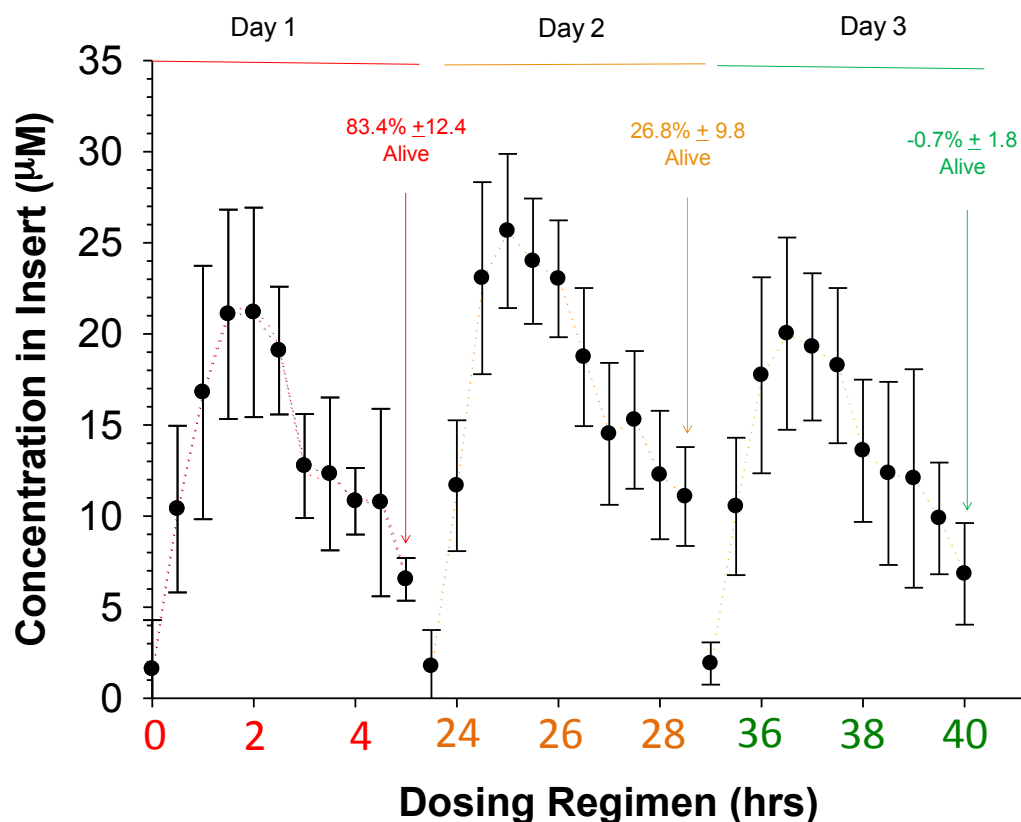


Figure 5.4 Multiple Day Dosing of *Escherichia coli* with the Levofloxacin Antibiotic. Concentrated levofloxacin (119.28 μM) was flowed through the channels for 1 hour, with the desired C_{max} reaching 25.6 μM , before being swapped for BSA free PSS buffer while *E. coli* was seeded in the cell culture inserts. The process was repeated over three days while the *E. coli* sample was monitored for cell death at the conclusion of each day. The resulting, significantly similar C_{max} , based on days were $18.66 \pm 6.48 \mu\text{M}$, $25.64 \pm 4.23 \mu\text{M}$, $20.01 \pm 5.27 \mu\text{M}$. $n \geq 4$

assay using the plate reader. Plating in future studies will confirm this number as well as determine if any bacteria, factored in as alive, were actually damaged to the point that they were not able to reproduce. Following the second day of dosing $26.8 \pm 9.8\%$ were alive and $-0.7 \pm 1.8\%$ were alive after Day 3. The data shown is preliminary due to lack of relevant controls, i.e., plating data, bacteria counts at the beginning of each day, static growth experiments, static drug experiments, however the potential of the device is displayed for applications in monitoring drug dosing of in a dynamic, diffusion based millifluidic 3D printed device.

5.4.2.2 Characterization of Multiple Dosing Before Steady State

An additional parameter, to further mimic *in vivo* PK profiles is the applying multi-day dosing to achieve steady state (Figure 5.5). A preliminary experiment (Figure 5.6) demonstrated the effect of administering three dosings, i.e., denoted by the red arrows in Figure 5.6, of fluorescein to a device over a 5.5 hour period. A sample of concentrated fluorescein ($120 \mu\text{M}$) was flowed through the 3D printed device's channels while $75 \mu\text{L}$ of deionized water was added to the membrane insert. The concentrated fluorescein was flowed for 30 minutes before being swapped for deionized water. After the water was flowed for 1 hour, a second dosing of concentrated fluorescein ($120 \mu\text{M}$) was dosed for 30 min. Just as in the last dosing, at the completion of the 30 minutes the concentrated

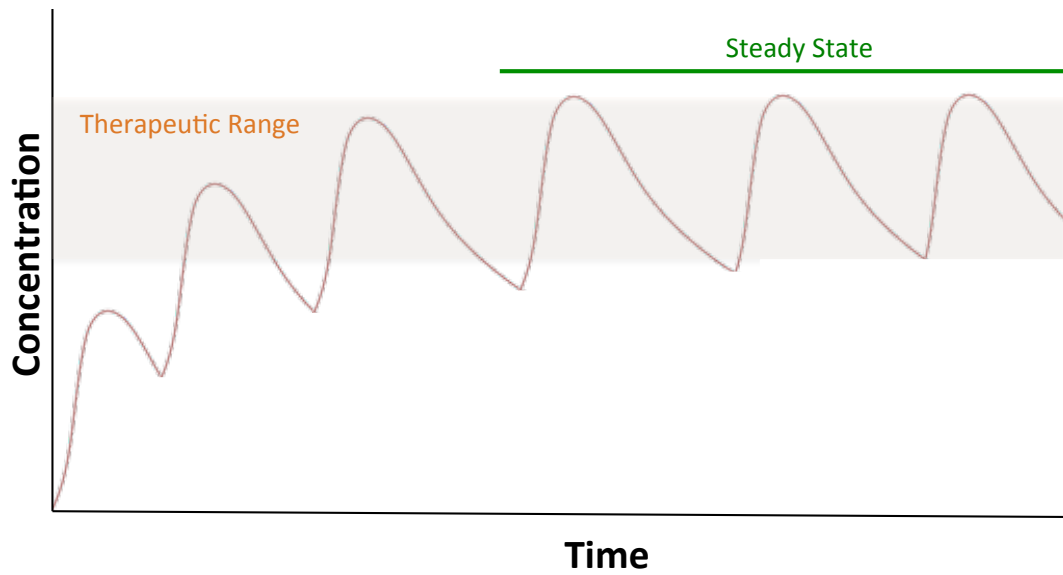


Figure 5.5 Schematic of Multiple Dosing Prior to, and Reaching Steady State. A schematic of the concentration versus time graph representing multiple dosings before steady state in the therapeutic range is reached.

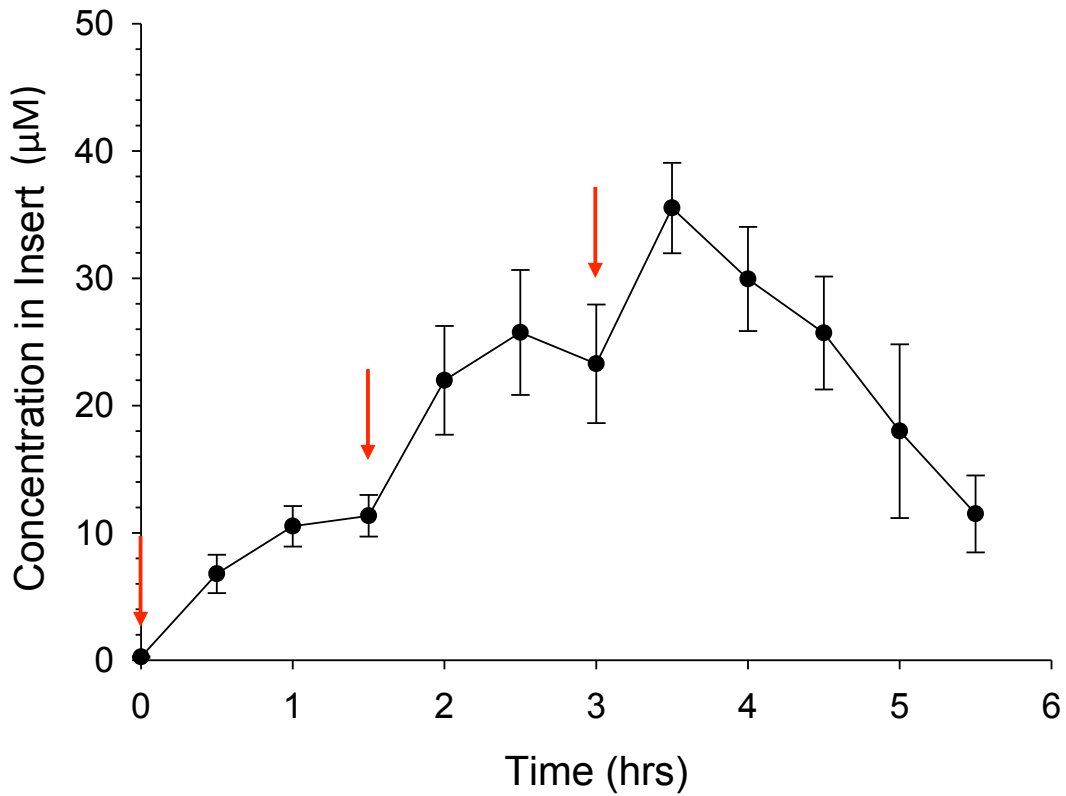


Figure 5.6 Preliminary Example of Multiple Dosing over 5.5 Hours on the 3D Printed *In Vitro* Device. Three sets of dosings of concentrated fluorescein (120 µM) were administered over 5.5 hours. The concentrated fluorescein was flowed through the channel for 30 minutes before being switched with deionized water for 1 hour and repeated a total of two more times. The red arrows indicate the beginning of flow for the concentrated fluorescein. $n \geq 4$, error = standard deviation

drug was replaced with deionized water that was flowed for a total of 1 hour, followed by the subsequent third dosing. Figure 5.6, while preliminary, demonstrates the ability to mimic the front part of Figure 5.5, in which the dosing has not reached steady state. Additional characterization of this process, such as predicting dosing concentrations and if steady state can be achieved in the 3D printed diffusion based dynamic *in vitro* PK device is needed. As this dosing is characterized, it further mimics *in vivo* environments, thus broadening the potential applications of the device for future studies in various PK/PD fields.

5.5 3D Printed Custom Labware

The 3D printing technology has only just begun to be utilized in academic research laboratories and has barely breached the surface of the impact in which that will be made, not only in experimental platforms such as the *in vitro* PK/PD device, but in customized, i.e., specialized, labware. Customized labware will revolutionize how experiments are set up. As seen in Figure 4.17, 3D printed T-junctions (clear) were used in tandem with commercially purchased T-junctions (black) with the same resulting effect. An example of the commercial and the 3D printed T-junction, in close proximity can be observed in Figure 5.7. The commercial fittings cost approximately \$50 per fitting and take a week or two to arrive, post ordering, in contrast to the printed parts, which cost under \$2 to print and are available mere hours after submitting to print. Moreover, custom locking

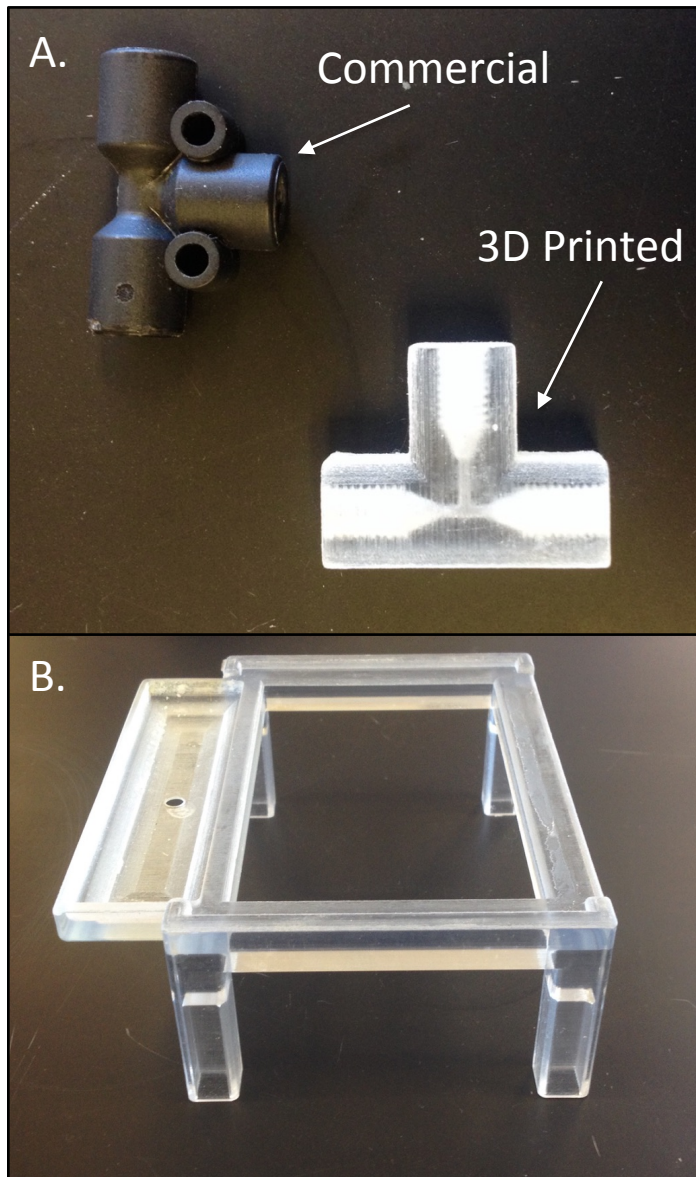


Figure 5.7 Images of 3D Printed Custom Labware. A. Comparison of the commercially purchased T-junction fitting and the 3D printed T-junction fitting. B. 3D printed base to hold the 3D printed device while simultaneously collecting waste.

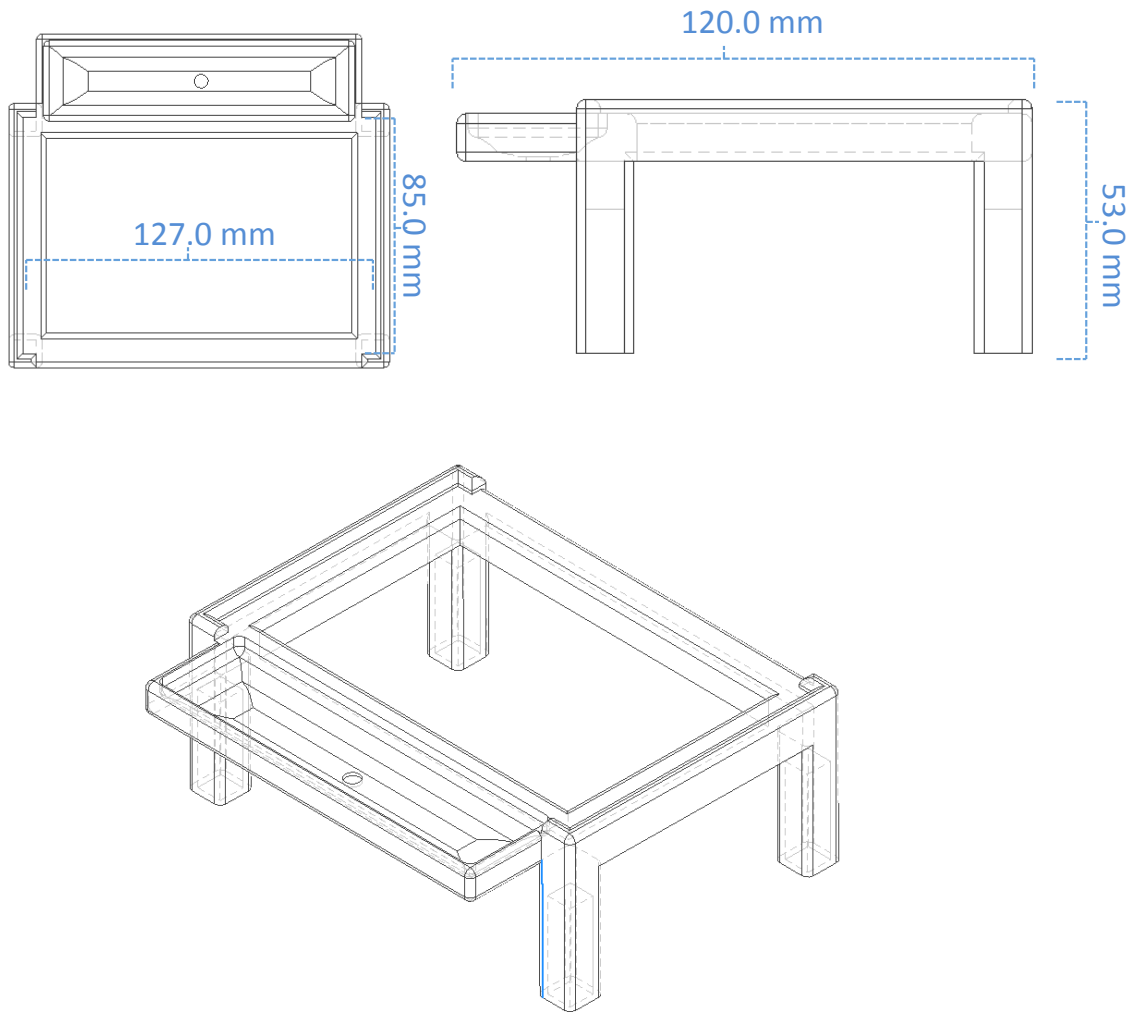


Figure 5.8 Computer Aided Design Images of 3D Printed Custom Labware. CAD file of the 3D printed base holder from various viewpoints, along with specific dimensions.

fittings, as seen in Figures 4.22, 4.23, and 2.24 would not be available for commercial ordering unless being custom embossed, which is costly and time consuming. Twelve of special fittings were printed in approximately an hour at under \$2 per fitting.

An additional example of custom labware can be seen in Figure 4.22 and 5.7, as the base holding the 3D printed *in vitro* device. Figure 5.8 shows the CAD files of the base, along with the corresponding dimensions. Initially waste was extremely difficult to collect and manage in early prototypes, thereby highlighting the need of a holder to collect and manage the waste. Using CAD software, the base was designed to, not only, collect waste, but also perfectly fit the 3D printed *in vitro* device.

A last example of 3D printed custom labware was the designing of a portable 3D printed peristaltic pump (Figure 5.9). The CAD file can be seen in Figure 5.10, as well as specific dimensions of the side, front, and top view of the pump, which can be found in Figure 5.11. The pump is hand held and can be pumped for over 24 hours. The only commercial parts are the motor (CNDF 140227, 5 RPM), one screw to hold the motor in place, peristaltic tubing, battery (Cabela's; 12V, 8.0 amp) and a circuit board to control the speed of rotation and on/off function (RioRand; RRCCM2SPC Adjustable DC Motor Speed PWM

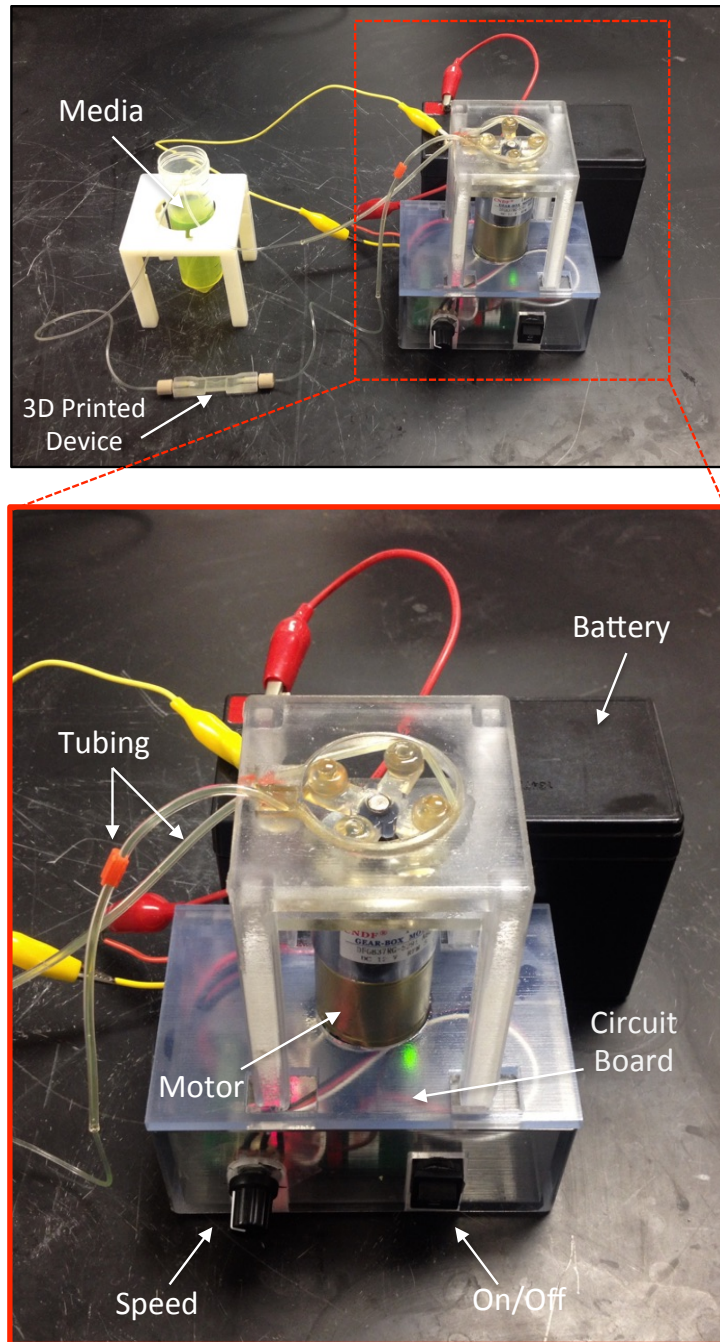


Figure 5.9 Images of the 3D Printed Peristaltic Pump Setup. Top. Images of 3D printed pump setup while tubing was incorporated with the 3D printed device containing endothelial cells and constantly perfusing media. In the image, the tube that traditionally holds media contains fluorescein for aesthetic purposes. Bottom. Zoomed in image of the 3D printed pump. Behind the pump is the 24V battery. The terminals are connected the a circuit board, i.e., on/off switch and speed control, contained below the pump and connected to the motor. The setup is isolated and can be contained in an incubator for at least 12 hour periods.

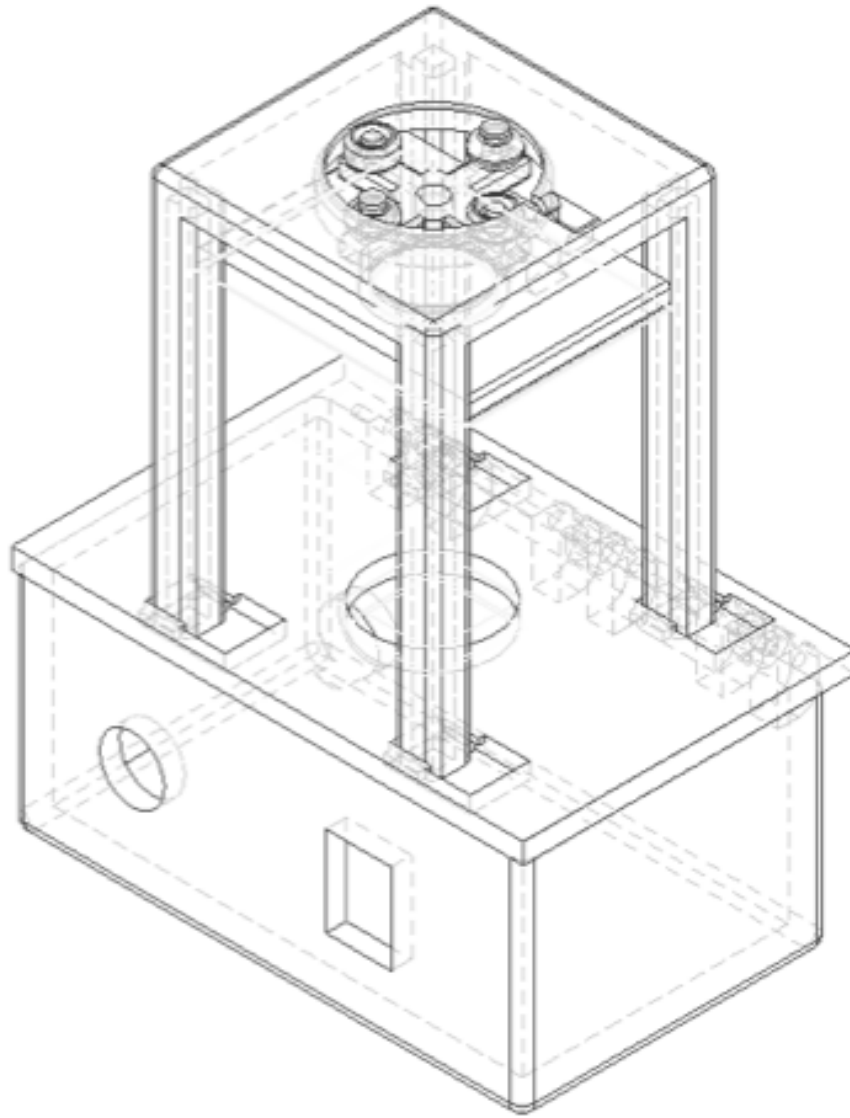


Figure 5.10 Computer Aided Design Model of the 3D Printed Peristaltic Pump Setup. CAD file of the 3D printed peristaltic pump with all of the 3D printed parts in place.

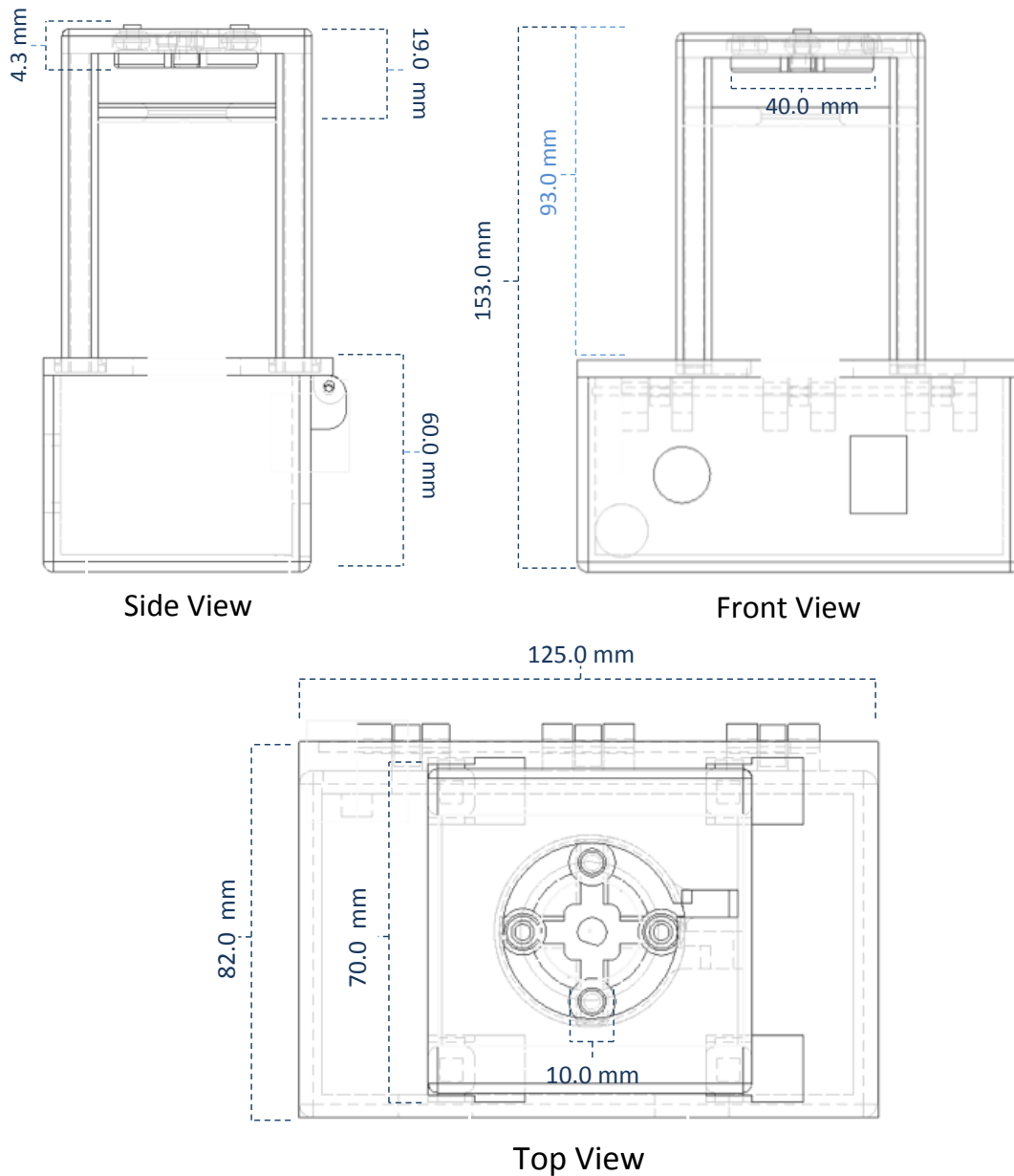


Figure 5.11 Computer Aided Design Model of the 3D Printed Peristaltic Pump Setup and Corresponding Dimensions. CAD file of the 3D printed peristaltic pump with all of the 3D printed parts in place from the top, side and front views. Corresponding dimensions are noted from the various view points.

Controller 12V, Reversing Switch, 120W). The 3D printed pump fits in cell culture incubators, and can be used in cell viability studies to incorporate flow into 3D printed devices, which contain cells seeded in their channels. By exposing the growing cells to continuously flow through the channel, an environment, closely mimicking that of *in vivo*, is experienced by the adhered cells. The pump is yet another example of 3D printing influencing studies in ways that would require outside design and extruding to implement in current research environments.

The adaptations made by 3D printing to the experimental setup not only reduced cost in some instances but made the set up easier on the researcher. In all honesty, upon access to a 3D printer, implementing and incorporating 3D printing into research laboratories will result in increased efficiency, maybe not for the actual measurements, but for the time spent by the actual researcher. 3D printing, on a broader scale, as the technology develops could potentially lead to the third industrial revolution.

REFERENCES

REFERENCES

- (1) Abbott, A.: Cell culture: biology's new dimension. *Nature* **2003**, *424*, 870-872.
- (2) Langer, R.; Tirrell, D. A.: Designing materials for biology and medicine. *Nature* **2004**, *428*, 487-492.
- (3) Lavik, E.; Langer, R.: Tissue engineering: current state and perspectives. *Applied microbiology and biotechnology* **2004**, *65*, 1-8.
- (4) Lee, J.; Cuddihy, M. J.; Kotov, N. A.: Three-dimensional cell culture matrices: state of the art. *Tissue Engineering Part B: Reviews* **2008**, *14*, 61-86.
- (5) Haycock, J. W.: 3D cell culture: a review of current approaches and techniques. In *3D Cell Culture*; Springer, 2011; pp 1-15.
- (6) Justice, B. A.; Badr, N. A.; Felder, R. A.: 3D cell culture opens new dimensions in cell-based assays. *Drug discovery today* **2009**, *14*, 102-107.
- (7) Pampaloni, F.; Reynaud, E. G.; Stelzer, E. H. K.: The third dimension bridges the gap between cell culture and live tissue. *Nat Rev Mol Cell Biol* **2007**, *8*, 839-845.
- (8) Liu, X.; Weaver, E. M.; Hummon, A. B.: Evaluation of Therapeutics in Three-Dimensional Cell Culture Systems by MALDI Imaging Mass Spectrometry. *Analytical Chemistry* **2013**, *85*, 6295-6302.
- (9) Fleming, A.: On the antibacterial action of cultures of a penicillium, with special reference to their use in the isolation of *B. influenzae*. *British journal of experimental pathology* **1929**, *10*, 226.
- (10) "ANTIMICROBIAL RESISTANCE Global Report on Surveillance " World Health Organization, 2014.
- (11) Huttner, A.; Harbarth, S.; Carlet, J.; Cosgrove, S.; Goossens, H.; Holmes, A.: Antimicrobial resistance: a global view from the 2013 World Healthcare-Associated Infections. **2013**.
- (12) " New Animal Drugs and New Animal Drug Combination Products Administered in or on Medicated Feed or Drinking Water of Food-Producing

Animals: Recommendations for Drug Sponsors for Voluntarily Aligning Product Use Conditions with GFI," Food and Drug Administration, 2013.

(13) Antimicrobial resistance: no action today, no cure tomorrow. World Health Organization, 7 April 2011.

(14) "Antibiotic resistance threats in the United States, 2013," Center For Disease Control and Prevention, 2013.

(15) Laxminarayan, R.; Duse, A.; Wattal, C.; Zaidi, A. K.; Wertheim, H. F.; Sumpradit, N.; Vlieghe, E.; Hara, G. L.; Gould, I. M.; Goossens, H.: Antibiotic resistance—the need for global solutions. *The Lancet infectious diseases* **2013**, *13*, 1057-1098.

(16) LEVAQUIN (levofloxacin) tablet, film coated U.S National Library of Med. , 2010; Vol. 2013.

(17) "Levofloxacin 250 mg Film Coated Tables," 2010.